

REPORT DOCUMENTATION PAGE

Public reporting burden for this collection of information is estimated to average 1 hour per reporting burden. This burden is caused by gathering and maintaining the data needed, and completing and reviewing the collection of information, including suggestions for reducing this burden, to Washington Head Davis Highway, Suite 1204, Arlington, VA 22202-4302, and to the Office of Management and Budget, Paperwork Reduction Project (0704-0188), Washington, DC 20503.

0521

existing data sources,
other aspect of this

1. AGENCY USE ONLY (Leave blank)			2. REPORT DATE	3. REPORT TYPE AND DATES COVERED
				Final Technical Report 1 May 93 to 31 Dec 97
4. TITLE AND SUBTITLE			5. FUNDING NUMBERS	
Integrated Microtransducer and Neural Network Systems for Distributed Control			F49620-93-1-0332	
6. AUTHOR(S)				
Professor Chih-Ming Ho				
7. PERFORMING ORGANIZATION NAME(S) AND ADDRESS(ES)			8. PERFORMING ORGANIZATION REPORT NUMBER	
Mechanical & Aerospace Engineering Department University of California, Los Angeles Bldg Eng. IV, Room 38-137J Los Angeles, CA 90095-1597				
9. SPONSORING/MONITORING AGENCY NAME(S) AND ADDRESS(ES)			10. SPONSORING/MONITORING AGENCY REPORT NUMBER	
AFOSR/NA 110 Duncan Avenue, Ste B115 Bolling AFB, DC 20332-8050			F49620-93-1-0332	
11. SUPPLEMENTARY NOTES				
12a. DISTRIBUTION AVAILABILITY STATEMENT			12b. DISTRIBUTION CODE	
Approved for public release; distribution unlimited.				
13. ABSTRACT (Maximum 200 words)				
For a phenomenon with a wide spread of length scales, e.g., turbulence, a large scale integrated transducer system can facilitate communication of the local information measured by individual sensors as well as identify the global characteristics through a collection of the sensors. The actuators then can, based on the local and global information, execute the proper control strategy.				
This concept is best illustrated by research in turbulence control. Surface shear stress reduction in the turbulent boundary layer is the grand challenge in fluid mechanics research. Many randomly distributed small flow structures in the boundary layer are responsible for drag production. In this project, we developed an integrated MEMS system to detect the high shear streaks and to reduce the surface shear stress.				
14. SUBJECT TERMS			15. NUMBER OF PAGES	
19980710 095				
			16. PRICE CODE	
17. SECURITY CLASSIFICATION OF REPORT		18. SECURITY CLASSIFICATION OF THIS PAGE	19. SECURITY CLASSIFICATION OF ABSTRACT	20. LIMITATION OF ABSTRACT
Unclassified		Unclassified	Unclassified	UL

*Integrated Microtransducer and Neural Network Systems
for
Distributed Control*

F49620-93-0332

Final Report

Principal Investigator

C. M. Ho
Mechanical and Aerospace Engineering Department
University of California, Los Angeles
Los Angeles, California 90095

Phone: 310-825-2369 Fax: 310-206-2302
E-mail: chihming@seas.ucla.edu

Co-Principal Investigators

R. Goodman
Y. C. Tai

C. J. Kim
K. Wang

J. Kim
J. Woo

J. Speyer

*Air Force Office of Scientific Research
University Research Initiative Program*

Integrated Microtransducer and Neural Network Systems for Distributed Control
F49620-93-0332

OBJECTIVES

The objective of this focused interdisciplinary program is to develop a microsensor-microelectronics-microactuator (m^3) system, which can execute real-time distributed control for reducing the surface shear stress in a turbulent boundary layer.

ACCOMPLISHMENTS

Major advances have been made in the following areas;

- Sensors
 - * vacuum insulated shear stress sensor array
 - * layered structure diaphragm for low heat conduction
- Actuator
 - * high off-plane displacement and large force electromagnetic actuator
 - * in-plane actuator electrostatic actuator
- Control Logic
 - * neural network based
 - * physical based
 - * model based
- M^3 System

Detailed summaries of these achievements can be found in the attached reports.

HONORS/AWARDS

Rodney Goodman
Promotion to Full Professor

Chih-Ming Ho
National Academy of Engineering (1997)
Fellow of APS (1989)
Fellow of AIAA (1994)
Ben Rich-Lockheed Martin Professor (1996)
Allied signal -UCLA Research Awards (1995)

C. J. Kim
NSF CAREER Award

John Kim

Fellow of APS (1989)
Rockwell Professor (1993)
NASA Medal for Exceptional Scientific Achievement (1985)
H. Jullien Allen Award from NASA Ames (1994)

Jason Speyer

Fellow AIAA
Fellow IEEE
AIAA Dryden Award

Y. C. Tai

Promotion to Associate Professor

K.L. Wang

Fellow of IEEE
Semiconductor Research Corporation Technical Excellence Award

J. Woo

Promotion to Full Professor

PERSONNEL SUPPORTED**Rodney Goodman**

David Babcock (Graduate Student)
Bhusan Gupta (Graduate Student) Ph.D. awarded

Chih-Ming Ho

Steve Tung (Post-Doc)
John Mai (Graduate Student). M.S. awarded

John Kim

Chang-hoon Lee (Post-Doc)

Y.C. Tai

Trevor Roper, Lab Engineer
Thomas Tsao, (Graduate Student) Ph.D. awarded
FuKang Jiang, (Graduate Student) Ph.D. awarded

Kang L. Wang

Xinyu Zheng, Research Scientist and Principal Researcher.
Shaozhong Li, (Post Doc)
Min Chen, (Graduate Student)

J. Woo/C. J. Kim

John Gill (Graduate Student) M.S. awarded

Faiz Sherman (Graduate Student) Ph.D. awarded

LIST OF PUBLICATIONS

1. Tai, Y.C. and Ho, C.M., "Silicon Micromachining and its Application", Proceedings of SPIE, vol.; 2448, pp. 141-151, 1995.
2. Huang, J.B. and Ho, C.M., "Micro Riblets for Drag Resuction", Proceedings of SPIE, Vol. 2448, pp. 245-250, 1995.
3. Tung, S., Hong, W., Ho, C.M. Liu C. and Tai, Y.C., "Control Of Streamwise Vortices in 2-D Channel Flow," *Proceedings, The 6th Congress of Asian Fluid Mechanics*, Singapore, May, 1995.
4. Huang, J., Ho, C.M., Tung, S., Liu C., and Tai, Y.C., "Micro Thermal Shear Stress Sensor With and Without Cavity Underneath," *Proceedings, IEEE Instrumentation and Measurement Technology Conference*, Waltham, Mass. U.S.A. April, 1995.
5. Joshi, Speyer, J. and Kim, J. "A systems theory approach to the control of transitional flows", Accept by *J. of Fluid Mech.* 1996.
6. Zheng, X. Y., Li, S., Chen M. and Wang, K. L., "Giant Reduction in Lateral Thermal Conductivity of Thin Si3N4/Silicon/SiO2 Membrane with a Micro Thermal Bridge", 1996 Microelectromechanical System Conference and Exposition (IMEC 1996), Atlanta, Georgia., November 1996.
7. Miller R., Burr, G., Tai, Y.C., Psaltis, D., Ho, C.M. and Katti, R, "Electromagnetic MEMS Scanning Mirrors for Holographic Data Storage," *Technical Digest, Solid-State Sensor and Actuator Workshop (accepted for publication)*, Hilton Head Island, South Carolina, U.S.A. June 1996.
8. Jiang, F., Tai, Y.C., Gupta, B., Goodman, R., Tung, S., Huang J. and Ho, C. M., "A Surface-micromachined Shear-stress Imager," Proceedings, IEEE Micro Electro Mechanical Systems Meeting, pp. 110-115, San Diego, California, Feb. 1996.
9. Ho, C. M. and Tai Y.C., "MEMS and its Applications for Flow Control". *J. of Fluids Eng.*, to appear in 1996.
10. Ho, C. M. Tung, S., Lee, G.B., Tai Y.C., Jiang, F., and Tsao, T. "MEMS - A Technology for Advancements in Aerospace Engineering", AIAA paper no. 97-0545, 1997.
11. Jiang, F., Tai, Y.C., Walsh, K., Tsao, T., Lee, G.B., Ho, C.M., " A Flexible MEMS Technology and Its First Application to Shear Stress Sensor Skin", IEEE MEMS-97 Workshop, pp. 465-470, Janpan, 1997
12. Tsao, F. Jiang, R. A. Miller, Y. C. Tai, B. Gupta, R. Goodman, S. Tung, and C. M. Ho, "An Integrated MEMS System for Turbulent Boundary Layer Control," *Technical Digest, Transducers '97*, Vol. 1, pp. 315-318, 1997.
13. Ho, C. M. and Tai Y.C., "Micro-Electro-Mechanical-Systems and Fluid Flows", Ann. Rev. of Fluid Mech., vol. 30, pp. 579-612, 1998.

14. Kimura, M., Tung, S., Liu, J., Ho, C.M., Jiang, F. and Tal, Y.C., "Measurements of Wall Shear Stress of Turbulent Boundary Layer Using Micro Shear Stress Imaging Chip", Journal of Japan Soc. of Mech. Eng., 1998.

PATENT

"A Micromachined Polysilicon Hot-wire Anemometer and Thermal Stress Sensor"

Chih-Ming Ho & Yu-Chong Tai

Patent Pending

"SOI Sensors"

Xinyu Zheng and Kang L. Wang

Patent pending

TRANSITIONS

C. M. Ho / Y.C. Tai

- NASA Dryden - flight test of micro sensors.
- Naval Surface Warfare Center - underwater shear stress sensor
- Boeing Co. – JSF wind tunnel test of shear stress sensor

J. Speyer / J. Kim

- NASA Dryden - a grant on the systems theory approach of transition control.

MEMS-Based Active Drag Reduction in Turbulent Boundary Layers

Thomas Tsao, Fukang Jiang, Chang Liu, Raanan Miller, Steve Tung, Jin-Biao Huang, Bhushan Gupta, Dave Babcock, Changhoon Lee, Yu-Chong Tai, Chih-Ming Ho, John Kim, and Rod Goodman

Abstract

Drag reduction is a problem of great interest. From a practical point of view, any object moving in a fluid experiences drag. When the objects in question are man-made vehicles, and the drag experienced by such vehicles results in increased fuel costs and decreased operating efficiencies, the effort spent to understand and reduce drag becomes an extremely worthwhile endeavor. Indeed, for as long as man has spent moving in vehicles, he has been interested in moving faster with less effort.

As an example of how important the reduction of drag would be for the airline industry, one can look at work done by Walsh [1], who, in 1985, estimated that if the viscous drag experienced on the fuselage of airplanes could be reduced by 10%, the cost savings would be on the order of \$350 million. By extrapolating to 1998 using a 3% annual rate of inflation and a more than doubling of air travel [2], those numbers translate into a savings of over \$1.1 billion.

This report is dedicated to explaining an ongoing effort to reduce drag in turbulent boundary layers through the use of a distributed MEMS (micro-electro-mechanical system) to enact active control. Emphasis will be placed on MEMS components, electronics, and control. Before details are presented, some background must be given regarding both the nature of drag and some examples of drag reduction in nature.

Background

There are many sources of drag on any object moving through a fluid. Here, we will only consider two types: pressure, or form, drag due to flow separation and viscous, or skin-friction, drag.

First of all, there is form drag, which is a result of a negative pressure differential between the front and the back of the object. A fluid moving past an object will separate from the object and cause a wake to be produced behind the object. The downstream velocity in this wake is less than the upstream velocity. By applying the laws of conservation of momentum, the velocity lost by the flow is transferred to a retarding force (which can also be thought of as a pressure differential) on the body. Race car drivers often take advantage of these pressure differentials by “drafting” or closely following the driver ahead of them and taking advantage of the fact that the leading driver is “pushing” most of the air out of the way. To reduce form drag, it is necessary to delay the onset of separation for as long as possible.

Secondly, there is viscous drag, which exists within a very thin region adjacent to the object. The existence of this “skin”, called the boundary layer, is a direct result of a boundary condition applied to the flow field known as the no-slip boundary condition. Essentially, this condition requires that the tangential velocity of any flow next to a solid boundary be equal to the velocity of the boundary itself. For a non-moving boundary, this implies a tangential velocity of zero. Within the boundary layer, then, the velocity increases in a very short distance from zero to the free-stream velocity. This fast change in

velocity results in a shearing force at the surface that is directly proportional to the gradient of the velocity with respect to the distance away from the surface. The shear stress and the drag, which is the shear stress integrated over an area, can be expressed as follows:

$$\tau = \mu \frac{du}{dy}$$

$$F_d = \int_A \tau dA$$

τ is the shear stress,
 μ is the fluid viscosity,

In a turbulent flow across a surface, many random structures [3] form. These structures are within the boundary layer, directly next to the wall, and are comprised of counter-rotating vortex pairs that travel downstream. [Figure 1] In between these vortices, faster moving (or higher momentum) fluid is brought down closer to the surface. This down-wash results in a higher velocity gradient, which results in higher shear stress and ultimately, higher surface drag. By preventing the occurrence of such structures, or by reducing their effect, it is conceivable that drag reduction is feasible in turbulent boundary layers. Typical flow conditions often yield structures which have sizes on the order of millimeters and lifetimes on the order of milliseconds. Any system designed to interact with these vortices must have sensors and actuators of the same size and with similar operating frequencies. Using MEMS, therefore, seems like a logical solution.

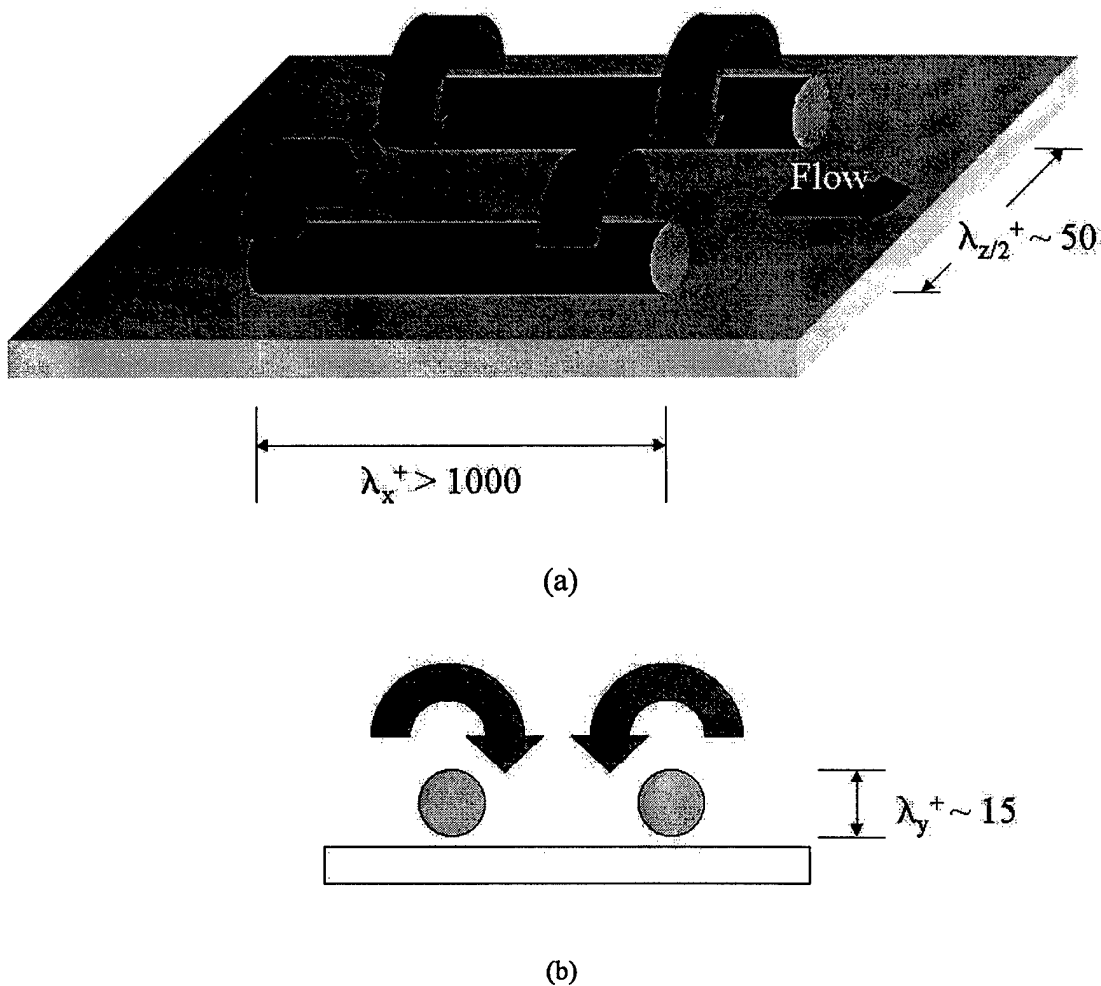


Figure 1. (a) Perspective and (b) side views of a counter rotating vortex pair where λ_x , λ_y , and λ_z refer to dimensionless lengths (kinematic viscosity divided by wall friction velocity).

In the past, much effort has been expended on the use of passive techniques, such as the use of riblets [4-9] aligned with the flow, to reduce drag in turbulent boundary layers. Drag reduction on the order of 8% [1] has been observed.

While passive drag reduction appears to be promising, it also has some drawbacks. Because the vortices occur randomly in space and time, any passive system with no sensors or feedback must necessarily be turned “on” at all times. As an example, riblets prevent high momentum fluid from being transferred down to the surface when counter-

rotating vortices pass over them. Immediately, one conclusion can be drawn from this fact: since riblets are fixed in size, they are apparently only effective when structures of a given size pass over them. Should flow parameters, and hence the structure size change, fixed-size riblets may not be effective. Riblets also result in a larger effective area over which drag can occur. As a consequence, the presence of riblets actually increases drag during unmatched flow conditions.

Therefore, any system designed to counter the effects of these vortices should be distributed and should have localized control. The distribution, however, does not necessarily need to be global. In fact, in simulations done by Choi [10], it was shown that by only controlling 5% of an area, 15% drag reduction could be effected. A conceptual drawing of a **microsensor/microactuator/microelectronics** (or M^3) unit cell is shown in Figure 2.

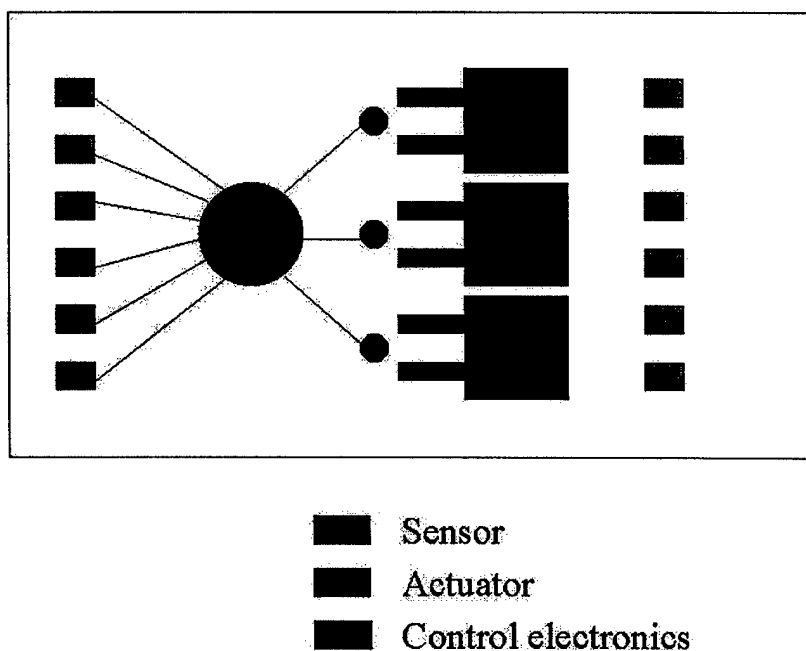


Figure 2. Drawing showing concept of a single sensor/actuator/electronic flow interaction unit.

The idea of localizing the control becomes important because of the large number of distributed M^3 units needed. In addition, it probably isn't necessary for any decision-making unit to know what is happening globally in order to make localized decisions. An example can be seen in the human nervous system. When a person accidentally touches a hot object with his hand, it is not the brain that makes the decision to pull away. Local areas of the central nervous system can make the decision, known as a reflex, before the brain is even aware of the situation. This is an example where no other information about other parts of the body is needed before the pull-back decision is made. The time saved in not sending the information to the brain minimizes the damage.

In fact, this is not the only concept in which a nature-inspired solution proves to be of interest. Much effort has been spent studying drag reduction in animals [11]. In particular to viscous drag reduction, many examples have been found in marine animals. Some involve the coverage of surfaces with various "slimes" [12]. Many fast swimming sharks [13] utilize a passive drag reduction scheme with small riblets. Passive here refers to the fact that the riblets are no more than simple attachments to the scales. No movement or control scheme is involved.

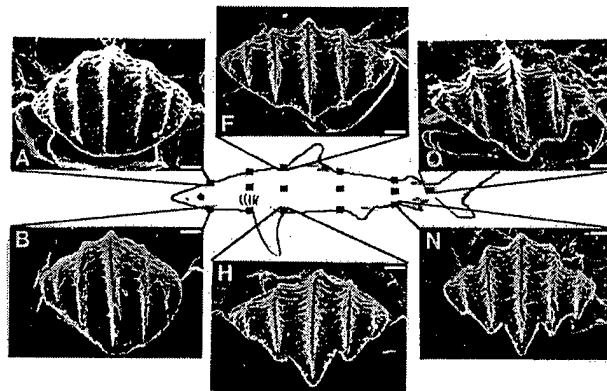


Figure 3. SEM of riblets on a fast-swimming shark. The length scale is on the order of 50 μm .

Dolphins and porpoises have been the focus of many studies. In 1936, Gray [14] performed some simple observations and calculations that resulted in his belief that the drag associated with the flow around a dolphin must be laminar, if not “better”. He believed that the flow could not be turbulent because the dolphins simply could not generate the power required to move through the water at the speeds he measured. Gray therefore postulated that dolphins have some means of turning turbulent flow laminar. In later works, others have speculated that this may be the result of compliant skins or perhaps even active control. Others [15,16,33], still, have postulated that many of Gray’s assumptions and measurement techniques were in error and that dolphins do not have any such means of reducing drag. To this day, no overwhelming evidence has been obtained proving either side correct. It is very difficult to obtain accurate experimental evidence, as the very act of observing can often affect the dolphins (i.e. the very presence of a boat may spook the dolphins into going underwater or the presence of a moving boat may generate wakes which affect the flow around the dolphins).

As a final note, whether the micromachined system will be used on aircraft for turbulent shear stress reduction remains to be seen. However, the fundamental knowledge obtained from building a M³ system for controlling an intricate natural phenomenon has broad applications for numerous engineering and scientific challenges.

Shear Stress Imager

A new MEMS shear stress sensor imager was developed for use in this project, and its capability of imaging spatial surface shear stress distributions has been demonstrated. The imager consists of multiple rows of vacuum-insulated shear stress sensors with a 300 μm pitch. This small spacing allows it to detect surface flow patterns that could not be directly measured before. The high frequency response (30 kHz) of the sensor under constant temperature bias mode also allows it to be used in high Reynolds number turbulent flow studies.

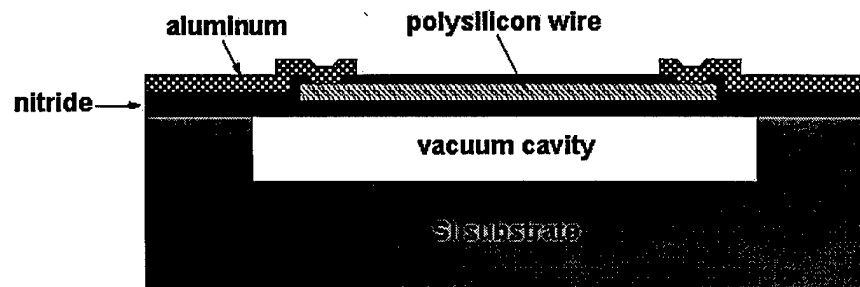
The statistical size of the drag-inducing vortex pair streak decreases as the Reynolds number of the flow increases. For a typical airflow of 15 m/s in our wind tunnel tests, and a Reynolds number of 10^4 , the vortex streaks have a mean width of about 1 mm. The length of a typical vortex streak can be about 2 cm, giving the streaks a 20:1 aspect ratio. The frequency of appearance of the streaks is approximately 100 Hz. The life-time is about 1 ms [3].

There are many ways exist to do a wall shear stress measurement [17]. Among them is the thermal method, which uses hot film sensors to determine the shear stress indirectly. This technique has many advantages over other methods for real-time flow measurement and control. For example, it can achieve high sensitivity and high frequency

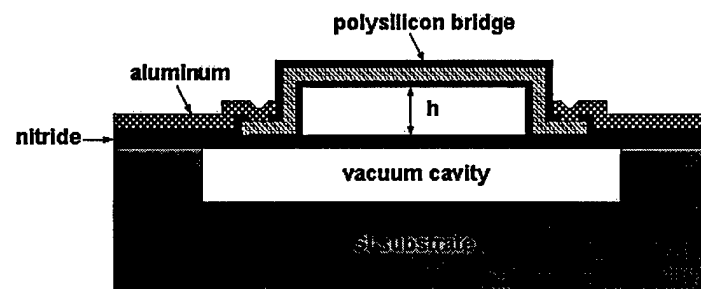
response while keeping the sensor size small. Traditional hot film sensors are electrically heated thin metal film resistors on substrates. Since the shear stress is dependant on the convection of heat, which alters the resistivity of the polysilicon, the thin film resistor needs to be isolated from the substrate, minimizing the conductive heat loss and thereby increasing sensitivity. In the past, the only way to partially solve the problem was to use low thermal conductivity materials such as quartz for the substrate. Reasonably good sensitivity could be obtained only when such sensors are used to measure high thermal conductivity fluid such as water. However, they are not sensitive enough for the measurement in low thermal conductivity fluids such as air. Moreover, the size of traditional sensors is typically in the mm range [17]. This may be tolerable in measuring the mean value of shear stress, but is definitely not acceptable in shear stress imaging with reasonable spatial resolution.

Thanks to the development of surface micromachining technology, we can optimize both the materials and the structure of the sensors. Figure 4 shows the cross-sectional structures of a few types of the micromachined shear stress sensors. Type I features a $2\text{ }\mu\text{m}$ deep vacuum cavity with a $0.25\text{ }\mu\text{m}$ thick polysilicon wire embedded in the nitride diaphragm. Here the vacuum cavity is designed to thermally isolate the diaphragm from the substrate [18]. Type II has a similar structure to type I except that the polysilicon wire is lifted $4\text{ }\mu\text{m}$ above the diaphragm, thus achieving better thermal isolation. Type III is a conventional polysilicon bridge sitting on the solid substrate [19]. Type IV is basically a micromachined hot wire close to a wall as has been previously reported. The wire is a few microns above the substrate surface and is in the linear velocity distribution region so that it measures the wall shear stress instead of velocity [20]. All

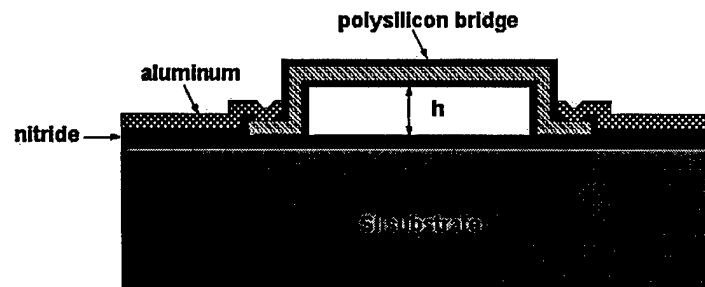
four types were fabricated on a single chip to ensure identical thermal and electrical properties of the sensor materials. Figure 5 shows their calibration results in wind-tunnel tests. The output changes are proportional to the one-third power of shear stress, which agrees with the heat transfer theory [17]. It is obvious that types I and II are the most sensitive ones. Moreover, type I has a much simpler fabrication process than type II. Therefore, it was chosen as the building block of this generation of shear stress imaging chip to be described below.



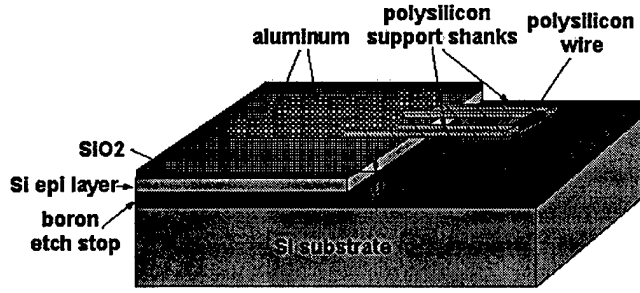
(a)



(b)



(c)



(d)

Figure 4. Structures of the sensors.

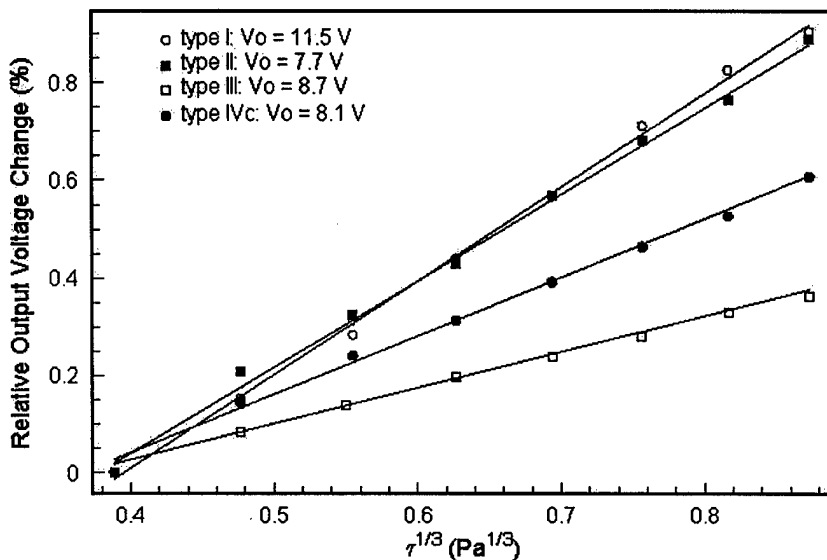
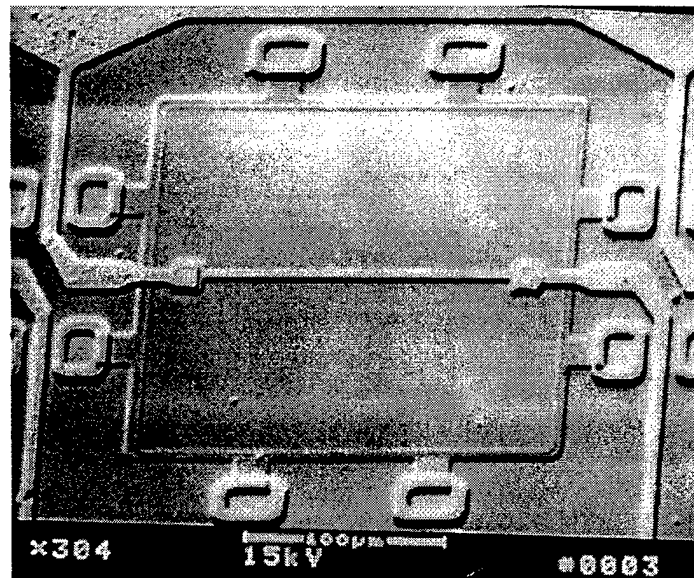


Figure 5. Wind-tunnel calibration of sensors.

After the structure is decided, the geometry of each layer is optimized to give maximum sensitivity. It is found that the sensitivity is higher for thinner diaphragms and larger aspect ratio polysilicon resistors (i. e. larger L/W , where L is the length and W the width). But the diaphragm can not be too thin as it would otherwise break during fabrication or operation. L is limited by the size of the whole device, which is at most 300 μm for the application in shear stress imaging. Therefore, L is chosen to be 150 μm . Also

w is limited by the photolithography and etching technology. In this case, it is designed to be 3 μm to ensure good uniformity.

Figure 6(a) shows the photomicrograph of an individual sensor while Figure 6(b) shows the 2.85 cm x 1.0 cm imaging chip using type I shear stress sensor. It is specifically designed for studies in turbulent flow with the Reynolds number near 10^4 . There are two identical sensor rows 5 mm apart, parallel to the broad side of the chip. There are also various test structures, including a 25 sensor test row, on this chip. This vertical pitch is chosen such that at least four data points can be taken from a streak in the streamwise direction. Each row has 25 sensors with 300 μm pitch, which is already the minimum for this type of sensor. It should give at least three data points from a streak in the spanwise direction and be able to catch more than one streak. The 1 cm spacing between the sensors and the left and right edges of the chip are necessary to avoid the upstream bonding wires from interfering with the downstream sensors.



(a)

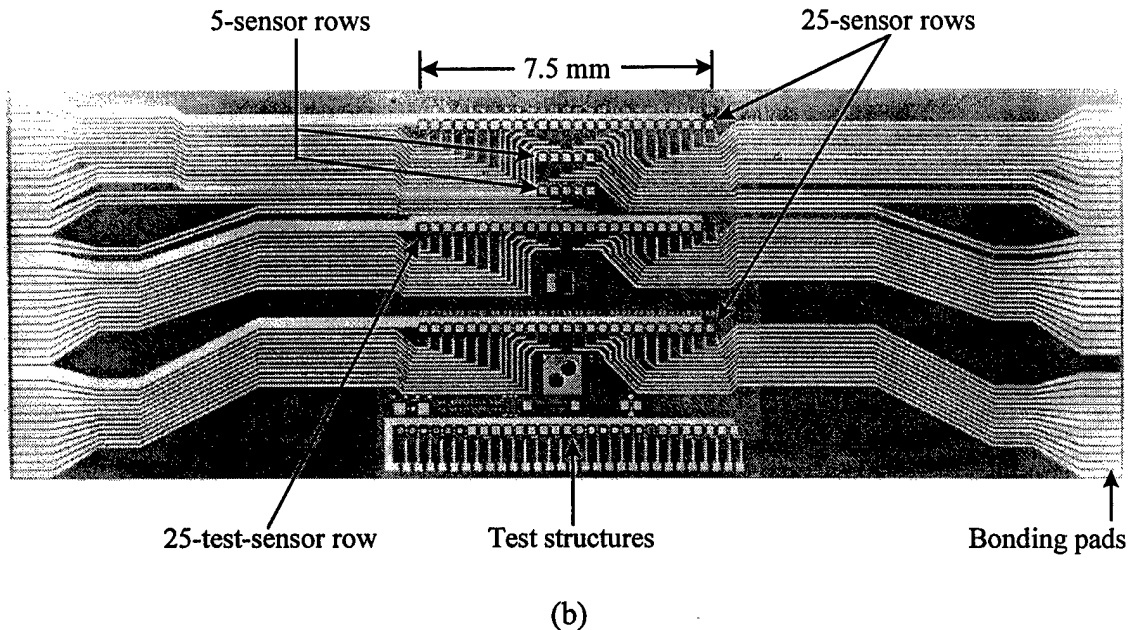


Figure 6. (a) SEM of individual sensor and (b) shear stress imaging chip.

The fabrication process of the shear stress imager starts with the deposition of 4000A of LPCVD low stress silicon nitride. Following a lithography, the nitride is removed by plasma with a little over-etch to give a 7000-8000A cavity. Then the wafer is put in oxidation furnace to grow 1.7 μm thick oxide in the cavity. After short time etch in BHF to remove the oxidized nitride, 4000A PSG is deposited, patterned and annealed to form the sacrificial layer etching channel. Next, 1.2 μm of LPCVD low stress nitride is deposited as the diaphragm material. Etching holes are opened to expose the end of the PSG etching channel, followed by a 49% HF etching to completely remove the PSG and thermal oxide underneath the diaphragm. The cavity is then sealed by LPCVD LTO and nitride deposition at a vacuum of 200 mTorr. The sealing materials on the diaphragm are removed by plasma and BHF etching to minimize the diaphragm thickness. 4000A polysilicon layer is deposited, doped, annealed and patterned to form the resistor on diaphragm. Another 2000A of low stress nitride is deposited to passivate the resistor. After

the contact hole opening, metallization is done and the wafer is diced to 2.85cm x 1cm chips. The fabrication process flow is shown in Figure 7.

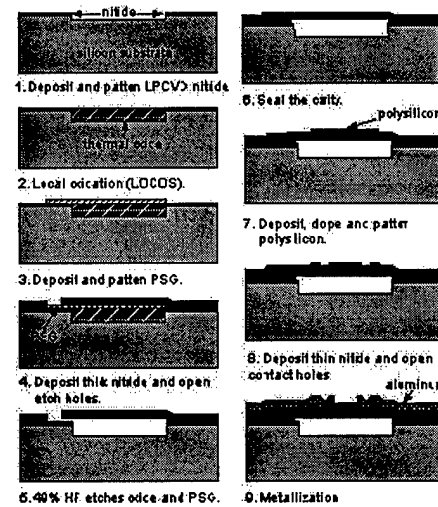


Figure 7. Process flow for shear stress imager.

The package for the imaging chip is a fine-line PC board with a recess in the center so that the imaging chip can be flush-mounted. The chip and the PC board are electrically connected by wire bonding. The electrical leads are soldered on the backside of the PC board. The PC board is then flush-mounted on a specially-made plug which fits into the wall of the wind-tunnel (Fig. 8), with the sensor row perpendicular to the flow direction.

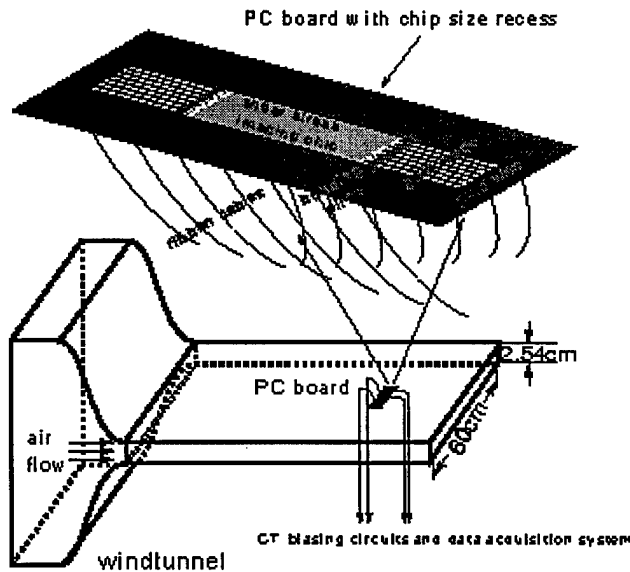


Figure 8. Imaging chip packaging and experimental set-up

The wind tunnel supplies a two-dimensional channel flow. The channel is 4.87m long with a cross-sectional area of 60cm x 2.5cm. The walls of the channel are constructed of 2.5cm thick Plexiglas and supported by a steel frame. An axial blower powered by a DC source supplies the air flow in the channel. At the highest blower speed, the centerline velocity in the channel is about 25 m/s. Hot-wire velocity measurements at 10 m/s indicate that the channel consists of a laminar entrance flow region which gradually transforms into a fully-developed turbulent flow in the downstream 2/3 portion of the channel. All calibration and testing of the imaging chip is carried out in this region of the channel.

In our experiments, the sensors are biased in constant temperature (CT) mode. Although it is more complicated than the constant current mode, it can achieve much higher frequency bandwidth which is crucial in turbulence measurement. Therefore, arrays of CT circuits and gain stages have been made on PC boards using op-amps and discrete components (Figure 9). The dc offset of the outputs can be adjusted individually, but the

gain is fixed to be 10. A computer-controlled data acquisition system is used to measure all the outputs simultaneously.

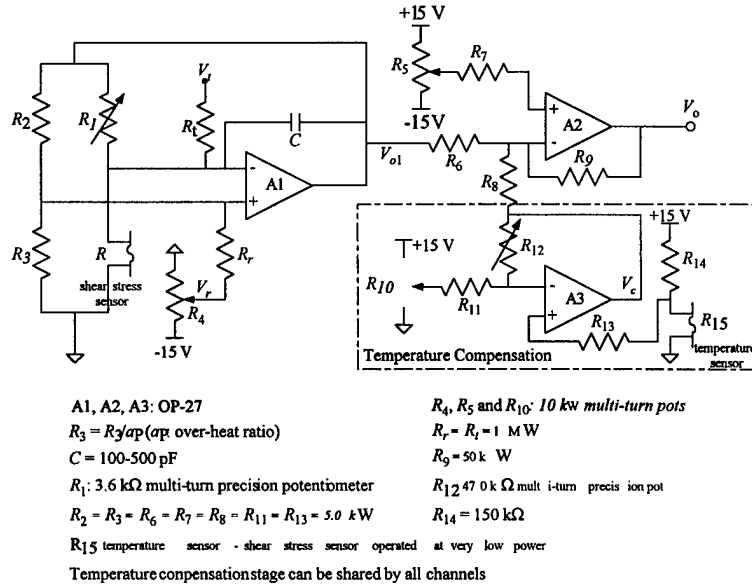


Figure 9. Constant temperature biasing circuit, gain stage and temperature compensation stage.

Before the sensors are used to measure the shear stress distribution, their dc outputs are calibrated against known wall shear stress levels which are calculated from the centerline velocity by using the following relationship [21],

$$\frac{u_\tau}{U_c} = 0.119 \text{Re}^{-0.089}$$

$$\tau_w = \rho_f u_\tau^2$$

$$\tau_w = 0.00427 U_c^{1.822}$$

where Re is the Reynolds number, U_c is the centerline velocity of the channel, U_τ is the friction velocity, d is the half width of the channel (=1.27 cm) and is used to calculate Re , τ_w is the wall shear stress, and ρ_f is the density of air.

Figure 10 shows the calibration results for 10 sensors in a row. Although each sensor has different offset, the trend of all curves are almost the same. Polynomial fitting is performed on each curve to extract the fitting parameters for later use in real data processing.

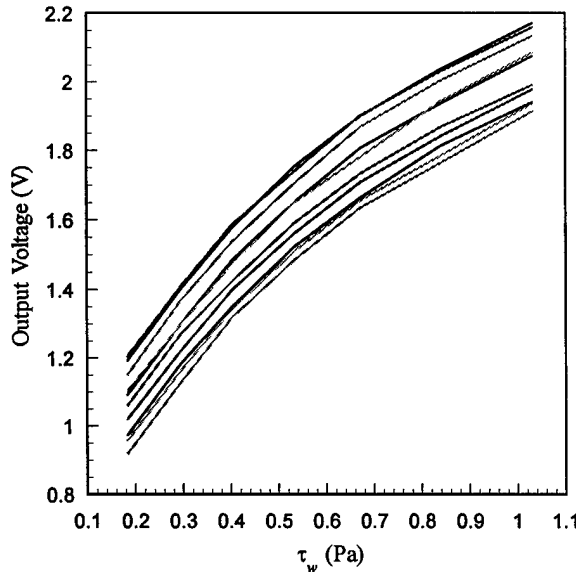


Figure 10. Calibration curves of 10 sensors in a row.

It is important to note that the dc outputs of the sensors are sensitive to the fluid temperature because the shear stress sensor is essentially a thermal sensor with temperature coefficient of resistance around $0.1\%/\text{ }^{\circ}\text{C}$. This dc drift can be compensated by measuring the sensor temperature sensitivity and monitoring the fluid temperature change using a temperature sensor. Figure 11 shows that an order of magnitude of improvement on the thermal stability has been achieved by the compensation circuit given in Figure 9. Here the temperature sensor is just another shear stress sensor operated at very low power such that the self-heating is negligible.

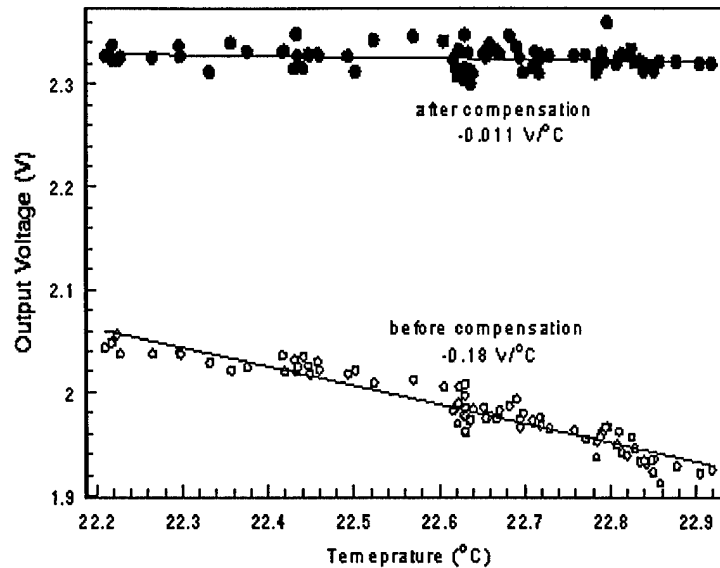


Figure 11. Typical temperature sensitivities before and after temperature calibration.

To confirm that the sensors have enough bandwidth to pick up all the information in a turbulent flow investigation, the frequency response of a sensor in CT mode is measured using a sinusoidal electrical testing signal v_t . Figure 12 shows that this bandwidth reaches 30 kHz, which is sufficient for the turbulent flow under study. The deviation between the experimental data and the fitted curve is due to the fact that a real sensor has multiple thermal time constants.

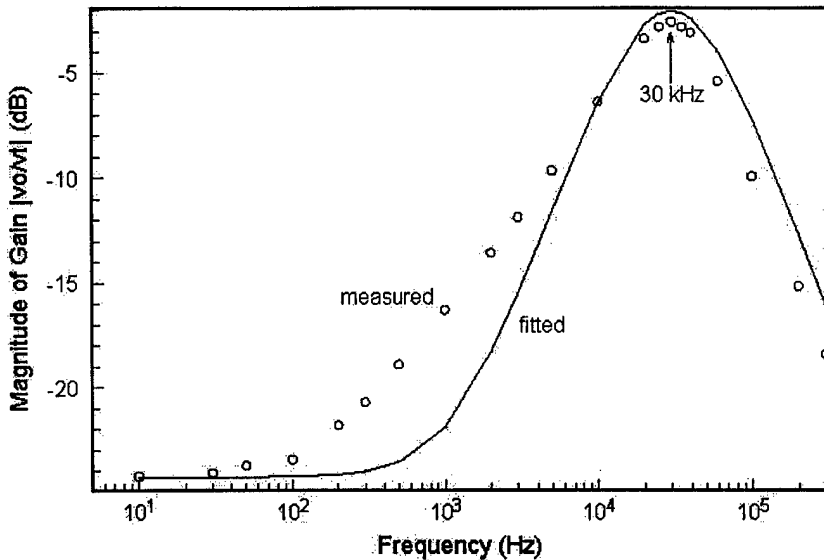


Figure 12. Frequency response of a CT sensor. Derivation of the theoretical curve is shown in [22].

Magnetic Actuator

Many generations of active magnetic flaps were designed and fabricated for use in the drag reduction project. The flap structure was chosen because it can provide relatively large displacements at high frequencies. Magnetic actuation was chosen due to the long range over which the force can be exerted and the fast manner in which the force can be felt. The first generation was fabricated as a proof of concept and to validate our ideas that the use of magnetic forces was a viable means to actuate micromachined devices. Later generations were designed and fabricated to provide more robust devices (here, the term robust implies both actual device robustness as well as process robustness) with the eventual goal of integration in mind. Sometimes, a new generation would be fabricated because our fluid mechanics partners believed that a particular geometry would prove to be advantageous.

The first generation [XXX] flap consisted of three layers (see Figures 13 and 14).

A structural layer of silicon nitride was sandwiched between a top layer of metal coils and a bottom layer of heavily phosphorous doped polysilicon. The polysilicon was used as a return path for the current. Several different geometries were fabricated. Plates of different sizes and shapes were designed. Some flaps had four corner supports instead of two bending beams. Different etch hole sizes and placements were also designed.

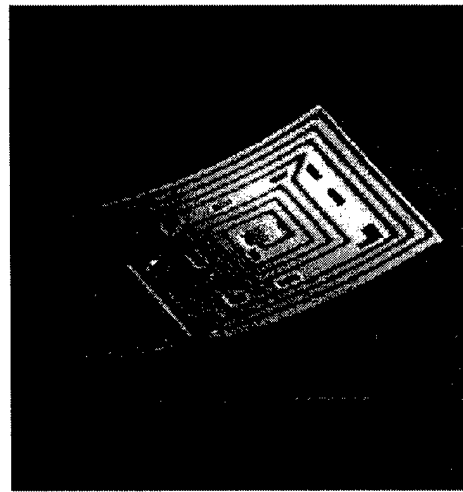
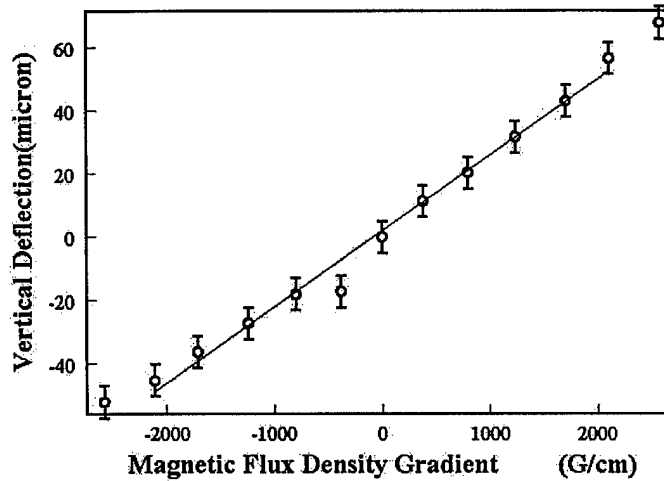
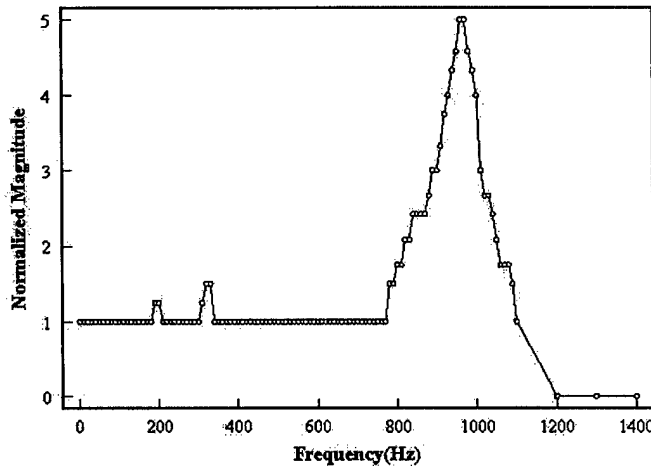


Fig 13. SEM of a first generation flap.



(a)



(b)

Figure 14. Typical (a) deflection and (b) resonant frequency curves for the first generation actuator.

Unfortunately, the use of polysilicon as the return path for current was the root of two major problems: bending due to stress and excessive plate heating. The mismatch of the stresses of the polysilicon and silicon nitride films caused the flaps to curl up considerably. In general, this would cause problems in the sense that there would be a flow disturbance at all times. For the first generation, however, this was actually a

serendipitous event because the stress served to provide a force to oppose the stiction forces. Without the natural bending, the flaps would have all stuck to the substrate.

Polysilicon has a resistivity that is orders of magnitude higher than that of metals. In fact, in IC processes, polysilicon is used as a resistor material. For our purposes, having a high resistance is detrimental. First of all, keeping in mind that the eventual goal is a distributed system with thousands of devices, the power consumption for each actuator must be minimized. Second, the heat generated induces a thermal bending of the plate that may not be desirable. Finally, the generation of heat may, in fact, affect the flow in a negative way by adding energy to an already turbulent flow.

Therefore, the second generation [XXX] was designed and fabricated with the intent of reducing the power consumption and also reducing the bending due to intrinsic stresses. As previously mentioned, the use of polysilicon is the cause of both problems. All second generation devices [Figure 15] are characterized by the use of PSG as the sacrificial layer while using two layers of metal for the coils.

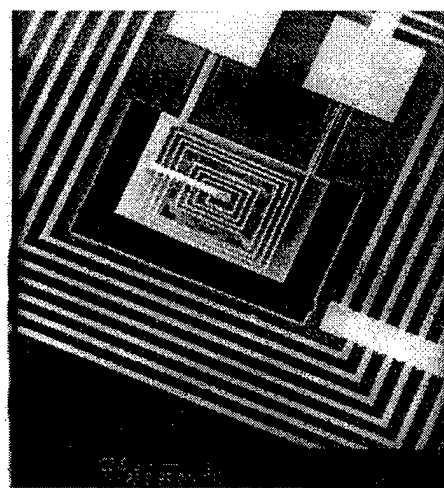


Figure 15. Second generation magnetic actuator.

Typically, the IC industry uses some sort of LPCVD LTO as metal insulation. Immediately, one problem with using LTO in this process becomes apparent. Oxide is also used as the sacrificial layer. Therefore, the metal insulation would also be etched away, leaving behind air bridges. Other LPCVD options were not available to us due to temperature considerations. The low deposition temperature of LTO is important because the metal must not be melted or evaporated during the deposition. Even though the melting points of chrome and gold are significantly higher than that of aluminum, neither metal can stand LPCVD silicon nitride temperatures.

One simple alternative to using LTO as the insulation is to use photoresist, which can be spun on in a room temperature process. Photoresist is attacked by high concentrated HF acid, but tends to break off in chunks as opposed to being dissolved away (as oxide is). Therefore, the possibility exists that while the resist integrity would be compromised, enough may remain to support the top layer of metal. Another alternative is to etch using buffered HF acid, which attacks oxide much slower than high concentrated HF acid does, but does not appreciably attack resist. Results of attempting these options are discussed below.

An alternative to LPCVD films for insulation would be PECVD films [Figure 16]. Our lab has the capability of depositing PECVD silicon nitride at a temperature of 300° C. Due to the nature of their deposition, PECVD films generally have poorer chemical resistance than LPCVD films. Therefore, PECVD nitride is appreciably etched in HF acid. However, if the flap can be freed before the insulating nitride is completely etched away, this process could also provide a viable means to insulate the coils.

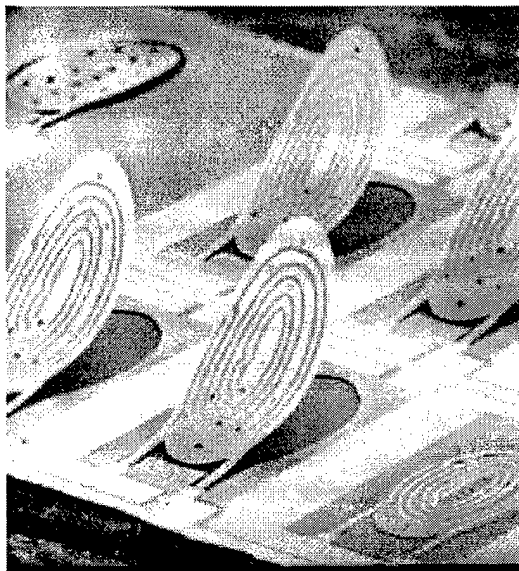


Figure 16. SEM of 2nd generation flap using PECVD nitride as the ILD.

The third generation of actuators was conceived with the idea of eventual process integration in mind. Up to this point, all of the actuators used PSG as the sacrificial layer. Unfortunately, as previously mentioned, IC processes typically use oxide both as inter-metal dielectrics, but also for overall circuit encapsulation (often called an overglass layer). Since the release step is usually the final step in any process involving the flap, the HF acid would horribly attack all of the oxide required for the electronics portion of the chip. Therefore, a different sacrificial layer process needed to be developed.

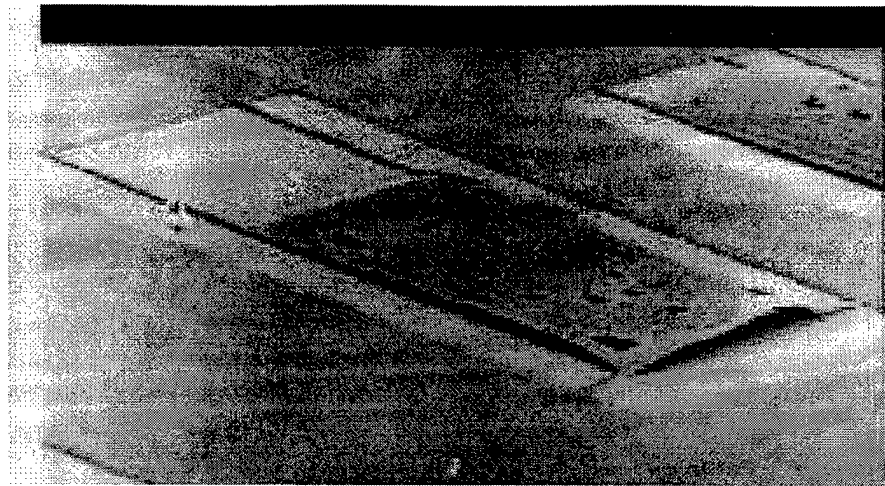


Figure 17. A low temperature actuator.

For integration reasons, metal was one option explored for use as a sacrificial layer. Metal can be deposited in thick layers relatively easily and at low temperatures. When using a metal sacrificial layer, care must be taken to choose a structural layer that can also be deposited at a low temperature. Therefore, using a metal sacrificial layer in conjunction with an LPCVD oxide structural layer was investigated. Two choices were considered for the sacrificial layer: aluminum and copper. An actuator fabricated using copper as the sacrificial layer is shown in Figure 17.

The fourth generation of flaps [Figure 18] was designed with the ideas in mind that (a) a combined passive/active flap may prove beneficial, and (b) the passive component, permalloy, could also be used to aid in a magnetic release step. This generation of flap was designed with the idea in mind of IC process compatibility. Therefore, some versions of these flaps used polysilicon as the sacrificial layer. One particularly nice aspect of using polysilicon as the sacrificial layer is the possibility of releasing structures using a dry, gas-phase etchant.

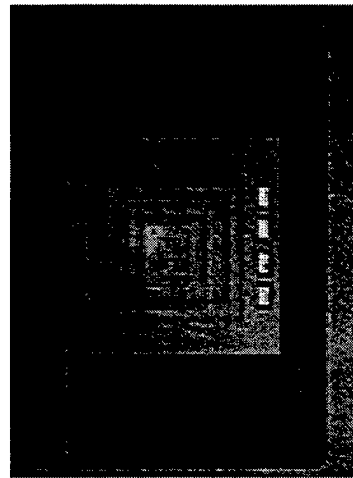


Figure 18. A hybrid flap.

Finally, a fifth generation was designed [Figure 19]. This generation is completely different from the previous four in the sense that it uses a bulk, rather than surface, micromachined process. The primary reason for this is the desire for thicker beams, which result in a higher resonant frequency, than possible with a surface micromachined process.

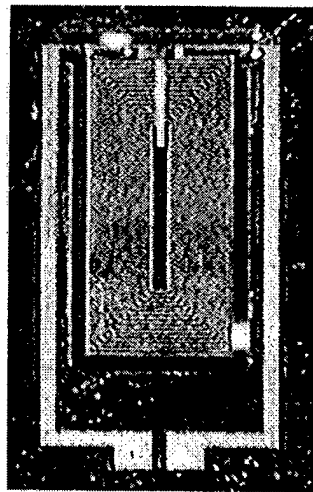


Figure 19. A bulk micromachined flap.

Shear Stress Measurements and Control

Single Point Surface Shear Stress Measurement

For real-time shear stress imaging, the output voltage is sampled at 10kHz and converted to shear stress signal based on the calibration performed previously. In order to establish the credibility of the imaging chip, the turbulence statistics calculated from the shear stress fluctuations recorded by a single shear stress sensor are compared to previously established results. Figure 20 shows the comparison in terms of the normalized RMS level, the skewness factor, and the flatness factor. It is obvious that the present results agree very well with previous studies in all three areas [23-25]. In addition, the present statistics appear to be independent of the Reynolds number which is predicted by turbulence theory.

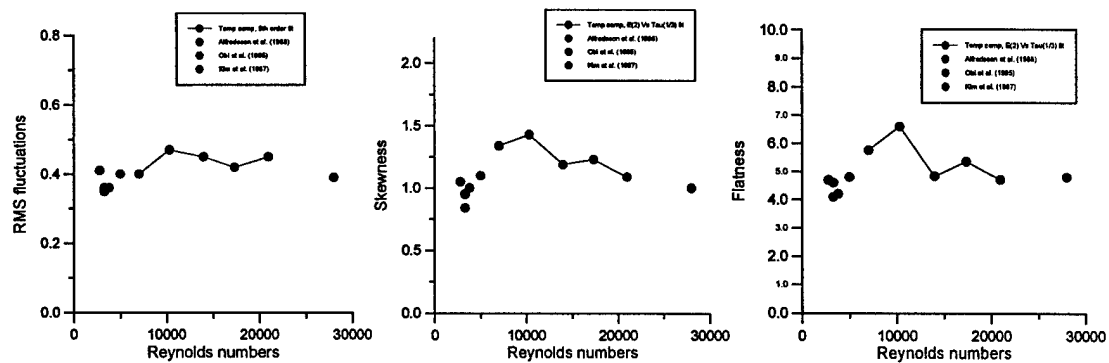


Figure 20. Turbulence statistics measured by a single micro shear-stress sensor.

As can be seen, the turbulence statistics measured by the micro sensor compare very well with both previous experimental and numerical results.

Distributed Measurement

Next, the instantaneous turbulent shear stress distributions of the channel were recorded by using one of the sensor rows on the imaging chip. Figure 21 shows the

contour plots of the instantaneous shear stress distributions at two different centerline velocities. The white streaky structures in the plots represent regions of high shear stress on the wall of the channel where the imaging chip is located. They are caused by the presence of near-wall streamwise vortices which bring high momentum fluid from the freestream to the wall. Due to the small-scale nature of these structures, previously experiments in turbulent boundary layers have only succeeded in qualitatively demonstrating their existence without obtaining any quantitative information. This is the first time that the instantaneous shear stress levels associated with the near-wall structures are recorded.

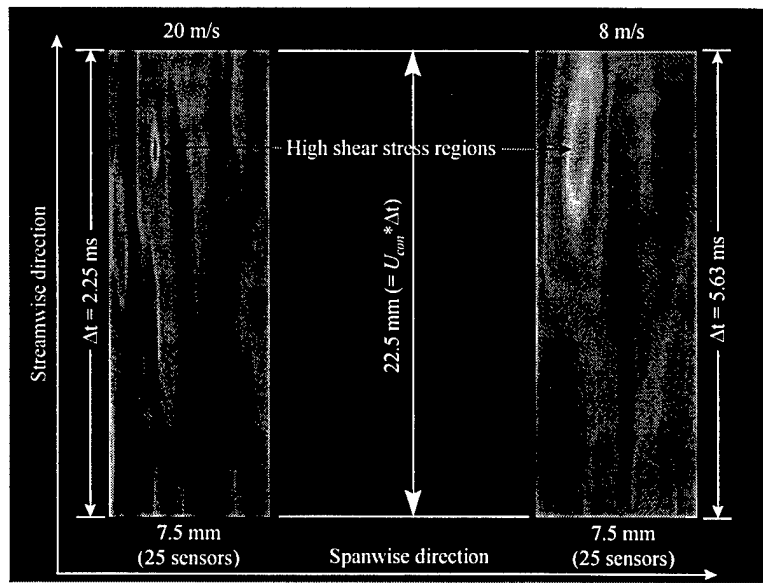
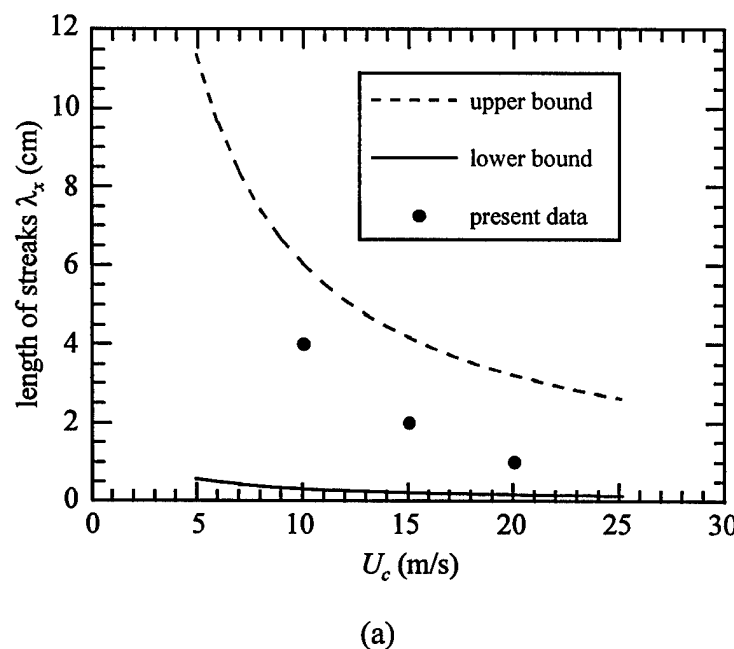
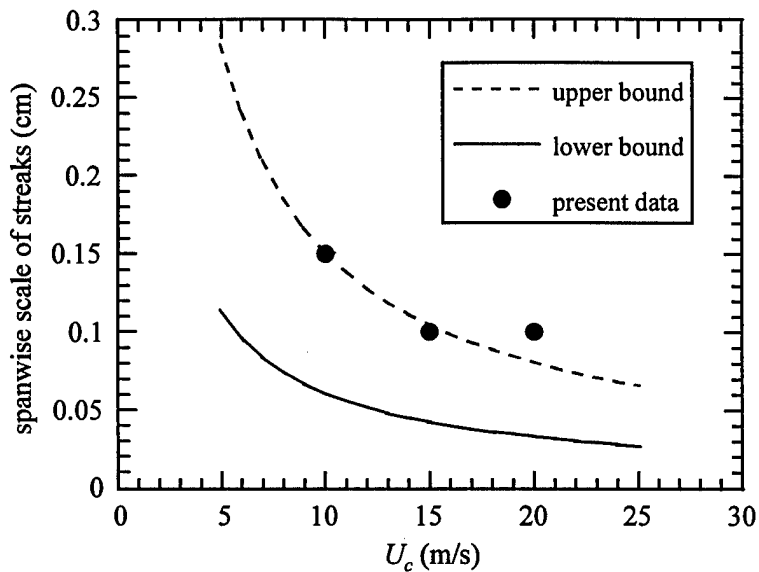


Figure 21. Contour plots of the pseudo 2-D shear stress distributions. Red area indicates high shear stress and blue area indicates low stress.

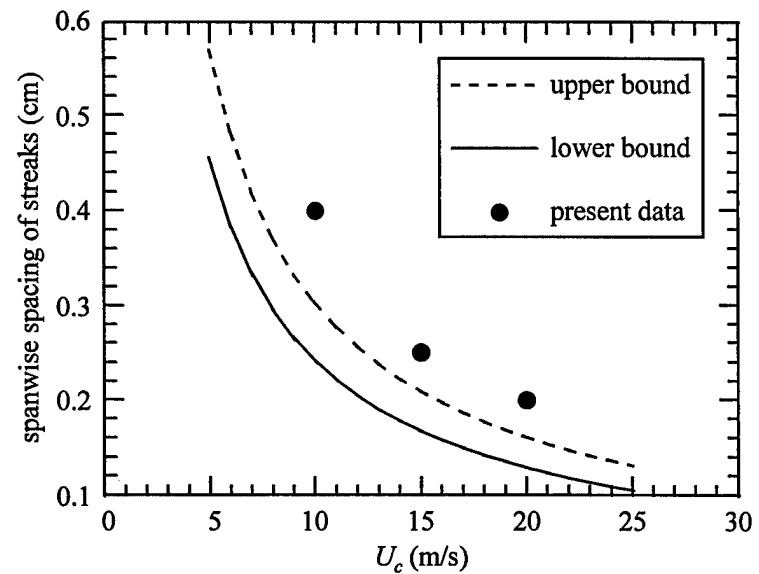
The contour plots in Figure 21 indicate that the scales of the streaks are different at different centerline velocities. The streaks in the high-speed (20 m/s) case appear to be thinner and more densely packed than those in the low-speed (8 m/s) case. Similar phenomena have also been observed in previous experiments. Based on real-time movies

generated from the contour plots similar to the ones in Figure 21, the average streamwise length, the average spanwise scale, and the average spanwise spacing of the streaks at three different centerline velocities are estimated and shown in Figure 22. Once again, the present results agree well with previous studies. The average length of the present streaks falls within the upper and lower bounds of the established results. The average spanwise scale and spacing of the present streaks are either on or slightly higher than the upper bound.





(b)



(c)

Figure 22. Scales of the near-wall streaky structures at different Reynolds numbers. (a) The length of streaks. (b) The spanwise scale of streaks. (c) The spanwise spacing of streaks.

The high-shear stress streaks are randomly distributed. A real-time detection scheme is needed to properly identify the streaks among the background fluctuations so that the downstream actuator can be activated. A neural network based detection circuit (described later) was developed for this purpose. In this circuit, the signal output of a sensor is compared with its neighboring sensors through a filter-threshold combination. Whenever a sudden change is detected, the boundary of the high shear stress region is marked. This circuit has been used in conjunction with the imaging chip and a typical result is shown in Figure 23. The light region in the control output (Fig. 23-b) represents 'positive' identification of high shear-stress streaks. The good matching between the light-color region and the high shear-stress area (light gray region) measured by the imaging chip indicates the effectiveness of the detection circuit.

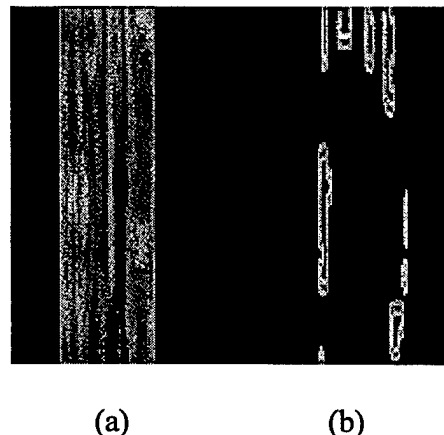


Figure 23. Contours of (a) the instantaneous surface shear stress and (b) the output of the control circuits.

Interaction between Micromachined Actuator and Streamwise Vortices

To properly control the high shear-stress streaks with micro actuators [26,27], an in-depth understanding of the interaction between the actuators and the flow structures is required. Experiments have been carried out to investigate the interaction between a single high shear-stress streak and a micromachined actuator. In this study, a 1.3 mm thick vortex generator is used to generate a longitudinal vortex pair in a laminar boundary layer. The micromachined actuator used is a silicon flap with 30 turns of copper coil and matches the physical size of the longitudinal vortex pair. Oscillation of the flap is achieved by the combination of an external permanent magnet and an AC coil current. The maximum deflection of the flap is about 30 degrees, which corresponds to height of 2 mm from the tip of the actuator flap to the wall. The maximum oscillation frequency is about 100 Hz. The actuator is placed downstream from the vortex generator where the longitudinal vortex pair is generated. Experiments are carried out for different combinations of actuator frequency (ω) and maximum tip height (d). For each combination, a two-component (streamwise and spanwise) hot-wire anemometer is used to measure the velocity distributions downstream from the actuator. From the velocity distributions, the vorticity and surface shear stress distributions are calculated and phase averaged.

The longitudinal vortices generated by the vortex generator convect high-speed fluid to the wall, inducing a local high shear-stress streak (Figure 24) on the surface. As the actuator oscillates, it generates perturbations in the flow which change the shear stress intensity of the streak. As indicated by the ensemble-average result shown in Figure 24, the intensity of the streak decreases as the flap actuator deflects away from the surface, reaching a minimum at the maximum actuator tip height (phase = π). As the actuator

moves back to the surface, the streak intensity reverses to its original level. To evaluate the net effect of the actuator oscillation on the shear stress distribution, the net shear stress coefficient, C_{DN} , defined as

$$C_D(\theta) = \frac{1}{0.5\rho U^2} \int_z^{\infty} \mu \frac{\partial u}{\partial y}, \text{ and}$$

$$C_{DN} = \int_0^{2\pi} [C_D(\theta) - C_{D,VG}] d\theta,$$

for different ω - d combinations are evaluated and shown in Figure 25. The $C_{D,VG}$ in the equation is the time-invariant shear stress coefficient associated with the stationary high shear-stress streak induced by the vortex generator. Defined this way, C_{DN} indicates a shear stress increase if positive and a drag decrease if negative. As shown in Figure 25, higher drag reduction is achieved at higher ω and higher d . In addition, similar shear stress reduction is the result if the product of ω and d is the same. Since the product of ω and d is a measurement of the transverse velocity of the actuator flap, this result indicates that the amount of shear stress reduction is directly related to the transport of high-speed fluid away from the surface by the vertical motion actuator.

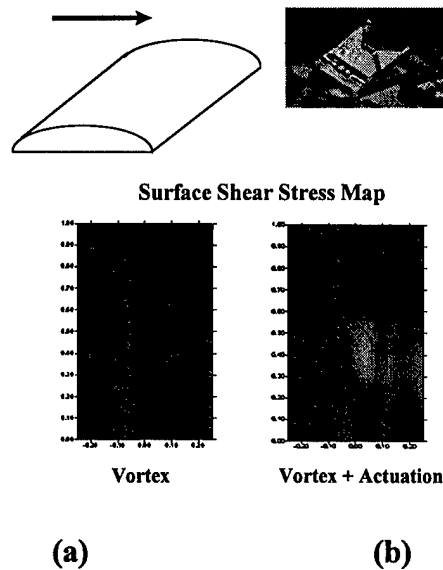


Figure 24. Contours of ensemble-average dU/dy . (a) Vortex generator only; (b) Vortex generator and an oscillating micro actuator.

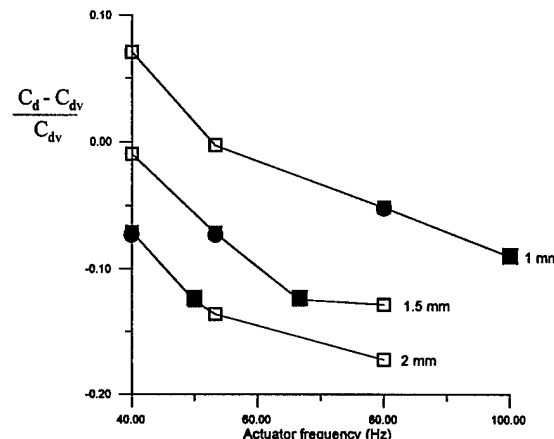


Figure 25. Variation of the shear stress coefficient, C_{DN} , with actuator frequency, ω , and maximum actuator tip height, d . Each line is the result of one d , as indicated at the end of the line. The solid O markers correspond to an ωd of 80 and the solid \square markers correspond to an ωd of 100.

Integration

As shown above, the results of sensor/flow and actuator/flow interaction are very promising. The next step, then, is to integrated sensors, actuators and electronics on the

same substrate to form the M³ system. Towards this goal, an integration chip was fabricated but has not yet been extensively tested [28]. There are many generic concerns in MEMS-Electronics integration that have been addressed in this work. Elements of this MEMS-Electronics integration effort can be applied to other, more generic integration efforts.

The primary concern of all integration efforts revolves around the choice of when the MEMS processing steps are completed relative to the IC processing steps. There are three options: (1) an interweaved process, (3) electronics first, followed by MEMS, (3) MEMS first, followed by electronics, and. Each alternative has its advantages and disadvantages.

One assumption being made while comparing these different options is that the MEMS designer does not have full and high priority access to an IC capable fabrication facility. This is a reasonable assumption for an academic environment where few laboratories even have basic MEMS capabilities, let alone IC fabrication facilities. In the few institutions (Berkeley and Stanford to name two) in the entire country which have CMOS capabilities, the electronics yield is usually unacceptably low compared with industry. The lack of dedicated access to a fabrication line is not limited to academia. Even in a corporation with large fabrication facilities, internal MEMS research facilities often are completely separate from VLSI lines and MEMS researchers often are not allowed full access to such lines. If full access were available to MEMS researchers, the interweaved process would almost definitely be the choice for reasons that will be discussed below.

From a device-robustness point of view, the interweaved process is ideal. The order in which steps are completed reflects a process flow designed with optimum device performance in mind. This is in stark contrast to the other approaches, which often require steps that are not needed for the eventual devices (or electronics) per se, but rather are crucial for the overall survival of the process. For example, in an electronics-first process, during the MEMS processing, layers are often deposited, patterned, and later removed simply to protect the aluminum metalization on the electronics portion of the wafer. In an interweaved process, the metalization steps could occur after any harsh MEMS processing steps have been completed. From this, it can be seen that the interweaved process also is usually the shortest (both in time and in number of processing steps). General processing wisdom holds that the fewer the steps, the more robust the process. For commercial applications, fewer steps also reduces the cost significantly while increasing the yield.

Extremely few IC facilities will allow pre-processed wafers to enter their fabrication lines due to fear of contamination, especially the fear of unknown (by VLSI standards) MEMS materials. Therefore, finishing the IC processing first has one primary advantage: one has many choices of IC foundries that can provide wafer level electronics. After the foundry fabricates the IC electronics, the wafers are then subject to MEMS processing, which can be completed in a facility separate from the VLSI fabrication line.

Oftentimes, the choice of which approach to take for integration depends on metalization concerns. Typically, VLSI fabrication uses aluminum metalization. Aluminum is considered a low temperature material and cannot withstand processing temperatures above 450° C. Therefore, certain steps such as diffusion and oxidation cannot be attempted after aluminum deposition. If electronics including metalization is

completed before MEMS processing, the user then can only use low temperature steps to finish the process. Other considerations regarding metalization are that (1) ideally only one deposition/pattern/etch step should be used for each metal layer, and (2) fine line widths are often required for the electronics portion of the chip. These two concerns may imply that the intelligent approach is to complete all the metalization (for a given layer of metal) at one time and to do it at the VLSI fabrication facility, where fine line metal patterning and etching are well characterized steps. There may exist some facilities which will take pre-processed wafers on a one-time basis, in which case MEMS processing up to but not including metalization can be done before submitting the wafers to the foundry. Complete CMOS processing is then completed, with the metalization connecting both electronic and MEMS devices.

Finally, although less interesting from a research point of view, economic reasons can often dictate which option is chosen. When choosing an outside foundry as a vendor, it should be noted that the least expensive option involves requesting as standard a package as possible. This usually implies that, of the three above-mentioned options, the second (electronics first, then MEMS) option may be the most viable. Cost, however, is often not the only economic concern. The idea of interweaving a process is often the most appealing option from a technological point of view. From a foundry's point of view, it is also the most costly. While most foundries will not turn down business that requires standard technology, they do require financial justification before attempting an expensive custom run which could divert their manpower and resources from other high-volume projects. Foundries such as Standard Microsystems Corporation (SMC) which have dedicated MEMS-Electronics fabrication facilities often also have long lines of corporate

customers buying high volumes of devices. They often are not interested in low volume applications (such as university research or small company products).

Therefore, oftentimes, small volume applications are limited to pursuing the electronics first approach. If high temperature MEMS steps are required, it is possible to switch to an interweaved approach where the electronics processing up to, but not including, metalization is completed at the VLSI foundry. Next come the MEMS steps, and the process is completed with metalization at the MEMS facility (or another facility willing to take pre-processed wafers). This approach requires the ability to dry etch contact holes, pattern fine lines, and dry etch aluminum in the post-IC facility. This may or may not be a limitation. This is the process we chose to complete our first attempt at integration. A picture of a completed chip is shown in Figure 26, and an abbreviated process flow is shown in Figure 27.

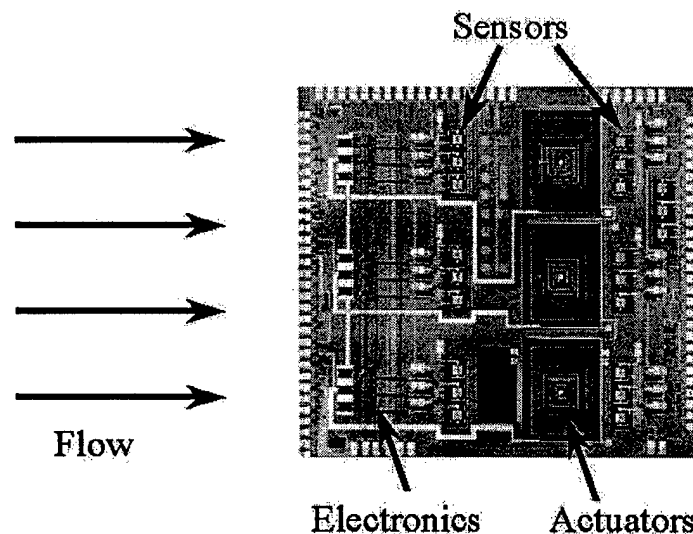


Figure 26. Picture of a fabricated integration chip.

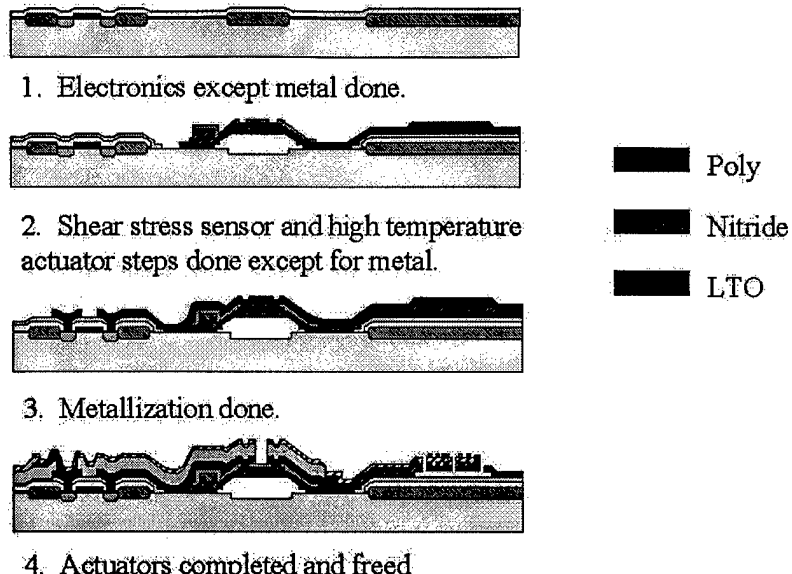


Figure 27. Abbreviated process integration process flow.

Control

A new adaptive controller based on a neural network was constructed and applied to our system of drag reduction. A simple control network, which employs blowing and suction at the wall based only on the wall-shear stresses in the spanwise direction, was shown to reduce the skin friction by as much as 20% in direct numerical simulations of a low-Reynolds number turbulent channel flow. Also, a stable pattern was observed in the distribution of weights associated with the neural network. This allowed us to derive a simple control scheme that produced the same amount of drag reduction. This simple control scheme generates optimum wall blowing and suction proportional to a local sum of the wall-shear stress in the spanwise direction. The distribution of corresponding weights is simple and localized, thus making real implementation relatively easy. Turbulence characteristics and relevant practical issues are also discussed.

Although a neural network generally requires no prior knowledge of the system (or “plant”), knowledge about the near-wall turbulence structures provides a guideline for the design of the network architecture. Initially $\partial u / \partial y$ and $\partial w / \partial y$ at the wall at several instances of time were used as input data fields and the actuation at the wall was used for the output data of the network. Experimentally we found that only $\partial w / \partial y$ at the wall from the current instance of time was necessary for sufficient network performance. Because we wanted the output to be based only on a local input area, we designed our network using shared weights. The network had a single set of weights (a template) that is convolved over the entire input space to generate output values; that is, we used the same set of weights for each data point and the training involves iterating over all data points. The template extracts spatially invariant correlations between input and output data. The size of the template was initially chosen to include information about a single streak and streamwise vortex, and then was varied to find an optimal size.

We used a standard two-layer feedforward network with hyperbolic tangent hidden units and a linear output unit (see Figure 28). The functional form of our final neural network is:

$$v_{jk} = W_a \tanh \left(\sum_{i=-(N-1)/2}^{(N-1)/2} W_i \frac{\partial w}{\partial y} \Big|_{j,k+i} - W_b \right) - W_c, \quad 1 \leq j \leq N_x \text{ and } 1 \leq k \leq N_z \quad (1)$$

where the W 's denote weights, N is the total number of input weights, and the subscripts j and k denote the numerical grid point at the wall in the streamwise and spanwise

directions respectively. N_x and N_z are the number of computational domain grid points in each direction. The summation is done over the spanwise direction. Seven neighboring points ($N = 7$), including the point of interest, in the spanwise direction (corresponding to approximately 90 wall units with our numerical resolution) were found to provide enough information to adequately train and control the near-wall structures responsible for the high-skin friction. Note that the blowing and suction are applied at each grid location according to the above equation as a numerical approximation of distributed blowing suction on the surface. A scaled conjugate gradient learning algorithm [29] was used to produce rapid training. For given pairs of $(v_{jk}^{des}, \partial w / \partial y|_{jk})$, network was trained to minimize the sum of a weighted-squared error given by

$$Error = \frac{1}{2} \sum_j \sum_k e^{\lambda |v_{jk}^{des}|} (v_{jk}^{des} - v_{jk}^{net})^2 \quad (2)$$

where v^{des} is the desired output value and v^{net} is the network output value given by equation (1). The weights were initialized with a set of random numbers. Note that the error defined in (2) exponentially emphasizes (proportional to λ) large actuations. This error scaling was chosen based on Choi *et al.*'s [10] observation that large actuations are more important for drag reduction. Usually within 100 training epochs, the error reached its asymptotic limit.

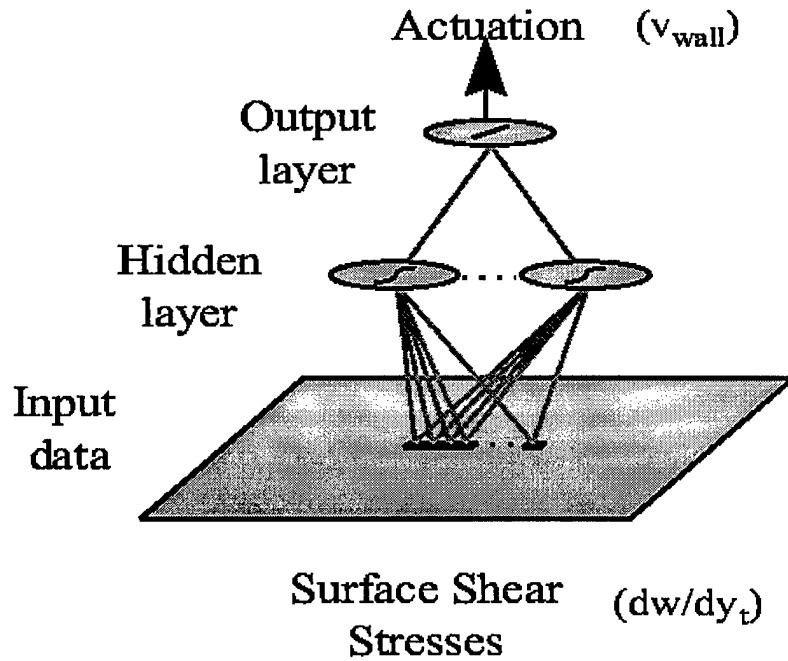


Figure 28. Neural Network Architecture

The computed flow fields for a no-control case and a successful control case, based on a 7-point weighted sum of $\partial w / \partial y|_w$ [30], were examined to investigate the mechanism by which the drag reduction is achieved. The most salient feature of the controlled case was that the strength of the near-wall streamwise vortices was drastically reduced. In Figure 29, contours of streamwise vorticity in a cross plane are shown. This result further substantiates the notion that a successful suppression of the near-wall streamwise vortices leads to a significant reduction in drag. Note that for the controlled case the wall actuations were applied at both walls. Also, Figure 29(c) shows the wall shear stress for various control mechanisms.

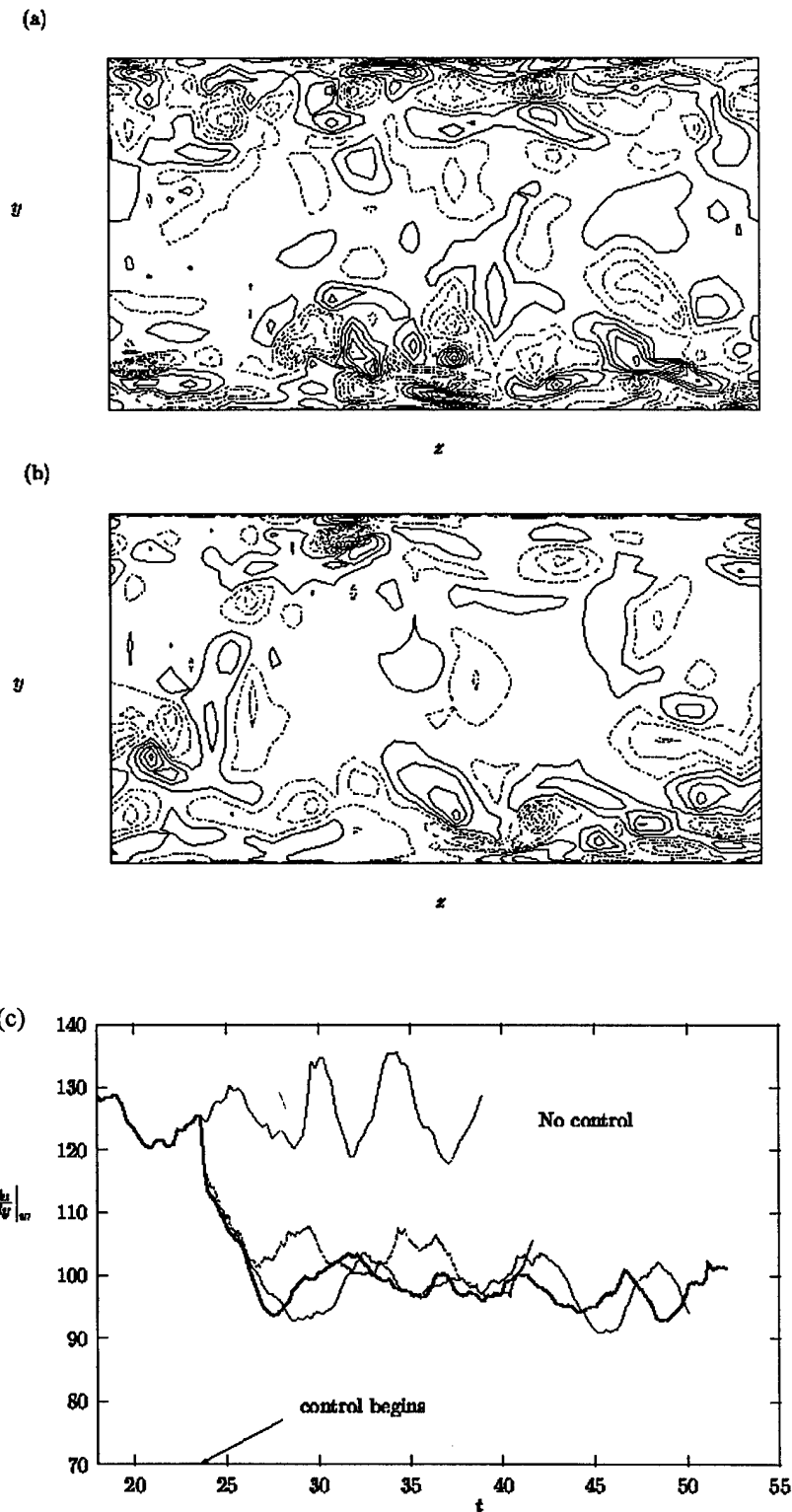


Figure 29. Contours of streamwise vorticity in a cross-flow plane: (a) no control; (b) control using 7 fixed weights. The contour level increment is

the same for both figures. Negative contours are chain-dotted. (c) Mean wall-shear stress histories for on-line control with different input template sizes: the top solid line is no control; the dotted line is control with 5×1 ; the lighter bottom line is control with 7×1 ; the darker bottom line is control with 9×1 .

The probability-density function of the wall-shear stress in the streamwise direction is shown in Figure 30. It is evident that the control is very effective in suppressing large fluctuations, thus reducing the mean-skin friction. Furthermore, the root-mean-square (rms) values of turbulent fluctuations in the wall region are also reduced as shown in Figure 31(a). The same trend was observed by Choi *et al.*[10] The rms vorticity fluctuations are also significantly reduced, except for ω_x very close to the wall. The increase for the latter is caused by additional $\partial v / \partial z$ due to the wall actuation. The rms fluctuations of ω_z at the wall, which is mainly due to $\partial u / \partial y$ at the wall, is also decreased. This indicates that the control scheme led to a reduction in the mean shear and its variance at the wall by suppressing large fluctuations as shown in Figure 30. The reduction in the rms fluctuations in ω_x and ω_y indicates that the control scheme indeed reduced the strength of the near-wall streamwise vortices and the wall-layer streaks.

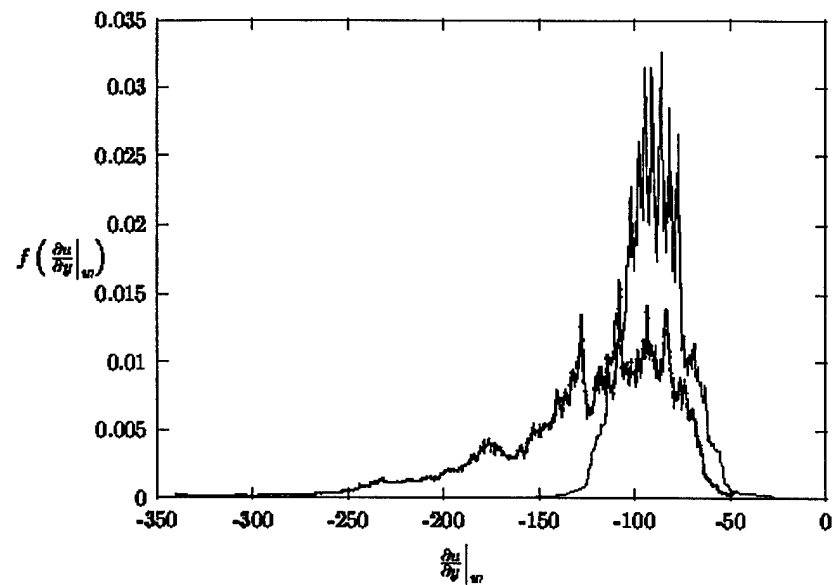


Figure 30. Probability-density function of the wall-shear stress: the darker line is no control; the lighter line is control with 7 fixed weights. The area under each curve is normalized to one.

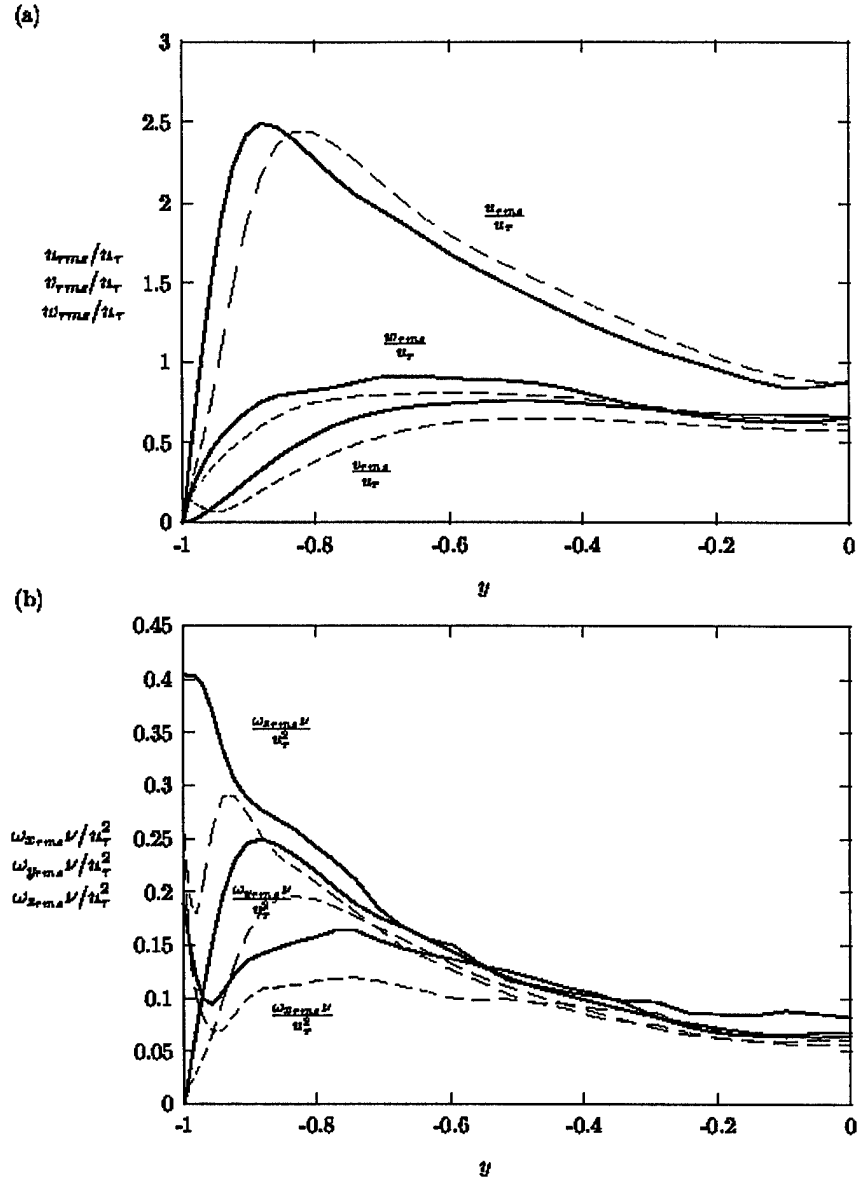


Figure 31. Root-mean-square fluctuations normalized by the wall variables: solid line is no control; dotted line is control with 7 fixed weights. (a) Velocity fluctuations; (b) vorticity fluctuations.

Figure 32 compares the distribution of wall actuation used in our control with that from Choi *et al.*'s [10] v -control using the information at $y^+ = 10$ for the same wall-shear stress distribution. The corresponding wall-shear stress distribution is also shown in

Figure 32. The wall actuations indicate a strikingly similar distribution to each other, even though the wall actuation of our control is based only on the wall-shear stress $\partial w/\partial y|_w$. Basically our control scheme detects edges of locally high-shear stress regions by measuring the spanwise variation of $\partial w/\partial y$, and applies appropriate wall actuation as shown in Figures 32(a) and 32(b). Since high-shear stress regions are usually elongated in the streamwise direction, only spanwise variation is necessary for detecting the edges. Since $\partial w/\partial y$ is a direct measurement of streamwise vortices, it provides more appropriate information than $\partial u/\partial y$. This is consistent with our finding that $\partial w/\partial y$ at several points in spanwise direction are enough for good performance of control.

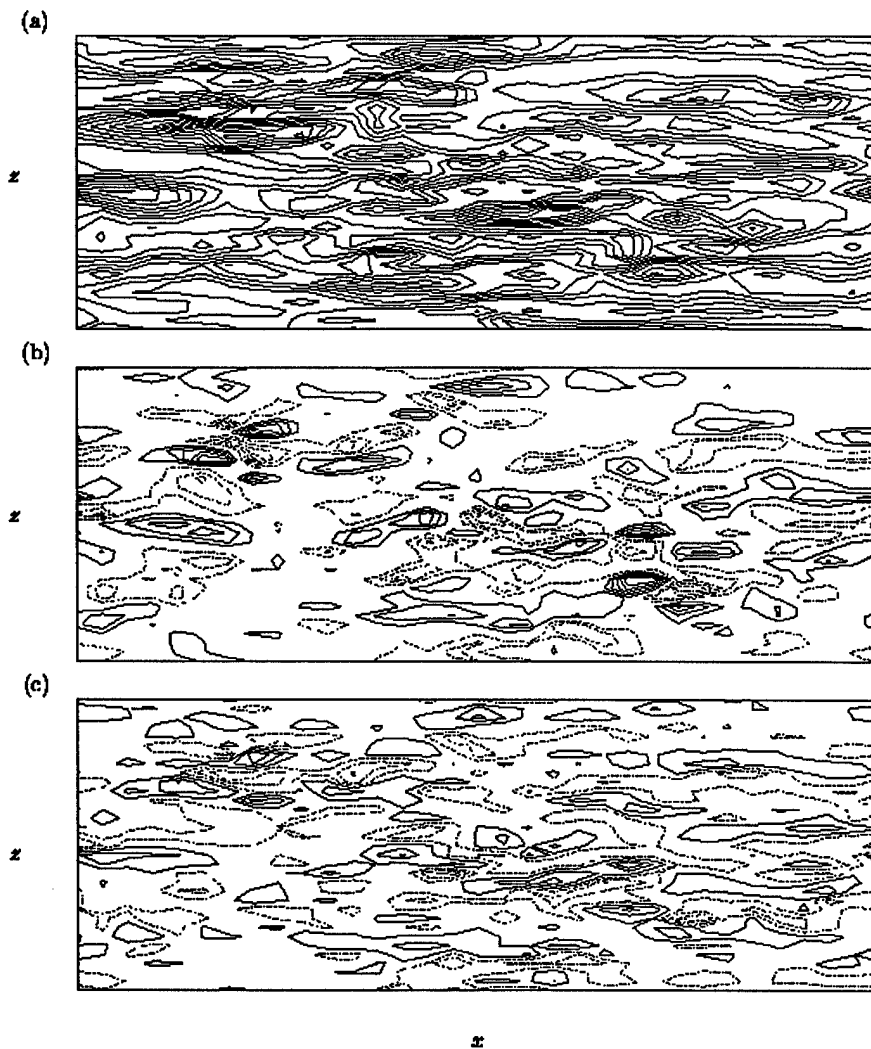


Figure 32. Contours of the wall actuation: (a) control using $\partial w / \partial y|_w$ with 7 fixed weights; (b) control using information at $y^+ = 10$. Negative contours are chain-dotted.

Electronics

Circuits process the signals from the sensors to find regions of high shear stress.

This detection process uses information about the spatial and temporal nature of the

streaks. Feature detection is based on a set of pre-defined templates for streak detection. We organize the sensor outputs into thin feature detectors oriented in the direction of the airflow. When several sensors in a column register either a larger or smaller output than their neighbors in a spanwise direction, this difference accumulates. If this accumulated difference exceeds a threshold, a vortex pair streak may be present in that column. The appropriate control action raises the associated actuator.

Figure 33 shows a plot of the detection and control chip. The CT output sensor signal feeds into a further stage of amplification. A buffer distributes the amplified signal to a non-linear resistive network composed of the HRES circuits [31]. Sensor outputs in the same column and sensor outputs in adjacent columns use different spatial filtering constants. The different constants serve to reinforce activity within a column and discourage activity between adjacent columns. The filtered signals feed to a symmetric anti-bump circuit [32]. The circuit's operation mimics a soft comparator with an adjustable dead zone. The function of the circuit is to indicate when a particular column has registered a large shear stress value while the neighboring columns have not. The output of the anti-bump circuit, a current, accumulates for a particular column and compared to a threshold. If the accumulated value exceeds the threshold, the circuit triggers the actuator by turning on a pull-down transistor.

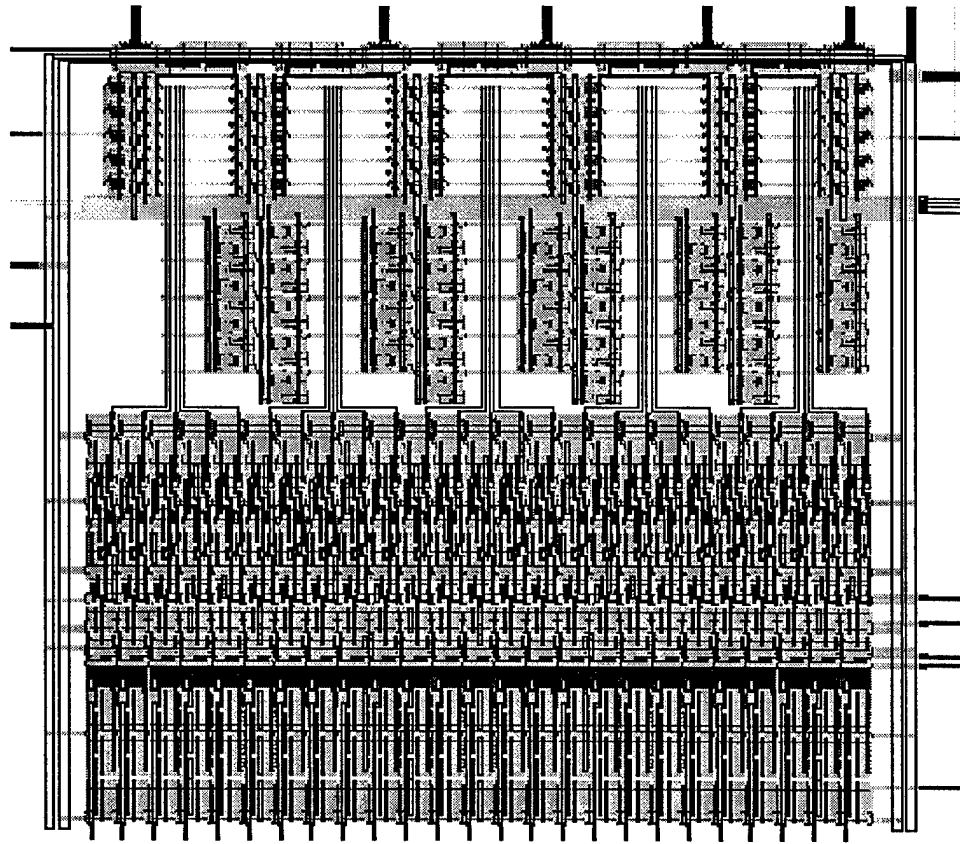


Figure 33. Layout of circuitry on integrate chip.

We designed this system to reduce the fully turbulent drag in our experimental setup. We present the system with a fully turbulent airflow profile. Figure 34 graphs the single column response of the system.

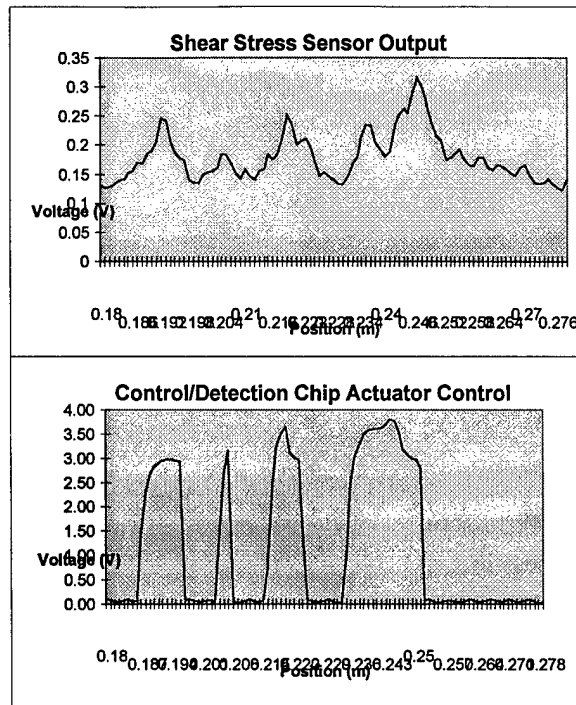


Figure 34. Graph of the output waveforms of one shear stress sensor and the corresponding channel from the detection/control chip. We record the data in a fully developed turbulent flow.

Conclusions

As can be seen by the work presented herein, the effort to reduce drag in turbulent boundary layers requires the collaboration of engineers in many different fields. The individual contributions within each field (MEMS, fluids, controls, and electronics) are novel even as a stand-alone effort. When combined together, such efforts can lead to tremendously exciting discoveries. Much work needs to be done in the future to obtain the desired drag reduction, but efforts to date have proven to be extremely promising and worthwhile.

1. Walsh, M., "Riblets as a Viscous Drag Reduction Technique," *AIAA Journal*, Vol. 21 (4), pp. 485-486, 1983.
2. International Civil Aviation Organization (ICAO), "World Airline Passenger Traffic Growth Rate to Continue Through to 1998", News Release, 1996.
3. Cantwell, B., "Organized Motion in Turbulent Flow," *Annual Review Fluid Mechanics*, Vol. 13, pp. 457-515, 1981.
4. Bechert, D. and Bartenwerfer, M., "The Viscous Flow on Surfaces with Longitudinal Ribs," *Journal of Fluid Mechanics*, Vol. 206, pp. 105-129, 1989.
5. Lazos, B. and Wilkinson, S., "Turbulent Viscous Drag Reduction with Thin-Element Riblets," *AIAA Journal*, Vol. 26 (4), pp. 496-498, 1988.
6. Park, S.-R. and Wallace, J., "Flow Alteration and Drag Reduction by Riblets in a Turbulent Boundary Layer," *AIAA Journal*, Vol. 32 (1), pp. 31-38, 1994.
7. Sirovich, L. and Karisson, S., "Turbulent Drag Reduction by Passive Mechanisms," *Nature*, vol. 388, pp. 753-755, 1997.
8. Vukoslavcevic, P., Wallace, J., and Balint, J.-L., "Viscous Drag Reduction Using Streamwise-Aligned Riblets," *AIAA Journal*, Vol. 30 (4), pp. 1119-1122, 1992.
9. McLean, J., George-Falvy, d., and Sullivan, P., "Flight-Test of Turbulent Skin-Friction Reduction by Riblets," *Turbulent Drag Reduction by Passive Means*, Vol. II, *Proceedings of the Royal Aeronautical society*, pp. 408-424, 1987.
10. Choi, H., Moin, P., and Kim, J., "Active Turbulence Control for Drag Reduction in Wall-Bounded Flows," *Journal of Fluid Mechanics*, Vol. 262, pp. 75-110, 1994.
11. Bushnell, D. and Moore, K., "Drag Reduction in Nature," *Annual Review Fluid Mechanics*, Vol. 23, pp. 65-79, 1991.
12. Hoyt, J.W., "Hydrodynamic Drag Reduction Due to Fish Slimes," *Swimming and Flying in Nature*, ed. Wu, T., Brokaw, C., and Brennen, C., Vol. 2, Plenum, New York, pp. 653-672. 1975.
13. Bechert, D., Bartenwerfer, M., and Hoppe, G., "Drag Reduction Mechanisms Derived from Shark Skin," Paper 86-1.8.3, 15th Congress of the International Council of the Aeronautical Sciences, 1986.
14. Gray, J., "Studies in Animal Locomotion. VI. The Propulsive Powers of the Dolphin," *Journal of Experimental Biology*, Vol. 13, pp. 192-199, 1936.
15. Au, D. and Weihs, D., "At High Speeds Dolphins Save Energy by Leaping," *Nature*, Vol. 284, pp. 548-550, 1980
16. Lang, T. and Pryor, K., "Hydrodynamic Performance of Porpoises (*Stenella attenuata*)," *Science*, Vol. 152, pp. 531-533.
17. Goodstein, R., **Fluid Mechanics Measurements**, Chapter 11, Hemisphere Publish Corp., 1983, pp. 559-615.
18. Liu, C., Tai, Y.-C., Huang, J.-B., and Ho, C. M, "Surface Micromachined Thermal Shear Stress Sensor", *ASME Application of Microfabrication to Fluid Mechanics*, Chicago (1994), pp. 9-15.
19. Tai, Y.-C., and Muller, R., "Lightly-Doped Polysilicon Bridges as Flow Meter", *Sensors and Actuators*, Vol. 15(1), 1988, pp. 63-75.
20. Jiang, F., Tai, Y.-C., Huang, J.-B., and Ho, C. M, "Polysilicon Structures for Shear Stress Sensors", *Digest IEEE TENCON'95*, Hong Kong, Nov. 1995, pp. 12-15.

21. Hussain A. and Reynolds, W., "The mechanics of a perturbation wave in turbulent shear flow", AFOSR Scientific Report 70-1655TR, 1970.
22. Jiang, F., Tai, Y.-C., Karan, R., and Garstenauer, M., "Theoretical and Experimental studies of the Micromachined Hot-Wire Anemometers", Tech. Digest 1994 IEDM, San Francisco, 1994, pp. 139-142.
23. Ferredoxin, P., Johansson, A., Haritonidis, J. and Eckelman, H., "The fluctuating wall-shear stress and the velocity field in the viscous sublayer", Physics of Fluids, Vol. 31, 1988, pp.1026-1033.
24. Obi, S., Inoue, K., Furukawa, T., and Masuda, S., "Experimental study on the statistics of wall shear stress in turbulent channel flows", Tenth symposium on turbulent shear flows, The Pennsylvania State University, Vol. 1, 1995, pp. 5-19 - 5-24.
25. Kim, J., Moin P. and Moser, R., "Turbulence statistics in fully developed channel flow at low Reynolds number", Journal of fluid Mechanics, Vol. 177, 1987, pp. 133-166.
26. Tsao, T., Liu, C., Tai, Y.-C., Ho, C.-M., "Micromachined Magnetic Actuator for Active Fluid Control", ASME Application of Microfabrication to Fluid Mechanics, Chicago (1994), pp. 31-38.
27. Miller, R., Tai, Y.-C., Burr, G., Psaltis, D., Ho, C.-M., and Katti, R., "Electromagnetic MEMS Scanning Mirrors for Holographic Data Storage", Solid State Sensor and Actuator Workshop 1996, pp 183-186, 1996.
28. Tsao, T., Jiang F., Miller R., Tai, Y.-C., Gupta B., Goodman R., Tung, S., and Ho, C.-M., "An Integrated MEMS System for Turbulent Boundary Layer Control," International Conference on Solid-State Sensors and Actuators (Transducers '97), Chicago (1997), pp. 315-318.
29. Moller, M., "Efficient Training of Feed-Forward Neural Networks," Ph.D. Thesis, Aarhus University, Denmark. (1993).
30. Lee, C., Kim, J., Babcock, D. and Goodman, R., "Application of neural networks to turbulence control for drag reduction," Physics of Fluids, Vol. 9, No. 6, 1997.
31. Mead, C., **Analog VLSI and Neural Systems**, Addison-Wesley, Reading, Massachusetts (1989).
32. Delbrück, T., "Bump Circuits for computing similarity and dissimilarity of analog voltages," *Computation and Neural Systems Dept. Memo 10*, California Institute of Technology, Pasadena (1991).
33. Kramer, M., "The Dolphins' Secret," Journal American Society Naval Engineering, Vol. 73, pp. 103-107, 1961.
34. Liu, C., Tsao, T., Tai, Y.-C., and Ho, C.-M., "Surface Micromachined Magnetic Actuators," *Proceedings from IEEE Micro Electro Mechanical Systems*, Oiso, Japan, pp. 57-56, 1994.
35. Tsao, T., Liu, C., Tai, Y.-C., and Ho, C.-M., "Micromachined Magnetic Actuator for Active Fluid Control," *ASME Application of Microfabrication to Fluid Mechanics 1994*, Chicago, IL, USA, pp. 31-38, 1994.

Chih-Ming Ho
Mechanical and Aerospace
Engineering Department,
University of California, Los Angeles,
Los Angeles, CA 90095

Yu-Chong Tai
Division of Engineering
and Applied Science,
California Institute of Technology,
Pasadena, CA 91125

REVIEW: MEMS and Its Applications for Flow Control

Emerging micromachining technology enables us to fabricate mechanical parts on the order of micron size. It provides us with micro-sensors and micro-actuators which facilitate the exploration of all areas of science. Furthermore, these miniature transducers can be integrated with microelectronics. With an integrated system, it then becomes possible to complete the loop of sensing, information processing, and actuation. This type of system enables us to perform real-time control of time varying events which are common in fluid dynamics. In this review paper, we will first briefly introduce Micro-Electro-Mechanical-Systems (MEMS) technology. Then, the applications of MEMS to flow control will be discussed.

Introduction

During the last three decades, the field of solid-state electronics kept improving the manufacturing technology involved in the miniaturization of electronic elements. At present, it is possible to make electronic feature sizes on a sub-micron scale. The integrated circuit (IC) evolved from a small number of transistors on a chip to several million transistors on a chip. The range of applications increased dramatically with time such that the IC has changed our lives. However, an IC cannot interact with the environment. The interaction between a system and the external world has to rely on sensors and actuators which are usually mechanical devices. In the past, almost all of the mechanical parts had sizes much larger than the electronic elements because traditional manufacturing technology had difficulty in fabricating small mechanical parts, say less than a mm. Interestingly enough, Feynman did raise the question of making miniature things in his inspiring paper entitled "There is plenty of room at the bottom" (1956). He even proposed a prize to the first person who could make a motor of $\frac{1}{64}$ in. cube. Though the prize was claimed a few years after 1959, it was accomplished by delicate handicraft not by a mass production technology. In the 1980s, a new manufacturing process, the surface micromachining technology (Howe and Muller, 1983), became available. It could be used to manufacture micron sized mechanical devices with sophisticated geometry. An example is the micro motor (Fan, et al., 1988a), which is shown in Fig. 1. A piece of human hair is also shown in the figure to indicate the size of the motor. These achievements signified the beginning of the era of micromachinery, which will be as valuable as the emergence of microelectronics thirty years ago.

The significance of micromachine technology is that it makes it possible to provide us with mechanical parts

1. of micron size,
2. batch fabricated in large quantities and
3. integrateable with electronics.

Length scale matching between transducers and investigated phenomena is essential so that enough spatial resolution can be achieved for sensing, and efficient momentum and energy transfers from the actuator to the controlled subject can happen. Our scientific knowledge spans the length scales from light years to the sub-atomic domain. Natural phenomena with length scales much larger than the size of human beings, such as the weather, are understood mainly through sensing. No actuation

of that scale is possible. At the other extreme is the atomic scale which we can explore both by sensing and actuation. Accelerated particles are used as actuators, because these particles match the size of the sub-atomic world. When we deal with natural phenomena of human size, there are abundant transducers for both sensing and actuation. However, a gap exists in the spectrum of our knowledge for scales on the order of microns. We do not know very much about the nature of physics in this range due mainly to the lack of transducers of this size. The miniature mechanical parts fabricated by micromachining technology are going to fill this gap.

Micromachining is a batch production process which employs lithographic processes. Since the micromachining technology is derived from the IC technology, it is possible to monolithically integrate the mechanical and electronic elements. The micro-electro-mechanical-systems (MEMS), with its integrated micron-size mechanical parts and IC, will be able to sense the physical world, to process the information, and to then manipulate the physical phenomena through actuators.

There are numerous opportunities for applying MEMS to flow control. It is known for example that shear flows are sensitive to perturbations. If these perturbations are exerted at the origin of the shear layer and are within the instability band, the streamwise development of the flow can be significantly modified (Ho and Huang, 1982 and Ho and Huerre, 1984). This type of flow control scheme has been demonstrated to be very effective on free shear flow because it takes advantage of the flow instability, which is a powerful flow amplifier. This point is especially important for micro actuators because these actuators cannot deliver large forces or high power.

For turbulent wall-bounded shear flow, we face different types of challenges. The flow structures responsible for viscous drag increase in turbulent flow are very small in size, typically several hundred microns in width and several mm in length. Their life time is short, in the millisecond range or less. Great difficulties arise from the fact that they are randomly distributed in time and space. In the past, direct manipulation of these structures was very difficult. The matching in length scale between the micro transducers and the structures makes this task possible.

In this review paper, several examples of micromachines will first be presented. Then, the manufacturing technology will be briefly summarized. Finally, we will discuss the science issues unique to the micron dimension and flow control using MEMS based transducers.

Micromachined Devices

MEMS technology provides transducers to enable us to perform sensing and actuation in various engineering applications.

Contributed by the Fluids Engineering Division for publication in the JOURNAL OF FLUIDS ENGINEERING. Manuscript received by the Fluids Engineering Division October 25, 1995; revised manuscript received June 10, 1996. Technical Editor: D. P. Telionis.

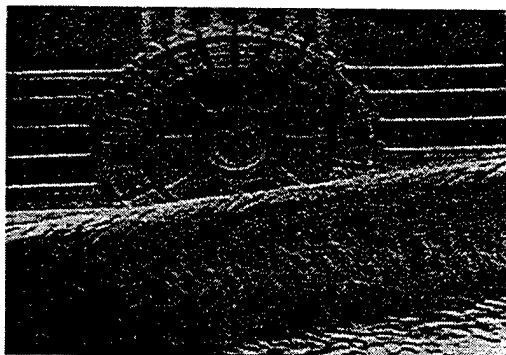


Fig. 1 Micro motor (Fan et al., 1988b)

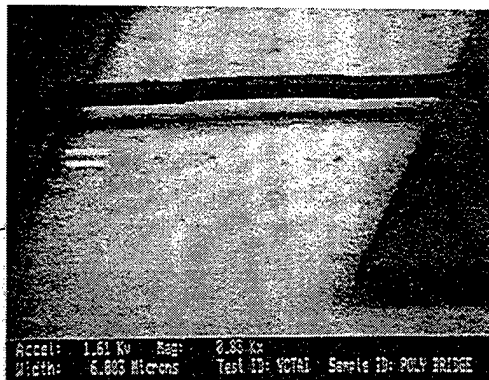


Fig. 2 A micro beam (Tai and Muller, 1988)

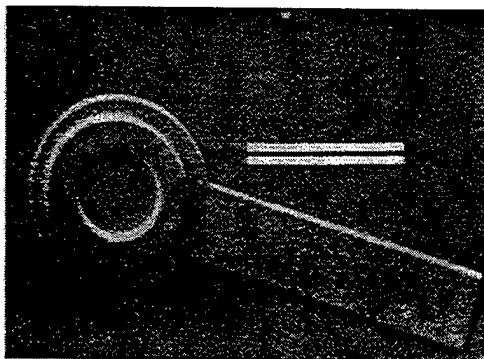


Fig. 3 Micro pin-joint (Fan et al., 1988)

Figures 2 and 3 are two fundamental micro mechanical elements, a beam and a pin joint, from which many micromachines can be derived. For example, the micro motor (Fig. 1) is a combination of a pin joint (rotor) and several short cantilever beams (stators).

Micro transducers also contribute to the advancement of science by enabling us to study the natural phenomena that occur in the order of microns in all branches of science; fluid dynamics, solid mechanics, materials science, biology, etc. The push-pull relationship between science and technology further enriches this field. Most biological cell sizes are in the order of microns which match the scale of micromachines. The micro gripper in Fig. 4 (Kim et al., 1992) shows that it is possible to hold a single cell of $7 \mu\text{m}$ in diameter by a micro device. With some imagination, we can now see a new world through the picture.

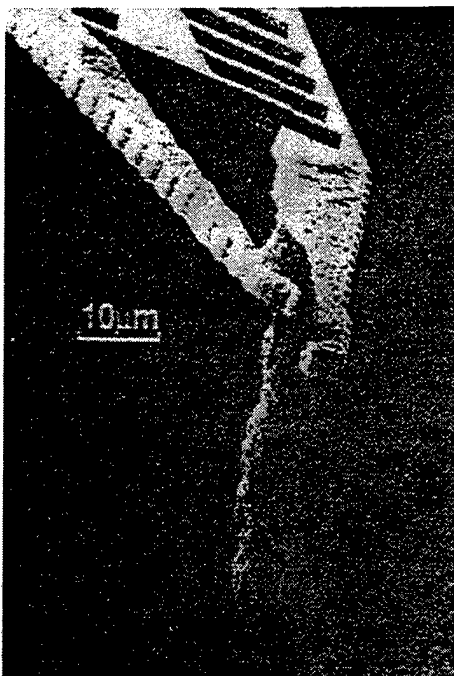


Fig. 4 Micro gripper (Kim et al., 1992)

In the near future, it should also be possible to sense and to manipulate the function of a cell through transducers (Najafi and Wise, 1986). It is interesting for us to understand the functions of neurons which facilitate our cognitive ability, our body's motion and sensing. Micromachines makes it possible to capture a single neuron in a micro cavity and to obtain the electrical signal between neurons (Fig. 5, Tatic-Lucic et al., 1993). It is even possible to receive the neuron signal *in vivo* by inserting micro neuron probes into the brain without disturbing much the neuron due to the probe's miniature size (Fig. 6, Tatic-Lucic et al., 1994).

In the field of material science, it is known that micron-sized subjects are much stronger than large subjects. The fracture strength can be an order of magnitude larger than the bulk fracture strength. Furthermore, silicon material at room temperature experiences only elastic deformation until fracture. Plastic deformation is not obvious. These two features provide a new design concept for micro parts. The buckled state, in a large deformed subject, has seldom been used in the engineering design of macro subjects because it poses the risk of experiencing plastic deformation and even the possibility of fracture. Buckled micro parts are much less prone to these problems. As

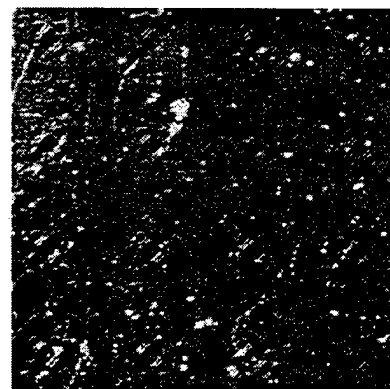


Fig. 5 Neurons in micro cavities (Tatic-Lucic et al., 1993)

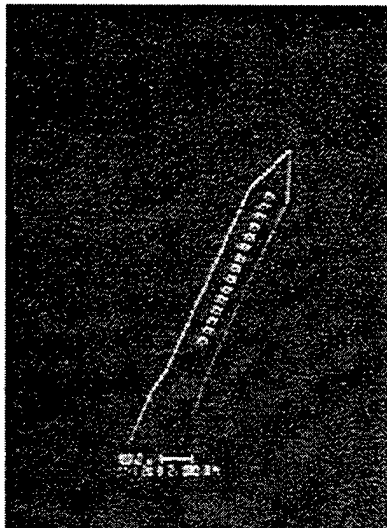


Fig. 6 Neuron probe (Tatic-Lucic et al., 1994)

a matter of fact, several designers have already created devices that utilize these advantages (Ataka, et al., 1994; Matoba, et al., 1994).

In the fluid mechanics arena, turbulence research can benefit from the micro transducers. The spread of the length scales is a function of Reynolds number. The fine dissipation scale in very high Reynolds number flows requires a time response in the order of μs and a spatial resolution in the order of μm . The traditional hot-wire has a spatial resolution of about one mm which is three orders of magnitude larger than the requirement. Its time constant is about one order of magnitude away from the requirement. Transducers made by micromachining technology make it possible to meet these requirements. Using the surface micromachining technique, a micron-sized hot-wire anemometer was made from doped polysilicon (Jiang et al., 1994a and 1994b). When operated in constant temperature mode, a one mega-Hertz bandwidth is possible. Due to the flexibility of the geometric design by lithographic techniques, manufacturing a multiple sensor array is not a painstaking process anymore (Fig. 7).

Micro transducers are already available for industrial applications. The automobile air-bag sensor (Fig. 8) developed by Analog Devices is used to sense the deceleration during an automobile accident to activate the air-bag. Monolithically integrated sensor-microelectronics (Fig. 8) are used for the detection of the capacitance variation of the comb structure (Fig. 9) due to impact, signal conditioner, calibration and many other functions. The integrability between sensor and electronics simplify the packaging process. The lithographic process can reproduce large numbers of integrated micro-sensors and decision circuits on a wafer and therefore greatly reduce the unit cost. The micro optical mirror (Fig. 10) developed by Texas Instrument illustrates a new concept for light beam steering. In a fairly small area, 2.3 cm^2 , about 400 thousand individually addressable mirrors are used to reflect images onto a large screen for a high definition television projection. These mirrors have high optical efficiency and at least a 15 year life span. This is an example of using a large number of distributed actuators to accomplish a complicated light steering task.

The above mentioned examples are a very small fraction of the available micromachines. Intensive research efforts in the last few years have brought forth many new devices as well as new processing techniques. Three basic manufacturing techniques are introduced in the following sections.

Micromachining Technology

Micromachining is the use of a sequence of microfabrication processes to make micromechanical components. As a result, the fundamentals of micromachining are very different from conventional machining. In fact, because of the use of microfabrication processes, micromachining has generally been regarded as being derived from integrated-circuit (IC) technology. There is no doubt that micromachining and IC technology do have many similarities. As an example, micromachining also relies heavily on the use of lithographic methods to first form

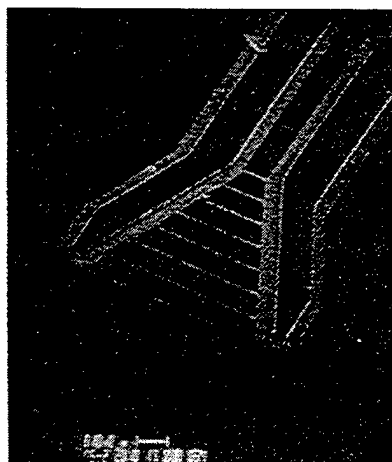


Fig. 7 Hot-wire rake (Jiang et al., 1994)

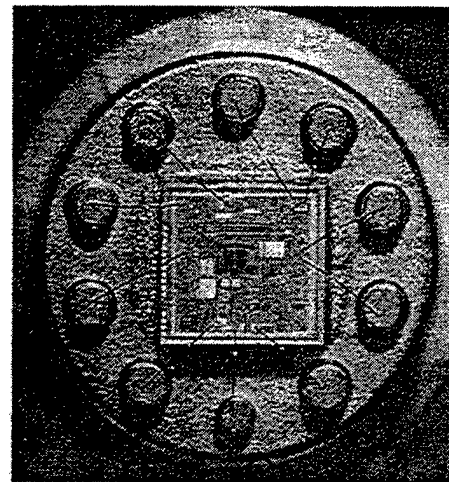


Fig. 8 Air bag sensor (Analog Devices)

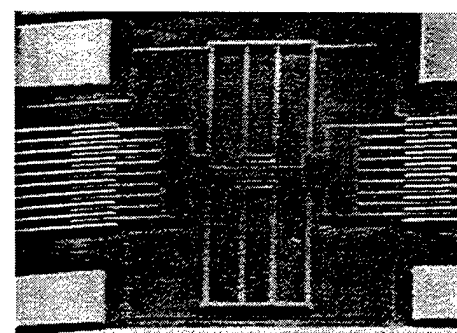


Fig. 9 Microcomb (Tang et al., 1990)

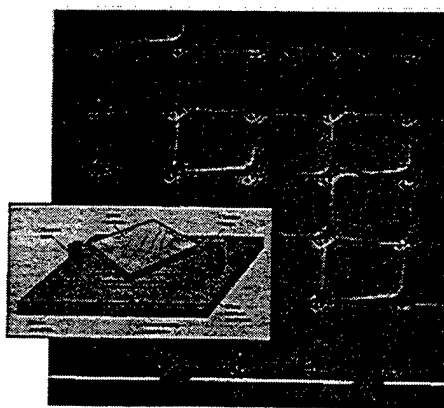


Fig. 10 Micro optic mirror (Texas Instrument)

pre-designed resist patterns (or masks) and then selectively etch the undesirable part away. Nevertheless, they still have many differences and one important difference is that in micromachining, selective etching is used purposely to create 3-D structures while in IC fabrication, distinctively 3-D structures must be avoided so as to facilitate the process of making smaller and smaller feature sizes on a planar wafer surface. Interestingly, it is then these 3-D or even free-standing structures that make micromachining useful as they have numerous micromechanical applications.

Since its beginning, micromachining has already developed into many branch technologies. Among them, bulk micromachining, surface micromachining, and LIGA technology are the most important ones. We will discuss them in the following section, but only briefly. For more information, the readers are referred to some excellent review papers. (Petersen, 1982; Seidel, 1987; O'Connor, 1992; Bryzek et al., 1994)

Bulk Micromachining. A general definition of bulk micromachining is to microfabricate microstructures from a starting substrate by removing the unwanted portion of it. Accordingly, there are many possible combinations of choosing the starting substrate materials and the means of material removal. The main stream of bulk micromachining, however, usually implies that the substrate is a single-crystalline silicon wafer and the material removal is done by selective wet-chemical etching, either isotropically or anisotropically. Moreover, the selective etching of silicon is often through the use of photolithographic masking in conjunction with etch-stop techniques such as using a heavily-doped boron layer (Raley, 1984) or a silicon p-n junction (Jackson, 1981). Altogether, many silicon microstructures can be made including cantilevers, beams, diaphragms, channels, nozzles, etc. These microstructures have formed the building blocks of many MEMS devices.

Chronologically, the development of silicon chemical etchants has been documented since the 1950's as researchers tried to find a precise way of etching silicon (Robbins, 1959). The developed aqueous silicon etchants were mainly isotropic and based on the mixture of hydrofluoric acid, nitric acid, and acetic acid (HNA). Anisotropic etchants for silicon started in the 1960's. The most studied etchants were potassium hydroxide (KOH) (Times, 1967), ethylene-diamine-pyrocatechol with water (EDP or EPW) (Finne, 1967), and hydrazine solutions (Lee, 1969). The anisotropic feature of these etchants is that they etch in the (100) and (110) silicon crystallographic directions much faster than in the (111) direction, which allows the design of microstructures to be naturally bounded by {111} crystalline planes. Figure 11 then shows the typical cases of both isotropic and anisotropic bulk micromachining. Note that etching happens only when the surface is not covered by the patterned mask. For the case of anisotropic etching, different surface orientations, either <100> or <110>, will give totally

different geometries although the saturating walls are all {111} planes.

This feature was broadly used and these anisotropic etchants were further refined in 1970s and 1980s (Kern, 1978; Bassous, 1978; Bean, 1978; Reisman, 1979; Kendall, 1985). Recently, even metal-exclusive anisotropic etchants of ammonium hydroxide (Schnakenberg, 1991a) and tetramethyl ammonium hydroxide (TMAH) (Schnakenberg, 1991b, Tabata, 1991) have been developed. As more and more MEMS devices are integrated with electronics, these etchants have become more important. Today, it is generally agreed that bulk micromachining using wet chemical etching is a mature technology and many MEMS devices are fabricated using it.

In addition to wet chemical etching, recently people also started to look at dry etching processes that can replace or even outperform it. For example, laser etching (Bloomstein, 1994), plasma etching (Miu, 1993), gas etching, reactive-ion etching (Linder, 1991), ion beam etching and even micro electro-discharge-machining (EDM) all have been demonstrated. Bulk micromachining using dry etching is not limited to special crystalline orientations and there will be no surface-tension problems as often encountered in wet etching. However, in order for dry bulk micromachining to become practical, a lot of research still needs to be done.

Surface Micromachining. As the name suggests, surface micromachining is performed on the surface of a substrate, which can be a piece of silicon, glass, alumina, or even metal. This substrate, however, only functions as a mechanical support and it does not participate in the processing. The micromachining then involves combinations of thin-film deposition and patterning. In the end, a selective etch will take away certain layers (called sacrificial layers) and leave other layers (called structural layers) standing free. Figure 12 demonstrates a simplified process of surface micromachining.

According to literature, this concept of surface micromachining was readily demonstrated in the 1950's [US Patent 1956].

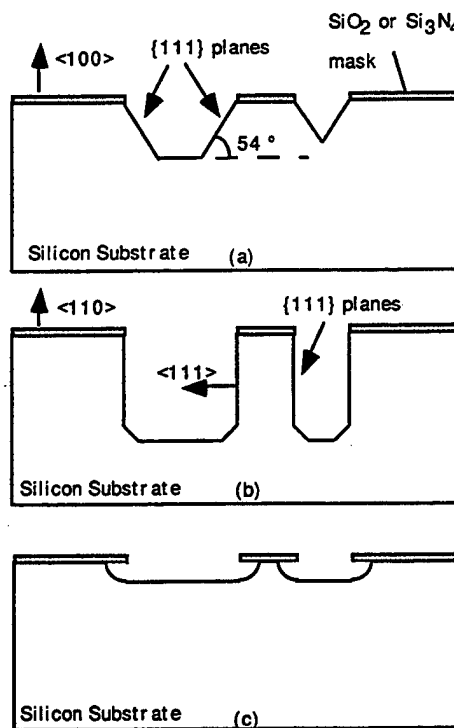


Fig. 11 Typical cases of silicon bulk micromachining (a) anisotropic etching of (100) Si wafer, (b) anisotropic etching of (110) wafer, (c) isotropic etching

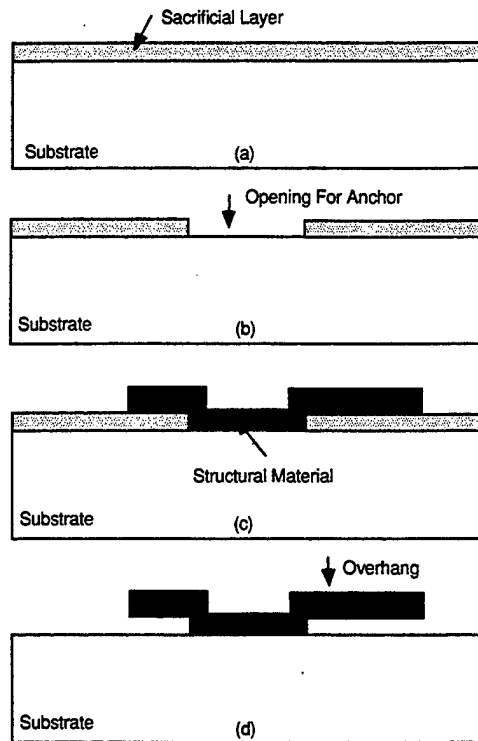


Fig. 12 A schematic process to demonstrate the surface micromachining technology. Note that the overhang structure in (d) can be part of a cantilever beam, a bridge, a plate, or even a diaphragm.

However, the use of it to make a complete MEMS resonant-gate transistor was done much later by Nathanson (1967). After this paper, a series of surface-micromachined devices were published including the early work of the digital mirror display (Preston, 1972). But, it was not until 1982 that Howe (1982) used LPCVD polycrystalline silicon to make micro cantilevers and bridges. The significance of this polysilicon surface micromachining process is that it is compatible with IC technology. The following work at Berkeley in the late 1980s (Fan, 1988; Tai, 1989; Tang, 1989; Kim, 1992) then demonstrated the broad use of polysilicon micromachining for various devices such as micro beams (Fig. 2), pin-joints (Fig. 3), sliders, resonators, tweezers (Fig. 4), and micromotors (Fig. 1). Today, polysilicon micromachining has established itself as one of the most important branches of surface micromachining. In addition to polysilicon surface micromachining, researchers have also explored many other materials such as aluminum (Sampsell, 1993) and silicon nitride (Tabata, 1991). Surface micromachining continues to flourish as MEMS devices become smaller, lighter, faster and cheaper.

LIGA Technology. Finally, there also is the LIGA technology (a German acronym for Lithographie Galvanoformung Anformung) (Becker, 1986; Ehrfeld, 1988). Basically, the LIGA process uses X-ray lithography to generate a deep pattern on a conductive substrate. The empty space in the X-ray resist then is electroplated from the bottom of the substrate to the top of the resist (Fig. 13), which generates a negative replica of the resist mold. This allows structures with submicron resolution from the capability of X-ray lithography. The microstructures can actually be one millimeter thick, and with a submicron precision, there is no other micromachining technique that can match up with it. However, the drawback is the cost for the X-ray source which requires a high-energy synchrotron. Because of this, LIGA may not be a popular technology but it is useful for some special applications which require a fine spatial resolution and a high aspect ratio. Otherwise, the rarity of the X-ray

source and the cost of the technique made others develop similar techniques but with ultraviolet (UV) light sources (Frazier, 1992), available in any IC manufacturing laboratory. Light-heartedly termed as "poor-man's LIGA" or simply "cheap LIGA," this UV-based micro-electroplating gained popularity in many areas and is used to fabricate motors, flaps, and channels (Frazier, 1991; Miu, 1993; Joo, 1995).

Design of Micromachines

A machine consists of several basic requirements: configuration, motion, function and efficiency. Each machine part has its specific geometry and moves in a required manner. The combination of configuration and motion makes the machine capable of carrying out its function. The efficiency or performance of the machine depends on its design.

A micromachine also has to satisfy the same requirements. However, the design is much more challenging because the governing physical mechanism might change in the micro scale. The drastic size reduction in the micro world results in the breakdown of the scaling laws used in traditional engineering fields because the large length scale change is significant enough such that the equations governing the momentum and energy balances need to be re-examined. In addition, the inter-link among these fields becomes important in micron scales, such that the surface physics and chemistry may significantly affect the boundary conditions in fluid and solid mechanics. The changes in the governing equations and boundary conditions prevent us from using the traditional approaches which were well developed in the past. Scaling from the macro to the micro world is questionable. Design rules developed for the macro

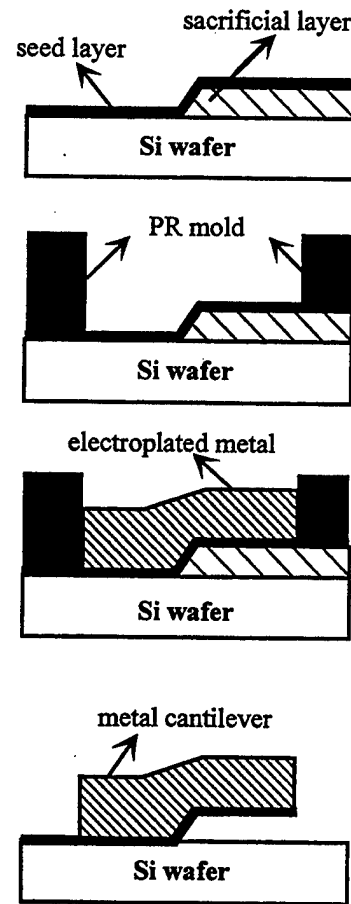


Fig. 13 Micro electro-plating

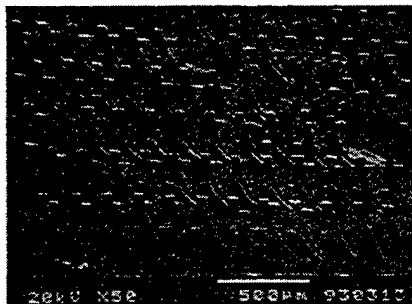


Fig. 14 Micro cilia (Ataka et al., 1994)

scale will not be valid for the micro scale. We need to develop new intuition to design micromachinery.

Relative motion between parts is essential for most machines. However, two micromachine parts designed to have a certain type of motion might not perform according to the desired way due to the large friction between two solid surfaces. A well-known example (Tai and Muller, 1989) is that the rotor of a micro motor will not rotate if the rotor is in full contact with the substrate. If dimples are placed between the rotor and the substrate to reduce the contact area, rotation becomes possible. This result leads to the conclusion that the friction force depends on the contact area which should not be a critical parameter in the conventional physics. It suggests that friction force in the micron scale has undergone a fundamental change. In general, the frictional force is a sum of the surface force and the contribution from the body force. In the macro scale, the body force is much larger than the surface force. Therefore, the frictional coefficient is a function of the body force normal to the contact surface and not a function of the contact area. In the force balance equation, the frictional force therefore has a simple expression. For surface micromachined subjects, the dimension normal to the wafer surface is typically two orders of magnitude smaller than the transverse length scale. This results in the volume per unit contact area of the micro subjects being much smaller than that of the macro subjects. Hence, surface force dominates in the frictional force in the motion of micro subjects. However, the scientific nature of various surface forces which contribute to the frictional force are largely unknown so the analytical form of the frictional force cannot be expressed explicitly or implicitly in writing. This fact leaves an unknown term in the equation of motion of the micro rigid body. The role switch between the body force and the surface force certainly poses a significant burden in designing a micromachine.

Due to the difference in governing mechanisms, we might also have to change the basic design principle. Most of the geometry used in the micromachines, e.g. gear and rotor, are still a size-reduced emulation from the macro world. It is not obvious that the direct emulation is the most appropriate design, especially the ones involving relative motion between large surfaces. Due to the large friction force, the efficiency of micromachines involving sliding motion cannot have high efficiency. Therefore, a new design is needed when a subject is to be transported from one place to another. Simulating the transport mechanism of the cilia, Ataka et al (1994) made an array of flexible silicon cilia (Fig. 14). By thermal actuation, the extension-contraction cycle can move a solid subject sitting on the top of the array. This design can transport a subject without encountering the large friction problem in the micro sliding surface.

Micro Transducers for Flow Control

The small physical size associated with the miniature transducers improves the spatial resolution. The temporal response can easily be increased to a large extent because of the low

inertia of the transducer. These transducers have obvious advantages for flow control problems (McMichael, 1996). Jacobson and Reynolds (1993) used resonant beam actuators to examined the effect on the surface shear stress produced by a stationary vortex pair. Smith and Glezer (1995) have demonstrated the concept of applying a micro jet to achieve thrust vectoring. On the other hand, the capability of providing large quantities of sensors and actuators allows us to perform distributed control. This potential opens a new horizon in many engineering applications and remains to be explored. Its impact could even be more profound than the size reduction of transducers.

Micro Hot-Wire Anemometer. Since the spatial resolution of the anemometers for flow measurement is determined by their physical dimensions, it is advantageous if the wire size can be reduced. In addition, miniature hot-wires also reduce power consumption and thermal interference to the flow. In the past, many anemometer designs have been demonstrated using either surface or bulk-micromachining. However, they are all in the form of a wire adjacent to the surface of a chip. None of them consists of a wire free-standing in space without any nearby structure so that undisturbed free space velocity can be measured. We have developed a micromachined anemometer that has the configuration of a conventional hot-wire anemometer but with a greatly reduced wire size (Jiang et al., 1994a and 1994b). Not only are the spatial resolution and device sensitivity better, the frequency response is also improved by at least one order of magnitude over the conventional hot-wire anemometers.

The micromachined hot-wire anemometer is made of a poly-silicon wire. The typical sensor wires are about $0.5 \mu\text{m}$ thick, $1 \mu\text{m}$ wide, $10\text{--}160 \mu\text{m}$ long. The dynamic performance and sensitivity of the micromachined hot-wire were tested. A heating time of $2 \mu\text{s}$ and a cooling time of $8 \mu\text{s}$ for the $30 \mu\text{m}$ long probe in constant current mode have been obtained. For constant temperature operation, a time constant of $0.5 \mu\text{s}$ for the $10 \mu\text{m}$ long probe can be reached. The corresponding cut-off frequency is 1.4 MHz . A calibration curve of the $20 \mu\text{m}$ long micromachined hot-wire is shown in Fig. 15. The average sensitivity is 20 mV/m/s at a heating current of 0.5 mA .

Micro Surface Shear Stress Sensor. Conventional hot-film type surface shear stress sensors have been used for several decades but the heat transfer to the substrate has always been a handicap in their operation. For measurements in air, the sensitivity is close to zero because of the low heat capacity of air. By using surface micromachining technology, a vacuum chamber is placed under the heating element, as shown schemat-

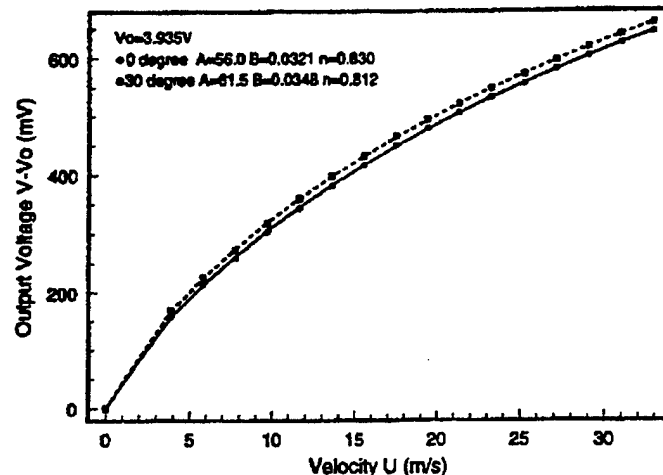


Fig. 15 Calibration of a $20 \mu\text{m}$ long micromachine hot-wire sensor at two different angles

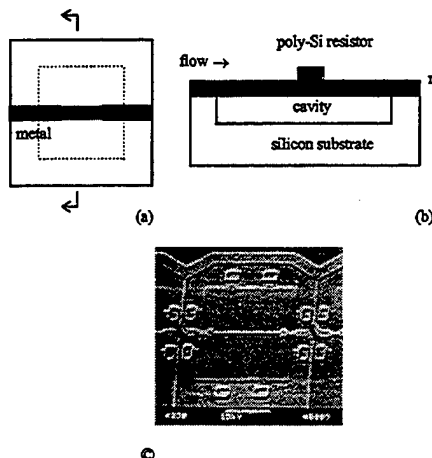


Fig. 16 Schematic of the top (a) and cross-sectional, (b) views of the micro shear-stress sensor, (c) SEM picture of the micro shear-stress sensor

ically in Fig. 16. This cavity significantly decreases the heat loss to the substrate and increases the shear stress sensitivity (Liu et al., 1994, Huang et al., 1995 and 1996).

A silicon nitride film is used as the diaphragm material which supports the heating element. The chamber is formed by etching away a sacrificial layer underneath the diaphragm. The heating element is made of a uniformly doped polysilicon resistor. The aluminum metalization forms the metal leads.

The typical sensitivity of the sensor with a cavity underneath is 15 mV/Pa, which is about one order of magnitude higher than that without a cavity. Figure 17 is a calibration curve of the shear stress sensor, which is plotted with the square of the output voltage versus the $\frac{1}{2}$ power of the shear stress. A linear relationship is obtained. The typical cut-off frequency of the sensor is 10 kHz when operating in the constant temperature mode. Another approach is to directly measure the shear stress by sensing the force on a micro floating element flush mounted on the wall (Shajji et al., 1992, Pan et al., 1995).

Micro Pressure Sensor. The pressure sensor can be designed and fabricated by a similar technology as the aforementioned shear stress sensor. A deposited polysilicon film is patterned as the piezoresistor for strain measurement (Liu et al., 1993). On a $250 \times 250 \mu\text{m}^2$ silicon nitride diaphragm, there are four polysilicon resistors placed around the center and another four on the edge of the diaphragm. The total thickness of the diaphragm is 1.5 μm . Polysilicon resistors are buried inside the diaphragm. The thickness of the polysilicon resistors is 500 nm. The polysilicon resistors are connected to form a

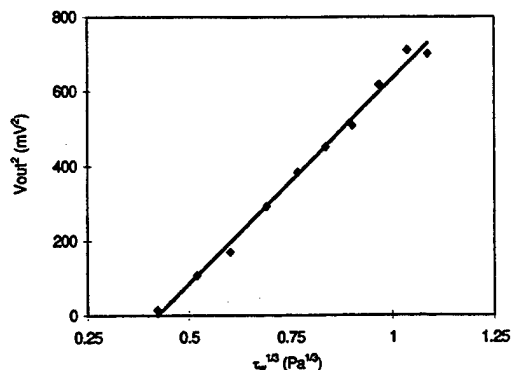


Fig. 17 Micro surface shear stress sensor output versus shear stress at constant temperature mode

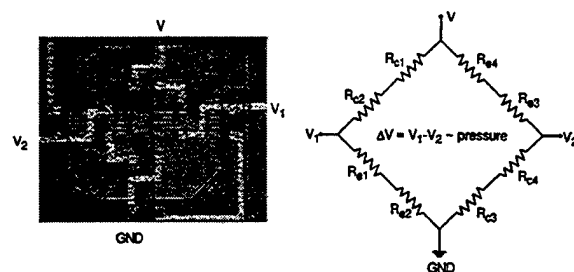


Fig. 18 A micromachined pressure sensor

Wheatstone bridge for temperature compensation although the heavily doped polysilicon shows a very small temperature coefficient. The output of the Wheatstone bridge is proportional to the pressure exerted on the diaphragm. Figure 18 shows a micromachined pressure sensor.

The pressure sensors are fabricated by surfacing micromachining which is compatible with other MEMS devices. We have already integrated this kind of pressure sensor into a micro-flow measurement system (Pong et al., 1994; Shih et al., 1995). The sensitivity of this sensor is about 245 $\mu\text{V/V-psi}$.

Micro Actuator. In flow control problems, we need actuators which are able to provide about one mm off-plane motion and about milli-Newton force per mm^2 for sustaining the wind loading. These requirements are several orders of magnitude higher than that available from existing micro actuators. In order to accomplish these stringent performances, we first select an actuator which has simple configuration so that we at least will not be overburdened by fabrication difficulties. A flap type actuator was chosen for the design. It obviously is fragile, sensitive to the wind load direction as well as has many other deficiencies. However, it does serve the purpose for concept demonstration in laboratory tests (Liu et al., 1994; Tsao et al., 1994; Liu et al., 1995a and 1995b). On the other hand, these flap actuators have many other applications, such as large angle light steering and heat transfer enhancement.

The integration of permalloy with surface-micromachined polysilicon flaps has been completed (Fig. 19). Such a flap uses polysilicon as a structural material for both its beam supports and plate. Permalloy (5 μm thick) is electrodeposited on the top of the plate to provide the actuation mechanism.

Two size flaps, $1 \times 1 \text{ mm}^2$ and $2 \times 2 \text{ mm}^2$, have been made and bending angles up to 80 deg have been achieved with a magnetic flux density of about 800 Gauss. Such a large bending angle equals a point force of 0.2 mN acting on the edge of the flap. These flaps have been mounted on the leading edge of a delta wing and have been proven to be useful for aerodynamic control of the wing.

In addition to the permalloy flaps, we have also developed a bulk-micromachined flap with both copper coils and permalloy (Fig. 20) so the control of the device has more alternatives. The active flap is fabricated by the integration of bulk micromachining and surface-micromachining.

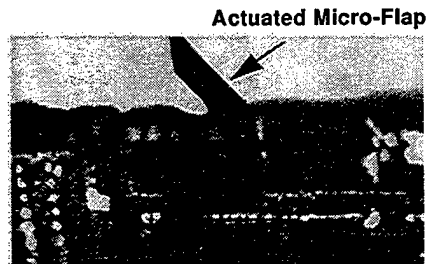


Fig. 19 A magnetically actuated surface-micromachined permalloy flap in a B-field of 400 Gauss

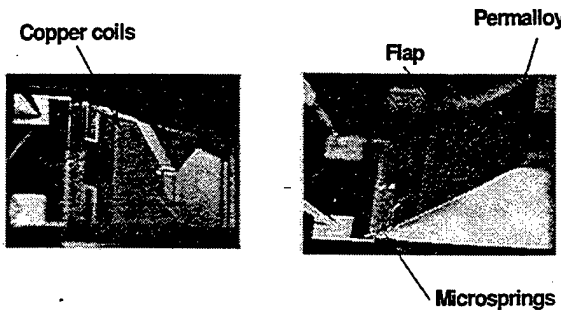


Fig. 20 An active flap integrated with both coil and permalloy. Both up and down positioning are achieved.

ching techniques with magnetic thin film processes. The mechanical structure consists of a $40 \mu\text{m}$ thick, 4 mm by 4 mm single crystal silicon plate, attached to bulk silicon through two $50 \mu\text{m}$ wide S-shaped springs. The electromagnetic component of the actuator sits on the plate surface and consists of a 30-turn planar copper coil, on top of which is a $10 \mu\text{m}$ triangular permalloy ($\text{Ni}_{80}\text{Fe}_{20}$) layer. Controllable deflection of the flap up to $\pm 60^\circ$ has been achieved by both external fields and coil current.

Control of Macro Aerodynamic Device by Micro Transducers

In flow control problems, it is desirable to be able to globally alter the flow by applying minute amounts of energy. We are interested in exploring the possibility of manipulating a macro aerodynamic device by using microactuators. The key point is finding a coupling between the macro physical world and the micro actuation. For a delta wing at high angle of attack, a large fraction of the lift is contributed by the vortices originated from boundary layers around the two leading edges. The coupling here is in the thin boundary layer before separation. If the off-plane displacement of the micro actuator matches the boundary layer thickness before flow separation, we will be able to either change the separation location or vary the vorticity of the delta wing's leading edge vortices. Once the symmetry of the two vortices is broken, it is possible to obtain a rolling torque or even other components of torque and force.

A delta wing model with a sweep angle of 56.5° deg was employed for the test (Fig. 21). The delta wing model had rounded leading edges. Micromachined actuators and micro shear stress sensors were placed on a cylindrical rod located at the leading edge. The rod can be rotated such that the positions of these transducers could be changed to cover the leading edge area. Microactuators with a flap size on the order of mm have been distributed from the apex to the trailing edge. An open-type wind tunnel was used for aerodynamic tests. The test-

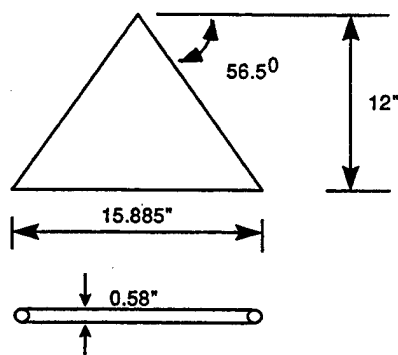


Fig. 21 Schematic of the delta wing

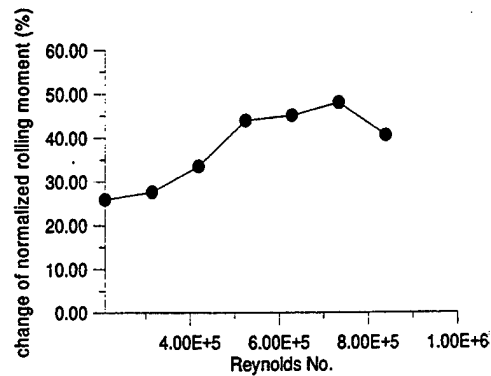


Fig. 22 Effect of micro actuators (both sides) on rolling moment of delta wing at AOA of 25°

section was $100 \text{ cm} \times 100 \text{ cm}$ and 730 cm long. The speed of this wind tunnel was from 10 m/s to 45 m/s. A six component force/moment transducer was used to measure aerodynamic forces and moments. However, only rolling moment was investigated at present.

After a detailed survey of the surface shear stress, we can correlate the effective actuation region with the flow separation region around the leading edge. The most exciting finding is that the rolling torque obtained by the actuation of the micro flaps can be a very significant amount compared with the torque contributed by the leading edge vortices. We use the pressure (suction) produced by one of the leading edge vortices multiplied by the distance between the pressure center and the center chord as the reference torque, T_r . Based on our recent experimental data, the amount of the torque produced by the microactuators can be on the order of 50 percent of T_r (Fig. 22).

Large Scale Integrated System for Distributed Control

For a phenomenon with a wide spread of length scales, e.g., turbulence, a large scale integrated transducer system can facilitate communication of the local information measured by individual sensors as well as identify the global characteristics through a collection of the sensors. The actuators then can, based on the local and global information, execute the proper control strategy.

This concept is best illustrated by research in turbulence control. Surface shear stress reduction in the turbulent boundary layer is the grand challenge in fluid mechanics research. Many randomly distributed small flow structures in the boundary layer are responsible for drag production. The width of these structures at high Reynolds number is only about several hundred microns, much smaller than conventional sensors and actuators. Furthermore, a large number of sensors spread around the surface are necessary to detect these random features and then the actuators can interactively manipulate these vortices. Micro-machine based transducers are small in size as well as capable of forming large scale integrated systems. Direct control of individual structures to understand the response to actuation and its underlying physics now becomes possible. However, only matching of the length scales between the micro transducers and the flow features will not be enough to accomplish the task because detection and control logic need to be implemented. Furthermore, the amount of data associated with a large number of transducers is tremendous. The bandwidth needed is currently beyond the capability of the existing data transmission instrumentation to handle the transmission between the transducer assembly and a computer. A more stringent requirement is that the detection-decision-actuation process needs to be accomplished in the life time of the wall structures. That means real-time operation in a necessity. In other words, on-board



Fig. 23 A surface shear stress imaging chip

signal processing is required. A micro-electro-mechanical-system with large scale integrated microsensors, microelectronics and microactuators offers an opportunity to solve these types of engineering problems which require distributed real-time control.

The Surface Shear Stress Reduction Experiment. The surface shear stress reduction experiment was carried out in a two-dimensional channel flow facility. The channel has a cross section of $2.54 \text{ cm} \times 61 \text{ cm}$. The channel is 488 cm long. The mean velocity can be varied from 5 m/s to 30 m/s. The background turbulence level is about 0.1 percent.

The detection of the high shear stress streaks was performed in the fully developed turbulent portion of the channel. An understanding of the interaction between the actuator and the wall structure is a crucial part of controlling the shear stress. Since the integrated sensing-decision-actuation is still under development, a stationary streamwise vortex embedded in the laminar part of the channel flow was used as a model to study the actuator-vortex interaction (Tung et al., 1995).

Detection of High Shear Stress Streaks. A surface shear stress imaging chip was developed for mapping the instantaneous shear stress (Jiang et al., 1996). The imaging chip contains eighty-five micro sensors (Fig. 23). Each of the three long rows contains twenty-five sensors and the two short rows have five sensors. By placing the imaging chip in the turbulent flow, the voltage outputs from twenty five sensors in the same row were sampled and processed against the calibration curve to convert into stress. The signals are displayed as 2-D shear stress contours in Fig. 24. The time axis is converted to a pseudo streamwise coordinate by multiplying by the convection speed. This surface stress map shows the long streaky pattern of the high stress region (light regions). When the Reynolds number is reduced, the mean width of the streaks increases (Fig. 24(b)). These data demonstrate the capability of distributed sensors in capturing random events.

In order to activate the actuator only in the high stress region, we first need to determine the transverse dimension of the high stress region. Then, the actuator located downstream will be moved. A single sensor which is much smaller than the size of the flow feature is not able to know whether itself is experiencing high stress or not. A detection logic circuit (Fig. 25) was designed for this purpose (Gupta et al., 1996). Basically, the signal output of a sensor is compared with its neighboring sen-

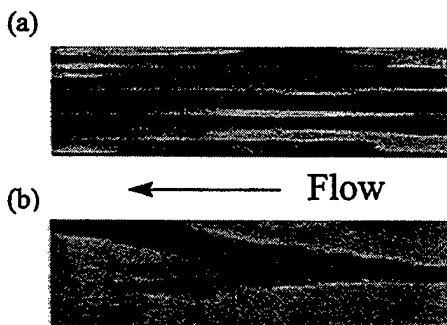


Fig. 24 Instantaneous surface shear stress measured by the imaging chip. (a) $Re = 17,517$; (b) $Re = 8,758$. Re is based on the half width and centerline velocity of the a turbulent channel flow.

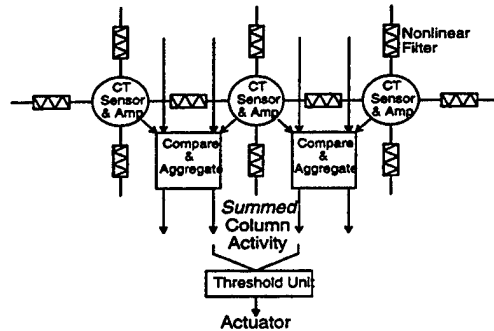


Fig. 25 Block diagram of the control circuits

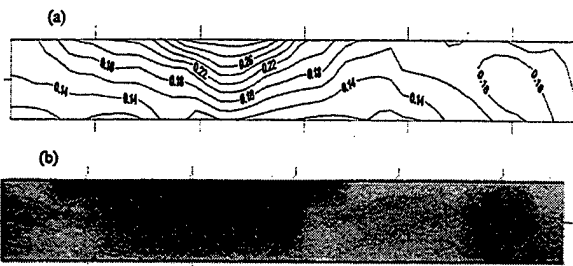


Fig. 26 Contours of (a) the instantaneous surface shear stress and (b) the output of the control circuits

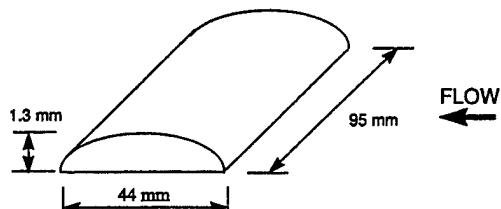


Fig. 27 Schematic of the vortex generator

sors through a filter-threshold combination. Whenever a sudden change is found, the edge of the high shear stress region is determined (Fig. 26). This chip can provide real-time decisions and also delivers current to energize the electro-magnetically driven actuator.

Interaction between Micromachined Actuator and Streamwise Vortices. A crucial part of shear stress control is to determine the efficient control scheme which needs to be developed with an in-depth understanding of the interaction between actuator and flow structures. As a first step, an actuator interacting with a stationary vortex embedded in a laminar flow is used to explore this phenomenon. A 1.3 mm thick vortex generator with a curved surface (Fig. 27) is placed on the surface of the channel. At the end of the vortex generator, a longitudinal vortex pair is produced. Between the two vortices, high speed fluid is brought toward the wall. It generates a high shear stress streak (Fig. 28(a)). The micromachined actuator is a silicon nitride flap with 30 turns of copper coil and matches the size of the longitudinal vortex pair. A permanent magnet is located under the actuator. When an a.c. current passes through the coils at a constant frequency, the flap oscillates at that frequency (Miller et al., 1996). The surface shear stress is measured and phase averaged (Fig. 28(b)). The surface shear stress map shows an appreciable reduction. We integrate the shear stress along the spanwise direction and plot the integrated stress as a function of the phase angle of the actuator motion (Fig. 29). Throughout the whole cycle, the surface shear stress is

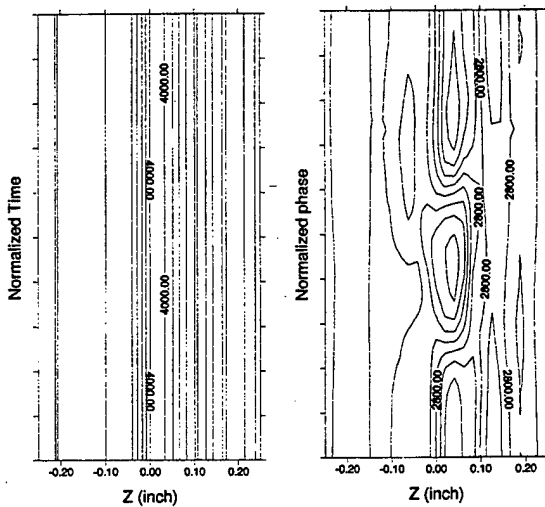


Fig. 28 Contours of ensemble-average dU/dy . (a) Vortex generator only; (b) Vortex generator and an oscillating micro actuator.

lower than that of the stationary vortex alone. The lowest duration is at around the time when the actuator stays at the uppermost location. At 20 Hz oscillation, the stress under controlled conditions can be lower than that of a Blasius velocity profile. This suggests that the flap type actuator can effectively transport the low speed fluid into the high speed stream. At frequencies higher than 20 Hz, the efficiency decreases. However, frequency should not be the proper operating parameter to characterize the actuation. We believe that the frequency multiplied by the oscillation amplitude of the flap is a more appropriate parameter because it is related to the perpendicular speed needed to transport the high speed fluid away from the surface in the high shear stress region. More experiments are underway to clarify the actuator-vortex interaction phenomenon.

Concluding Remarks

The emerging Micro-Electro-Mechanical-Systems (MEMS) technology deals with phenomena in a very distinct length scale, the micron size. In this range, the surface to volume ratio is much larger than that in the macro scale. Hence, the surface effects, e.g. force and chemistry, become a dominating factor. On the other hand, MEMS technology provides us with sensors and actuators in the micron size. These micro transducers enable

us to explore and control the natural phenomena in a length scale regime in which we have not had much experience. The integrated micro-electro-mechanical system can execute in real-time a sensing-decision-actuation process which enables us to control randomly distributed events in intricate turbulence control problems. MEMS is a field which is rich in scientific challenges as well as an enabling technology for broad engineering applications.

Acknowledgment

The authors appreciate the help from R. Goodman, B. Gupta, J.B. Huang, F.K. Jiang, G.B. Lee, C. Liu, R. Miller, T. Tsao, and S. Tung. This work is supported by Air Force Office of Scientific Research and Defense Advanced Research Project Agency.

References

- Allen M. G., 1993, "Polyimide-based Processes for the Fabrication of Thick Electroplated Microstructures," *Transducers '93*, pp. 60-65.
- Arkilic, E., and Breuer, K. S., 1993, "Gaseous Flow in Small Channels," AIAA Paper No. 93-3270.
- Ataka, M., Omodaka, A., and Fujita, H., 1994, "A Biomimetic Micro Motion System—A Ciliary Motion System," *Transducer '93*, pp. 38-41.
- Bandyopadhyay, P. R. and Gad-el-Hak, M., 1994, "Reynolds Number Effects in Wall-bounded Turbulent Flows," to appear in *Applied Mechanics Reviews*.
- Bassous, E., 1978, "Fabrication of Novel Three-Dimensional Microstructures by the Anisotropic Etching of (100) and (110) silicon," *IEEE Trans. on Electron Devices*, Vol. ED-25, No. 10, Oct., pp. 1178-1185.
- Bean, K., "Anisotropic Etching of Silicon, 1978," *IEEE Trans. on Electron Devices*, Vol. ED-25, No. 10, Oct., pp. 1185-1193.
- Becker, E. W., Ehrfeld, W., Haggmann, P., Maner, A., and Munchmeyer, D., 1986, "Fabrication of Microstructures With High-aspect Ratios and Great Structural Heights by Synchrotron Radiation Lithography, Galvoformung, and Plastic Moulding (LIGA Process)," *Microelectronic Engineering*, Vol. 4, pp. 35-36.
- Beskok, A., and Karniadakis, G. E., 1993, "Simulation of Heat and Momentum Transfer in Complex Micro-Geometries," AIAA Paper No. 93-3269.
- Bloomstein, T. M., and Ehrlich, D. J., 1994, "Laser Stereo Micromachining at One-Half Million Cubic Micrometers per Second," *Solid-State Sensors and Actuators Workshop*, Technical Digest, June 13-16, Hilton Head, North Carolina, U.S.A., pp. 142-144.
- Bryzek, J., Petersen, K., Mallon, J., Christel, L., and Pourahmadi, F., 1990, *Silicon Sensors and Microstructures*, NovaSensors.
- Bryzek, J., Petersen, K., and McCulley, W., 1994, "Micromachines on the March," *IEEE Spectrum*, pp. 20-31.
- Ehrfeld, W., Gotz, F., Munchmeyer, D., Schelb, W., and Schmidt, D., 1988, "LIGA Process: Sensor Construction Techniques Via X-ray Lithography," Technical Digest, Solid-State Sensor and Actuator Workshop, Hilton Head, SC, June 6-9, pp. 1-4.
- Fan, L. S., Tai, Y. C., and Muller, R. S., 1988a, "Integrated Movable Micro-mechanical Structures for Sensors and Actuators," *IEEE Trans. on Electronic Devices*, Vol. 35, No. 6, pp. 724-730.
- Fan, L. S., Tai, Y. C., and Muller, R. S., 1988b, "IC-processed Electrostatic Micromotors," *Technical Digest, IEDM*, pp. 666-669.
- Feynman, R. P., 1959, "There's Plenty of Room at the Bottom," Annual Meeting of the APS, Caltech.
- Finne, R. M., and Klein, D. L., 1967, "A Water-Amine-Completing Agent System for Etching Silicon," *J. Electrochem. Soc.*, Vol. 114, No. 9, Sept., pp. 965-970.
- Frazier, A. B., and Allen, M. G., 1992, "High Aspect Ratio Electroplated Microstructures Using a Photosensitive Polyimide Process," *Proc. of Micro Electro Mechanical Systems Workshop*, Travemunde, Germany, Feb., pp. 87-92.
- Guckel, H., Skrobis, K. J., Christenson, T. R., Klein, J., Han, S., Choi, B., and Lovell, E. G., 1991, "Fabrication of Assembled Micromechanical Components via Deep X-ray Lithography," *Proc. of 1991 IEEE Micro Electro Mechanical System Conf.*, pp. 74-79.
- Gupta, B., Goodman, R., Jiang, F., Tai, Y. C., Tung, S., and Ho, C. M., 1996, "Analog VLSI System for Active Drag Reduction," *Proceedings of the Fifth International Conference on Microelectronics for Neural Networks and Fuzzy Systems*, MicroNeuro '96, Lausanne, Switzerland, Feb. 12-14, pp. 45-52.
- Ho, C. M., and Huang, L. S., 1982, "Subharmonics and Vortex Merging in Mixing Layers," *JOURNAL OF FLUID MECHANICS*, Vol. 119, pp. 443-473.
- Ho, C. M., and Huerre, P., 1984, "Perturbed Free Shear Layers," *Ann. Rev. of Fluid Mech.*, Vol. 16, pp. 365-424.
- Ho, C. M., and Tai, Y. C., 1994, "MEMS: Science and Technology," Application of Microfabrication to Fluid Mechanics, *Proceedings of the 1994 International Mechanical Engineering Congress and Exposition*, Chicago, IL.
- Howe, R. T., and Muller, R. S., 1983, "Polycrystalline silicon Micromechanical Beams," *J. Electrochemical Soc.*, Vol. 130, pp. 1420-1423.
- Huang, J., Ho, C. M., Tung, S., Liu, C., and Tai, Y. C., 1995, "Micro Thermal Shear Stress Sensor With and Without Cavity Underneath," *Proceedings, IEEE Instrumentation and Measurement Technology Conference*, Waltham, MA.

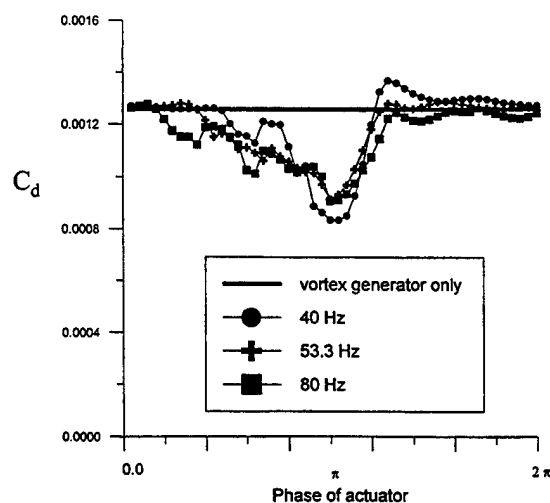


Fig. 29 Variation of the drag coefficient with actuator phase angles for different actuator oscillating frequencies

Huang, J., Tung, S., Ho, C. M., Liu, C., and Tai, Y. C., 1996, "Improved Micro Thermal Shear-Stress Sensor," *IEEE Transactions on Instrumentation and Measurement*, Vol. 45, No. 2, Apr.

Jackson, T. N., Tischler, M. A., and Wise, K. D., 1981, "An Electrochemical P-N Junction Etch-Stop for the formation of Silicon Microstructures," *IEEE Electron Device Letters*, Vol. EDL-2, No. 2, Feb., pp. 44-45.

Jacobson, S. A., and Reynolds, W. C., 1993, "Active Boundary Layer Control Using Mounted Surface Actuators," *Bulletin of American Physical Society*, Vol. 38, pp. 2197.

Jiang, F., Tai, Y. C., Ho, C. M., and Li, W., 1994a, "A Micromachined Polysilicon Hot-wire Anemometer," 1994 Solid-State Sensor and Actuator Workshop, Hilton Head Island, SC.

Jiang, F., Tai, Y. C., Ho, C. M., Karan, R., and Garstenauer, M., 1994b, "A Theoretical and Experimental Studies of Micromachined Hot-Wire Anemometers," *Technical Digest, IEDM*, San Francisco, CA, pp. 264-267.

Jiang, F., Tai, Y. C., Gupta, B., Goodman, R., Tung, S., Huang, J., and Ho, C. M., 1996, "A Surface-Micromachined Shear Stress Imager," *Proceedings of the 9th International IEEE Workshop on MEMS*, pp. 110-115, San Diego.

Joo, Y., Dieu, K., and Kim, C.-J., 1995, "Fabrication of Monolithic Microchannels for IC Chip Cooling," *Proc. of IEEE Micro Electro Mechanical Systems Workshop*, Amsterdam, The Netherlands, Jan.-Feb., pp. 362-367.

Kern, W., 1978, "Chemical Etching of Silicon, Germanium, Gallium Arsenide, and Gallium Phosphide," *RCA Review*, Vol. 39, No. 6, June, pp. 278-308.

Kendall, D. L., and De Guel, G. R., 1985, "Orientations of The Third Kind: The Coming of The Age of (110) Silicon," *Micromachining and Micropackaging of Transducers*, edited by C. D. Fung, P. W. Cheung, W. H. Ko, and D. G. Fleming, eds., Elsevier Science Publishers B. V., Amsterdam, The Netherlands.

Kim, C. J., Pisano, A. P., and Muller, R. S., 1992, "Silicon-Processed Overhanging Microgripper," *J. Microelectromechanical Systems*, Vol. 1, No. 1, pp. 31-36.

Lee, D. B., 1969, "Anisotropic Etching of Silicon," *J. Appl. Phys.*, Vol. 40, No. 11, Oct., pp. 4569-4574.

Linder, C., Tschau, T., Rooij, N. F., 1991, "Deep Dry Etching Techniques As a New IC Compatible Tools For Silicon Micromachining," *Technical Digest, Transducers '91*, San Francisco, pp. 54-57.

Liu, C., Tai, Y. C., Huang, J., and Ho, C. M., 1994, "Surface-Micromachined Thermal Shear Stress Sensor," *Application of Microfabrication to Fluid Mechanics*, FED-Vol. 197, pp. 9-16, ASME.

Liu, C., Tsao, T., Tai, Y. C., and Ho, C. M., 1994, "Surface Micromachined Magnetic Actuators," *Proceed. IEEE International Workshop on MEMS, MEMS '94*, Oiso, Japan.

Liu, C., Tsao, T., Tai, Y. C., Leu, J., Ho, C. M., Tang, W. L., and Miu, D., 1995a, "Out-Of-Plane Permanent Magnetic Actuators for delta Wing Control," *Proceedings, IEEE Micro Electro Mechanical Systems*, Amsterdam, the Netherlands, Jan. 29, pp. 7-12.

Liu, C., Tsao, T., Tai, Y. C., Liu, W., Will, P., and Ho, C. M., 1995b, "A Micromachined Permalloy Magnetic Actuator Array for Micro Robotics Assembly Systems," *Technical Digest, Transducers '95*, pp. 328-331.

Matoba, H., Ishikawa, T., Kim, C. J., and Muller, R. S., 1994, "A Bistable Snapping Microactuator," *IEEE Micro Electro Mechanical System Workshop*, Oiso, Japan, pp. 45-50.

McMichael, J. M., 1996, "Progress and Prospects for Active Flow Control Using Microfabricated Electro-Mechanical Systems (MEMS)," AIAA paper 96-0306.

Miller, R., Burr, G., Tai, Y. C., Psaltis, D., Ho, C. M., and Katti, R., 1996, "Electromagnetic MEMS Scanning Mirrors for Holographic Data Storage," *Technical Digest, Solid-State Sensor and Actuator Workshop*, Hilton Head Island, SC.

Miu, D., Wu, S., Tatic, S., and Tai, Y. C., 1993, "Silicon Micromachined Microstructures for Super-Compact Magnetic Recording Rigid Disk Drives," *Technical Digest, Yokohama, Japan, Transducers '93*, pp. 771-773.

Nathanson, H. C., Newell, W. E., Wickstrom, R. A., and Davis, J. R., 1967, "Resonant Gate Transistors," *IEEE Trans. on Electron Devices*, Vol. 14, pp. 117.

Najafi, K., and Wise, K. D., 1986, "An Implantable Multielectrode Array with On-chip Processing," *IEEE Trans. on Biomed. Eng.*, Vol. 35, pp. 1035-1044.

Nature-Times News Service, 1967, *The London Times*, 23, Nov.

O'Connor, L., 1992, "MEMS: Microelectromechanical Systems," *Mechanical Engineering*, Vol. 114, pp. 40-47.

Pan, T., Hyman, D., Mehregany, M., Reshotko, E., and Willis, B., 1995, "Calibration of microfabricated shear stress sensors," *Digest of Technical Papers, TRANSDUCERS '95, Stockholm, Sweden, June*, pp. 443-446.

Petersen, K., 1982, "Silicon as a Mechanical Material," *Proceedings of the IEEE*, Vol. 70, No. 5, pp. 420-456.

Preston, K., 1972, *Coherent Optical Computers*, McGraw-Hill, New York.

Raley, N. F., Sugiyama, Y., and Van Duzer, T., 1984, "(100) Silicon Etch-Rate Dependence on Boron Concentration in Ethylenediamine Pyrocatechol Water Solutions," *J. Electrochem. Soc.*, Vol. 131, No. 1, Jan., pp. 161-171.

Reisman, A., Berkenblit, M., Chan, S. A., Kaufman, F. B., and Green, D. C., 1979, "The Controlled Etching of Silicon in Catalyzed Ethylenediamine-Pyrocatechol-Water Solutions," *J. Electrochem. Soc.*, Vol. 126, No. 8, Aug., pp. 1406-1415.

Robbins, H., and Schwartz, B., 1959, "Chemical Etching of Silicon," *J. Electrochem. Soc.*, Vol. 106, No. 6, June, pp. 505-508.

Sampsell, J. B., 1993, "The Digital Micromirror Device and Its Application to Projection Display," *Technical Digest, Transducers '93*, Yokohama, Japan, pp. 24-27.

Schnakenberg, U., Benecke, W., Lochel, B., Ullerich, S., and Lange, P., 1991, "NH4OH-based Etchants for Silicon Micromachining: Influence of Additives and Stability of Passivation Layers," *Sensors and Actuators*, A, 25-27, pp. 1-7.

Schnakenberg, U., Benecke, W., and Lange, P., 1991, "TMAHW Etchants for Silicon Micromachining," *Technical Digest, Transducers '91*, pp. 815-818.

Seidel, H., 1987, "The Mechanism of Anisotropic Silicon Etching and Its Relevance for Micromachining," *Technical Digest, Transducers '87*, Tokyo, Japan, pp. 120-125.

Shajii, J., Ng, K.-Y., and Schmidt, M. A., 1992, "A microfabricated floating-element shear stress sensor using wafer-bonding technology," *IEEE/ASME J. of Microelectromechanical Systems*, Vol. 1, No. 2, pp. 89-94.

Shulman, M. A., Ramaswamy, M., Heytens, M. L., and Senturak, S. D., 1991, "An Object-Oriented Material-Property Database Architecture for Microelectromechanical CAD," *Transducers '91*, pp. 486-489.

Smith, B. L., and Glezer, A., 1995, "Jet Vectoring by Synthetic Jet Actuators," *Bulletin of American Physical Society*, Vol. 40, pp. 2025.

Tabata, O., Asahi, R., Funabashi, H., and Sugiyama, S., 1991, "Anisotropic Etching of Silicon in (CH₃)₄NOH Solutions," *Technical Digest, Transducers '91*, pp. 811-814.

Tai, Y. C., and Muller, R. S., 1988, "Polysilicon Bridge as a Flow Meter," *Sensors and Actuators*, Vol. 15, pp. 63-75.

Tai, Y. C., and Muller, R. S., 1989, "IC-Processed Electrostatic Synchronous Micromotors," *Sensors and Actuators*, Vol. 20, pp. 49-55.

Tang, W. C., Nguyen, T. H., and Howe, R. T., 1989, "Laterally Driven Polysilicon Resonant Microstructures," *Sensors and Actuators*, Vol. 20, pp. 25-32.

Tang, W. C., Nguyen, T. C. H., Judy, M. W., and Howe, R. T., 1990, "Electrostatic-Comb Drive of Lateral Polysilicon Resonators," *Sensors and Actuators A Physical*, Vol. 21 (1-3), pp. 328-331.

Tatic-Lucic, S., Tai, Y. C., Wright, J., Pine, J., and Deunison, T., 1993, "Silicon-micromachined Cultured Neurochip for in vitro Studies of Cultured Neural Networks," *Transducer '93*, pp. 943-945, Japan.

Tatic-Lucic, S., Tai, Y. C., Wright, J., and Pine, J., 1994, "Silicon-micromachined Cultured Neuron Probes for in vivo Studies of Neural Networks," to be published in ASME Winter Meeting, Chicago.

Tsao, T., Liu, C., Tai, Y. C., and Ho, C. M., 1994, "Micromachined Magnetic Actuator for Active Fluid Control," *Application of Microfabrication to Fluid Mechanics*, FED-Vol. 197, pp. 31-38, ASME.

Tung, S., Hong, W., Huang, J., Ho, C. M., Liu, C., and Tai, Y. C., 1995, "Control of a Streamwise Vortex by a Mechanical Actuator," *Tenth Symposium on Turbulent Shear Flows*, Pennsylvania State University, University Park, U.S. Patent 2,749,598 (1956).



AIAA 97-0545

**MEMS - A Technology for Advancements
in Aerospace Engineering (Invited Talk)**

**Chih-Ming Ho, Steve Tung and Gwo-Bin Lee
University of California, Los Angeles, California**

**Yu-Chong Tai, Fukang Jiang, and Thoma Tsao
California Institute of Technology, Pasadena, California**

**35th Aerospace Sciences
Meeting & Exhibit
January 6-10, 1997 / Reno, NV**

MEMS - A Technology for Advancements in Aerospace Engineering

Chih-Ming Ho*, Steve Tung and Gwo-Bin Lee
University of California, Los Angeles, California

Yu-Chong Tai†, Fukang Jiang and Thomas Tsao
California Institute of Technology, Pasadena, California

ABSTRACT

A technology, Micro-Electro-Mechanical-Systems (MEMS), emerged in the late 1980s which enables us to fabricate mechanical parts on the order of microns. Micromachining technology is suitable for developing new transducers or improving existing transducer designs. Due to the dramatic reduction in size, micro transducers can outperform traditional ones by orders of magnitude. Furthermore, MEMS is a fundamental technology which has the potential to influence advancements in many fields. In the automobile, electronics, bio-medical and television industries, MEMS products have already made appreciable impacts. In this paper, the applications of MEMS for aerodynamic control will be presented.

INTRODUCTION

A new technology with broad applications may spark a revolutionary change in industry. Three decades ago, microelectronics technology made such an advance: the computer became an indispensable part for our lives. On the other hand, the computer is a collection of solid state transistors which perform fast calculations and carry out preset logic decisions, but it does not interact with the environment. For sensing and manipulating the environment, sensors and actuators are needed, most of which are mechanical. MEMS technology provides sensors and actuators that are micron sized. Furthermore, the MEMS fabrication process is a derivative of microelectronics fabrication technology. It is possible, though not necessarily straightforward, to integrate micro-transducers with the microcomputer such that an integrated system capable of sensing, decision, and actuation becomes feasible. The potential of this micro-electro-mechanical-system is immeasurable and could parallel the progress of microelectronics technology.

Micromachining is a batch production process which utilizes lithographic processes. Three fabrication techniques, bulk micromachining, surface micromachining, and the LIGA process, are commonly used in producing mechanical parts on the micron scale. A brief introduction of these fabrication process can be found in a review paper¹. A micro beam of 6 microns in width and 150 microns in length made by surface micromachining² is shown in Fig. 1. The beam is a basic configuration and is used in various mechanical designs. When surface micromachining is combined with bulk micromachining, we can make the beam structure into a hot-wire probe^{3,4} for turbulence research. The micro hot-wire probe can be moved in free space similar to the conventional one and has a frequency response reaching 1 MHz. A series of beams can be made into a micro-comb structure⁵ (Fig. 2) which is the heart of the micro accelerometer used in airbag sensor produced by Analog Devices (Fig. 3). This microsensor has replaced the traditional automobile collision sensor in all American made cars since 1995.

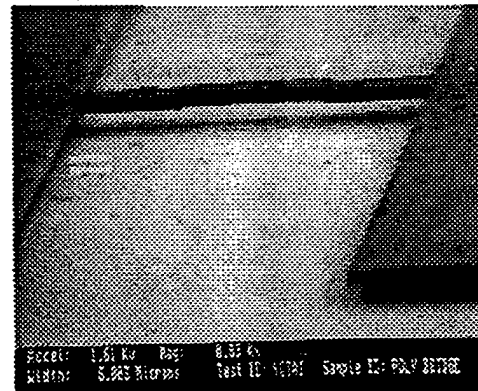


Fig. 1. A micro beam (Tai and Muller 1988).

*Professor, AIAA Fellow

†Associate Professor

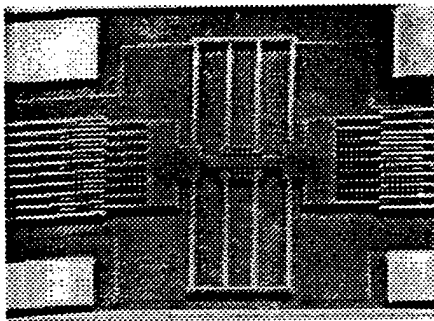


Fig. 2. Comb-drive resonator (Tang, Nguyen, and Howe 1990).

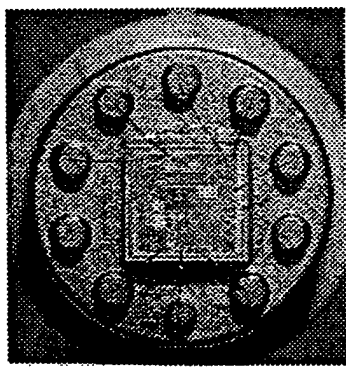


Fig. 3. Air bag sensor (Analog Devices).

The lithographic process can be used to make a large number of transducers on a single wafer. This capability enables us to use distributed transducers to detect physical phenomena. Texas Instruments developed an array of micro mirrors for image projection. In a 2.3 cm^2 area, about 400 thousand individually addressable mirrors are used to direct light in a manner so that high intensity and high contrast images can be produced for slide or television projections (Fig. 4).

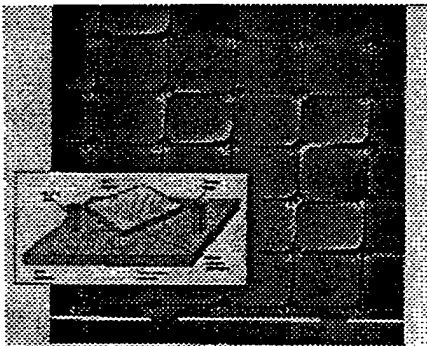


Fig. 4. Micro optic mirror (Texas Instrument).

Distributed control has many applications in aerodynamics⁶. We will discuss two case studies: one is surface shear stress reduction^{7,8,9} and the other is the maneuvering of aircraft by micro actuators¹⁰. Reducing surface shear stress in a turbulent boundary layer has remained one of the most challenging tasks in fluid mechanics research. The roots of the problems are:

1. the transverse length scale of the near wall structures is on the order of hundreds of microns
2. the life time of the structure is about one millisecond or less
3. the near wall structures are spread over the surface area covered by the boundary layer.

Traditional transducers can not satisfy the requirements for detecting and interactively controlling the individual near-wall flow structures. MEMS based transducers are small enough to sense the surface high-shear region and can be used as the basis of the decision made by the onboard circuit to manipulate flow structures. It is possible to build such a Microsensors-Microelectronics-Microactuators system (a M³ system) on a wafer for distributed real-time control. This approach enables us to obtain basic understanding of how a near-wall structure responds to artificial perturbations as well as to develop the process for fabricating a M³ system. The active control of near-wall structures may lead to the reduction of viscous shear stress. Whether the micromachined transducers will be used on aircraft for turbulent shear stress reduction remains to be seen. The fundamental knowledge obtained from building a M³ system for controlling an intricate natural phenomenon has broad applications for numerous engineering and scientific challenges.

As a matter of fact, the concept of using micro transducers for fluidic control has led us to discover a way of controlling a macro aerodynamic device, an aircraft, by using micro actuators. On a delta wing a large portion of the lift is contributed by the leading-edge separation vortices which originate from a thin boundary layer. The thin boundary layer at the leading edge provides a region for coupling between the micro actuator and the global aerodynamic flow field. By using the micro actuators to alter the separation region, the symmetry of the vortex pair is destroyed and a rolling torque is produced. In wind tunnel tests of a delta wing model, the measured torque is appreciable. For this case, we performed a flight test of a 1/7 model of a Mirage III fighter. The effect is phenomenal.

In this paper, we will first discuss the turbulent surface shear stress reduction experiment and then the delta wing control results will be presented.

TURBULENT SHEAR-STRESS CONTROL

The presence of near-wall longitudinal streaks in turbulent boundary layers contributes to a significant portion of the total skin friction. The streaks are on the scale of several hundred microns at the Reynolds number range tested in the wind tunnel. The experiment is carried out in a two-dimensional channel-flow wind tunnel. The channel, constructed of Plexiglas plates, is 24" x 1" in cross-section and 192" long. An axial blower supplies the air flow in the channel.

Single Point Surface Shear Stress Measurement

A micro shear-stress sensor^{11,12,13,14} has been specifically developed to measure the local surface shear stress in a turbulent channel-flow wind tunnel. The micro sensor measures the shear-stress based on the heat transfer from a micro heating element. A 1 micron thick vacuum chamber beneath a silicon nitride diaphragm supporting the heating element significantly reduces heat loss to the substrate. The sensor is flush-mounted on the wall at 168" from the inlet of the wind tunnel where hot-wire and static pressure measurements have confirmed the presence of a fully-developed turbulent channel flow. The DC output of the micro sensor is calibrated against time-average surface shear stress calculated from the streamwise pressure gradient. Time traces of the micro sensor output are recorded for five different Reynolds numbers ranging from 7,000 to 20,000. The Reynolds number is calculated based on the centerline velocity and the half width (1.27 cm) of the channel. The time traces are converted into surface shear stress based on the calibration. The statistics of the fluctuating turbulence surface shear stress are computed.

Figure 5 shows the comparison in the RMS, the skewness factor, and the flatness factor of the surface shear stress as measured by the micro shear-stress sensor and in other studies.

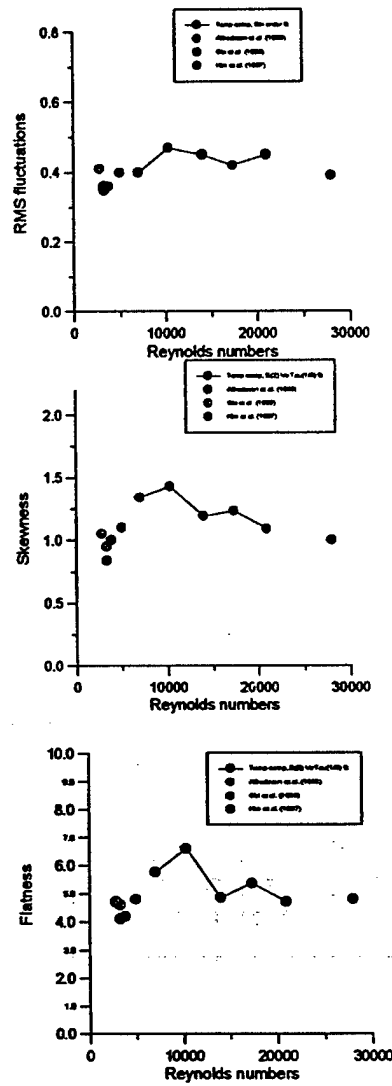


Fig. 5. Turbulence statistics measured by a single micro shear-stress sensor.

As can be seen, the turbulence statistics measured by the micro sensor compare very well with both previous experimental and numerical results.

Distributed Measurement

After the performance of a single micro shear-stress sensor was demonstrated, a surface shear-stress imaging chip¹⁵ (Fig. 6) was developed to measure the instantaneous turbulent shear-stress distribution. Each imaging chip consists of 85 micro sensors. On the chip, the sensors are arranged into multiple arrays, and the spacing between consecutive sensors is designed to provide adequate spatial resolution in measuring the near-wall streamwise streaks. The imaging chip is

packaged into a specially designed PC board which allows the micro sensors to be flush mounted to the wall of the turbulent channel-flow wind tunnel where the experiment is carried out. One array of 25 micro sensors covering a spanwise distance of 7.5 mm is used in the measurement. Each sensor in the array is driven by an external constant temperature circuit, and the output is similarly calibrated as in the single sensor test. Figure 3 shows the instantaneous surface shear-stress contours measured by the micro sensor array. The horizontal axis of the contour plots is the spanwise distance covered by the sensor array and the vertical axis is a pseudo-streamwise distance computed from the sampling time of the sensor signals and the convective velocity of the flow. The shear-stress contours show randomly-distributed high shear-stress streaks. An estimate of the length, the width, and the spacing of the streaks indicate that the scales of the streaks measured by the micro sensors agree very well with previous flow visualization observations.

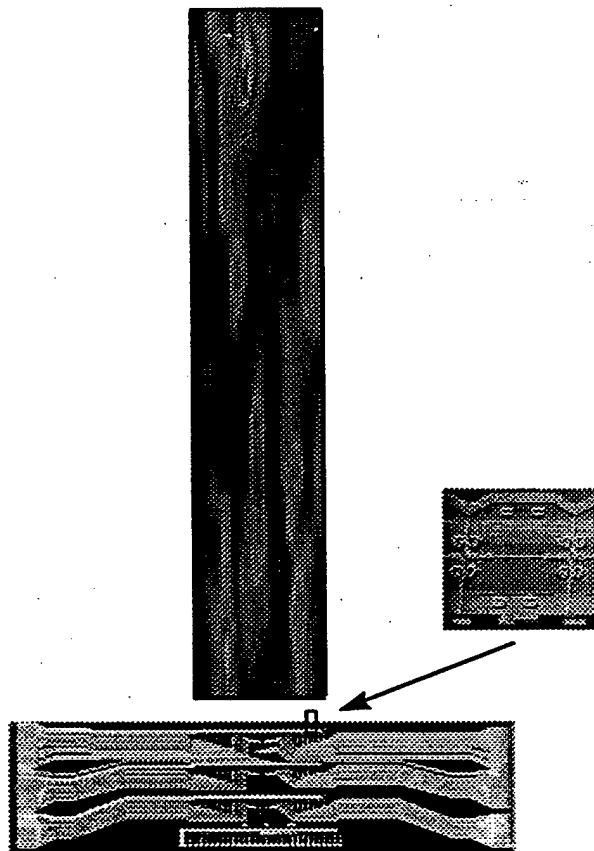


Fig. 6. Instantaneous surface shear stress measured by the imaging chip. $Re = 17,517$.

Edge Detector for Detecting High Shear-Stress Regions

The high-shear stress streaks are randomly distributed. A real-time detection scheme is needed to properly identify the streaks among the background fluctuations so that the downstream actuator can be activated. A neural network based detection circuit has been developed for this purpose¹⁶. In this circuit, the signal output of a sensor is compared with its neighboring sensors through a filter-threshold combination. Whenever a sudden change is detected, the boundary of the high shear stress region is marked. This circuit has been used in conjunction with the imaging chip and a typical result is shown in Fig. 7. The light region in the control output (Fig. 7-b) represents 'positive' identification of high shear-stress streaks. The good matching between the light-color region and the high shear-stress area (light gray region) measured by the imaging chip (Fig. 7-a) indicates the effectiveness of the detection circuit.

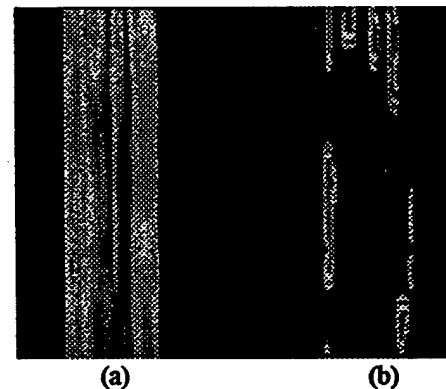


Fig. 7. Contours of (a) the instantaneous surface shear stress and (b) the output of the control circuits.

Interaction between Micromachined Actuator and Streamwise Vortices

To properly control the high shear-stress streaks with micro actuators, an in-depth understanding of the interaction between the actuators and the flow structures is required. Experiments have been carried out to investigate the interaction between a single high shear-stress streak and a micromachined actuator^{17,18,19,20,21}. In this study, a 1.3 mm thick vortex generator is used to generate a longitudinal vortex pair in a laminar boundary layer. The micromachined actuator used is a silicon flap with 30 turns of copper coil and matches the physical size of the longitudinal vortex pair. Oscillation of the flap is achieved by the combination of an external permanent magnet and an AC coil current. The maximum

deflection of the flap is about 30 degrees, which corresponds to height of 2 mm from the tip of the actuator flap to the wall. The maximum oscillation frequency is about 100 Hz. The actuator is placed downstream from the vortex generator where the longitudinal vortex pair is generated. Experiments are carried out for different combinations of actuator frequency (ω) and maximum tip height (d). For each combination, a two-component (streamwise and spanwise) hot-wire anemometer is used to measure the velocity distributions downstream from the actuator. From the velocity distributions, the vorticity and surface shear stress distributions are calculated and phase averaged.

The longitudinal vortices generated by the vortex generator convect high-speed fluid to the wall, inducing a local high shear-stress streak (Fig. 8) on the surface. As the actuator oscillates, it generates perturbations in the flow which change the shear stress intensity of the streak. As indicated by the ensemble-average result shown in Fig. 8, the intensity of the streak decreases as the flap actuator deflects away from the surface, reaching a minimum at the maximum actuator tip height (phase = π). As the actuator moves back to the surface, the streak intensity reverses to its original level. To evaluate the net effect of the actuator oscillation on the shear stress distribution, the net shear stress coefficient, C_{DN} , defined as

$$C_D(\theta) = \frac{1}{0.5\rho U^2} \int_{-z}^{+z} \mu \frac{\partial u}{\partial y}, \text{ and}$$

$$C_{DN} = \int_0^{2\pi} [C_D(\theta) - C_{D,VG}] d\theta,$$

for different ω -d combinations are evaluated and shown in Fig. 9. The $C_{D,VG}$ in the equation is the time-invariant shear stress coefficient associated with the stationary high shear-stress streak induced by the vortex generator. Defined this way, C_{DN} indicates a shear stress increase if positive and a drag decrease if negative. As shown in Fig. 9, higher drag reduction is achieved at higher ω and higher d. In addition, similar shear stress reduction is the result if the product of ω and d is the same. Since the product of ω and d is a measurement of the transverse velocity of the actuator flap, this result indicates that the amount of shear stress reduction is directly related to the transport of high-speed fluid away from the surface by the vertical motion actuator.

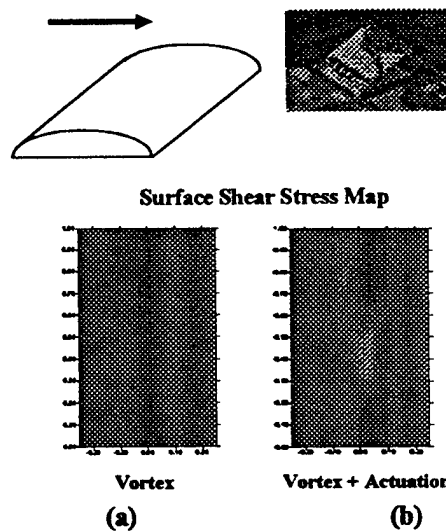


Fig. 8. Contours of ensemble-average dU/dy . (a) Vortex generator only; (b) Vortex generator and an oscillating micro actuator.

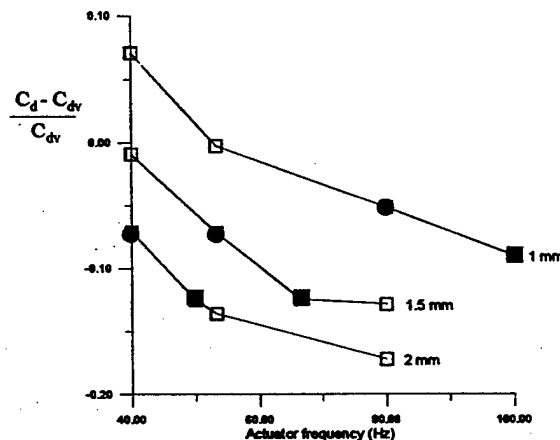


Fig. 9. Variation of the shear stress coefficient, C_{DN} , with actuator frequency, ω , and maximum actuator tip height, d. Each line is the result of one d, as indicated at the end of the line. The solid O markers correspond to an ωd of 80 and the solid \square markers correspond to an ωd of 100.

A M³ System for Shear Stress Reduction

To integrate microsensors, microelectronics and microactuators on a chip is possible, yet is not a trivial task. The transducers may need to be fabricated at a much higher temperature than that of the circuits which means the diffusion of the doping material in the circuits may affect its performance. The process flow needs to be carefully planned to eliminate cross-contamination possibilities. We have fabricated a M³ system for shear stress reduction (Fig. 10). On this 1

cm by 1 cm die, 18 micro shear stress sensors, 3 micro flap actuators as well as circuits for logic, sensor driver and actuator drivers are monolithically integrated. It is not fully functional yet. Experience gained through this exercise are extremely valuable for us to proceed toward a working system.

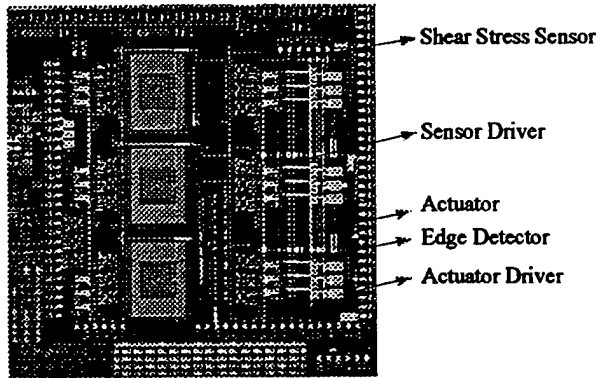


Fig. 10. A M³ system for shear stress reduction

MACRO AERODYNAMIC DEVICES CONTROLLED BY MICRO ACTUATORS

For controlling the motion of an aircraft with a delta wing, we need to manipulate the vortices which have a length scale of the wing. This is very different from controlling the small near wall structures in the surface shear stress control experiment. The problem is to find a coupling between the micro actuators and the wing-size flow structures. It is known that the evolution of the vortex is sensitive to perturbations at its origin^{22,23}. The leading edge vortices develop from a thin boundary layer separated from the surface. We can employ micro actuators with a displacement comparable to the boundary layer thickness to manipulate the separation process, and therefore achieve control of the global motion by minute perturbations.

Experimental Setup

An open-type wind tunnel was used for aerodynamic tests. The test-section is 3 ft. x 3 ft. and 22 ft. long. The maximum operating speed of this wind tunnel is 45 m/s. The turbulence level of the wind tunnel is about 0.6 %.

A delta wing model with a swept angle of 56.5° was used for this study. The delta wing model has rounded leading edges. Micromachined actuators and micro shear stress sensors were placed on a cylindrical rod located at the leading edges of a delta

wing. The rod can be rotated such that the locations of these transducers can be altered to cover the whole leading edge area. Using micro shear stress sensors, we can map the shear stress distribution on the leading edge, and consequently determine the separation line. We also can find the optimum actuator location for micro actuators which use this type of setup¹⁰.

Control of Rolling, Pitching, and Yawing Moments

A delta wing with a swept angle of 56.5° is mounted on a six-component force/moment transducer (AMTI, INC.) which records forces and moments in all three axes. First, we used actuators which extend from the apex to the trailing edge, the A-T actuator. The location of the actuator is indicated by the angle, θ , which is measured from the lower surface of the wing (Fig. 11). At different angles of attack (α) the incremental torque generated by the miniature actuator, M_a , was normalized by the torque produced by the vortex lift, M_v , which is the product of the lift generated by a single leading edge vortex and the distance between the centroid of the half wing and the center line⁸. In this paper, M_v at $\alpha = 30^\circ$ is used for all the normalization.

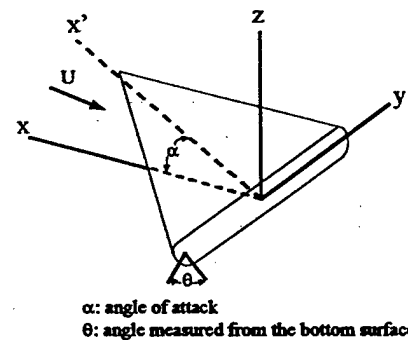


Fig. 11. Schematic representation of delta wing system

The data for $\alpha = 25^\circ$ are presented in Figs. 12 - 14. In general, the curves of all three moments collapse when they are normalized to M_v . Here, M_v is proportional to the velocity to the second power. Inertia of the wing is a function of weight distribution and geometry, but is independent of velocity. Using miniature actuators the torque can be achieved with high angular acceleration and an increase in velocity.

Figure 12 shows that rolling moment has a positive peak of 40% at around $\theta = 40^\circ\text{--}50^\circ$ which has been identified as the separation region in a previous

paper¹⁰. Around $\theta = 80^\circ\text{--}90^\circ$, a negative peak of 40 % was detected. Using this feature, we can obtain an additional rolling moment by using two A-T actuators placed on two leading edges, one at the positive peak and the other one at the negative peak. The test results show that resultant rolling torque is equal to the sum of the two effects. At $\text{AOA} = 25^\circ$, the normalized rolling moment can reach 70% using this combination.

The pattern of the pitching moment is different from that of rolling moment (Fig. 13). For $\theta < 30^\circ$, the pitching moment is close to zero and has its peak of 15% at $\theta = 50^\circ\text{--}60^\circ$. If we use two-sided actuation, about 30% of the pitching moment can be achieved.

The yawing moment (Fig. 14) also has a different profile from that of the rolling and pitching moment. When the actuator is placed around the lower surface, i.e. $\theta < 40^\circ$. Only -4 % change of yawing moment is found at $\theta = 40^\circ$ and 8% at $\theta = 90^\circ$. About 12% of yawing moment can be obtained if two-sided actuation is employed.

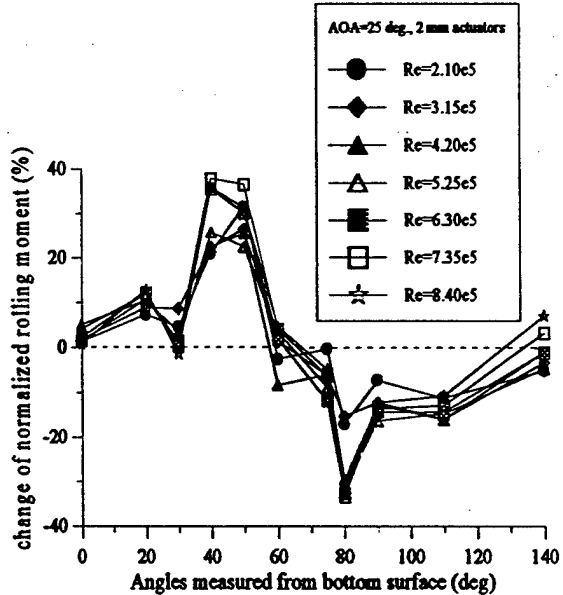


Fig. 12. Normalized rolling moment vs. actuator location at $\text{AOA} = 25^\circ$, A-T actuation

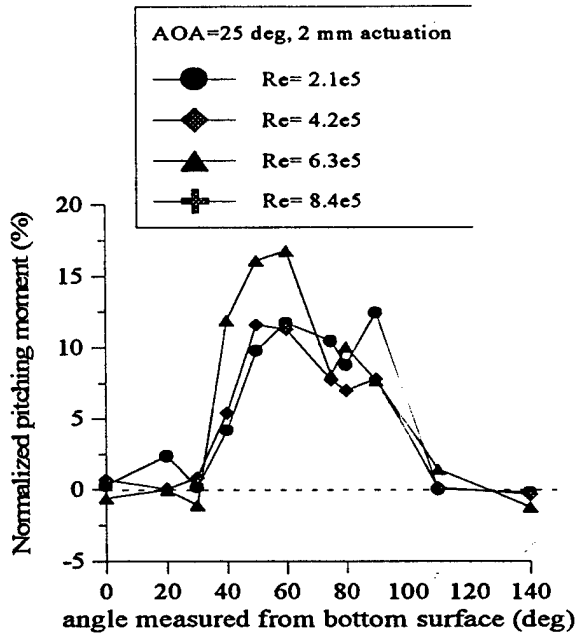


Fig. 13. Normalized pitching moment vs. actuator location at $\text{AOA} = 25^\circ$, A-T actuation

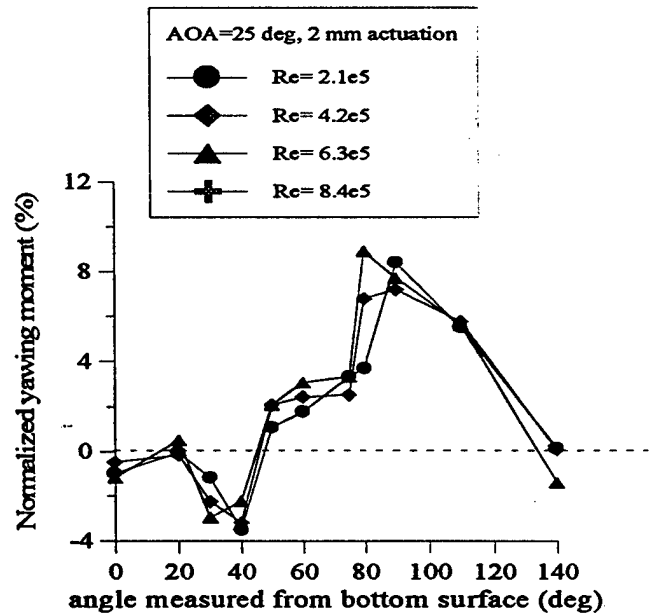


Fig. 14. Normalized yawing moment vs. actuator location at $\text{AOA} = 25^\circ$, A-T actuation

The actuator design which extends half-way between the apex and trailing edge, the H-A-T actuator, has been tested. Two H-A-T actuators were placed on both leading edges. Data shows that about 30% of the normalized pitching moment and 8 % of the normalized yawing moment can be generated by using this kind of actuation (Figs. 15 - 16). Moreover,

if two H-A-T actuators are positioned at the corresponding location of each leading edge, the actuation provides zero rolling moment and a finite pitching moment. These tests suggest that extensive possibilities of controlling aerodynamic moments exist. In other words, a system of distributed actuators can be used to optimize the control of the three moments.

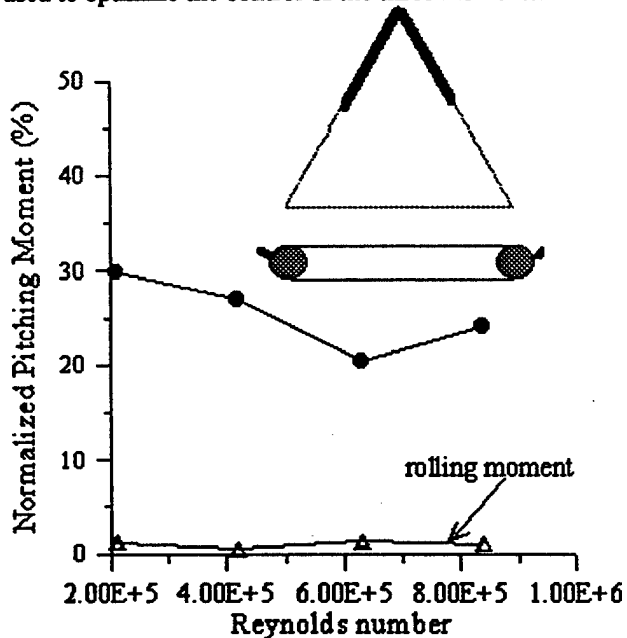


Figure 15. Normalized pitching moment vs. Reynolds number at $AOA=25^\circ$, two-sided H-A-T actuators

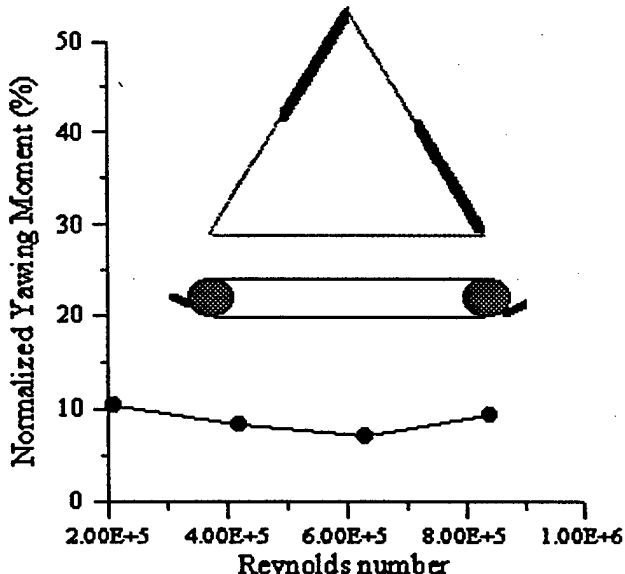


Figure 16. Normalized yawing moment vs. Reynolds number at $AOA=25^\circ$, two-sided H-A-T actuators

Flight Test of a Scaled Model Airplane

An one-seventh scale Mirage III airplane with a rounded leading edge was built for a proof-of-concept test. Miniature mechanical actuators (3mm and 6mm) were mounted at different locations on the leading edge to investigate the optimum location for torque control. Five different locations, 0° , 40° , 60° , 90° , and 120° , have been tested and video footage shows that 60° is the most effective location. Video footage also shows that several maneuver modes can be achieved by using miniature actuators including a 180° roll in 0.8 second as well as swift turning and looping of the airplane. No appreciable difference can be observed for 3 mm and 6 mm actuators which suggests that the boundary layer at the leading edge should be 3 mm or less for this scale. Further reduction in the size of the actuators will be tested. In the future, extensive experiments on scaled aircraft will be carried out for investigating moment control by micro actuators.

CONCLUDING REMARKS

MEMS technology can be used to fabricate sensors and actuators in sizes which are one or more orders of magnitude smaller than the ones made by traditional techniques so that the temporal and spatial resolutions can be greatly improved. Another property of the MEMS sensor is that it can be monolithically integrated with microelectronics. The MEMS airbag sensor uses this advantage to increase its functionality and lower the unit costs such that it occupies a major share of the market in a short time. Using a large number of actuators to control the light beam in a distributed manner, the Texas Instruments DLP mirror array introduces a completely new approach to image projection.

These three features of MEMS transducers,

1. small physical size
2. ability to be integrated with microelectronics
3. distributed control by utilizing arrays of transducers,

can make many difficult flow control tasks possible. The M^3 system reported in this paper enables us to directly perturb individual near-wall flow structures in the turbulent boundary layer for better understanding of the flow physics and possible reduction of the surface shear stress. The delta wing experiment has demonstrated that micro actuators are possible to influence the global aerodynamics.

MEMS is a revolutionary technology which has and will continue to facilitate basic research and make impacts to numerous industries. The experience of the last few years in the flow control area shows that:

1. the small physical size is idea for sensor applications. We have demonstrated the air-worthiness of the micro sensors by placing them around the leading edge of a wing of an F-15 which flew at $M=1$ speed. The sensors are robust enough without suffering structure damage.
2. when microelectronics is used for real-time control, a simple circuit is necessary to save the processing time and real estate on the chip. A neural network can be a useful choice for satisfying these requirements, and its use has been illustrated in a drag reduction numerical experiment²⁴.
3. the force and displacement outputs of actuators used in flow control tasks are usually much higher than typical MEMS actuators can provide. Special efforts of developing actuators for satisfying these requirements are in need.

ACKNOWLEDGMENT

This work is support by the DARPA ETO and AFOSR.

REFERENCES

1. Ho, C.M., and Tai, Y.C., 1996, "Review: MEMS and Its Applications for Flow Control", *J. of Fluids Engineering*, Vol. 118, pp. 437-447.
2. Tai, Y. C. and Muller R. S., 1988, "Polysilicon Bridge as a Flow Meter", *Sensors and Actuators*, Vol.15, pp. 63-75.
3. Jiang F., Tai Y. C., Ho, C. M. and Li, W., 1994a, " A Micromachined Polysilicon Hot-wire Anemometer", 1994 Solid-State Sensor and Actuator Workshop, Hilton Head Island, SC.
4. Jiang, F., Tai, Y.C., Ho, C.M., Karan, R. and Garstenauer, M., 1994b,"A Theoretical and Experimental Studies of Micromachined Hot-Wire Anemometers," *Technical Digest, IEDM, San Francisco, CA*, pp. 264-267.
5. Tang, W. C., Nguyen, T. C. H., Judy, M. W., and Howe, R. T., 1990, "Electrostatic-Comb Drive of Lateral Polysilicon Resonators", *Sensors and Actuators A Physical*, Vol. 21(1-3), pp328-331.
6. McMichael, J. M., 1996, "Progress and Prospects for Active Flow Control Using Microfabricated Electro-Mechanical Systems (MEMS)", *AIAA paper 96-0306*.
7. Bhusan Gupta, Rodney Goodman, Fukang Jiang, Yu-Chong Tai, Steve Tung and Chih-Ming Ho , "Analog VLSI System for Active Drag Reduction", *IEEE MICRO*, Volume 16, No. 5, page 53, October, 1996.
8. Lee, G. B., Ho, C. M., Jiang, F., Liu, C., Tsao, T., and Tai, Y. C., 1996, "Distributed Flow Control by MEMS", *ASME 1996 International Mechanical Engineering Congress and Exposition*, Atlanta, Georgia, USA, Nov. 17-22, 1996.
9. Jacobson, S. A. and Reynolds, W.C., 1993, " Active Boundary Layer Control Using Mounted Surface Actuators", *Bulletin of American Physical Society*. Vol. 38, pp. 2197.
10. Lee, G. B., Jiang, F., Tsao, T., Tai, Y. C, and Ho, C. M., 1997, "Macro Aerodynamic Devices Controlled by Micro Systems", *1997 IEEE Aerospace Conference ,Snowmass, Colorado*.
11. Liu, C., Tai, Y.C. Huang, J. and Ho, C. M., 1994, "Surface-Micromachined Thermal Shear Stress Sensor," *Application of Microfabrication to Fluid Mechanics*, FED-Vol. 197, pp. 9-16, ASME.
12. Huang, J., Ho, C.M., Tung, S., Liu C., and Tai, Y.C., 1995, "Micro Thermal Shear Stress Sensor With and Without Cavity Underneath," *Proceedings, IEEE Instrumentation and Measurement Technology Conference*, Waltham, Mass.
13. Huang, J., Tung, S., Ho, C. M., Liu, C., and Tai, Y. C., 1996, "Improved Micro Thermal Shear-Stress Sensor", *IEEE transactions on Instrumentation and Measurement*, Vol. 45, No. 2, April.
14. Pan, T., Hyman, d., Mehregany, M., Reshotko, E., and Willis, B., 1995, "Calibration of microfabricated shear stress sensors", *Digest of Technical Papers, TRANSDUCERS '95, Stockholm, Sweden*, June, pp. 443-446.
15. Jiang, F., Tai, Y. C., Gupta, B., Goodman, R., Tung, S., Huang, J., and Ho, C. M., 1996, "A Surface-Micromachined Shear Stress Imager", *Proceedings of the 9th International IEEE Workshop on MEMS*, p110-115, San Diego.
16. Gupta, B., Goodman, R., Jiang, F., Tai, Y. C., Tung, S., and Ho, C. M., 1996, "Analog VLSI System for Active Drag Reduction", *Proceedings of the Fifth International Conference on Microelectronics for Neural Networks and Fuzzy*

Systems, page 45-52, MicroNeuro '96, Lausanne, Switzerland, February 12-14.

- 17. Liu C., Tsao T., Tai Y. C. and Ho C. M., 1994, "Surface Micromachined Magnetic Actuators", *Proceed. IEEE International Workshop on MEMS*, MEMS'94, Oiso Japan.
- 18. Liu, C., Tsao, T., Tai, Y.C., Leu, J., Ho, C.M., Tang, W.L. and Miu, D., 1995a, "Out-Of-Plane Permanent Magnetic Actuators for delta Wing Control," *Proceedings, IEEE Micro Electro Mechanical Systems*, pp. 7-12, Amsterdam, the Netherlands, Jan. 29, 1995.
- 19. Liu, C., Tsao, T., Tai, Y.C., Liu, W., Will P. and Ho. C.M., 1995b, "A Micromachined Permalloy Magnetic Actuator Array for Micro Robotics Assembly Systems," *Technical Digest, Transducers'95*, pp. 328-331.
- 20. Miller R., Burr, G., Tai, Y.C., Psaltis, D., Ho, C.M. and Katti, R, 1996, "Electromagnetic MEMS Scanning Mirrors for Holographic Data Storage," *Technical Digest, Solid-State Sensor and Actuator Workshop*, Hilton Head Island, South Carolina.
- 21. Tsao, T., Liu, C., Tai, Y.C. and Ho, C. M., 1994, "Micromachined Magnetic Actuator for Active Fluid Control," *Application of Microfabrication to Fluid Mechanics*, FED-Vol. 197, pp. 31-38, ASME.
- 22. Ho, C.M. and Huang, L.S., 1982, "Subharmonics and Vortex Merging in Mixing Layers", Journal of Fluid Mechanics, Vol. 119, pp. 443-473.
- 23. Ho, C.M. and Huerre, P., 1984, "Perturbed Free Shear Layers," Ann. Rev. of Fluid Mech., Vol. 16, pp. 365-424.
- 24. Babcock, D., Lee, C., Gupta, B., Kim, J., and Goodman, R, "Active drag reduction using neural network", International Workshop on Neural Networks for Identification, Control, Robotics, and Signal/Image Processing, Venice, Italy, August 21-23, 1996.

MICRO-ELECTRO-MECHANICAL SYSTEMS (MEMS) AND FLUID FLOWS

Ho, Chih-Ming

Mechanical and Aerospace Engineering Department, University of California, Los Angeles,
Los Angeles, California 90095

Tai, Yu-Chong

Electrical Engineering Department, California Institute of Technology,
Pasadena, California 91125

KEY WORDS: flow control, MEMS, micro transducer, size effect, surface force

ABSTRACT

The micromachining technology that emerged in the late 1980s is able to provide micron-sized sensors and actuators. These micro transducers can be integrated with signal conditioning and processing circuitry to form micro-electro-mechanical systems (MEMS) that can perform real-time distributed control. This capability opens up new territory for flow control research. However, because of the large surface-to-volume ratio in micron-scale configurations, surface effects dominate the fluid flowing through these miniature mechanical devices. For this reason, we need to re-examine the surface forces in the momentum equation. Because of the small size, gas flows experience large Knudsen numbers and, therefore, boundary conditions need to be modified. In addition to being an enabling technology, MEMS also provides many challenges for fundamental flow-science research.

1. INTRODUCTION

During the past decade, micromachining technology has become available to fabricate micron-sized mechanical parts. Micromachines have made major impacts on many disciplines (e.g., biology, medicine, optics, and aerospace, mechanical and electrical engineering). In this article, we will limit our discussion to transport phenomena, specifically emphasizing the fluid dynamics issues. This emerging field not only provides miniature transducers for sensing and actuation in a domain that we could not examine in the past, but also allows us to venture into a research area in which the surface effects dominate most of the phenomena.

Figure 1 shows a scanning-electronic-microscope (SEM) picture of an electrostatically driven motor (Fan, Tai & Muller 1988a). This device signifies the beginning of the micromachine field. A comb structure (Tang et al 1989) derived from the micro motor concept eventually evolved into the airbag sensor, which reduces the damage caused by automobile collisions and is used now on almost all American-made cars. During the development of the micro motor, it was found that the frictional force between the rotor and the substrate is a function of the contact area. This result departs from the traditional frictional law (i.e., $f = \mu N$), which says that the frictional force

is linearly proportional to the normal force, N , only. In the micro motor case, the surface forces between the rotor and the substrate contribute to most of the frictional force. However, the traditional frictional law describes situations with a dominating body force that do not depend on the contact area. Deviations from the conventional wisdom are commonly found in the micro world. This makes the micromachine field a new technology as well as a new scientific frontier.

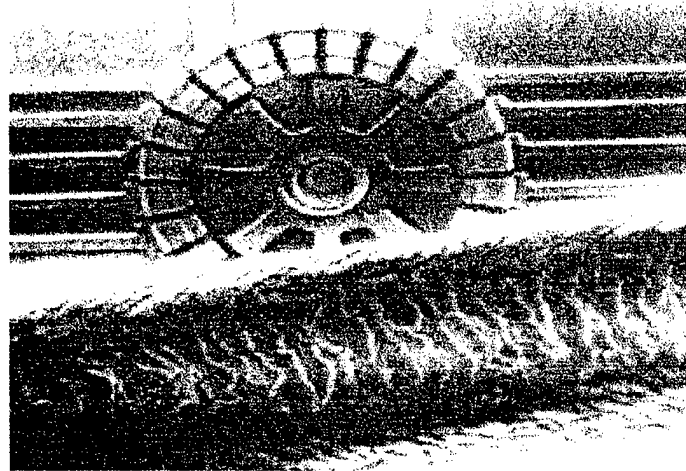


Figure 1 A micro motor (from Fan, Tai & Muller 1988a). A piece of human hair is shown in front of the motor to illustrate the minute size.

The micromachining process uses lithography to expose the designed photo-resist patterns; the unwanted portion is then selectively etched away. These procedures are similar to those used in integrated circuit (IC) fabrication but with a difference: 3-D and freestanding structures are common features, because of the nature of mechanical parts. Several manufacturing technologies, such as bulk micromachining, surface micromachining, and LIGA (a German acronym for lithographie, galvanoformung, and abformung), have been developed to make various micromachines. A brief introduction of these technologies can be found in a paper by Ho and Tai (1996). For detailed information, readers are referred to several extensive articles (Peterson 1982, Seidel 1987, Ristic 1994).

Micromachines have several unique features. First, typical micromachined transducer sizes are on the order of 100 microns, which can be one or more orders of magnitude smaller than traditional sensors and actuators. The drastic reduction in inertia due to these smaller sizes means a substantial increase in the frequency response. Second, the batch processing, which is characteristic of IC fabrication, can be used to make a large number of transducers for distributed sensing and actuation over a wide area. This capability enables us to sense certain flow characteristics in a 2-D domain and to perform control at the proper locations. Potential application areas include the manipulation of separation over a smooth contour or the reduction of surface shear stress in a turbulent boundary layer. Third, micromachine manufacturing technology is derived from (though not completely compatible with) IC fabrication, so it is possible to integrate the IC with micro transducers to provide logic capability. The integrated microelectronics and micromachines constitute the micro-electro-mechanical system, which is capable of executing sense-decision-actuation on a monolithic level.

In biomedical applications, fluid transport is commonly required in drug delivery and in chemical and DNA analysis. When dealing with flow in configurations of microns or less, we have observed many unexpected phenomena that are similar to the aforementioned experience of frictional force between solid surfaces. Sir Eddington (1928) once said, "We used to think that if we know one, we know two, because one and one are two. We are finding that we must learn a great deal more about 'and'." Indeed, the flows in macro *and* micro configurations are not quite the same. The unique features in micromechanics are perhaps the most intriguing ones for researchers in basic fluid mechanics. We still have a great deal of difficulty in understanding these features, because not much is known about the complex surface effects that play major roles in these events. The search for answers will excite researchers for years to come. In this paper, we will first report and discuss the fundamental micro fluid-mechanics issues and then proceed to review flow sensing and control using MEMS.

2. SIZE EFFECTS

2.1 *Ratio between Surface Force and Body Force*

The length scale is a fundamental quantity that dictates the type of forces governing the physical phenomena. Body forces are scaled to the third power of the length scale. Surface forces depend on the first or second power of the characteristic length. Because of the difference in slopes, the body force must intersect with the surface force. In biological studies (Went 1968), empirical observations indicated that a millimeter is the approximate order of the demarcation length. The experiences gathered in MEMS also show that surface forces dominate in sizes smaller than a millimeter. For example, the friction experienced by the 100-micron-diameter micro motor (Fan, Tai & Muller 1988a & b) must be caused mainly by the surface force, because the rotor started to move when the contact area between the rotor and the substrate was reduced by placing dimples on the lower surface of the rotor.

2.2 *Ratio between Device and Intrinsic Length Scales*

In addition to the large surface force, the large surface-to-volume ratio is another characteristic inherent in small devices. This ratio is typically inversely proportional to the smaller length scale of the cross section of the device and is about one micron in surface micromachined devices. Therefore, the surface-to-volume ratio is much larger in a micro device than in a macro device, which accentuates the role of surface force as well as other surface effects in general.

In micro flows, the Reynolds number is typically very small and shows the ratio between the viscous and inertial forces. However, in the case when gas is the working fluid, the size can be small enough to further modify the viscous effect when the device length scale is on the order of the mean free path. For large Knudsen-number flows, the flow velocity at the surface starts to slip (Knudsen 1909, Kennard 1938); therefore, the viscous shear stress is much reduced. For liquid flows, the distance between molecules is on the order of angstroms. The non-slip condition has always been used as an empirical result. By using a molecular dynamics approach (Koplik et al 1989, Koplik & Banavar 1995), the non-slip condition at the solid surface is

established in Couette and Poiseuille liquid flows. On the other hand, molecular ordering has been observed and results in oscillatory density profiles in the vicinity of the wall, which has a thickness of a few molecular spacings. In the case of a moving contact line at the fluid fluid solid interface, the non-slip condition needs to be relaxed (Dussan & Davis 1974). Typical micromachined devices have a length scale much larger than the molecular spacing of simple liquids. Hence, the non-slip boundary condition should hold in the absence of a moving contact line.

In other situations, the bulk flow is modified instead of the boundary condition. For example, most solid surfaces have electrostatic surface charges, which can attract ions in liquid flows to form an electric double layer (EDL) (see Section 3.2). The thickness of the EDL varies from a few nm to 100s of nm (Hunter 1981), which can be comparable to the order of micro-flow length scale. In these cases, the bulk flow can be affected by this electrically charged layer (Mohiuddin Mala et al 1996).

3. SURFACE FORCES

For fluid flows in MEMS, new phenomena arise because of certain surface forces that are usually ignored in macro scales. Here, a brief survey is given on several kinds of surface forces (Israelachvili 1991). Before the discussion of some seemingly different surface forces, it is important to know that these forces originate from intermolecular forces. Moreover, even though basic intermolecular forces are short range (< 1 nm) in nature, they can cumulatively lead to very long-range (> 0.1 μm) effects (e.g., surface-tension effects in liquids). Another important point is that all intermolecular forces are fundamentally electrostatic (coulombic). This is established by the Hellman-Feynman theorem that once the spatial electron distribution is determined from the Schrödinger equation, all intermolecular forces can then be calculated using classical electrostatics. However, in practice this cannot always be done, and empirical or semi-empirical laws of forces are still useful. Therefore the following, we treat the following surface forces differently, even though they are quantum mechanically the same in origin.

3.1 *The van der Waals Forces*

The van der Waals forces are the weakest among all the forces, but they are important because they are always present. The van der Waals forces are short range in nature but, in cases where large molecules or surfaces are involved, they can produce an effect longer than 0.1 μm . In general, the van der Waals forces have three parts: orientation force, induction force, and dispersion force. All have an interaction free energy that varies with the inverse sixth power of the distance ($1/r^6$) and are, hence, short range. The orientation force is the dipole-dipole interaction force between polar molecules. The induction force arises from the interaction between a polar molecule and a non-polar molecule. The permanent dipole of the polar molecule induces a weak dipole in the non-polar molecule and then produces a dipole-induced dipole-interaction force. The dispersion force is then the induced-dipole-induced-dipole interaction force. Interestingly, the dispersion forces act on all atoms and molecules even when they are totally neutral, as are those of helium and oxygen. The source of the dispersion force between two non-polar molecules is the following: Although the averaged dipole moment of a non-polar

molecule is zero, at any instant there exists a finite dipole moment depending on the exact position of the electrons around its nucleus. This instantaneous dipole moment can then generate an interaction force with nearby molecules.

Altogether, the van der Waals forces play an important role in many macroscopic phenomena (e.g., adhesion, surface tension, physical adsorption, wetting of surfaces, properties of thin films, and behaviors of condensed proteins and polymers). In MEMS, the van der Waals forces can have significant effects in structures with large surface-to-volume ratios (e.g., long and thin polysilicon beams (Mastrangelo & Hsu 1992) and large-and-thin comb-drive structures (Tang et al 1989)) whenever they are in contact with another surface. Stiction or adhesion of the structure to the substrate can often be observed as a major problem in the operation of these structures. Nevertheless, the van der Waals forces between two contacting surfaces are in many cases hard to be separately distinguished from electrostatic (coulombic) forces, which are discussed in the next section.

3.2 Electrostatic Force

Electrostatic, or coulombic, force is present between charged molecules or particles. The force has an inverse-square dependence on the distance, $1/r^2$, so it is rather long range when compared to the van der Waals forces. In MEMS devices, the electrostatic force can have a significant effect even up to 10 μm away and becomes more important when lengths are less than 0.1 μm . One can always produce an electrostatic force by providing an electrical potential difference between two electrodes. However, problems due to electrostatic force in MEMS often occur because of rather uncontrollable surface-trapped charges. In fact, any surface is likely to carry some charge, because of broken bonds and surface charge traps. In the case where the surface is a good insulator, such as with SiO_2 , trapped charges can induce very high voltage from a few 100 to a few 1000 volts (Wolf 1990).

For charged surfaces in liquids (e.g., water), new phenomena happen mainly as a result of charge redistribution in the liquid. Basically, the final surface charge is balanced by counterions in the liquid with an equal but opposite total charge. The surface electrical potential attracts counterions to the wall and forms a thin ($< 1 \text{ nm}$) layer of immobile ions. Outside of this layer, the distribution of the counterions in liquid mainly followed the exponential decaying dependence away from the surface, which is called the diffuse electric double layer (EDL). The EDL has a characteristic length, the Debye length, which depends inversely on the square root of the ion concentration in the liquid. For example, in pure water the Debye length is about 1 μm ; in 1 M of NaCl solution, the Debye length is only 0.3 nm. Inside the EDL, a very large electrostatic force then exists. This may cause a behavior change in the fluid flow if the double layer thickness is significant compared to the flow field size (Mohiuddin Mala et al 1996). This is especially true in dilute solutions where the Debye length is large.

3.3 Steric Forces

This is a special case involving chain molecules (e.g., polymers) attached at the surface on one end with the other end dangling into the solution (liquid for most of the cases) where they are

mobile. A different class of forces, known as steric forces, arises whenever another molecule or surface approaches and is a result of an entropy change caused by the confined chain molecules. The complex molecules can produce complex interactions, and steric forces can be either attractive or repulsive. They can be rather long range ($> 0.1 \mu\text{m}$), and they are important when a fluid flow has a significant number of long-chain molecules.

4. FLOWS IN MICRO CONFIGURATIONS

Fluids driven by pumps flowing through channels and valves are generic configurations in biomedical analytical systems. When the sizes of these devices are in the micron range, the measured data show different behaviors from those expected in larger devices. The exact physical mechanisms are not known, although the surface forces, which were not considered in classical analyses, are believed to be responsible for these interesting phenomena. This provides new research opportunities. In this review, we will limit the discussion to simple fluids, which have small molecules. More complex fluids (e.g., non-Newtonian or multi-phase fluids) are commonly used in biomedical systems. Much richer findings are expected in the future.

4.1 *Gas Flows in Micro Channels*

Flow through a straight channel is one of the simplest but most common configurations in micro fluidic systems. Mass flow rates in small channels with diameters of about 30 microns were measured by Knudsen (1909) while studying the non-slip/slip boundary condition. Recent interests are triggered by micromachine activities (Pfahler et al 1990), which include applications for transporting fluids in biomedical diagnosis and electronic device cooling (Tuckermann & Pease 1982, Joo et al 1995). Helium is a common gas used in most experiments, because it has a large mean free path (about $2 \times 10^7 \text{ m}$ under laboratory conditions). The Knudsen number based on a channel height of one micron is 0.2. A micro channel with integrated micro pressure sensors (Fig. 2) was fabricated to study the flow field (Liu et al 1993b). This channel has a cross section of 1.2 microns \times 40 microns. Slip flow is observed, and the measured mass flow rate (Pfahler et al 1991, Pong et al 1994, Arkilic et al 1995, Harley et al 1995, Liu et al 1995, Shih et al 1995, Shih et al 1996) is higher than that based on the non-slip boundary condition (Fig. 3). For other gases (e.g. nitrogen, oxygen, and nitrous oxide), the Knudsen number is about a factor of four smaller, but surface slip still exists. The mass flow rate can be calculated from the Navier-Stokes equation with a slip boundary condition (Kennard 1938, Beskok & Karniadakis 1992 & 1993, Arkilic & Breuer 1993). An accommodation constant is introduced to represent the tangential momentum transfer between the impinging molecules and the wall. The value of the constant should be ≤ 1 . However, the predicated mass flow rate is sensitive to the accommodation constant (Fig. 3), which actually functions as a matching coefficient. Direct simulation of the Monte Carlo method (DSMC) has been carried out by many investigators (Oh et al 1995, Piekos & Breuer 1995 & 1996, Beskok et al 1996, Oran et al 1998). The mean streamwise velocity in the micro channel is typically in the very low subsonic range ($< 1 \text{ m/s}$), which can be several orders of magnitude smaller than the molecular thermal velocity of 1000 m/s

(Oh et al 1995). Computing the converging solution is a challenge for very low Mach- number flows.

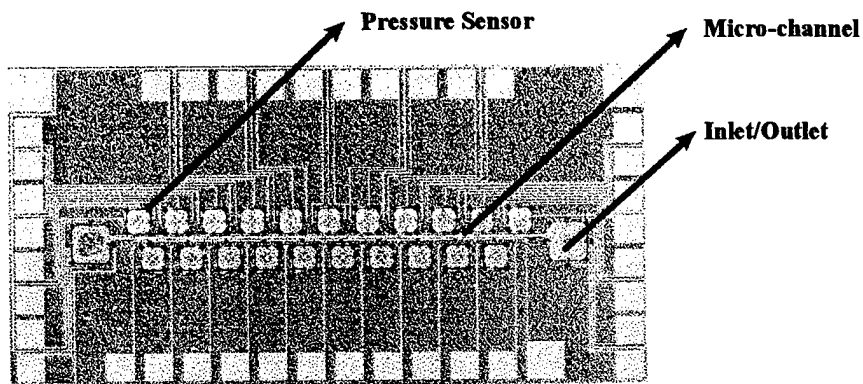


Figure 2 A micro channel system with integrated micro pressure sensors (Pong et al 1994).

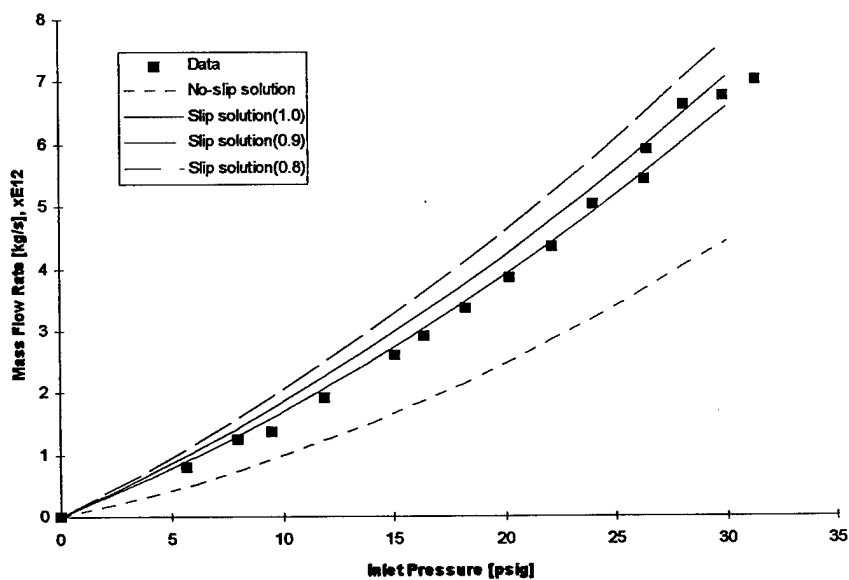


Figure 3 Mass flow rate and pressure drop of helium in a micro channel (Shih et al 1996).

In the micro channel, high pressure drops are observed. This is because of the small transverse dimension, which causes high viscous dissipation. A drop of a few atmospheres in pressure in several mm is common (Pong et al 1994, Shih et al 1995). The density of the gas can change to such a large extent that the pressure does not decrease linearly with streamwise distance as in typical creeping flows. Rather, the compressibility effect causes the pressure to decrease at a slower rate. On the other hand, the rarefaction effect due to the high Knudsen number works against the compressibility and keeps the pressure towards the linear distribution (Arklic & Breuer 1993). The two effects are not equal, so the net result is a non-linear pressure distribution. Since,

the pressure distribution is not sensitive to the accommodation constant, it turns out to be a useful property for examining the analytical results. When the accommodation constant is varied, no appreciable change in the predicted pressure distribution can be observed. The measured pressure distributions along the channel are plotted against the theoretical prediction. The measured pressure distribution agrees well with the analytical result.

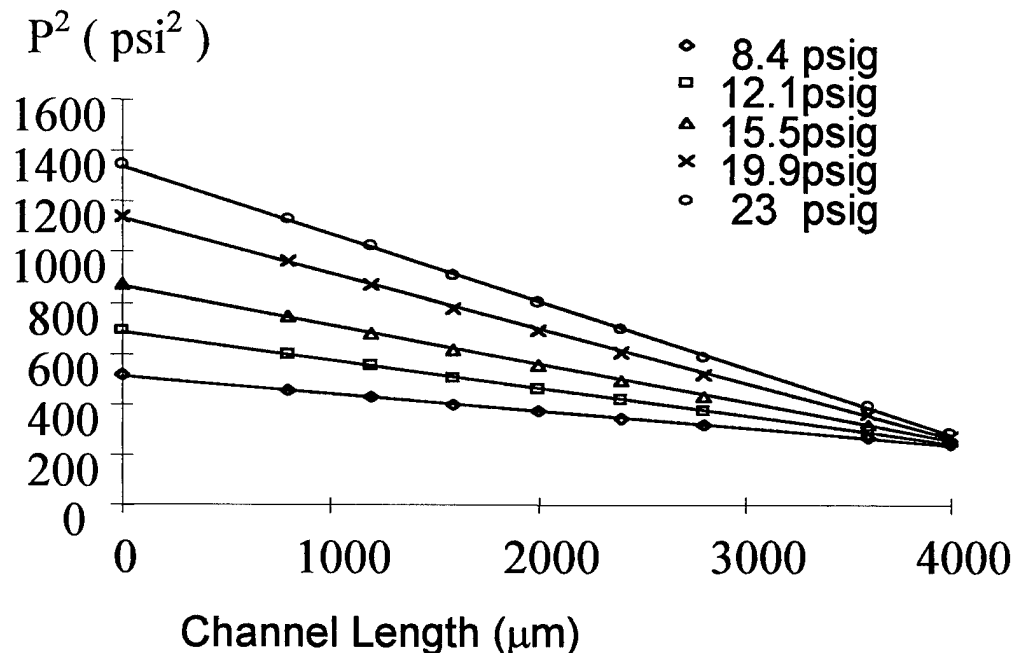


Figure 4 Pressure distribution of nitrous oxide in a micro channel

4.2 Liquid Flows in Micro Channels

Even though the non-slip boundary of simple liquids with molecules is established by experimental studies and by molecular dynamics simulation (Koplik 1989), the study of liquid flow through micro channels is not a routine process. In fact, it seems to be an even richer problem than gas flow. For liquid flows through capillary tubes (Migun & Prokorenko 1987) or micromachined channels (Pfahler et al 1990, 1991), the measured flow rates and pressure drops across the channel were compared with the Stokes flow solution, with viscosity as the matching constant. The size effects are apparent in these results, and the value of viscosity deviates from the conventional value for micron-size channels. The molecular structure of the liquid also affects the flow. Molecules with no electrical charge can have a dipole configuration (e.g., water). Pfahler et al (1991) found that the value of the viscosity of polar isopropanol decreases from the nominal value for a channel height smaller than 40 microns and reaches an asymptotic value at a channel

height of about 10 microns (Fig. 5). The vertical axis is the ratio between the apparent viscosity and nominal viscosity. It is reasonable that the size effect becomes more pronounced for a narrow channel. However, it is interesting to note that the apparent viscosity is lower, not higher, in the narrower channel. The apparent viscosity actually represents the integral effects of the surface forces. More definitive experiments are needed to identify the role of specific surface effects. For example, when the surface-to-volume ratio gets large, will the surface viscous force also be a function (i.e., hydrophobic or hydrophilic) of the surface property? For non-polar silicon oil, the data (Fig. 5) can not support a clear trend of viscosity variation in this range of channel size.

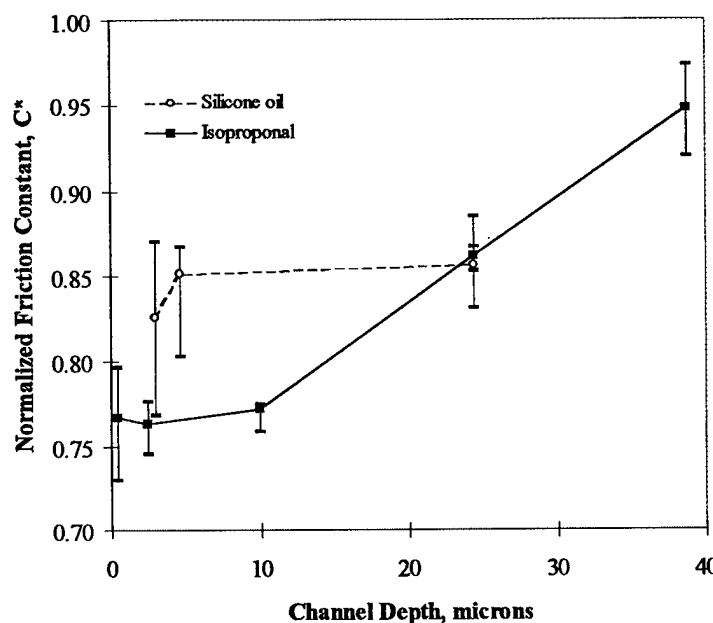


Figure 5 Size effect on liquid flow in channels (Pfahler et al 1991).

4.3 Diffusion in Micro Channels

The sacrificial etching technique (Nathanson 1967, Preston 1972, Howe & Muller 1983) is a fundamental technique used in surface micromachining for producing a free standing structure, such as the diaphragm above a cavity or cantilever beam. The micro channel shown in Fig. 2 was also fabricated by this method. The sacrificial etching process for making that channel was to deposit a thin line of sacrificial material, in this case phosphosilicate glass (PSG), after which a structural layer of silicone nitride was placed on top. Hydrofluoric acid (HF) was used as an etchant to remove the PSG from one end of this thin line. When the PSG was etched away, a long micro channel was formed (Monk et al 1993, Liu et al 1993a). The channel in Fig. 2 is 1.2 microns high and 4000 microns long.

This process is an important micromachine manufacturing technique, and it also motivates us to examine mass diffusion in micro geometries. The HF diffuses from the reservoir, which is located at one end of the micro channel, towards the PSG/HF interface. The rate at which the solid PSG dissolves into the HF acid is a function of the reaction rate and the acid concentration. The

concentration of HF at the moving interface is dictated by the diffusion process and the reaction rate. Basically, this phenomenon is governed by a 1-D diffusion equation with an unknown boundary condition. It is similar to the Deal-Grove problem, but the reaction rate changes its power dependence on the acid concentration (Judge 1971) in the present case. Nevertheless, a close-form analytical solution can be obtained (Liu 1993a), and it matches well with the measured data (Fig. 6). On the other hand, a size effect is observed. The etch rate is not a constant during the etching, and it decreases as etching time increases. During the whole etching period, the etch rate of a thicker channel is always higher than that of a thin channel (Liu et al 1993a). The etch rate at the beginning of the etching process is plotted in Fig. 7, and it almost decreases linearly with the channel thickness in the tested range of 1.2 microns to 0.25 microns. This is not expected from the 1-D diffusion analysis. There are many types of ions in the liquid phase. It is possible that the thickness of the EDL in this case is on the order of the thickness of the micro channel. The F^- ions and HF_2^- ions are responsible for removing the PSG, and their diffusion is very likely to be retarded by the electric double layer.

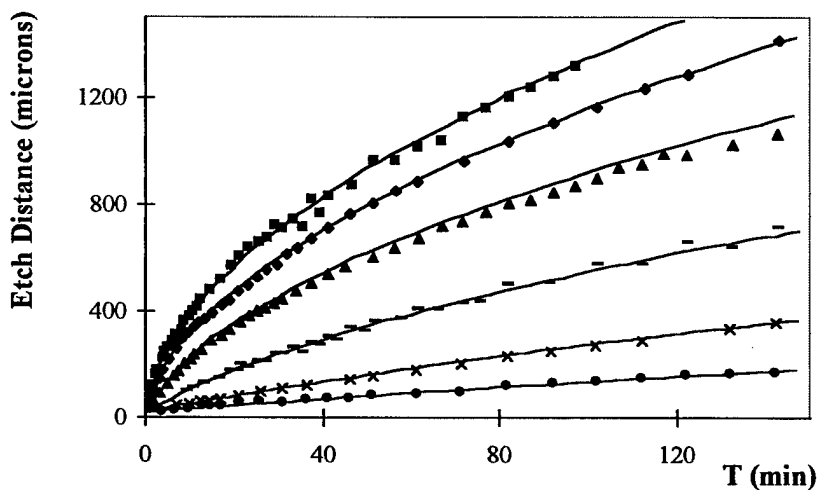


Figure 6 The progress of the etching front as a function of time for various HF concentrations (Liu et al 1993a). ■ - 49%, ♦ - 38.2%, ▲ - 26.5%, — - 13.8%, × - 7.2%, ● - 3.6%. Data points are plotted against predicted curves.

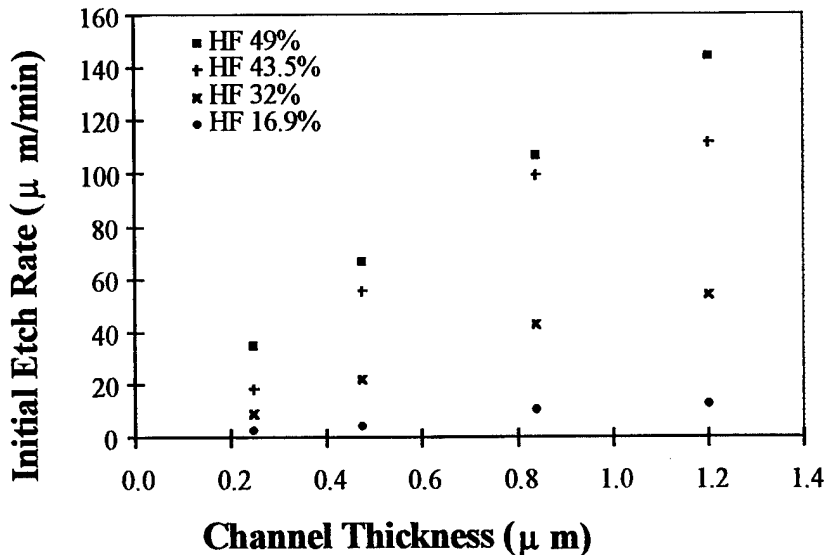


Figure 7 Size effect as a function of etching rate.

4.4 Flow Through Micro Nozzles

Flow through a nozzle experiences viscous dissipation. In the case of Stokes flow, the pressure drop increases with decreasing Reynolds number -- a well-established result. A recent experiment (Hasegawa et al 1997) shows that the predicted pressure drop underestimates the measured value when the size of the nozzle is smaller than 35 microns (Fig. 8). The excess pressure drop can be a factor of four or five times higher than the predicted value for water flow through an 8.8-micron nozzle. When non-polar silicon oil was used, the excess pressure drops are lower than that of water, which has polar molecules. The dependence of the measured flow property on the fluids used in the test is a common feature in micro flows whenever a size effect is observed. It is interesting to note that differences between polar and non-polar materials, which has been reported in micro channel flow (Pfahler et al 1991), is observed again in this flow.

It has been reported that the EDL retards the flow. This causes an apparent viscosity that is higher than the nominal viscosity (Mohiuddin Mala, Li & Dale 1996). This is the opposite of the results observed in the micro-channel liquid-flow data (Pfahler et al 1991) but follows the trends reported in the micro-nozzle flow experiment (Hasegawa et al 1997). In this nozzle experiment, the ion content in the water was varied by adding NaCl in order to examine the effect of the EDL. No discernible difference in the pressure measurements was reported by the authors. Unfortunately, distilled water rather than de-ionized water was used before the NaCl was added. Water is known to contain ions easily, but the level of the ion content in their distilled water is unknown. Nevertheless, the excess pressure drop across the micro nozzle provides additional evidence for the size effect in the micro flows.

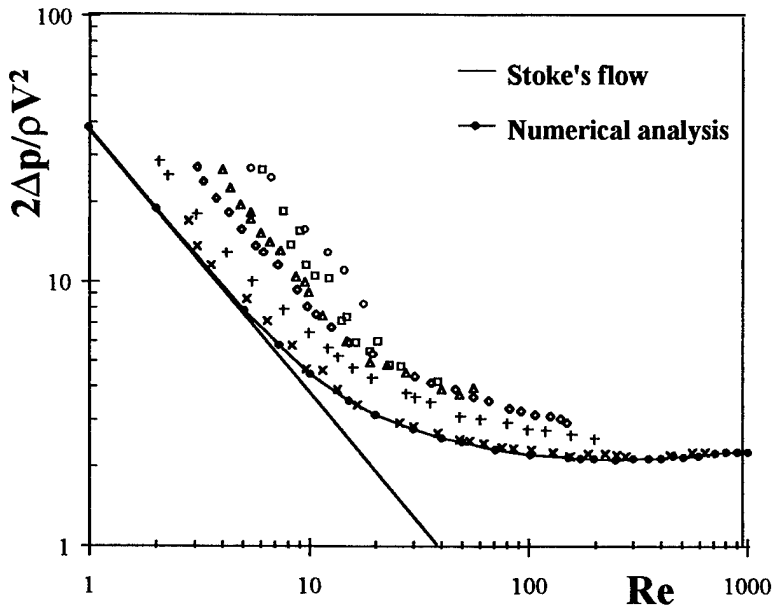


Figure 8 Size effect of pressure drop across micro nozzles as a function of Re number (Hasegawa et al 1997). (o - 8.8 μm , \square - 9.2 μm , Δ - 13 μm , \diamond - 27 μm , + - 35 μm , \times - 109 μm -●- numerical simulation)

4.5 Air Damping in MEMS

Mechanical or electromechanical resonant devices have been widely used in oscillators or filters, and operational theories for these devices have been established in large apparatus. As MEMS technology develops, these resonators are becoming smaller. Typically, these devices are 1- to 2- μm thick and about $100 \times 100 \mu\text{m}^2$ in area. Some important milestones for these kinds of devices are the laterally driven comb-drive polysilicon micro resonators (Tang et al 1989), Analog Device's integrated polysilicon ADXL-50 accelerometers (Analog Device 1991), flexural polysilicon micro gyros (Juneau & Pisano 1996), and the cascade 300-kHz micromechanical filters (Wang & Nguyen 1997). In these cases, the micro flows are shear-driven (Bekok et al 1996) instead of pressure-driven, as in the channel and nozzle flows.

Air damping in microstructures is an under-explored but important issue, because it directly influences the quality (Q) factor, of the devices. For example, it has been shown (Nguyen 1995) that the Q factor of a polysilicon resonator can be as high as 100,000 in a vacuum but drops to 100 in atmospheric air. This actually illustrates that air damping may be the most important factor when compared to other effects like thermal vibration and fatigue. The strong air damping is due to the dramatic increase in surface-to-volume ratio.

In order to systematically investigate air damping, the air pressure is divided into three regions (Newell 1968). In the first region where the pressure is in low vacuum, air damping is negligible when compared to the intrinsic damping (internal friction) within the resonator. Experimentally, this region happens roughly below 10–100 Pa for micro-resonators. The damping in this region is

largely dependent on the surface-to-volume ratio, the surface quality (the surface may be more lossy than the bulk material), and the material. In the second region, momentum transfer between the resonator and individual air molecules dominates the damping. Here, there is little or no interaction between air molecules, and a simple model has been derived based on the assumption that the rate of momentum transfer is proportional to the difference in velocity between the air molecules and the resonators (Christian 1966). The result is that the Q factor is inversely proportional to the ambient pressure ($Q \propto 1/p$). This region typically ends around 10^3 Pa. In the third region, the pressure is high enough that air molecules do interact with each other, and viscous damping dominates the behavior of the resonators. In this region, the Q factor is inversely proportional to the fluid viscosity ($Q \propto 1/\mu$). The boundary condition must change from slip to non-slip flow when the surrounding pressure increases. What is the Knudsen number for this change in the boundary condition? Do other surface forces play a role in resonator performance? There is not enough experimental evidence to answer these questions yet. When the viscous damping of laterally driven microstructures was studied (Zhang & Tang 1994), it was found that the simple Couette and Stokes flow model can significantly underestimate the damping in microstructures, and that this discrepancy is larger for smaller resonators. Most of the microstructures have a complex configuration. For example, the comb structure and the surrounding walls, can also play an important role. The detailed geometry of the device (e.g., the resonator's thickness and edges) needs to be considered for more accurate modeling. An example illustrating the importance of the geometry details is the dynamic response of a thin squeeze-film. In a numerical simulation of a micro accelerometer (Yang & Senturia 1996), the squeeze-film in a low air-pressure environment has a frequency response about four orders of magnitude better than at atmospheric pressure conditions. When the geometry is slightly altered by placing small etching holes through the accelerometer film, the flat portion of the frequency response is extended by three decades from that of a solid film (Fig. 9).

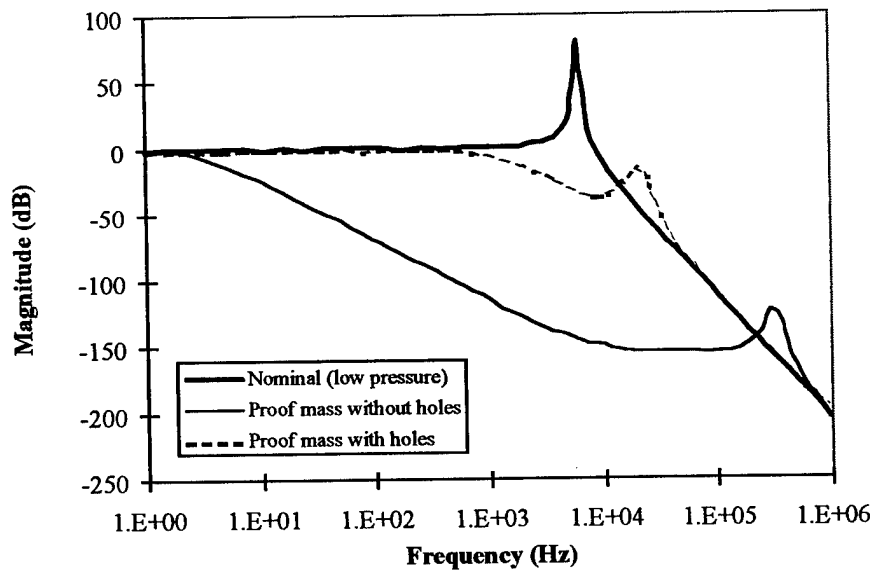


Figure 9 The dynamic response of a thin squeeze-film. (Yang and Senturia 1996)

For some MEMS devices, their displacement can be much larger than their transverse dimension. Other interesting air-damping problems arise. A flap device (Miller et al 1996) driven by an

electro-magnetic field has an off-plane displacement a thousand times larger than the thickness of the flap. The measured Q factors depend on the magnitude of the displacement. It is believed that the non-linear viscous damping contributes to this phenomenon. This, again, is a rather unexplored issue.

4.6 Micro Flow Diagnosis

Measuring flow properties in a micro configuration is a challenging task, because the sensors need to be much smaller than the size of the device under study. In addition, the momentum and the energy of the flow is very small. For example, the kinetic energy flux in the channel with helium flow (Fig. 2) is about 5.4×10^{-13} J/s for inlet pressure at 20 psig. Therefore, only an extremely small amount of momentum and energy exchange between flow and sensor is allowed so as to not alter the flow. For these reasons, a very limited number of sensors have been developed for micro flow measurements. The micro channel with integrated pressure sensors (Fig. 2) is one example. A very small duct (0.25-micron high and one-micron wide) is used to connect not-very-small (compared to the size of the channel) micro sensors to the channel for increased spatial resolution. Time averaged pressure can be obtained by this arrangement. If unsteady pressure data are needed, questions about the calibration procedures and even the physical meaning of the data may arise. Furthermore, even though the pressure sensor has a high frequency response, we do not know the constraints of the small duct imposed on the unsteady pressure field. For temperature measurement, thermocouples of 4 microns \times 4 microns have been developed for measuring surface temperature along a 20-micron channel (Fig. 10, Zohar et al 1996). In high Knudsen-number flows, a temperature jump can occur between the wall and the bulk flow. Fabricating an in-flow temperature sensor without introducing large disturbances to the micro flow is not a trivial task.

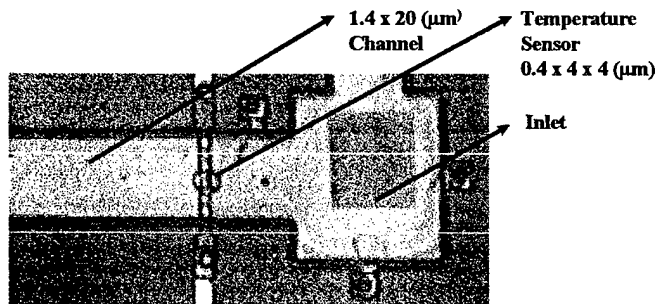


Figure 10 The in-situ temperature sensor in a micro channel (Zohar et al 1996).

Flow visualization has been proven to be a very useful technique in macro fluid-dynamics research, and extensive effort has been expended on developing methods for visualizing flow in micro channels and valves (Lanzillotto et al 1996). The wavelength of visible light is not short enough for this purpose, so X rays (with wavelengths of 0.62 angstrom), generated by a synchrotron, are used. An advantage is that they can be utilized for visualizing flows behind certain silicon structures, such as polysilicon, which are not transparent to visible light. Figure 11 shows the motion of a water/air interface during a filling process inside a 100-micron-deep and 140-micron-wide channel with a triangular cross section. Water climbs along the sharp corners of

the triangle at a rate so fast that it is beyond the resolution limit of the current technique. The meniscus surface in the middle of the channel is left far behind the corner interface. This phenomenon is caused by the large surface-tension force associated with the extremely small corner curvature of the micro channel.

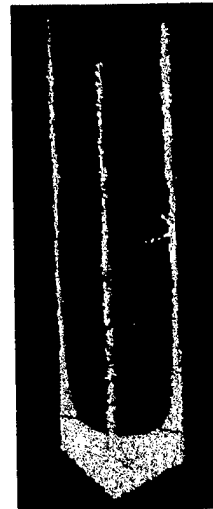


Figure 11 Flow visualization by X ray in a micro channel (Lanzillotto et al 1996).

5. FLOW TRANSDUCERS

A typical micro transducer is about 100 microns in size, which is at least one order of magnitude smaller than the traditional transducers. The improvement in spatial resolution comes naturally, since the significant reduction of inertial mass and thermal capacity can increase the frequency response to an inaudible frequency (> 1 MHz for a micro hot wire (Jiang et al 1994)). The lithographic process and the small size enable us to use 100, 1000, or even more transducers for sensing and/or controlling a phenomenon that has distributed features, such as the high speed streaks in a turbulent boundary. However, a few problems are associated with using multiple transducers. Traditionally, the leads of each transducer are connected to an external signal-conditioning instrument. Handling 100s or 1000s of signal paths is tedious and usually prohibitive. In addition, these leads occupy a large portion of the precious surface area on the chip. For example, the surface shear-stress sensor array containing 85 sensors (Jiang et al 1996) only takes about 1% of the area, while the leads occupy about 50% of the surface. Another problem is the limitation in signal bandwidth. Depending on the number of transducers used, we may sometimes not be able to take full advantage of the high-frequency response. However, these problems can be alleviated by integrating the signal conditioning, and even the decision circuits, with the micro transducers in such a way that the leads can be connected locally and thereby significantly reduce the required surface area. The output and input then can be only a few wires. Furthermore, the local circuit will only process the output from one or a few transducers, so bandwidth limitation will no longer be a problem. However, the signal processing circuitry still needs to be kept simple. It is not feasible to integrate a powerful microprocessor with each sensor-actuator pair in a large transducer array. Neural networks are a feasible approach, and numerical experiments (Lee et al 1997) show successful examples of using simple

neural-network-based processing for controlling transitional or turbulent flows. Another issue is the energy expenditure of the transducers. In the case of flow control, we usually need to have a net energy saving for the whole system. Typically, the energy requirement for a micro flow sensor can be kept around a few milliwatts, but the energy expended for micro actuators is usually much higher. Improvements in this area are clearly needed.

5.1. Micro Flow Sensor

5.1.1 HOT-WIRE ANEMOMETER Micro-machined polysilicon hot wires (Jiang et al 1994) can have a cross section as small as $0.5 \times 0.5 \mu\text{m}^2$ and a length of from one to several hundredths of a micron (Fig. 12), and their utilization can achieve significant increase in spatial resolution. There are many other advantages of using polysilicon. One is that its temperature coefficient of resistance (TCR) of polysilicon can be varied from -2 % to 0.2 %/°C by using a range of doping concentration of boron or phosphorus from 10^{17} to 10^{20} atoms/cm³. By comparison, conventional platinum wires only have a TCR of around 0.1 %/°C. We can use this large TCR variation to design a hot wire that specifically exhibits thermal sensitivity. The other advantage of the polysilicon wire then is that a hot wire's time constant is inversely proportional to its resistivity (Blackwelder 1981). The resistance of conventional hot wires, which use metals exclusively, is typically low (5–30 Ω). On the other hand, the resistance of polysilicon wires can be adjusted over a wide range (from $\text{k}\Omega$ to several $100 \text{k}\Omega$). When a constant temperature mode is used, a bandwidth of 1.4 MHz has been achieved with the aid of a heavily doped polysilicon wire. The extremely high-frequency response of a micro hot wire is mainly achieved by adjusting the material properties rather than by simply reducing its size.

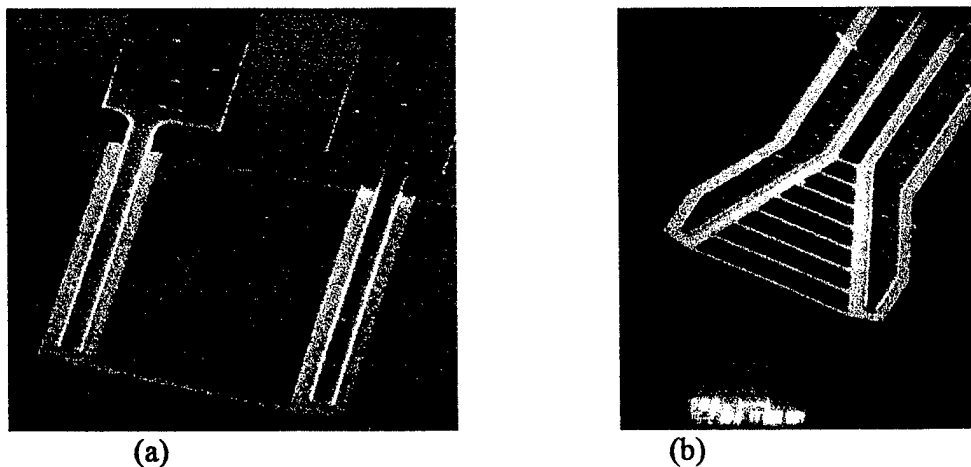


Figure 12 Micro hot wire: (a) a $1\text{-}\mu\text{m} \times 70\text{-}\mu\text{m}$ single hot wire and (b) a hot-wire array (Jiang et al, 1994).

5.1.2 SHEAR STRESS SENSOR A thermal surface shear-stress sensor is a hot film placed on a surface (Haritonidis 1989). This sensor has reasonable sensitivity while it is used in water. When air is the working medium, most of the heat is conducted into the substrate rather than into the air, because of the very low heat capacity of air. The use of a surface-micromachined shear-stress sensor (Jiang et al 1996, Huang et al 1995, 1996) has resolved the problem. A polysilicon

wire is placed on a 1.2- μm -thick and $200 \times 200\text{-}\mu\text{m}^2$ silicon-nitride diaphragm. Underneath the silicon-nitride diaphragm is a 2- μm -deep vacuum cavity (Fig. 13a). Significant thermal insulation has been achieved by using the vacuum chamber and the silicon-nitride diaphragm with low thermal conductivity. Figure 14 shows that the resistance of the polysilicon wire on a vacuum-insulated diaphragm is almost an order-of-magnitude higher than that on a solid substrate. The micro-surface shear-stress sensor has a sensitivity of 100 mV/Pa and a bandwidth of 10 kHz and higher. This type of micro sensor can also be integrated into a large array and even can form a flexible skin to be placed on a curved surface (Jiang et al 1997). Mechanically the flexible skin (Fig. 13b) consists of 128 separated silicon islands ($1\text{ mm} \times 1\text{ mm} \times 80\text{ }\mu\text{m}$) that are connected together by a thin polyimide film (1–20- μm thick). The shear stress sensors are built on the silicon islands. This skin has been taped on a semi-cylindrical (1.3-cm-diameter) delta-wing leading edge to perform real-time 2-D shear-stress mapping. Flow separation along the leading edge has then been successfully measured using the skins.

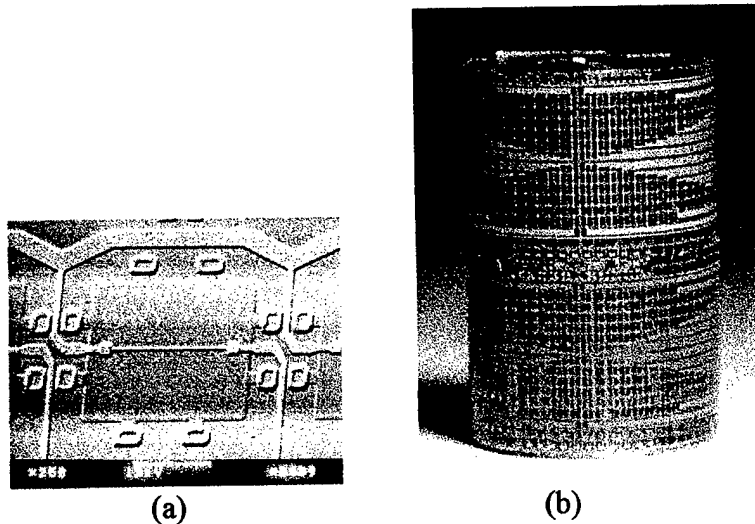


Figure 13 Micro-surface shear-stress sensor: (a) a single sensor (Jiang et al 1994) and (b) a flexible array of 128 sensors (Jiang et al 1997).

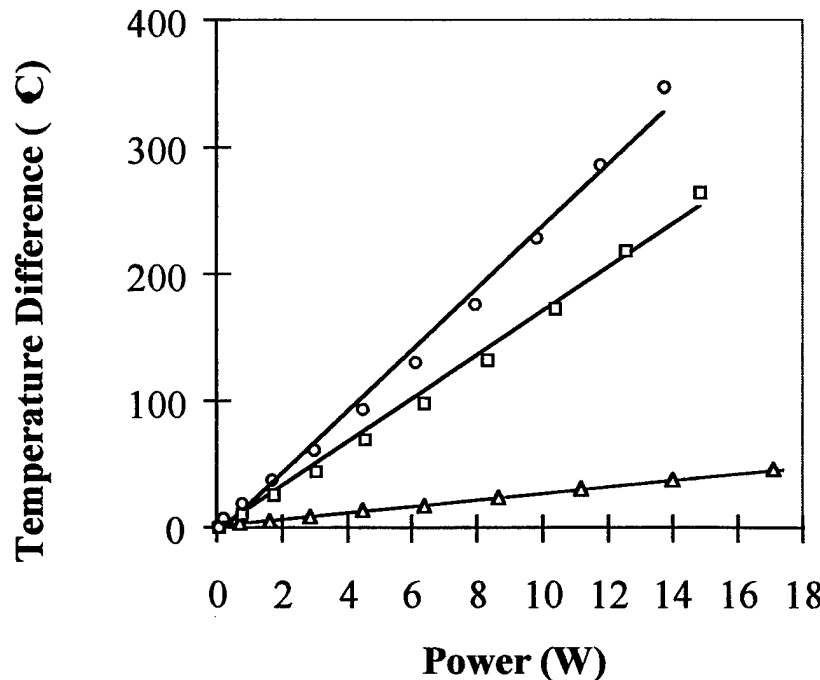


Figure 14 Heating element temperature of the shear stress sensor (Jiang et al 1994). (○ - on vacuum chamber, □ - on air-filled chamber, △ - on solid substrate)

A different design of a thermal-based-wall shear-stress micro sensor has been reported by Löfdahl et al (1996). In this case, the sensor is a $300 \times 60 \times 30\text{-}\mu\text{m}^3$ silicon chip that utilizes a temperature-sensitive silicon diode as the temperature sensing element. This chip is embedded in a silicon diaphragm with polyimide-filled trenches to improve thermal isolation. This device takes about 40 mW of power in order to obtain a biased differential temperature of 100°C. The uniqueness of this work is that a polysilicon-diaphragm piezoresistive pressure sensor is also integrated with the shear stress sensor.

By suspending a micro floating element, a direct measure of the shear stress can be achieved. Schmidt et al (1988) first reported a micro floating-element shear-stress sensor. It was designed to provide a spatial resolution of 100 μm and a bandwidth of 20 kHz. The floating element was a $500 \times 500 \times 30\text{-}\mu\text{m}^3$ polyimide plate tethered by polyimide beams. When exposed to shear stress, the plate movement is sensed capacitively with two integrated FET transistors and off-chip electronics. A sensitivity of 52 $\mu\text{V/Pa}$ was reported. Pan et al (1995) then reported a different floating element. Pan's device is made of thin film polysilicon. A typical device includes a polysilicon floating element ($\sim 100 \times 100 \times 2.2 \text{ }\mu\text{m}^3$) and several suspension beams ($\sim 100 \text{ }\mu\text{m}$ long). These floating elements have much smaller sizes and better sensitivities (167 mV/Pa), owing to delicate force-balance electronics. Padmanabhan et al (1995) reported a single crystalline-silicon bulk-micromachined and silicon fusion-bonded sensor. The movement of the element is measured by two photo diodes underneath the element.

5.1.3 PRESSURE SENSOR Micro piezoresistive pressure sensors represent the most mature and successful application of MEMS devices, having a wide range of applications from automobiles to biomedical instruments. Micromachined piezoresistive silicon-based pressure sensors were first introduced in 1958 by Kulite, Honeywell, and MicroSystems (Brysek et al 1990). At that time, the devices were typically made with silicon piezoresistors glued to metal diaphragms. The much more advanced micro pressure sensors used today are made by anisotropic etching of silicon, which requires no hand assembly. Some examples are the fully integrated Motorola pressure sensor (Fraden 1993) and the silicon fusion-bonded millimeter- and sub-millimeter-size pressure sensors (Brysek et al 1990). Polysilicon has been a popular material for the piezoresistors, but many diaphragm materials have been explored, such as polysilicon (Guckel et al 1986, Sugiyama et al 1991) and silicon nitride (Liu et al 1995). Piezoresistive pressure sensors are available in a wide range of sensitivities (up to 10,000 psi) and with typical uncompensated full-scale pressure sensitivity of about 20 mV/V. Capacitive pressure sensors have the advantages of better sensitivity and less temperature drift (Lee 1982, Ko 1982); however, their performance depends heavily on electronics.

5.1.4 TEMPERATURE SENSOR Many different types of temperature sensors have long been available (Fraden 1993), and most of these temperature-sensing schemes can be utilized in micro scales. For example, the silicon-resistive and pn-junction temperature sensors are widely used for temperature compensation in silicon diaphragm-type pressure sensors (Brysek et al 1990). An interesting example (Lahiji and Wise 1980) is an IR detector that uses a thin diaphragm to absorb incoming IR light, converting the photon energy into heat. Sixty thin-film thermal couples (Bi–Sb and Au–polysilicon) were fabricated in series on a $2 \times 2\text{-mm}^2$, 1- μm thick diaphragm. The device shows an impressive sensitivity of 30 V/W and a time constant below 10 ms.

5.2 *Micro Flow Actuator*

Several actuating mechanisms, including electrostatic, electromagnetic, thermopneumatic, etc., are used in micro actuators. Among them, electrostatic actuation is most popular, mainly because of ease of fabrication. However, the electrostatic actuation has intrinsic limitations on force ($\sim \mu\text{N}$) and displacement ($\sim \mu\text{m}$) outputs; they can be used to study flow instability problems where only small displacement is required. For example, Huang et al (1996) made an electrostatic actuator to control screech in high speed jets. With the design of 70- μm peak-to-peak displacement at the resonant frequency of 5 kHz of the device, it has been shown that proper disturbances in the jet flow can be provided.

Electromagnetic actuation can provide much larger force (100s of μN) and higher displacements (mm). For example, a micro magnetic flap (Miller et al 1996) with a 30-turn copper coil and a layer of permalloy ($\text{Ni}_{80}\text{Fe}_{20}$) was fabricated on a $4 \times 4\text{-mm}^2$ silicon plate (40- μm thick). In a magnetic field of 1 kG, the device can be driven to a rotational angle of more than 30°, because of the induction of magnetization in the permalloy. In addition, a ± 100 mA of current can then be applied to the coil to move the flap another $\pm 10^\circ$. This allows total control of the flap for more than 2 mm of tip motion (Fig. 15). These and other similar devices have been shown to be

effective in changing the separation of a flow around a leading edge (Liu et al 1995) and to achieve drag reduction in boundary layer flow (Tsao et al 1994, Ho et al 1997).

The thermopneumatic actuation mechanism is a technique which can provide force ($> N$) and displacement ($> mm$) even larger than that of the electromagnetic method. Thermopneumatic actuation, first demonstrated by Zdeblick and Angell (1987), showed that a heater in a liquid-filled cavity can heat the fluid and cause significant pressure inside the cavity. If a wall of the cavity is a diaphragm, it will be pushed outward, because of the differential pressure increase. Since the pressure increase can easily be several psi, the force acting on the diaphragm is large. However, an earlier demonstration used only flat silicon diaphragms, so the deflection is limited by the mechanical structures. A recent demonstration that used a silicone rubber diaphragms showed more than a mm displacement with about 10 psi pressure (Yang et al 1997). It is foreseeable that such an actuator may have important applications in flow actuation.

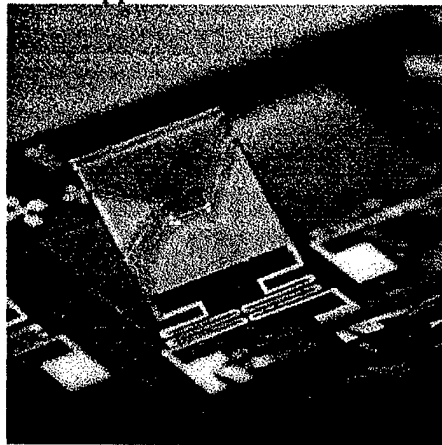


Figure 15 Micro electro-magnetic flap actuator (Miller et al 1996).

6. FLOW CONTROL BY MICRO SYSTEMS

A micro system that contains transducers and/or logic circuitry is capable of sensing, signal processing, and actuation. Such a system obviously has numerous engineering applications (Gadel-Hak 1993, Ho & Tai 1996, McMichael 1996, Ho et al 1997). A few examples of using micro systems for flow control are reviewed here.

6.1 *Moments Control of a Delta Wing*

On a delta wing, the two leading-edge separation vortices contribute up to 40% of the lift at high angles of attack. If we can break the symmetry of these vortices, a net rolling torque may be achieved that can be used for maneuvering the wing. Leading edge vortices develop from a boundary layer separated from the surface. In free shear flows, it has been demonstrated that minute perturbations at its origin can globally modify the flow field (Ho & Huang 1982, Oster & Wygnanski 1982). Therefore, a coupling between micro actuators and wing-size flow structures can be made by manipulating the thin boundary layer.

A delta wing with a 56.5° sweep angle was used in this experiment (Lee et al 1996). Electromagnetically driven microactuators are placed along the leading edges with a circular cross section. The location of the actuators on the leading edge is indicated by an angle, θ , which is measured from the lower surface, $\theta = 0^\circ$, of the wing towards the upper surface, $\theta = 180^\circ$. The measured rolling torques are normalized by the torque produced by the vortex lift, M_v , which is the product of the lift generated by a single leading-edge vortex and the distance between the centroid of the half wing and the center chord. The magnitude of the maximum torque reaches 15% of M_v at $\sim \theta = 60^\circ$ for small actuators (Fig. 16). When the actuators match the thickness of the boundary layer, the maximum normalized torque can be about 40% (Ho et al 1997). A flexible skin containing 128 sensors (Fig. 13b) is used to measure the surface shear stress. The measurements show that the flow separates immediately downstream from $\theta = 60^\circ$. A negative torque was found for actuators placed at $\theta = 80^\circ$. When actuators are placed on both leading edges but at two angles ($\theta = 60^\circ, 80^\circ$), the measured resultant torque is equal to the sum of the two peaks. Therefore, the two vortices act independently on this delta wing with a sweep angle of 56.5° . Interactions of the two leading-edge vortices are expected for wings with a larger sweep angle (Lee & Ho 1990). Pitching and yawing torques can also be obtained by using the miniature actuators (Ho et al 1997).

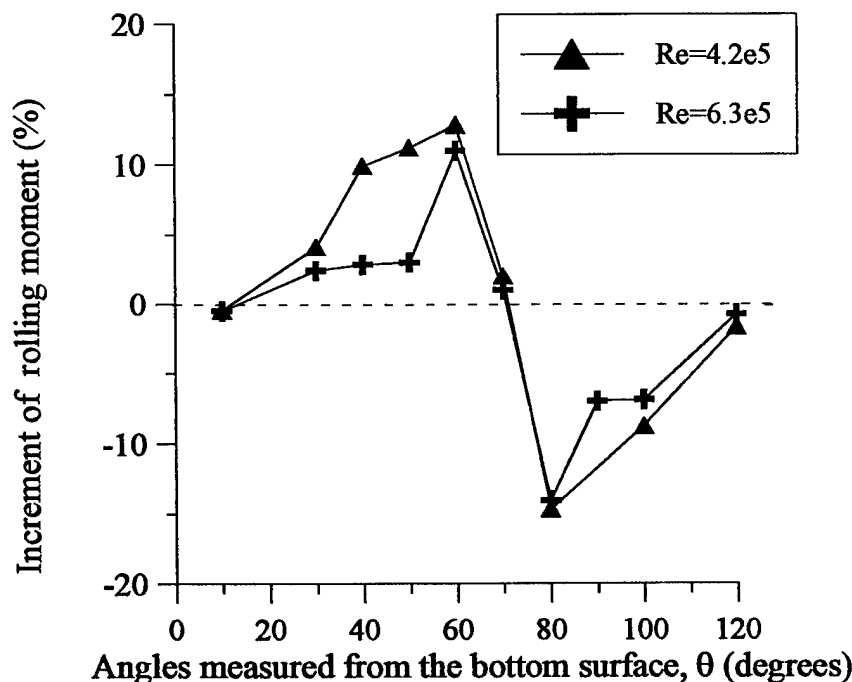


Figure 16 Normalized rolling moment as a function of actuator location at angle (25°) of attack.

6.2 Thrust Vectoring

Deflecting the momentum of a jet to a direction other than the one normal to the nozzle plane is useful in applications such as fluidic switching and aircraft maneuvering. Coe et al (1994) used a

micromachined vibrating diaphragm driven by electrostatic force under a cavity to generate a miniature jet. This jet is established by asymmetric entrainment during the push-pull phase. In the pushing phase, the fluid near the jet axis is moved away from the diaphragm. When the diaphragm is pulled back, fluid all around the cavity flows toward the diaphragm and a net concentrated jet flow is established. Acousticians refer to this phenomenon as a quartz wind (Kuttruff 1991), because quartz has been used as the diaphragm material in acoustic transducers. When the micro jets are placed at the nozzle of a rectangular jet with a 7.62-cm \times 1.27-cm nozzle, the direction of the large jet can be changed according to the amplitude of the micro jets (Fig. 17). This capability provides a simple thrust-vectoring technique (Smith & Glezer 1997), which is obviously much more advantageous than the present method of using paddles to deflect the jet. The paddles suffer high static and dynamic loading, which causes frequent structural damage.

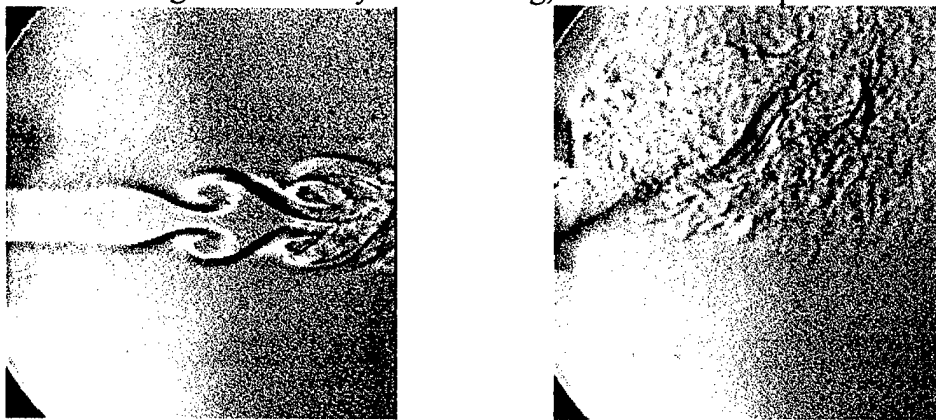


Figure 17 Thrust vectoring by a micro jet (Smith & Glezer 1997).

6.3 Control of Turbulent Skin Friction

The discovery of organized structures (Brown & Roshko 1974) has significantly facilitated turbulence control of free shear flows (Ho & Huang 1982, Oster & Wygnanski 1982). However, attempts to control wall flows have been much less successful. The dynamics of the large-scale structures in free shear flows are relatively well understood (Ho & Huerre 1984, Huerre & Monkewitz 1990) through the instability process. The underlying mechanism by which the organized structures are produced and sustained in wall flows are less well known (Robinson 1991). The following are problems for experimental studies:

1. The transverse length scale of the streaks is on the order of 100s of microns.
2. The lifetime of the streaks is about one ms or less.
3. The streaks spread over the entire surface area covered by the turbulent boundary layer.

The small size is a direct cause of great difficulties, because traditional transducers are larger than the structures. These relatively large transducers do not have enough spatial resolution to measure the structure's properties and to explore the structure's response to perturbations. We cannot devise control schemes analogous to research we have conducted in the past on free shear layers. The micromachined transducers match the size of the streaks, and integrated logic circuitry enables real-time decisions. A micro system provides an opportunity to directly manipulate individual wall structures. This is the reason that wall-bounded turbulent-flow control is chosen as a testbed for developing a micro system that comprises sensors, logic circuitry, and actuators.

6.3.1 DISTRIBUTED MEASUREMENT A surface shear-stress imaging chip that comprises 85 micro sensors was developed to measure the instantaneous turbulent shear stress in a distributed manner. The size of the sensors and the spacing between them are chosen to match the length scale of near-wall stream-wise streaks in the tested number range. Figure 18 shows the instantaneous surface shear-stress contours measured by the sensor array. Only 25 sensors in a linear span-wise array are used. The vertical direction is a pseudo-stream-wise plot generated by multiplying time by the convection speed. The capability of measuring the surface shear stress is not only essential for the interactive control of the high speed streaks but also provides interesting statistical properties of the streaks (Motoaki et al 1997).

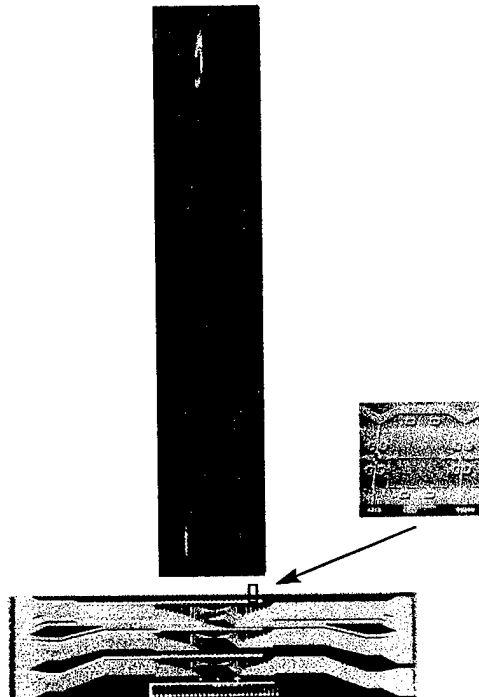


Figure 18 Instantaneous surface shear stress measured by an imaging chip (Ho et al 1997).

6.3.2 INTERACTION BETWEEN THE ACTUATOR AND WALL STRUCTURES Being able to perform distributed sensing is a major step forward. Understanding how the actuator interacts with the near wall structure is an even more important part of the control process. Actuators are wall mounted devices that can produce surface deformation and/or flow disturbances. The flow altered by a rising obstacle was studied by direct numerical simulation (Carlson & Lumley 1996). Vortical structures are produced by the unsteady motion of the actuator and are deformed while the actuator moves through the boundary-layer velocity shear. These actuator-produced perturbations are expected to alter the near wall structure in such a way that a skin friction reduction is achieved. Obviously realizing this concept depends on finding proper actuation commands, which in turn requires an in-depth understanding of the non-linear interaction between the artificial disturbance and the high speed streaks. However, almost all of the current experiments investigate the effect of an actuator on stationary vortices embedded in a laminar flow (Jacobson & Reynolds 1995, Ho & Tai 1996), because studies of the effect on the

streaks in turbulent flow require a complete micro system (see Section 6.3.3), which is still under development.

At the entrance region of a 2-D channel flow, the boundary layer is laminar. A 1.3-mm-thick bump was placed normal to the flow and terminates half way in the span-wise direction (Ho & Tai 1996). At the terminating position of the bump, a stationary longitudinal-vortex pair is produced. A micromachined actuator (Fig. 16), which is a silicon nitride flap driven by an electromagnetic field, is placed downstream of the vortex generator. During the upward moving phase, the ensemble-averaged vertical velocity field (Fig. 19) shows the transport of high velocity fluid away from the surface. It is interesting to note that the downward motion of the actuator does not produce a symmetric cancellation effect. Because of the presence of the wall, the low speed fluid under the flap is pushed upward during the downward motion of the flap so that a net reduction in the skin drag is achieved through a complete cycle of the flap motion. The surface shear stress was integrated along the span-wise direction and over the whole cycle of the motion of the actuator. The integrated shear stress normalized to the dynamic head is defined as the skin drag coefficient (C_{dv}). If a proper driving signal is applied to the actuator, the skin drag coefficient of the vortex actuator interaction (C_d) is lower than the drag coefficient of the stationary vortex alone. The net reduction of the surface shear stress is the difference between these two coefficients. The net reductions are plotted for various actuator frequencies (ω) and maximum tip heights (d) in figure 20.. The product of ω and d is the maximum normal velocity of the actuator. For constant ωd , the net reductions in the skin friction drag are the same for different combinations of ω and d . This result indicates that the amount of shear stress reduction is directly related to the ability to transport high-speed fluid. In other words, we need to seek actuators that can efficiently pump high-speed fluid away from the wall with low power expenditure and low form drag.

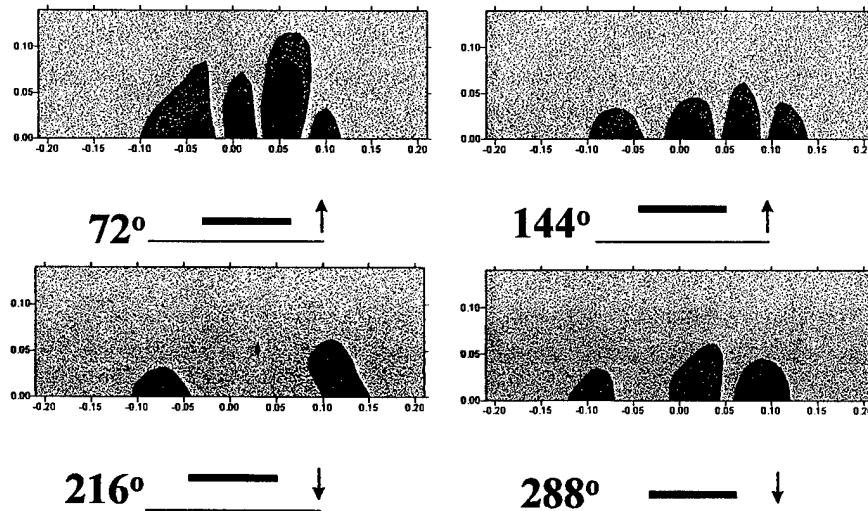


Fig. 19 Vertical velocity contours of an flap actuator interacting with a longitudinal vortex pair. The phase angle: 0° and 360° - flap on the surface, 180° - flap at its up most location

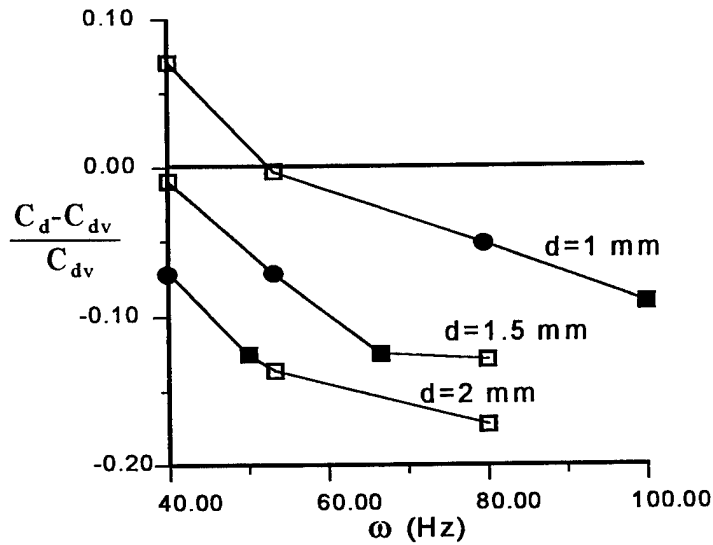


Figure 20 Surface shear-stress reduction as a function of actuator frequency, ω , and maximum actuator tip height, d . (● - $\omega d = 80$ mm/s and ■ - $\omega d = 100$ mm/s, (Ho et al 1997))

In a water channel, the interaction between a piezo-electrically-driven actuator with a vortex pair developed from a cylinder was studied (Jacobson & Reynolds 1995). Surface-mounted hot-film sensors were used to measure the surface shear stress, which serves as an input for feedback control. The optimum amplitude of the actuator obtained from the feedback control can delay the laminar turbulent transition to about 40 displacement thicknesses from the natural transition region (Fig.21).

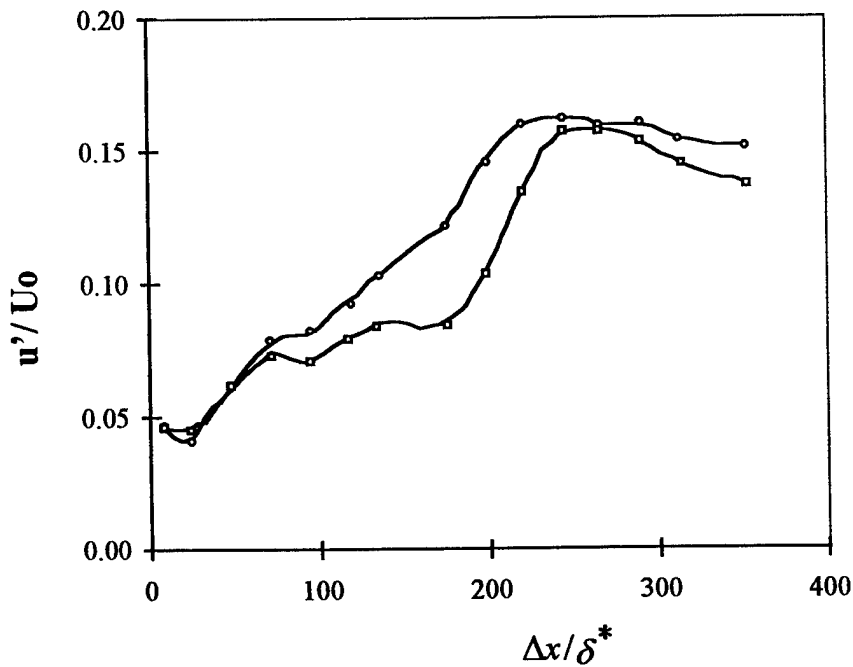


Figure 21 Transition delay, u'/u_0 , by actuation, , where δ^* is the displacement thickness (Jacobson and Reynolds 1995).

6.3.3 A MICRO SYSTEM FOR SURFACE SHEAR-STRESS REDUCTION The lifetime of the high speed streaks is short, and a large number of the streaks need to be controlled at the same time. If all of the sensor outputs were to be sent to a central computer and the control command were to be sent from the computer to each actuator, a very high-bandwidth signal path and large number of leads would be required. Implementing local and simple signal processing is obviously a necessity for alleviating these problems. Neural networks are a viable approach (Jacobson & Reynolds 1995, Lee et al 1997). A neural-network-based circuit was developed to determine the time and the spatial extent of the high speed streaks passing the shear-stress-sensor array (Gupta et al 1996). The output of the circuit was used for actuation. The task of integrating a micro system containing micro sensors, microelectronics, and micro actuators on a chip is possible, yet it is not trivial. The micro transducers, which integrate the circuit, need to be fabricated at a much higher temperature than that of the circuits, which means that the diffusion of the doping material in the circuits may affect their performance. The process flow needs to be carefully planned to eliminate cross-contamination possibilities. A micro system for shear stress reduction was fabricated on a 1-cm \times 1-cm die; 18 micro shear-stress sensors, 3 micro flap actuators, as well as circuits for logic sensor drivers and actuator drivers are monolithically integrated (Fig. 22). This is a prototype design, and various tests of the functionalities are still underway.

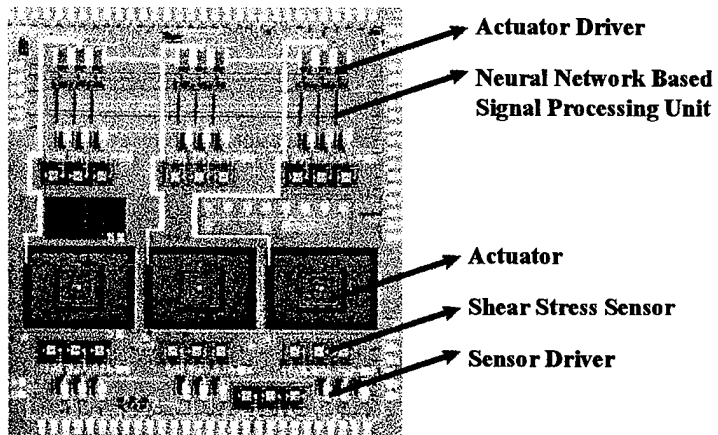


Figure 22 A micro system for surface shear-stress reduction (Ho et al 1997).

7. CONCLUDING REMARKS

The capability of applying a large number of transducers with on-board signal processing provides a paradigm shift for flow control. This type of micro system enables us to perform real-time distributed control. Hence, the ability to interactively manipulate individual high-speed streaks in the turbulent boundary layer is made possible and could be effective in decreasing the surface friction force. A near-term industrial application for the skin-friction-drag experiment is not obvious. This approach, however, will definitely facilitate our exploration of the near wall structure under artificial perturbations, and the findings will lead us toward a fundamental understanding of the grand challenge in turbulence research. Furthermore, other types of flow

control may also be inspired by the real-time, distributed control ability of MEMS-based transducers. The large torque on a delta wing and the thrust vectoring achieved by micro actuation are examples. We expect that a stream of new flow phenomena will be introduced by MEMS-based sensing and control schemes.

In the field of biomedical analysis, MEMS technology has already sparked a major transformation. Flows through micro channels or nozzles are the most common configurations in all of the biomedical applications. Many unexpected phenomena have been observed in Newtonian fluid flows through these simple configurations. These types of flows are extremely intriguing, because they challenge the fundamentals of fluid dynamics; the non-slip boundary condition clearly should be relaxed for gas flows. In liquid flows, extra surface-force terms may need to be added to the momentum balance equation. Whether any modification needs to be made to the constitutive equation for a simple fluid remains to be investigated. It is evident that micro flow has opened a new domain for basic fluid-mechanics research.

ACKNOWLEDGMENTS

MEMS is a multi-disciplinary field and, as such, cooperation among scientists with different backgrounds is essential to accomplish this work. It is our privilege and pleasure to work with researchers who make these nearly impossible tasks become reality. We thank Professors R. Goodman, C.J. Kim, J. Kim, J. Speyer, K. Wang, J. Woo, Drs. B. Gupta, S. Joshi, S. Tung, Mr. D. Babcock, F. Jiang, C. Lee, G. B. Lee, C. Liu, J. Shih, and T. Tsao. This work is supported by Dr. J. McMichael of AFOSR, as well as Drs. K. Gabriel and M. Francis of DARPA. Their willingness to take risks is a key factor enabling the research community to unveil the exciting Aero-MEMS area.

Literature Cited

Analog Device Inc. 1991. ADXL50 Catalog

Arkilic E, Breuer KS. 1993. Gaseous flow in small channels. *AIAA Pap. 93-3270*

Arkilic E, Schmidt, MA, Breuer KS. 1995. Gaseous slip flow in long microchannels. *J. MEMS*.6:167-178

Beskok A, Karniadakis GE. 1992. Simulation of slip-flows in complex micro-geometries. *ASME DSC* 40:355-70

Beskok A, Karniadakis GE. 1993. Simulation of heat and momentum transfer in complex micro-geometries. *AIAA Pap. 93-3269*

Beskok A, Karniadakis GE, Trimmer W. 1996. Rarefaction and compressibility effects in gas microflows. *J. Fluids Eng.* 118:448-56

Blackwelder RF. 1981. Hot-wire and hot-film anemometers. In *Methods of Experimental Physics: Fluid Dynamics*, ed. RJ Emrich, 18:259-314. New York: Academic. 403 pp.

Brown GL, Roshko A. 1974. On density effects and large structure in turbulent mixing layers. *J. Fluid. Mech.* 64:775-816

Brysek J, Petersen K, Mallon J, Christel L, Pourahmadi F. 1990. *Silicon Sensors and Microstructures*. San Jose, CA: NovaSensor

Carlson HA, Lumley JL. 1996. Flow over an obstacle emerging from the wall of a channel. *AIAA J.* 34:924-31

Christian RG. 1966. The theory of oscillating-vane vacuum gauges. *Vacuum* 16:175-8

Coe DJ, Allen MG, Trautman MA, Glezer A. 1994. Micromachined jets for manipulation of macro flows. In *Technical Digest, Solid-State Sensor and Actuator Workshop* (Catalog No.

64TRF-0001), Hilton Head Island, SC, June 13-16, 1994, pp. 243-7. Cleveland Heights, OH: Transducers Research Foundation, Inc., 1994

Dussan EB, Davis SH. 1974. On the motion of fluid-fluid interface along a solid surface. *J. Fluid Mech.* 65:71-95

Eddington AS. 1928. *Nature of the Physical World*. Cambridge/London/New York: Cambridge Univ. Press. 361 pp.

Fan LS, Tai YC, Muller RS. 1988a. IC-processed electrostatic micromotors. *Technical Digest, International Electron Devices Meeting*, pp. 666-69. San Francisco, December 11-14.

Fan LS, Tai YC, Muller RS. 1988b. Integrated movable micromechanical structures for sensors and actuators. *IEEE Trans. Electron Devices* ED-35(6):724-30

Fraden J. 1993. *AIP Handbook of Modern Sensors*. New York: American Institute of Physics. 552 pp.

Gad-el-Hak M. 1993. Innovative control of turbulent flows. *AIAA Pap. 93-3268*

Guckel H, Burns DW, Rutigliano CR. 1986. Design and construction techniques for planar polysilicon pressure transducers with piezoresistive read-out. In *Technical Digest, IEEE Solid-State Sensor and Actuator Workshop*, Hilton Head Island, SC, June 3-6, 1986, pp. 76-9

Gupta B, Goodman R, Jiang F, Tai YC, Tung S, Ho CM. 1996. Analog VLSI system for active drag reduction. *IEEE Micro.* 16:53-9

Haritonidis JH. 1989. The measurement of wall shear stress. In *Advances in Fluid Mechanics Measurements*, ed. M Gad-el-Hak, pp. 229-61. Berlin/Heidelberg/New York: Springer Verlag. 606 pp.

Harley JC, Huang Y, Bau H, Zemel JN. 1995. Gas flow in micro-channels. *J. Fluid Mech.* 284:257-74

Hasegawa T, Suganuma M, Watanabe H. 1997. Anomaly of excess pressure drops of the flow through very small orifices. *Phys. Fluids* 9:1-3

Ho CM, Huang LS. 1982. Subharmonics and vortex merging in mixing layers. *J. Fluid Mech.* 119:443-73

Ho CM, Huerre P. 1984. Perturbed free shear layers. *Annu. Rev. Fluid Mech.* 16:365-424

Ho CM, Tai YC. 1996. MEMS and its applications for flow control. *J. Fluids Eng.* 118:437-47

Ho CM, Tung S, Lee GB, Tai YC, Jinag F, Tsao T. 1997. MEMS - A technology for advancements in aerospace engineering. *AIAA Pap. 97-0545*

Howe RT, Muller RS. 1983. Polycrystalline silicon micromechanical beams. *J. Electrochem. Soc.* 130:1420-3

Huang C, Papp J, Najafi K, Nagib H. 1996. A microactuator system for the study and control of screech in high speed jets. In *An Investigation of Micro Structures, Sensors, Actuators, Machines and Systems* (Proc., IEEE 9th Ann. Intl. Wksp. on Micro Electro Mechanical Systems, Amsterdam, Feb. 11-15, 1996), pp. 19-24. IEEE 1084-6999, New York: IEEE

Hunter RJ. 1981. *Zeta Potential in Colloid Science: Principles and Applications*. New York: Academic. 386 pp.

Huerre P, Monkewitz PA. 1990. Local and global instabilities in spatially developing flows. *Annu. Rev. Fluid Mech.* 22:473-537

Israelachvili J. 1991. *Intermolecular and Surface Forces*. New York: Academic Press. 450 pp. 2nd ed.

Jacobson SA, Reynolds WC. 1995. An experimental investigation towards the active control of turbulent boundary layers. *Stanford Univ. Rep. TF-64*, Palo Alto, Calif.

Jiang FK, Tai YC, Ho CM, Li WJ. 1994. A micromachined polysilicon hot-wire anemometer. In *Technical Digest, Solid-State Sensor and Actuator Workshop* (Catalog No. 64TRF-0001), Hilton Head Island, SC, June 13-16, 1994, pp. 264-7. Cleveland Heights, OH: Transducers Research Foundation, Inc., 1994

Jiang F, Tai YC, Gupta B, Goodman R, Tung S, Huang J, Ho CM. 1996. A surface-micromachined shear-stress imager. In *An Investigation of Micro Structures, Sensors, Actuators, Machines and Systems* (Proc., IEEE 9th Ann. Intl. Wksp. on Micro Electro Mechanical Systems, Amsterdam, Feb. 11-15, 1996), pp. 110-5. IEEE 1084-6999, New York: IEEE

Jiang FK, Tai YC, Walsh K, Tsao T, Lee GB, Ho CM. 1997. A flexible MEMS technology and its first application to shear stress sensor skin. In *An Investigation of Micro Structures, Sensors, Actuators, Machines and Robots* (Proc., IEEE 10th Ann. Intl. Wksp. on Micro Electro Mechanical Systems, Nagoya, Jan. 26-30, 1997), pp. 465-70. IEEE 97CH36021, New York: IEEE

Joo Y, Dieu K, Kim CJ. 1995. Fabrication of monolithic microchannels for IC chip cooling. In *An Investigation of Micro Structures, Sensors, Actuators, Machines and Systems* (Proc., IEEE 8th Ann. Intl. Wksp. on Micro Electro Mechanical Systems, Amsterdam, Jan. 29-Feb. 2, 1995), pp. 362-7. IEEE 95CH35754, New York: IEEE

Judge JS. 1971. A study of the dissolution of SiO_2 in acidic fluoride solutions. *Solid-State Sci.* 118:1772-5

Juneau T, Pisano AP. 1996. Micromachined dual input axis angular rate sensor. In *Technical Digest, Solid-State Sensor and Actuator Workshop* (Catalog No. 96TRF-0001), Hilton Head Island, SC, June 3-6, 1996, pp. 299-302. Cleveland Heights, OH: Transducers Research Foundation, Inc., 1996

Kennard EH. 1938. *Kinetic Theory of Gases*. New York: McGraw-Hill. 483 pp.

Knudsen M. 1909. Die gesetze der molecular stromung und die inneren reibungstromung der gase durch rohren. *Ann Phys. (Leipzig)* 28:75-130

Ko WH, Bao MH, Hong YD. 1982. A high-sensitivity integrated-circuit capacitive pressure sensors. *IEEE Trans. Electron Devices* ED-29(1):48-56

Koplik J, Banavar JR, Willemsen JF. 1989. Molecular dynamics of fluid flow at solid surfaces. *Phys. Fluids A* 1:781-94

Koplik J, Banavar JR. 1995. Continuum deductions from molecular hydrodynamics. *Annu. Rev. Fluids Mech.* 27:257-92

Kuttruff H. 1991. *Ultrasonics Fundamentals and Applications*. London/New York: Elsevier Applied Science. pp. 452

Lahiji GR, Wise KD. 1980. A monolithic thermopile detector fabricated using integrated-circuit technology. *Technical Digest, International Electron Device Meeting*, Washington DC, Dec. 8-10, 1980, pp. 676-9. New York: IEEE. 1980

Lanzillotto A, Leu TS, Amabile M, Wildes R. 1996. An investigation of microstructure and microdynamics of fluid flow in MEMS. *ASME AD* 52:789-96

Lee C, Kim J, Babcock D, Goodman R. 1997. Application of neural networks to turbulence control for drag reduction. *Phys. Fluids*. In Press

Lee GB, Ho CM, Jiang F, Liu C, Tsao T, Tai YC, Schsuer F. 1996. Control of roll moment by MEMS. *ASME DA*. UCLA

Lee M, Ho CM. 1990. Lift force of delta wings. *Appl. Mech. Rev.* 43:209-21

Lee YS, Wise KD. 1982. A batch fabricated silicon capacitive pressure transducers. *IEEE Trans. Electron Devices* ED-29(1):42-47

Liu J, Tai YC, Lee J, Pong KC, Zohar Y, Ho CM. 1993a. In situ monitoring and universal modeling of sacrificial PSG etching using hydrofluoric acid. In *An Investigation of Micro Structures, Sensors, Actuators, Machines and Systems* (Proc., IEEE 6th Ann. Intl. Wksp. on Micro Electro Mechanical Systems, Fort Lauderdale, FL, Feb. 7-10, 1993), pp. 71-6. IEEE 93CH3265-6, New York: IEEE

Liu J, Tai YC, Pong K, Ho CM. 1993b. Micromachined channel/pressure sensor systems for micro flow studies. In *Transducers '93* (Digest of Technical Papers, 7th Intl. Conf. on Solid-State Sensors and Actuators, Yokohama, June 7-10, 1993), pp. 995-9. Japan: Institute of Electrical Engineers of Japan, 1993

Liu J, Tai YC, Pong K, Ho CM. 1995. MEMS for pressure distribution studies of gaseous flows in microchannels. In *An Investigation of Micro Structures, Sensors, Actuators, Machines and Systems* (Proc., IEEE 8th Ann. Intl. Wksp. on Micro Electro Mechanical Systems, Amsterdam, Jan. 29-Feb. 2, 1995), pp. 209-15. IEEE 95CH35754, New York: IEEE

Liu C, Tsao T, Tai YC, Leu TS, Ho CM, Tang WL, Miu D. 1995. Out-of-plane permalloy magnetic actuators for delta-wing control. In *An Investigation of Micro Structures, Sensors, Actuators, Machines and Systems* (Proc., IEEE 8th Ann. Intl. Wksp. on Micro Electro Mechanical Systems, Amsterdam, The Netherlands, Jan. 29-Feb. 2, 1995), pp. 7-12. IEEE 95CH35754, New York: IEEE

Lofdahl L, Kalvesten E, Hadzianagnostakis T, Stemme G. 1996. An integrated silicon based wall pressure-shear stress sensor for measurements in turbulent flows. *ASME DSC MEMS*. 59:245-51

Mastrangelo C, Hsu CH. 1992. A simple experimental technique for the measurement of the work of adhesion of microstructures. In *Technical Digest, IEEE Solid-State Sensor and Actuator*

Workshop (Catalog No. 92TH0403-X), Hilton Head Island, SC, June 22-25, 1992, pp. 208-12.

New York: IEEE. 1992

McMichael JM. 1996. Progress and prospects for active flow control using microfabricated electro-mechanical systems (MEMS). *AIAA Pap. 96-0306*

Migun NP, Prokhorenko PP. 1987. Measurement of the viscosity of polar liquids in microcapillaries. *Colloid J. USSR* 49:894-7

Miller R, Burr G, Tai YC, Psaltis D. 1996. Electromagnetic MEMS scanning mirrors for holographic data storage. In *Technical Digest, Solid-State Sensor and Actuator Workshop* (Catalog No. 96TRF-0001), Hilton Head Island, SC, June 3-6, 1996, pp. 183-6. Cleveland Heights, OH: Transducers Research Foundation, Inc., 1996

Mohiuddin Mala G, Li D, Dale JD. 1996. Heat transfer and fluid flow in microchannels. *ASME DSC* 59:127-36

Monk DJ, Soane DS, Howe RT. 1993. A review of the chemical reation mechanism and kinetics of hydrofluoric acid etching of silicon dioxide for surface micromachining applications. *Thin Solid Films* 232:1-12

Motoaki K, Tung S, Hoffelner J, Ho CM, Jiang F, Tai YC. 1997. Turbulent surface shear stress measurement by micro sensor arrays. *Proc. of Intern. Conf. on Science and Arts*. ed. F. Fiedler

Nathanson HC, Newell WE, Wickstrom RA, Davis JR. 1967. Resonant gate transistors. *IEEE Trans. Electron Devices* 14(3):117-133

Newell WE. 1968. *Science* 161:1320

Nguyen T-C. 1995. Micromechanical resonators for oscillation and filters. *Proc. IEEE Int. Ultrasonic Symp.* pp. 489-99. Seattle, USA. Nov. 7-10

Oh CK, Oran ES, Cybyk ZC. 1995. Microchannel flow computed with the DSMC-MLG. *AIAA Pap. 95-2090*

Oran ES, Oh CK, Cybyk ZC. 1998. Direct-simulation Monte Carlo - recent advances and applications. *Annu. Rev. Fluid Mech.* In press

Oster D, Wygnanski I. 1982. The forced mixing layer between parallel streams. *J. Fluid Mech.* 123:91-130

Padmanabhan A, Goldberg HD, Breuer KS, Schmidt MA. 1995. A silicon micromachined floating element shear-stress sensor with optical position sensing by photodiodes. In *Transducers '95/Eurosensors IX* (Digest of Technical Papers, 8th Intl. Conf. on Solid-State Sensors and Actuators, Stockholm, 25-29, 1995), pp. 436-9. Stockholm: Royal Swedish Academy of Engineering Sciences, IVA, 1995

Pan T, Hyman D, Mehregany M, Reshotko E, Willis B. 1995. Calibration of microfabricated shear stress sensors. In *Transducers '95/Eurosensors IX* (Digest of Technical Papers, 8th Intl. Conf. on Solid-State Sensors and Actuators, Stockholm, 25-29, 1995), pp. 443-6. Stockholm: Royal Swedish Academy of Engineering Sciences, IVA, 1995

Petersen K. 1982. Silicon as a mechanical material. *Proc. IEEE* 70:420-56

Pfahler J, Harley JC, Bau H. 1990. Liquid transport in micron and submicron channels. *Sensors and Actuators A* 22:431-4

Pfahler J, Harley JC, Bau H, Zemel JN. 1991. Gas and liquid flow in small channels. *ASME DSC* 32:49-60

Piekos ES, Breuer KS. 1995. DSMC modeling of micromechanical devices. *AIAA Pap. 95-2089*

Piekos ES, Breuer KS. 1996. Numerical modeling of micromechanical devices using the direct simulation Monte Carlo method. *J. Fluids Eng.* 118:464-9

Pong KC, Ho CM, Liu J, Tai YC. 1994. Nonlinear pressure distribution in uniform microchannels. *ASME FED* 197:51-6

Preston K. 1972. *Coherent Optical Computers*. New York: McGraw-Hill. 315 pp.

Ristic L, ed. 1994. *Sensor Technology and Devices*. Boston: Artech House. 524 pp.

Robinson SK. 1991. Coherent motions in the turbulent boundary layer. *Annu. Rev. Fluid Mech.* 23:601-39

Schmidt M, Howe RT, Senturia S, Haritonidis JH. 1988. Design and fabrication of a microfabricated floating element shear-stress sensor. *IEEE Trans. Electron Devices* 35:750-7

Seidel H. 1987. The mechanism of anisotropic silicon etching and its relevance for micromachining. *Transducers' 87* (Digest of Technical Papers, the 4th Intl. Conf. on Solid-State Sensors and Actuators, Tokyo, Japan. June 3-5), pp. 120-5

Shih JC, Ho CM, Liu J, Tai YC. 1995. Non-linear pressure distribution in uniform microchannels. *ASME AMD-MD* 238

Shih JC, Ho CM, Liu J, Tai YC. 1996. Monatomic and polyatomic gas flow through uniform microchannels. *ASME DSC* 59:197-203

Smith BL, Glezer A. 1997. Vectoring and small-scale motions effected in free shear flows using synthetic jet actuators. *AIAA Pap. 97-0213*

Sugiyama S, Shimaoka K, Tobata O. 1991. Surface micromachined micro-diaphragm pressure sensors. In *Transducers '91* (Digest of Technical Papers, the 6th Intl. Conf. on Solid-State Sensors and Actuators, San Francisco, CA, USA. June 24-27, 1991, Catalog No. 91CH2817-5), pp. 188-91. Piscataway, NJ: IEEE. 1991

Tang WC, Nguyen T-C, Howe RT. 1989. Laterally driven polysilicon resonant microstructures. *Sensors and Actuators* 20:25-32

Tsao T, Liu C, Tai YC, Ho CM. 1994. Micromachined magnetic actuator for active fluid control. *ASME FED* 197:31-8

Tuckermann DB, Pease RFW. 1982. Optimized convective cooling using micro-machined structures. *J. Electrochem. Soc.* 129(3):98C

Wang K, Nguyen T-C. 1997. High-order micromechanical electronic filters. In *An Investigation of Micro Structures, Sensors, Actuators, Machines and Robots* (Proc., IEEE 10th Ann. Intl. Wksp. on Micro Electro Mechanical Systems, Nagoya, Japan, Jan. 26-30, 1997), pp. 25-30. IEEE 97CH36021, New York: IEEE

Went FW. 1968. The size of man. *American Scientist* 56:400-13

Wolf S. 1990. *Silicon Processing for the VLSI Era*. Vol. II, Sunset Beach, CA: Lattice Press. 753 pp.

Yang YJ, Senturia SD. 1996. Numerical simulation of compressible squeezed-film damping. In *Technical Digest, Solid-State Sensor and Actuator Workshop* (Catalog No. 96TRF-0001), Hilton Head Island, SC, June 3-6, 1996, pp. 76-9. Cleveland Heights, OH: Transducers Research Foundation, Inc., 1996

Yang X, Grosjean C, Tai YC, Ho CM. 1997. A MEMS thermopneumatic silicone membrane valve. In *An Investigation of Micro Structures, Sensors, Actuators, Machines and Robots* (Proc., IEEE 10th Ann. Intl. Wksp. on Micro Electro Mechanical Systems, Nagoya, Jan. 26-30, 1997), pp. 114-8. IEEE 97CH36021, New York: IEEE

Zdeblick MJ, Angell JB. 1987. A miniature electric-to-fluidic valve. *Transducers'87. Technical Digest*, Tokyo, Japan, June 3-5. pp. 827-9

Zhang X, Tang W. 1994. Viscous air damping in laterally driven microstructures. In *An Investigation of Micro Structures, Sensors, Actuators, Machines and Systems* (Proc., IEEE 7th Ann. Intl. Wksp. on Micro Electro Mechanical Systems, Oiso, Japan, Jan. 25-28, 1994), pp. 199-204. IEEE 94CH3404-1, New York: IEEE

Zohar Y, Jiang L, Wong M, Wang Y. 1996. Microchannels with integrated temperature sensors. *Bull. Amer. Phys. Soc.* 41:1790

Linear Stabilization of Plane Poiseuille Flow Using an Optimal Control Approach*

Sanjay S. Joshi[†], Jason L. Speyer, & John Kim

School of Engineering and Applied Science
University of California, Los Angeles
Los Angeles, California 90095

December 3, 1997

Abstract

In this paper, we consider linear stabilization of plane, Poiseuille flow using linear quadratic Gaussian (LQG) optimal control theory. In prior investigations, it has been shown that plane, Poiseuille flow may be stabilized using extremely simple, integral compensator controllers, given that sensor locations produce minimum phase zeros. However, the controller is marked by slow dissipation of perturbation energy. In this investigation, we exploit LQG methods to give faster perturbation energy dissipation. We show that we may achieve approximately double the dissipation rate than that reported in integral compensator control schemes. This increase in performance comes with a cost. Controllers built using LQG methods for infinite-dimensional systems must, in theory, be infinite-dimensional. Since it is impossible to implement infinite-dimensional controllers, we implement reduced-order controllers on the full-order plant.

*Part of this material was first presented at the Conference on Decision and Control, New Orleans, LA, December, 1995 [1].

[†]Current Address: Guidance and Control Analysis Group, Jet Propulsion Laboratory, California Institute of Technology, Pasadena, CA 91109.

We show that this procedure can in theory lead to de-stabilization of unmodelled dynamics. We then show that this may be avoided using distributed control or, dually, distributed sensing. An additional problem in high-plant-order LQG controller design is numerical instability in the synthesis equations. We show a sub-optimal LQG synthesis method that uses an extremely, low-order plant model for synthesis of a high-order controller. This sub-optimal controller produces results essentially equivalent to the optimal controller. Finally, we apply our LQG controller to a plant of differing Reynolds number from that used in the LQG design. Using this new plant, we show that the system is still stabilized. However, the goal of double dissipation rate is not achieved, showing the inherent non-robustness (in terms of degree of stabilization) of this controller.

1 Introduction

The basic concepts of feedback control of plane, Poiseuille flow were laid out in [2]. In [2], it was shown that the governing Navier-Stokes equations can be converted to control-theoretic transfer function and state space models using a numerical discretization method. Using the transfer function models, it was shown that plane Poiseuille flow (channel flow) can be stabilized using a simple, constant gain feedback, integral compensator controller. The goal of the control design in [2] was stability. By choosing proper sensor locations, we were able to achieve a stable, closed loop system that was extremely robust to changing Reynolds numbers. The goal of the present paper is to design an optimal controller by moving away from classical transfer function control design to modern, state space methods. State space control methods have several advantages. State space methods allow straightforward design of controllers for multiple-input/multiple-output systems. Furthermore, state space and optimal control methods allow far greater control of the position of closed loop eigenvalues. In the transfer function design used thus far, the system was stabilized, but the stable system still had closed loop eigenvalues very near the imaginary s axis. This translated to very slow dissipation of perturbation energy. The goal of the present paper is to design an optimal, stabilizing controller that constrains the controllable and observable closed loop poles to be farther to the left of the imaginary s axis, thus leading to faster dissipation of perturbation

energy.

The increased flexibility of state space methods does not come without cost. Unlike the simple integral feedback control of [2], optimal controllers are complicated systems in themselves. This adds considerably to the complexity of the overall closed loop system. In fact, many beneficial qualities have been proven assuming the dimension of the controller is the same as that of the plant. In the flow case, this brings a special problem since the plant is of infinite dimension. Theoretically, the controller must also be of infinite dimension. This is impractical for many reasons. First, it is impossible to physically implement an infinite-dimensional controller. Secondly, the use of even very high-order finite-dimensional plants leads to numerical problems in the optimal control synthesis equations. As a result, we will design an optimal controller using a reduced-order model of the infinite-dimensional plant and then apply the resulting controller to a full-order plant. However, applying reduced order controllers to full order plants has the risk of making unmodelled, stable parts of the plant unstable. Therefore, controllers must be designed to ensure this does not happen. Furthermore, LQG controllers have been shown to be very non-robust [3] in many applications. We will provide one example investigating robustness in the channel flow case.

This paper is organized as follows. In section 2, the linear channel flow problem, state-variable control models, and the single-wavenumber flow model are reviewed. This section is essentially a review of those contained in [2]. In section 3, linear quadratic Gaussian (LQG) controller design is introduced and ways in which closed loop eigenvalues can be made stable to a prescribed degree is shown. Section 4 explains how the unavoidable unmodelled dynamics of any reduced order model of an infinite-dimensional plant can lead to closed loop instability in LQG design. Distributed actuation and distributed sensing are shown to be dual solutions to the stability problem. Section 5 demonstrates the performance of high-order optimal controllers. Section 6 presents the concept of a sub-optimal, extremely low-order controller design that achieves comparable performance to the high-order optimal controller design. Finally, the synthesized controller is used on a plant of different Reynolds numbers to investigate robustness.

2 The Linear Channel Flow Control Problem

2.1 Dynamic Equations

We consider the same plant as in [2], i.e. two-dimensional, plane, Poiseuille flow between two parallel, stationary plates. Let the channel be of finite length and finite height, with the centerline at zero. The flow in the channel is described by the unsteady, non-linear, incompressible Navier-Stokes equations. In order to study the linear stability of the system, we follow the standard procedure. Consider small perturbations in the velocities of $\hat{u}(x, y, t)$ in the horizontal direction, $\hat{v}(x, y, t)$ in the vertical direction, and $\hat{p}(x, y, t)$ in the pressure field. Let the primary flow be represented by $U(y)$ with U_c being the centerline velocity. The linearized, incompressible Navier-Stokes equations may be formed by substituting the primary flow and small perturbations into the non-linear, incompressible Navier-Stokes equations and disregarding the second-order terms involving the perturbations,

$$\frac{\partial \hat{u}(x, y, t)}{\partial t} + U(y) \frac{\partial \hat{u}(x, y, t)}{\partial x} + \frac{dU(y)}{dy} \hat{v}(x, y, t) = -\frac{\partial \hat{p}(x, y, t)}{\partial x} + \frac{1}{Re} \nabla^2 \hat{u}(x, y, t) \quad (1)$$

$$\frac{\partial \hat{v}(x, y, t)}{\partial t} + U(y) \frac{\partial \hat{v}(x, y, t)}{\partial x} = -\frac{\partial \hat{p}(x, y, t)}{\partial y} + \frac{1}{Re} \nabla^2 \hat{v}(x, y, t) \quad (2)$$

$$\frac{\partial \hat{u}(x, y, t)}{\partial x} + \frac{\partial \hat{v}(x, y, t)}{\partial y} = 0 \quad (3)$$

where the flow variables are non-dimensionalized by the channel half-height, H , and centerline velocity, U_c . Re is the Reynolds number defined as $(U_c H / \nu)$ where ν is the kinematic viscosity. By introducing a “stream function”, $\psi(x, y, t)$,

$$\hat{u}(x, y, t) \triangleq \frac{\partial \psi(x, y, t)}{\partial y} \quad (4)$$

and

$$\hat{v}(x, y, t) \triangleq -\frac{\partial \psi(x, y, t)}{\partial x} \quad (5)$$

(1- 3) may be combined into a single equation,

$$\frac{\partial}{\partial t} \frac{\partial^2 \psi}{\partial x^2} + \frac{\partial}{\partial t} \frac{\partial^2 \psi}{\partial y^2} = -U(y) \frac{\partial^3 \psi}{\partial x^3} - U(y) \frac{\partial}{\partial x} \frac{\partial^2 \psi}{\partial y^2} + \frac{d^2 U(y)}{dy^2} \frac{\partial \psi}{\partial x} + \frac{1}{Re} \nabla^2 (\nabla^2 \psi) \quad (6)$$

Assume periodic boundary conditions in the streamwise (x) direction. For channel flow, with rigid plates at $y = -1$ and $y = 1$ the no-slip boundary conditions become,

$$\psi(x, y = -1, t) = 0 \quad (7)$$

$$\frac{\partial \psi}{\partial y}(x, y = -1, t) = 0 \quad (8)$$

$$\psi(x, y = 1, t) = 0 \quad (9)$$

$$\frac{\partial \psi}{\partial y}(x, y = 1, t) = 0 \quad (10)$$

With an initial condition,

$$\psi(x, y, t = 0) = g(x, y) \quad (11)$$

the boundary value problem is completely formed. Equations (6-11) represent the starting point for construction of a feedback control system. These equations neither include any control terms nor do they describe any sensing of flow field variables.

2.2 Boundary Input

We consider the case of blowing/suction at the lower wall of the channel. The boundary conditions are now modified from before to include boundary input, represented as the *known* separable function $q(t)l(x)f(y)$,

$$\psi(x, y = -1, t) = q(t)l(x)f(y = -1) \quad (12)$$

$$\frac{\partial \psi}{\partial y}(x, y = -1, t) = q(t)l(x)\frac{\partial f(y = -1)}{\partial y} = 0 \quad (13)$$

$$\psi(x, y = 1, t) = 0 \quad (14)$$

$$\frac{\partial \psi}{\partial y}(x, y = 1, t) = q(t)l(x)\frac{\partial f(y = 1)}{\partial y} = 0 \quad (15)$$

Note that these conditions constrain the function $f(y)$ such that

$$f(y = -1) \neq 0 \quad (16)$$

$$\frac{\partial f(y = -1)}{\partial y} = 0 \quad (17)$$

$$f(y = 1) = 0 \quad (18)$$

$$\frac{\partial f(y=1)}{\partial y} = 0 \quad (19)$$

Many functions may be appropriate. One such function is

$$f(y) = \frac{1}{2}y^4 + \frac{1}{4}y^3 - y^2 - \frac{3}{4}y + 1 \quad (20)$$

In order to relate boundary conditions on ψ to blowing/suction in the wall-normal direction, we use (5) to relate $\hat{v}(x, y, t)$ and $\psi(x, y, t)$. Then (12) becomes

$$\hat{v}(x, y = -1, t) = -q(t) \frac{\partial l(x)}{\partial x} f(y = -1) \quad (21)$$

Note that $\hat{v}(x, y, t)$ is related to the *derivative* of $l(x)$.

The homogeneous equation (6) and the inhomogeneous boundary condition (12) can be converted into an inhomogeneous equation with homogeneous boundary conditions by introducing

$$\phi(x, y, t) \triangleq \psi(x, y, t) - q(t)f(y)l(x) \quad (22)$$

Then by substituting into (6), we obtain

$$\begin{aligned} \frac{\partial}{\partial t} \frac{\partial^2 \phi}{\partial x^2} + \frac{\partial}{\partial t} \frac{\partial^2 \phi}{\partial y^2} &= -U(y) \frac{\partial^3 \phi}{\partial x^3} - U(y) \frac{\partial}{\partial x} \frac{\partial^2 \phi}{\partial y^2} + \frac{d^2 U(y)}{dy^2} \frac{\partial \phi}{\partial x} + \frac{1}{Re} \frac{\partial^4 \phi}{\partial x^4} + 2 \frac{1}{Re} \frac{\partial^2}{\partial x^2} \frac{\partial^2 \phi}{\partial y^2} + \frac{1}{Re} \frac{\partial^4 \phi}{\partial y^4} - \\ \frac{\partial q(t)}{\partial t} \frac{\partial^2 l(x)}{\partial x^2} f(y) - \frac{\partial q(t)}{\partial t} l(x) \frac{\partial^2 f(y)}{\partial y^2} - q(t) \frac{\partial^3 l(x)}{\partial x^3} U(y) f(y) - q(t) \frac{\partial l(x)}{\partial x} U(y) \frac{\partial^2 f(y)}{\partial y^2} + \\ q(t) \frac{\partial l(x)}{\partial x} \frac{d^2 U(y)}{dy^2} f(y) + \frac{1}{Re} q(t) \frac{\partial^4 l(x)}{\partial x^4} f(y) + 2 \frac{1}{Re} q(t) \frac{\partial^2 l(x)}{\partial x^2} \frac{\partial^2 f(y)}{\partial y^2} + \frac{1}{Re} q(t) l(x) \frac{\partial^4 f(y)}{\partial y^4} \end{aligned} \quad (23)$$

The boundary conditions in terms of ϕ are now

$$\phi(y = -1) = 0 \quad (24)$$

$$\frac{\partial \phi(y = -1)}{\partial y} = 0 \quad (25)$$

$$\phi(y = 1) = 0 \quad (26)$$

$$\frac{\partial \phi(y = 1)}{\partial y} = 0 \quad (27)$$

The first line of (23) is the original dynamical equation, (6), and the next two lines are all known input terms.

2.3 Boundary Output

We use the streamwise component of shear at a single boundary point, $z(x_i, y = -1, t)$, as our boundary output, which is given by

$$z(x_i, y = -1, t) = \frac{\partial \hat{u}(x_i, y = -1, t)}{\partial y} \quad (28)$$

By expressing $\hat{u}(x_i, y = -1, t)$ in terms of the stream function (4),

$$z(x_i, y = -1, t) = \frac{\partial^2 \psi(x_i, y = -1, t)}{\partial y^2} \quad (29)$$

and by observing (22)

$$z(x_i, y = -1, t) = \frac{\partial^2 \psi(x_i, y = -1, t)}{\partial y^2} = \frac{\partial^2 \phi(x_i, y = -1, t)}{\partial y^2} + q(t) \frac{\partial^2 f(y = -1)}{\partial y^2} l(x_i) \quad (30)$$

2.4 State Variable Control-Theoretic Models

Much of modern control theory is based on the state variable representation of a dynamic system. This representation relies on the basic fact that the motion of any finite-dimensional, dynamic system may be expressed as a set of first-order, ordinary-differential equations in matrix form,

$$\frac{dx}{dt} = Ax + Bq \quad (31)$$

$$z = Cx \quad (32)$$

The vector x is called the state-vector of the system, q is the input variable, and z is the output variable. The matrix A , and the vectors B and C are called the state space matrices of the single-input, single-output (SISO) system. More specifically, the A matrix is referred to as the dynamic matrix of the system. It can be shown that the poles of the system are simply the eigenvalues of the A matrix. In the more general case of multiple-input, multiple-output (MIMO) systems, B and C are matrices. For generality, we may add another term, Dq , to the output equation to account for systems in which there is direct feedthrough from the input to the output. Then,

$$z = Cx + Dq \quad (33)$$

In the case of no direct feedthrough, $D = 0$, the state space and transfer function models are related as

$$H(s) \triangleq \frac{Z(s)}{Q(s)} = \frac{\prod_{j=1}^J (s - \zeta_j)}{\prod_{i=1}^I (s - p_i)} = C(sI - A)^{-1}B \quad (34)$$

where $p_1 \dots p_I$ are the *poles* of the system and $\zeta_1 \dots \zeta_J$ are the *zeros* of the system.

It is important to note that the channel flow problem is defined by partial differential equations and therefore, no finite-dimensional model will capture all its dynamics. Therefore, any finite-dimensional controller synthesized from any finite-dimensional model may cause unmodelled dynamics to become unstable. This issue will be taken up in section 4.

2.5 Single Wavenumber Model

We consider the periodic channel model shown in figure 1 with boundary blowing/suction and boundary shear measurement. The Reynolds number considered is $Re = 10,000$. The

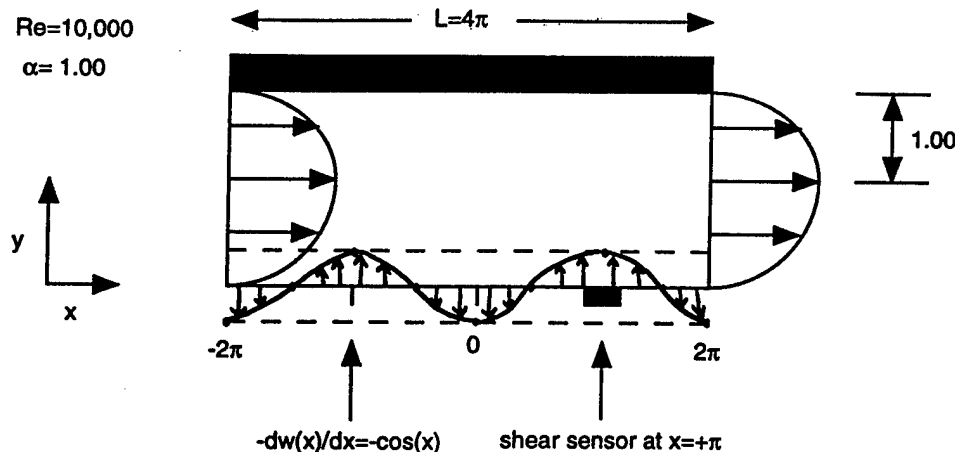


Figure 1: System model for Poiseuille channel flow. The flow is periodic with the period of 4π . Input is applied along bottom plate as $w(x) = \sin(x)$ and shear is measured at π . $Re = 10,000$.

total length of the channel is $L = 4\pi$ leading to fundamental wavenumber, $\alpha_0 = 0.5$, see [4]. Recall, only integral multiples of this fundamental wavenumber may exist in the periodic

channel. For the single wavenumber model, only one wavenumber is included in the model, corresponding to $\alpha = l\alpha_0 = 1.00$. This wavenumber is selected since it is the only wavenumber that leads to unstable modes for this channel geometry as can be seen from the linear stability curve of the Orr-Sommerfeld equation.

Input is distributed along the entire bottom plate with a sinusoidal weighting function. In terms of the input function, $w(x)$, (12)

$$w(x) = \sin(x) \quad (35)$$

This type of distributed input has very favorable properties. It will be shown in section 4 that a distributed input of this type leads to a system in which all modes are *uncontrollable* except those associated with the wavenumber of $w(x)$. In this case, the wavenumber of, $w(x) = \sin(1.0x)$, is $\alpha = 1.0$. Therefore, all modes resulting from all wavenumbers other than 1.0 are uncontrollable. This will allow us to consider only those poles and zeros associated with $\alpha = 1.0$ since the control will affect these modes only. Note that the physical blowing/suction, $\hat{v}(x, y, t) = -q(t)\frac{\partial w(x)}{\partial x}f(y = -1) = -q(t)\cos(x)f(y = -1)$, (21). The $f(y)$ function in the input is chosen as in (20). Exactly as in [2], a state variable model is created of this system. In order to visualize the control theoretic model, the A , B , and C matrices are transformed to transfer function form, $H(s)$; see (34). In [2] it was shown that the A matrix can be block decomposed by wavenumbers included and not included in the model. Figure 2 shows the locations of the poles and zeros in the s plane for the channel flow system of figure 1. The

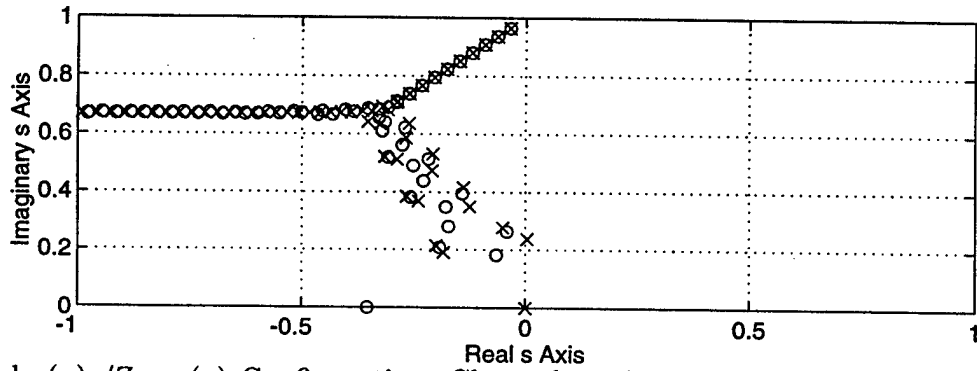


Figure 2: Pole (x) /Zero (o) Configuration, Channel model: $Re = 10,000$, shear sensor at π , $w(x) = \sin(x)$, $L=4\pi$, $\alpha = 1.0$. Only the top half of the s plane is shown.

numerical verification of these poles and zeros was described in [2].

3 Linear Quadratic Optimal Control Design

In order to design an optimal controller, the first step is to define in what sense the controller is optimal. Consider the standard finite-dimensional state space formulation, derived for the channel flow problem in [2] and shown in transfer function form in Figure 1,

$$\frac{dx(t)}{dt} = Ax(t) + Bu(t) \quad (36)$$

$$z(t) = Cx(t) \quad (37)$$

$$x_0 \triangleq x(t=0) \quad (38)$$

where the state vector $x(t)$ is $(n \times 1)$, the input vector $u(t)$ is (1×1) , the output vector, $z(t)$, is (1×1) , the dynamic matrix, A , is $(n \times n)$, the input influence matrix, B , is $(n \times 1)$, and the output influence matrix, C , is $(1 \times n)$. In optimal control design, an optimal controller is defined as a controller which produces an input signal, $u(t)$, that minimizes a cost functional $J(u)$ such that

$$J(u_{opt}) \leq J(u) \quad \forall u(\cdot) \in \mathcal{U} \triangleq \{u(\cdot) : u(\cdot) \text{piecewise-continuous, } \int_0^T \|u(t)\|^2 dt < \infty\} \quad (39)$$

In the following, we will assume that the model of (36)-(38) is reduced by removing all uncontrollable and unobservable modes. Therefore, (A, B) is controllable and (A, C) is observable in the reduced model.

3.1 Infinite Optimal Control Time Problem

Consider a cost functional

$$J(u) \triangleq \lim_{T \rightarrow \infty} \frac{1}{T} \int_0^T [Rx(t), x(t)] + [\Lambda u(t), u(t)] dt \quad (40)$$

where R is a semi-positive-definite matrix and Λ is a positive-definite matrix which are defined a-priori. The R matrix defines the penalty on the state and the Λ matrix defines penalty on the control. We may show that the optimal control is given by¹

$$u_{opt}(t) = -\Lambda^{-1} B^* P x(t) \quad (41)$$

¹In the following, $*$ will denote the complex conjugate transpose operation.

where the matrix, P , is given as the positive-definite solution of the algebraic Riccati equation (A.R.E.),

$$PA + A^*P - PBA\Lambda^{-1}B^*P + R = 0 \quad (42)$$

and B is the input influence matrix in the state space system (34). Consider the plant equation (36) with the optimal control (41) applied,

$$\frac{dx}{dt} = (A - B\Lambda^{-1}B^*P)x \quad (43)$$

The closed loop system is stable iff the eigenvalues of the matrix, $(A - B\Lambda^{-1}B^*P)$, are stable. It can be shown [5] if the pair (A, B) is controllable² and (A, R) is observable³, then there exists $P > 0$ such that

$$PA + A^*P - PBA\Lambda^{-1}B^*P + R = 0$$

for $R \geq 0$.

3.2 Prescribed Degree of Controller Stability

In order to achieve a prescribed degree of stability [5] with an optimal controller, consider the exponential cost functional

$$J(u) \triangleq \lim_{T \rightarrow \infty} \frac{1}{T} \int_0^T e^{2\gamma t} ([Rx(t), x(t)] + [\Lambda u(t), u(t)]) dt \quad (44)$$

where the matrix R is again semi-positive-definite, Λ is again positive-definite and defined a-priori and γ is a positive scalar. We may show [5] that we may convert this problem into a quadratic form and solve for a controller that prescribes all eigenvalues of the closed loop system to be to the left of $s = -\gamma$. Rewrite the cost functional as

$$J(u) = \lim_{T \rightarrow \infty} \frac{1}{T} \int_0^T [Re^{\gamma t}x(t), e^{\gamma t}x(t)] + [\Lambda e^{\gamma t}u(t), e^{\gamma t}u(t)] dt \quad (45)$$

²A system is said to be controllable if and only if it is possible, by means of the input, to transfer the system from any initial state $x(t) = x_i$ to any other state $x_T = x(T)$ in a finite time $T - t \geq 0$. For a linear, time invariant system described in state space, the system is controllable if its controllability grammian, given by $P(T) = \int_0^T e^{At} B B^* e^{A^* t} dt$ is invertable. [6]

³An unforced system is said to be observable if and only if it is possible to determine any (arbitrary initial) state $x(t) = x_i$ by using only a finite record, $z(\tau)$ for $t \leq \tau \leq T$, of the output. For a linear, time invariant system described in state space, the system is observable if its observability grammian, given by $M(T) = \int_0^T e^{A^* t} C^* C e^{At} dt$ is invertable. [6]

Define

$$\overline{x(t)} \triangleq e^{\gamma t} x(t) \quad (46)$$

and

$$\overline{u(t)} \triangleq e^{\gamma t} u(t) \quad (47)$$

Then

$$J(\overline{u}) = \lim_{T \rightarrow \infty} \frac{1}{T} \int_0^T [R\overline{x}, \overline{x}] + [\Lambda\overline{u}, \overline{u}] dt \quad (48)$$

Note

$$\frac{d\overline{x(t)}}{dt} = \frac{d}{dt}(e^{\gamma t} x(t)) = \gamma e^{\gamma t} x(t) + e^{\gamma t} \frac{dx(t)}{dt} \quad (49)$$

By substituting for $\frac{dx(t)}{dt}$,

$$\frac{d\overline{x}}{dt} = (A + I\gamma)\overline{x} + B\overline{u} \quad (50)$$

Let $\overline{A} \triangleq A + I\gamma$. Then the optimal control is given by

$$\overline{u_{opt}}(t) = -\Lambda^{-1} B^* \overline{P} \overline{x}(t) \quad (51)$$

and

$$u_{opt}(t) = -\Lambda^{-1} B^* \overline{P} x(t) \quad (52)$$

where \overline{P} is obtained by solving the Riccati equation

$$\overline{P}\overline{A} + \overline{A}^* \overline{P} - \overline{P}B\Lambda^{-1}B^* \overline{P} + R = 0 \quad (53)$$

The new closed loop system dynamics matrix becomes

$$A - B\Lambda^{-1}B^* \overline{P} \quad (54)$$

whose eigenvalues are all to the left of $s = -\gamma$. It can be shown [4] that if (A, B) is controllable and (A, R) is observable, then $(A + \gamma I, B)$ is controllable and there exists a positive definite solution, \overline{P} , of the matrix Riccati equation (53) for $R \geq 0$.

In theory, for full order plant models, there is no restriction on the value of γ . In practice, however, for controllers built using reduced order plant models, γ is limited by robustness of the controller when applied to the full order system.

3.3 Optimal Estimator Design

In the previous subsections, we derived an optimal controller. As can be seen from equation (41), the control is always represented in terms of the current state, $x(t)$. These states, however, are not available to us in the channel problem. Instead, we have access to shear measurements at only one or several locations along the boundary. Therefore, we must construct an observer to estimate the state, $x(t)$, from the measured shear outputs, $z(t)$. In order to see how this is done, consider a slightly more complicated version of the state space model shown earlier

$$\frac{dx(t)}{dt} = Ax(t) + Bu(t) + v(t) \quad (55)$$

$$z(t) = Cx(t) + w(t) \quad (56)$$

$$x_0 \triangleq x(t=0) \quad (57)$$

where (A, B) is again assumed controllable and (A, C) is again assumed observable. The variables $v(t)$ and $w(t)$ are Gaussian, white process and measurement noises, respectively. They are stochastic variables at any given time. As a result of their inclusion in the system model, the state, $x(t)$, and the measurement, $z(t)$, become stochastic processes that may be analyzed only in terms of probability.

Assumption 1 *The noise processes $v(t)$ and $w(t)$ are white, Gaussian, of zero mean, independent of each other, and have known covariances. The matrices P_0 , Q_e , and W_e are positive-definite.*

$$E[v(t)v^*(\tau)] = Q_e \delta(t - \tau) \quad E[v(t)] = 0$$

$$E[w(t)w^*(\tau)] = W_e \delta(t - \tau) \quad E[w(t)] = 0$$

$$E[x(t_0)] = m$$

$$E([x(t_0) - m][x(t_0) - m]^*) = P_0$$

where $E(\cdot)$ is an expectation operator.

It may be shown that a steady state estimator may be constructed that minimizes the error covariance between the actual state, $x(t)$, and the estimated state, $\hat{x}(Z_t)$, where $Z_t = \{z(l) :$

$-\infty < l \leq t\}$, i.e. the measurement history.

$$\hat{x}(Z_t) \stackrel{\min}{=} E([x(t) - \hat{x}(Z_t)][x(t) - \hat{x}(Z_t)]^*) \quad (58)$$

It can be shown [7] that the optimal estimate, in the sense of (58), is given by the conditional expectation

$$\hat{x}(t) \triangleq \hat{x}(Z_t) = E(x(t)/Z_t) \quad (59)$$

where $E(\cdot/Z_t)$ is the conditional mean operator. In the linear case with Gaussian noises, the structure of the estimator is

$$\frac{d\hat{x}(t)}{dt} = A\hat{x}(t) + Bu(t) + K_e(C\hat{x}(t) - z(t)) \quad (60)$$

where

$$K_e = -P_e C^* W_e^{-1} \quad (61)$$

and P_e is calculated from a matrix Riccati equation

$$P_e A^* + A P_e - P_e C^* W_e^{-1} C P_e + Q_e = 0 \quad (62)$$

Note that the stability of (60) depends on the stability of $(A - P_e C^* W_e^{-1} C)$. The assumptions that $W_e, Q_e > 0$ and (A, C) observable assure $\exists P_e > 0$ such that (62) is satisfied.

3.4 Prescribed Degree of Estimator Stability

By considering a slightly different estimator Riccati equation, we may constrain the closed loop estimator poles to be stable to a prescribed degree. It can be shown [4] that if (A, C) is observable, then $(A + \gamma I, C)$ is observable and there exists a positive definite solution of the matrix Riccati equation

$$\overline{P}_e (A + \gamma I)^* + (A + \gamma I) \overline{P}_e - \overline{P}_e C^* W_e^{-1} C \overline{P}_e + Q_e = 0$$

for $Q_e > 0$, where γ is a real, positive scalar. Then all eigenvalues of $(A - \overline{P}_e C^* W_e^{-1} C)$ are all to the left of $s = -\gamma$.

3.5 Separation Principle in LQG Control

The goal of linear quadratic Gaussian (LQG) design is to combine the results of deterministic linear quadratic control theory and stochastic estimation theory to form an overall control system. As we have seen, our system equations become stochastic with the addition of noise terms. Therefore, in our controller design, we may no longer minimize a deterministic cost functional. Rather, we now minimize the expected value of the cost functional,

$$E(J) = E \left(\lim_{T \rightarrow \infty} \frac{1}{T} \int_0^T [Rx(t), x(t)] + [\Lambda u(t), u(t)] dt \right) \quad (63)$$

where $x(t)$ is now a stochastic process. It can be shown that the optimal control is now expressed in terms of the estimated state,

$$u_{opt}(t) = -\Lambda^{-1} B^* P \hat{x}(t) \quad (64)$$

The complete LQG solution is then

$$\frac{dx(t)}{dt} = Ax(t) + Bu(t) + v(t) \quad \text{plant} \quad (65)$$

$$z(t) = Cx(t) + w(t) \quad \text{observation} \quad (66)$$

$$x_0 \triangleq x(t=0) \quad \text{initial condition} \quad (67)$$

$$\frac{d\hat{x}(t)}{dt} = A\hat{x}(t) + Bu(t) + K_e(C\hat{x}(t) - z(t)) \quad \text{estimator} \quad (68)$$

$$u_{opt}(t) = -\Lambda^{-1} B^* P \hat{x}(t) \quad \text{feedback} \quad (69)$$

where P is the positive-definite solution of (42) and K_e is given in (61).

We may show that the overall estimator/controller system is stable by stacking the state, $x(t)$, and the error, $e(t) \triangleq \hat{x} - x$, into one vector and studying the dynamics of the new system.

$$\begin{bmatrix} \frac{dx(t)}{dt} \\ \frac{de(t)}{dt} \end{bmatrix} = \begin{bmatrix} (A - B\Lambda^{-1}B^*P) & -B\Lambda^{-1}B^*P \\ 0 & (A - P_eC^*W_e^{-1}C) \end{bmatrix} \begin{bmatrix} x(t) \\ e(t) \end{bmatrix} + \begin{bmatrix} v(t) \\ -K_e w(t) - v(t) \end{bmatrix} \quad (70)$$

The stability of the system is determined by the eigenvalues of the dynamical matrix. Clearly, the eigenvalues are comprised of the eigenvalues of the closed loop controller, $(A - B\Lambda^{-1}B^*P)$ and the eigenvalues of the closed loop estimator, $(A - P_eC^*W_e^{-1}C)$. We have already proven

that both of these matrices are stable (under appropriate assumptions). Therefore, the overall control system is stable also. This is known as the separation principle in LQG control.

4 Effects of Unmodelled Wavenumber Dynamics on the LQG Problem

We have already seen that the separation principle in LQG control allows us to show that if the controller and estimator are both stable, then the overall system is stable. We will see in this section that this principle breaks down in the presence of unmodelled dynamics.

As described in [2] , any finite-dimensional model is a reduced-order model for the infinite-dimensional channel flow problem. In terms of poles and zeros studied earlier, more poles and zeros exist in the system than are accounted for in the model and the subsequent controller design. It is easy to imagine that an unmodelled pole could be drawn to the unstable s plane by a reduced-order controller. As a result, even though the designed controller may stabilize the reduced-order plant, it may not stabilize the actual infinite-dimensional plant. Consider the following partition of the state space model with noise terms added

$$\frac{dx}{dt} = \begin{bmatrix} \frac{dx_m}{dt} \\ \frac{dx_u}{dt} \end{bmatrix} = \begin{bmatrix} A_m & 0 \\ 0 & A_u \end{bmatrix} \begin{bmatrix} x_m \\ x_u \end{bmatrix} + \begin{bmatrix} B_m \\ B_u \end{bmatrix} u(t) + \begin{bmatrix} v_m(t) \\ v_u(t) \end{bmatrix} \quad (71)$$

$$z = \begin{bmatrix} C_m & C_u \end{bmatrix} x + w(t) \quad (72)$$

where the subscripts m and u represent the modelled and unmodelled parts of the system. The process noise, v , and the measurement noise, w , are assumed to be Gaussian, independent, zero mean, white noise processes such that

$$E[v(t)v^*(\tau)] = Q_e \delta(t - \tau) \quad (73)$$

$$E[w(t)w^*(\tau)] = W_e \delta(t - \tau) \quad (74)$$

The unmodelled part is meant to denote only the dynamics of wavenumbers left out of the reduced order model. A_u is assumed stable. Recall [2] that both A_u and A_m are of

infinite dimension; A_u because of the infinite number of wavenumbers left out of the reduced order model and A_m because of the infinite number of poles for each of the finite number of modelled wavenumbers.

Since we only know the modelled part of the system, we design an LQG controller/observer based on that part. Minimize the expected value of a cost functional, J ,

$$E(J) = E \left(\lim_{T \rightarrow \infty} \frac{1}{T} \int_0^T [Rx_m(t), x_m(t)] + [\Lambda u(t), u(t)] dt \right) \quad (75)$$

where R is any semi-positive definite matrix and Λ is any positive definite matrix. The optimal control is of the form

$$u_{opt}(t) = -\Lambda^{-1} B^* P \hat{x}_m(t) \quad (76)$$

where $\hat{x}_m(t)$ is the estimate of the modelled state and the matrix, P , is calculated by solving the algebraic Riccati equation

$$A_m^* P + P A_m - P B_m \Lambda^{-1} B_m^* P + R = 0 \quad (77)$$

assuming the same assumptions as in (65)-(69) for the modeled parts.

Since we cannot obtain direct measurements of the current state, $x_m(t)$, we construct an observer as described earlier

$$\frac{d\hat{x}_m(t)}{dt} = A_m \hat{x}_m(t) + B_m u(t) + K_e (C_m \hat{x}_m(t) - z(t)) \quad (78)$$

where the estimator gain

$$K_e = -P_e C_m^* W_e^{-1} \quad (79)$$

requires the solution of another matrix Riccati equation

$$P_e A_m^* + A_m P_e - P_e C_m^* W_e^{-1} C_m P_e + Q_e = 0 \quad (80)$$

where Q_e and W_e are the power spectral densities of the process and measurement noises of the modelled modes.

Define the error between the estimated, modelled state, $\hat{x}_m(t)$, and the actual state, $x_m(t)$, as $e_m(t)$. Then as in [8]

$$\frac{de_m(t)}{dt} \triangleq \frac{d\hat{x}_m(t)}{dt} - \frac{dx_m(t)}{dt} =$$

$$\begin{aligned}
& [A_m - P_e C_m^* W_e^{-1} C_m] e_m(t) + P_e C_m^* W_e^{-1} C_u x_u(t) \\
& + P_e C_m^* W_e^{-1} w - v_m
\end{aligned} \tag{81}$$

where the unmodelled state acts as a forcing term.

In order to study the entire controller/observer system, stack the modelled state, the modelled error, and the unmodelled state and consider the dynamics of the stacked system (82).

$$\begin{bmatrix}
\frac{dx_m}{dt} \\
\frac{de_m}{dt} \\
\frac{dx_u}{dt}
\end{bmatrix} = \begin{bmatrix}
(A_m - B_m \Lambda^{-1} B_m^* P) & -B_m \Lambda^{-1} B_m^* P & 0 \\
0 & (A_m - P_e C_m^* W_e^{-1} C_m) & P_e C_m^* W_e^{-1} C_u \\
-B_u \Lambda^{-1} B_m^* P & -B_u \Lambda^{-1} B_m^* P & A_u
\end{bmatrix} \begin{bmatrix}
x_m \\
e_m \\
x_u
\end{bmatrix} + \begin{bmatrix}
v_m \\
-K_e w - v_m \\
v_u
\end{bmatrix} \tag{82}$$

From the LQG theory of the past sections,

$$(A_m - B_m \Lambda^{-1} B_m^* P)$$

and

$$(A_m - P_e C_m^* W_e^{-1} C_m)$$

are stable. However, from (82), the overall system may not be stable due to the unmodelled actuator influence, B_u , and sensor influence, C_u , matrices. Therefore, we have seen that in the LQG framework, we cannot insure overall stability unless the unmodelled parts of the system are accounted for.

There are two ways to ensure system (82) is stable, assuming $A_m + B_m K C_m$ and A_u are stable. One way is to ensure $B_u = 0$, i.e., make sure the unmodelled dynamics are uncontrollable with respect to the actuator. The other way to ensure a stable system is to assure $C_u = 0$, i.e., make sure the unmodelled dynamics are unobservable with respect to the sensor. Controllability and observability for the plane, Poiseuille flow problem were introduced in [2]. We now explore how we may achieve these conditions.

4.1 Point Actuation vs. Distributed Actuation

One way to guarantee the overall system (82) is stable is to assure all modes associated with unmodelled wavenumbers are uncontrollable with respect to the input by making $B_u = 0$. In the fully developed channel flow system, this would account for the wavenumbers left out of the reduced-order model. If

$$w(x) \triangleq \text{Real} \left(\sum_{n=-N}^N e^{in\alpha_0 x} \right) \quad (83)$$

where the n range corresponds to the modelled wavenumbers only, then the projection of $w(x)$ onto unmodelled wavenumbers is zero due to the orthogonality of Fourier components. As a result, $B_u = 0$ and stability of unmodelled dynamics is retained. Note that since $w(x) \neq 0$ for all but a finite number of points in the x direction, this type of scheme is a distributed actuation scheme. Therefore, by moving from a physically easier to implement “point” actuator to a more difficult distributed actuator, we have retained stability of the unmodelled dynamics. Physically, a distributed actuator is obtained by a large number of independently programmable actuators placed along the lower wall. Constraining $w(x)$ to be composed of modelled wavenumbers only, thus rendering $B_u = 0$, is manifested in the transfer function as pole/zero cancellation due to uncontrollable modes. Figure 3 shows the poles and zeros for a two wavenumber model, $\alpha = 0.5$ and $\alpha = 1.0$. The input forcing function, $w(x)$, is $\sin(x)$. We see that all poles associated with $\alpha = 0.5$ are canceled by zeros. This signifies that the modes are uncontrollable. Indeed, all poles of all wavenumbers except $\alpha = 1.0$ are uncontrollable. If distributed actuation is infeasible or undesirable, we must look to the dual problem of sensing to gain stability.

4.2 Point Sensing vs. Distributed Sensing

It is seen from (82), that if $B_u \neq 0$, stability may still be maintained if $C_u = 0$. This corresponds to making all unmodelled wavenumber dynamics unobservable with respect to the shear sensor. Placing a single shear sensor at a point along the lower channel wall results in a measurement that includes the effects of all wavenumbers, both modelled and unmodelled. Clearly, $C_u \neq 0$, and stability is not guaranteed. This corresponds to the

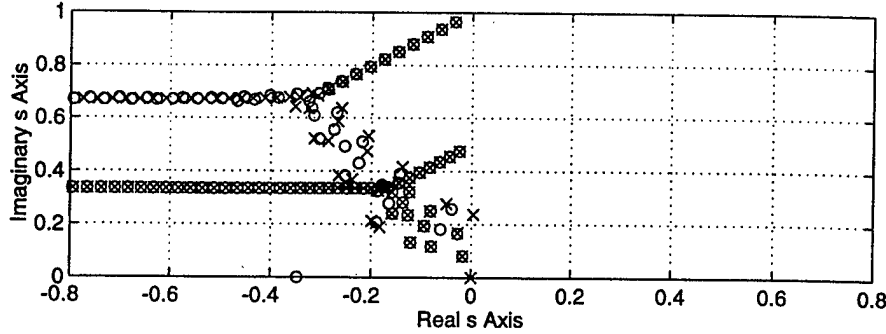


Figure 3: Pole (x) and zero (o) configuration of channel system of length 4π , including wavenumbers of 0.50 and 1.00; Channel model: $Re = 10,000$, shear sensor at π , $w(x) = \sin(x)$. Only the top half of the s plane is shown.

point forcing case in the dual problem of actuation. By using a distributed sensing scheme, however, we may form a new measurement that includes only the effects of the modelled wavenumbers. This is done by projecting a distributed shear function, $z(x, y = -1, t)$, onto the modelled wavenumbers. The distributed shear function, $z(x, y = -1, t)$ is physically created by measuring the shear at all points along the lower channel wall. Then a new projected shear measurement, denoted $\tilde{z}(t)$, is defined as

$$\tilde{z}(t) \triangleq \text{Real}[z(x, y = -1, t)], \sum_{n=-N}^N e^{in\alpha_0 x}]_x \quad (84)$$

where again the n range corresponds to modelled wavenumbers only. Note that just as in the actuator case, we have implemented a more physically complicated series of sensors in order to achieve overall stability.

In terms of modeling, we need not include either unobservable or uncontrollable modes in our plant models. Therefore, distributed actuation or control allows models to be created using only a finite number of wavenumbers. Note, however, that even a single wavenumber model contains an infinite number of modes due to the infinite number of poles extending

out into the left hand s plane as shown in Figure 1 (see also [2]).

5 Control Design Using High Order Models

As we have seen in section 4, we may reduce the problem of including an infinite number of wavenumbers in a reduced-order model to a problem of including a finite number of wavenumbers by using distributed actuation or sensing. However, even with a model containing only a finite number of wavenumbers, the problem is still infinite-dimensional because of the infinite number of poles extending into the left hand s plane for *each* wavenumber. Furthermore, we do not know the exact position of poles far into the left hand s plane due to the finite number of basis functions used in the y direction [4]. Still, these poles must be accounted for in the control design. As we shall see, the fact that uncertain poles appear only at higher frequencies in the bandwidth will be advantageous. It will allow a robust controller to be designed that “rolls off” at high frequencies. Just as in [5], consider the control loop shown in figure 4. Using the same notation as in [5],

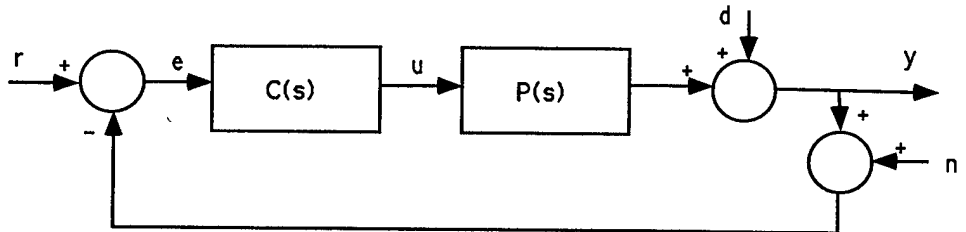


Figure 4: Feedback control loop. $P(s)$ represents the plant and $C(s)$ represents the controller in the frequency domain. This figure taken from [5].

- $r \triangleq$ external (reference) input
- $e \triangleq$ measured tracking error
- $u \triangleq$ plant input
- $y \triangleq$ plant output

- $d \triangleq$ disturbance signal
- $n \triangleq$ measurement noise

Note that the reference input in the channel flow case is zero since we would like to suppress all output. The following relations hold for the closed loop system [5].

$$y = PC(I + PC)^{-1}(r - n) + (I + PC)^{-1}d \quad (85)$$

$$e = r - y - n = (I + PC)^{-1}(r - d) - (I + PC)^{-1}n \quad (86)$$

We assume that the closed loop system is stable. The quantity

$$S \triangleq (I + PC)^{-1} \quad (87)$$

is called the sensitivity function and the quantity

$$T \triangleq PC(I + PC)^{-1} \quad (88)$$

is called the complementary sensitivity function. Note

$$S + T = I \quad (89)$$

As can be seen from (86), for good tracking, $\| r - y \|$ small when d and n are zero, S should be small [5]. This corresponds to having a high gain at all frequencies. Similarly, as can be seen from (86), for good disturbance rejection, i.e. d affects y at little as possible, again S should be small [5]. On the other hand, for good output noise suppression, n affects y as little as possible, (85) shows that T should be small. This indicates that the gain should be *low* at all frequencies in which the noise enters [5]. It is generally assumed that noise is most destructive at higher frequencies. As a result, control design focuses on high gain at low frequencies where tracking and disturbance rejection are most important and low gain at high frequencies where noise is more of a problem.

In addition to noise at high frequencies, the other major problem at high frequencies is unmodelled dynamics. We have already pointed out that there are two types of unmodelled dynamics in the channel flow problem. The first type is unmodelled dynamics of unmodelled wavenumbers. We accounted for these dynamics through distributed control or distributed

sensing. The second type is unmodelled dynamics at high frequencies for modeled wavenumbers. This type of unmodelled dynamics has yet to be considered and is common to most infinite dimensional systems. To account for these dynamics, controllers are designed that give low gain at the high frequencies of the open-loop, controller/plant series where unmodelled dynamics exist in order not to stimulate modes at those frequencies. This is known as “roll-off”. Roll-off may be given a more analytic framework by considering multiplicative, unstructured uncertainty in the plant, P . Suppose that we are uncertain of the exact form of P . Assume that P can be perturbed to

$$P_N(s) = [I + N(s)]P(s) \quad (90)$$

This type of uncertainty is generally prescribed to unmodelled high frequency dynamics. It has been shown [9] that, in this case, T should be low in order to preserve closed loop stability. Again, this corresponds to “roll-off” of the open loop controller/plant series.

We now design an LQG controller and then observe the roll-off characteristics of the resulting system. In the following, γ will refer to the degree of closed loop stability in the both the LQ controller and the observer as shown in (44). R is the state weighting matrix in the LQ cost functional (75), Λ is the input weighting matrix in the LQ cost functional (75), Q_e is the power spectral density matrix of the process noise (62) , and W_e is the power spectral density matrix of the measurement noise matrix (62).

We consider the one wavenumber model shown in figure 1 with $Re = 10,000$. Only $\alpha = 1.0$ is included in the model. All other wavenumbers are uncontrollable due to the distributed input of $w(x) = \sin(x)$ as shown in section 4.1. A single point sensor is located at π . The length of the channel is 4π leading to a fundamental wavenumber of $\alpha_0 = \frac{1}{2}$. We consider two models in evaluating the resulting LQG controller as shown in table 1.

Model 1 contains all poles and zeros to the left of $s = -4$. Model 2 contains all observable and controllable poles and zeros to the right of $s = -2$. This model was created by using the *minreal* function within the *MATLAB Control Toolbox* [10] with the parameter value *tol*=1e-3. The *lqr* and *lqe2* functions of the *MATLAB Control Toolbox* were used to create an LQG controller using model 2 as the system model. The A matrix supplied to each of these *MATLAB* functions were modified to $(A + I\gamma)$ in order to achieve a prescribed degree

Models		
Number	Name	Poles/Zeros
1	high-order	253/251
2	slightly-reduced-order	141/139

Table 1: Models used in LQG controller design. Note that the difference in number of poles and zeros is dictated by truncation of the model in s space.

of stability as described in sections 3.2 and 3.4. The following parameters were used:

$$\gamma = -.08 \quad (91)$$

$$R = .001C^*C \quad (92)$$

$$\Lambda = I \quad (93)$$

$$Q_e = 10BB^* \quad (94)$$

$$W_e = 1 \quad (95)$$

The R matrix was chosen so as to minimize shear in the cost functional 63; the Q_e matrix was originally chosen to recover robustness properties using loop transfer recovery techniques [11]; γ , W_e , and Λ were chosen using trial and error.

In analyzing the resulting control system, consider the following model, figure 5. The

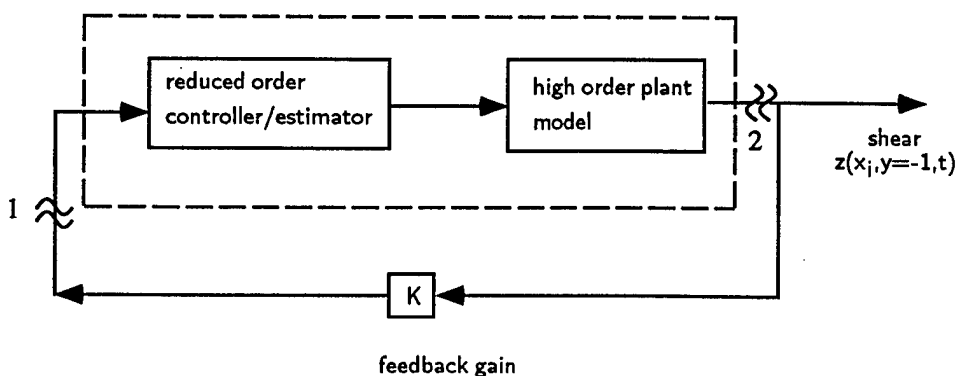


Figure 5: LQG control loop for high-order plant (model 1) and reduced order controller (obtained from model 2). The value of $K=1$ will lead to the optimal control.

optimal control is defined at $K = 1$ with a properly designed LQG controller. Figure 6 shows the high-order plant (model 1) used for validation. Figure 7 shows the slightly-reduced-order model (model 2). Figure 8 shows a series combination of the high-order plant (model 1) and the low-order *controller* obtained from the LQG design. Finally, figure 9 shows the root locus of the controller/estimator in series with the plant for gain values, K , varying from 0 to 4.

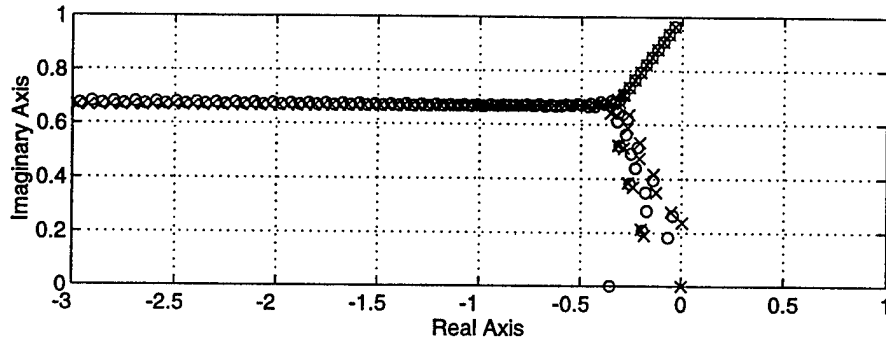


Figure 6: High-order plant (model 1) contains all poles and zeros to the right of $s = -4$. (Only poles/zeros to the right of $s = -3$ are shown.) Note many poles are either uncontrollable or unobservable as shown by pole/zero cancellations. These poles cannot be moved. We concentrate on moving only the observable/controllable poles.

From figure 9, we see that the poles of the closed loop system achieve the goal of being to the right of $s = -0.08$ with gain, $K = 1$. This represents placement of closed loop poles at approximately double the distance into the left hand plane than that achieved by the integral feedback control scheme of [2]. Finally, figure 10 shows the magnitude response for the open loop transfer function from point 1 on figure 5 to point 2. Note that the gain is higher at low frequencies and lower at higher frequencies. At $f = 1.0$, the magnitude response “rolls-off”. Ideally, we would like to see roll-off at a lower frequency. In this case, however, any energy input at frequencies above $f = 1$ did not hamper our stability goals.

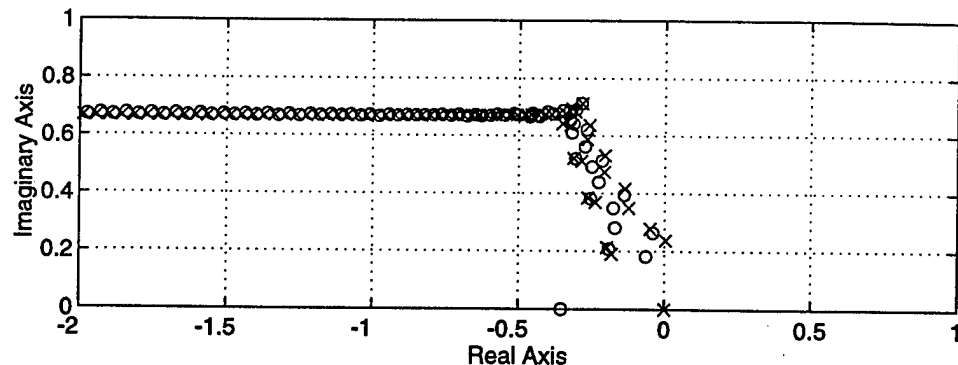


Figure 7: Reduced order plant used for LQG design. This model contains only controllable and observable poles and zeros.

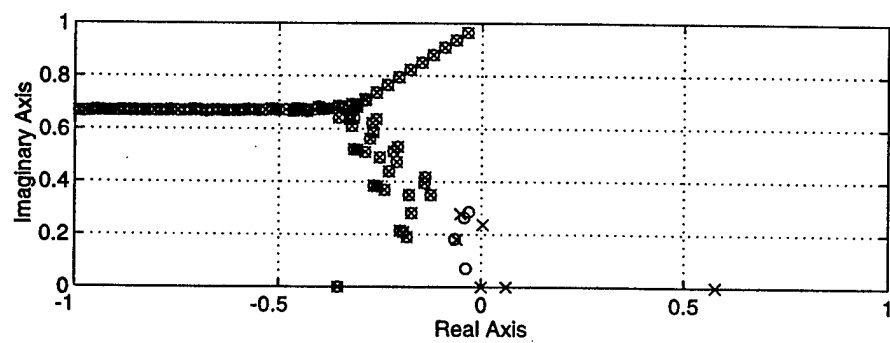


Figure 8: Series connection of high-order plant (model 1) of Figure 6 and LQG controller obtained from reduced order model (model 2) of Figure 7.

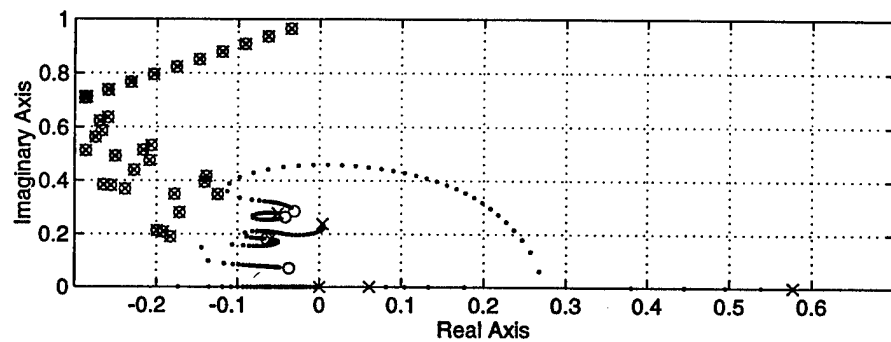


Figure 9: Root locus of Figure 8 with gain varying from 0 to 4.

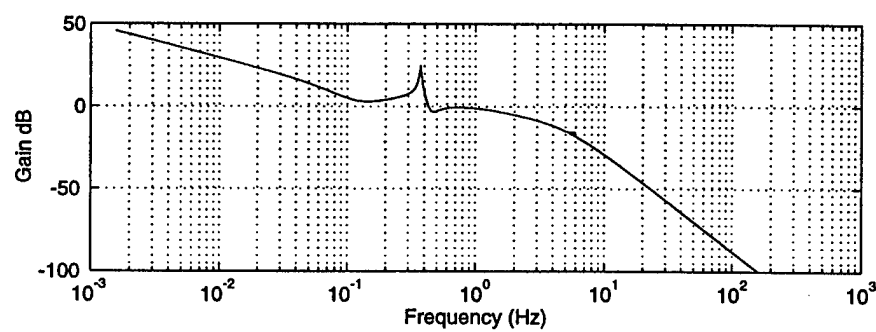


Figure 10: Magnitude response of open LQG control loop.

6 Suboptimal Control

Although we achieved our goal in section 5, we designed our LQG controller with a very high dimensional slightly-reduced-order plant model (model 2). This may lead to numerical problems if the design were attempted with a new model that contained several wavenumbers as the model would be even larger. As a result, we would like to develop a method that uses extremely low-order models in the LQG design. By examining figure 8, we observe that most of the poles and zeros of the high-order plant appear to be inverted⁴ by controller poles and zeros; i.e. controller poles are placed on top of plant zeros and vice-versa. In fact, these poles and zeros are not actually inverted by the optimal controller, but nearly so. A suboptimal controller, then, may be designed that a-priori inverts most of the poles and zeros, except for a few. Only the poles and zeros that are *not* inverted are used in the LQG design procedure. This scheme is shown in figure 11.

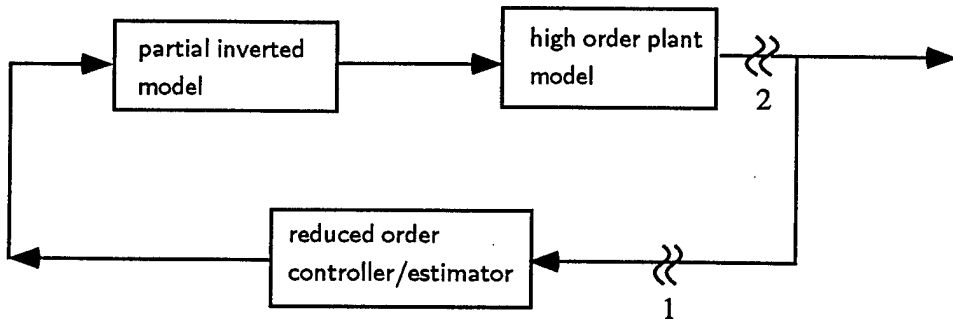


Figure 11: LQG control loop for high-order plant (model 1), inverted model (model 3), and reduced-order controller obtained from model 4.

We define a few new models to use as part of this scheme as shown in table 2. Model 3 contains the poles and zeros used to invert most of the poles and zeros in model 2. Model 4 contains the poles and zeros that are not inverted.

Note that pole/zero cancellation is a bad idea in the right hand s plane. If a non-minimum phase zero is not exactly canceled, a new instability may be created in the system. In fact,

⁴A pole or zero is said to be inverted if a zero (for the pole) or pole (for the zero) is placed in the same position.

Models		
Number	Name	Poles/Zeros
3	partial-inverted	132/132
4	very-low-order	9/7

Table 2: Models used in low-order LQG controller design.

we can never actually invert any pole or zero because we can never know the exact locations of the poles or zeros. However, non-exact cancellation is not a problem in this case since all poles and zeros we cancel are in the left hand s plane. The slightly-reduced-order model is shown in figure 7. Our approach is to a-priori invert most of the poles and zeros with model 3. The few poles and zeros that are not inverted (model 4) are shown in figure 12. A LQG controller is designed using only these poles and zeros (model 4). The parameters

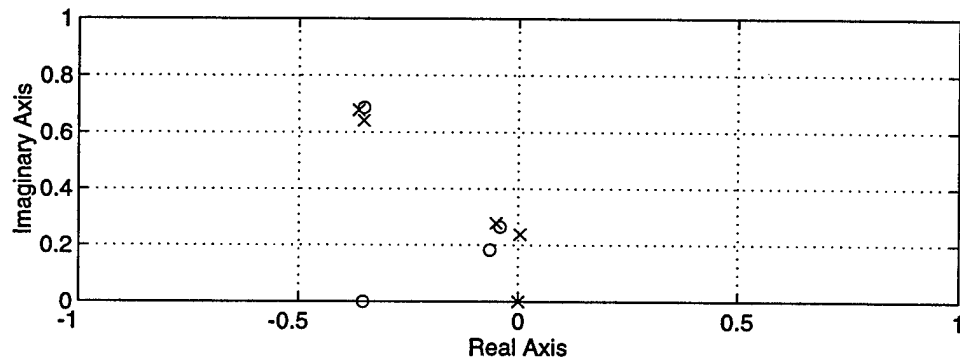


Figure 12: Very-low-order model (model 4).

for the design are the same as in section 5. Figure 13 shows the transfer function of the series connection of high-order model (model 1), partial inverted model (model 3), and low-order controller obtained from model 4. The root locus of the system is shown in figure 14. By comparing the root locus' shown in figures 9 and 14, we see that the closed loop pole placement is very similar in both cases. Indeed, the inverted model controller scheme achieves the objective of all observable/ controllable poles to the left of $s = -0.08$.

There are a few points that should be noted. First, the controllers designed for the two cases are not the same, even though they are similar. This can be particularly noted by

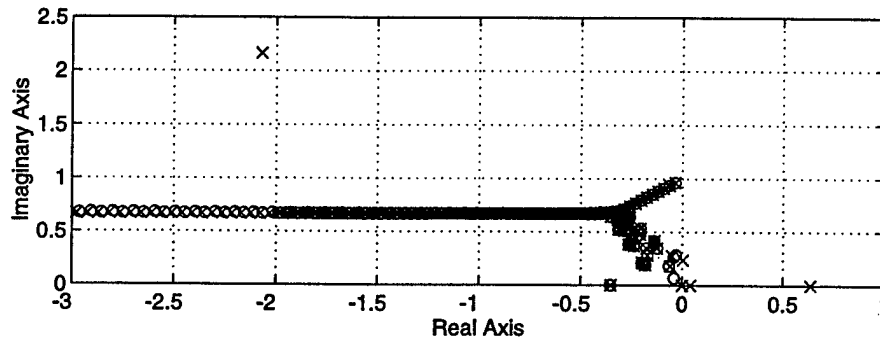


Figure 13: Series connection of high-order model (model 1), partial inverted model (model 3), and low-order controller obtained from model 4.

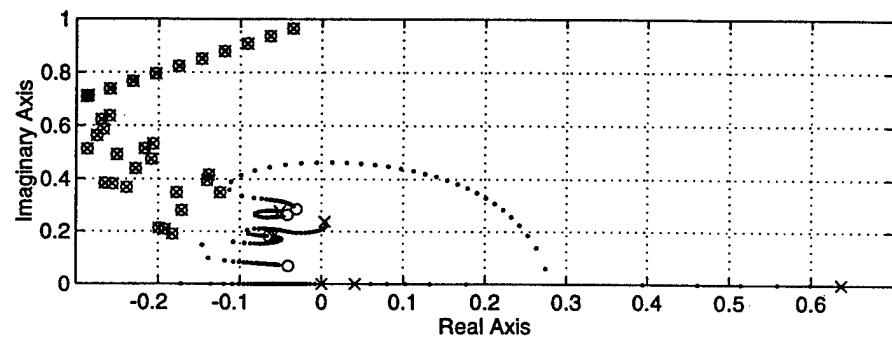


Figure 14: Root locus of series connection shown in figure 13

observing the open loop controller poles on the real axis. In the slightly-reduced-order-model case, figure 9, one pole is between $s = .5$ and $s = .6$, while in the partial-inverted-model case, figure 13, two one pole is between $s = .6$ and $s = .7$. Second, the inverted model scheme does *not* reduce the overall order of the controller that must be implemented. The partial-inverted model (model 3) as well as the LQG controller must be considered together as the overall controller. The order of this combination is the same as that of the original slightly-reduced-order LQG controller. However, the inverted scheme does allow a very-low-order model to be used in the LQG design synthesis.

Finally, figure 15 shows the magnitude response for the open loop transfer function from point 1 on figure 11 to point 2. Note just as in the previous section, the gain is higher at low frequencies and lower at higher frequencies. Again, at $f = 1.0$, the magnitude response “rolls-off”.

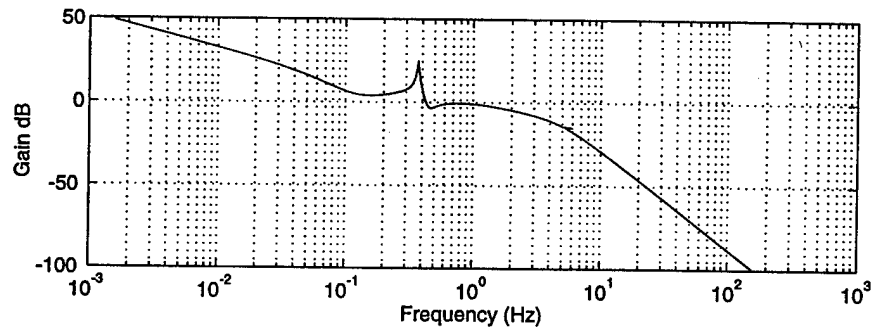


Figure 15: Magnitude response of open LQG control loop for inverted model scheme.

In order to investigate the robustness of the inverted model scheme for varying Reynolds numbers, we apply the inverted-model/very-low-order LQG controller constructed for figure 1 with $Re = 10,000$ to a single-wavenumber system for $Re = 12,500$ (figure 16). The root locus for the higher Reynolds number system with inverted scheme controller is shown in figure 17. It can be seen that although the system is stabilized, the objective of all observable/controllable poles to the left of $s = -.08$ is *not* achieved. As may have been expected, the inverted model scheme is not robust in terms of *degree* of stability. However, overall stability is preserved.

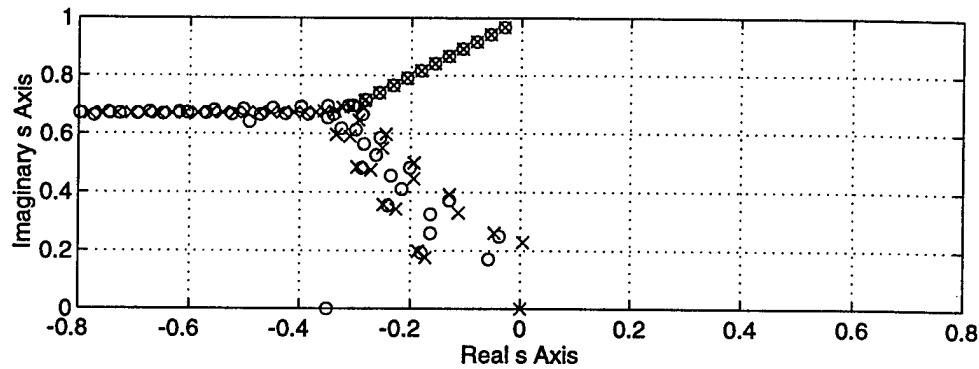


Figure 16: Pole (x) /Zero (o) Configuration, Channel model: $Re = 12,500$, shear sensor at π , $w(x) = \sin(x)$, $L=4\pi$, $\alpha = 1.0$. Only the top half of the s plane is shown.

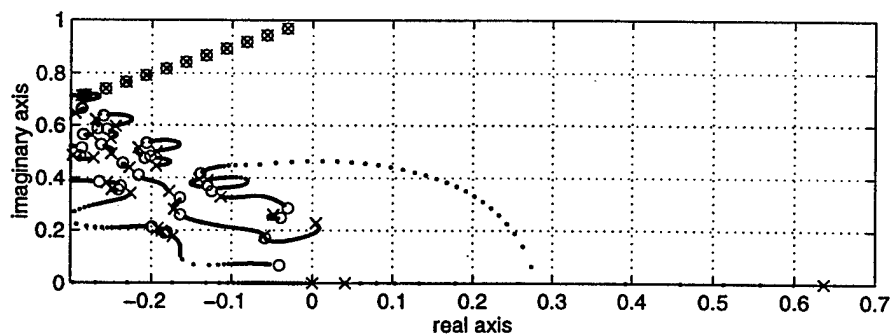


Figure 17: Root locus of series connection of partial-inverted model (model 3), low-order controller obtained from model 4, and $Re=12,500$ system model of figure 16. It is seen that the original pole near $s = -0.05 + .25i$ never moves to the left of $s = -0.08$.

7 Conclusion

In this paper, we considered linear stabilization of plane, Poiseuille flow using linear quadratic Gaussian (LQG) optimal control theory. In prior investigations, it was shown that plane, Poiseuille flow may be stabilized using extremely simple, integral compensator controllers, given that sensor locations produced minimum phase zeros. However, the controller was marked by slow dissipation of perturbation energy. In this investigation, we exploited LQG methods to give faster perturbation energy dissipation. We showed that we may achieve approximately double the dissipation rate than that reported in integral compensator control schemes. This increase in performance came with a cost. Controllers built using LQG methods for infinite-dimensional systems must, in theory, be infinite-dimensional. Since it is impossible to implement infinite-dimensional controllers, we implemented reduced-order controllers on the full-order plant. We showed that this procedure can in theory lead to de-stabilization of unmodelled dynamics. We then showed that this may be avoided using distributed control or, dually, distributed sensing. An additional problem in high-plant-order LQG controller design is numerical inaccuracy in the synthesis equations. We showed a sub-optimal LQG synthesis method that uses an extremely, low-order plant model for synthesis of a high-order controller. This involved the use of a left-hand-plane inversion model. This sub-optimal controller produced results essentially equivalent to the optimal controller. Finally, we applied our LQG controller to a plant of Reynolds number 12,500 instead of 10,000 used in the LQG design. Using this new plant, we showed that the system was still stabilized. However, the goal of double dissipation rate was not achieved, showing the inherent non-robustness (in terms of degree of stabilization) of this controller. In this paper, we have examined LQG control methods. Other control approaches exist that are based on worst-case design. These approaches include disturbance attenuation design [12] and H^∞ design [13]. In the future, these designs may lead to enhanced performance in fluid control problems.

References

- [1] JOSHI, S.S., SPEYER, J.L., AND KIM, J. 1995 Feedback Stabilization of Plane Poiseuille Flow, *Proceedings of the Conference on Decision and Control*, New Orleans, LA, 1995.
- [2] JOSHI, S.S., SPEYER, J.L., AND KIM, J. 1997 A Systems Theory Approach to the Feedback Stabilization of Infinitesimal and Finite-amplitude Disturbances in Plane Poiseuille Flow, *Journal of Fluid Mechanics*, Vol. 331, 1997.
- [3] DOYLE, J.K. 1978 Guaranteed Margins for LQG Regulators *IEEE Transactions on Automatic Control*, Vol. AC-23.
- [4] JOSHI, S.S. 1996 A Systems Theory Approach to the Control of Plane Poiseuille Flow *UCLA* , Department of Electrical Engineering, Ph.D. Dissertation.
- [5] ANDERSON, B.O. AND MOORE, J.B. 1990 *Optimal Control: Linear Quadratic Methods* Prentice-Hall.
- [6] FRIEDLAND, B. 1986 *Control System Design: An Introduction to State Space Methods* McGraw-Hill Book Company.
- [7] SPEYER, J.L. 1995 *Optimal Control Theory for Scientists and Engineers: Notes from UCLA MAE 270* Academic Publishing Notes.
- [8] SESAK, J.R., LIKINS, P. AND CORADETTI, T. 1979 Flexible Spacecraft Control by Modal Error Sensitivity Suppression *Journal of Aeronautical Science*, Vol. XXVII, No. 2, April-June.
- [9] DOYLE, J. AND STEIN, G. 1981 Multivariable Feedback Design: Concepts for a Classical/Modern Synthesis *IEEE Transactions on Automatic Control*, Vol. AC-26, pp. 4-16.
- [10] GRACE, A., LAUB, A.J., LITTLE, J.N., AND THOMPSON, C.M. 1992 *Control System Toolbox: For use with MATLAB*, The Math Works.
- [11] DOYLE, J. AND STEIN, G. 1979 Robustness with Observers *IEEE Transactions on Automatic Control*, Vol. AC-24, No. 4, pp. 607-611.

- [12] RHEE, I. AND SPEYER, J.L. 1991 A game theoretic approach to a finite-disturbance attenuation problem. *IEEE Transactions on Automatic Control*, AC-36(9), September.
- [13] DOYLE, J.K., GLOVER, K., KHARGONEKAR, P.P. , AND FRANCIS, B.A. 1989 State Space Solutions to Standard H_2 and H_∞ Control Problems *IEEE Transactions on Automatic Control*, Vol. 34, No. 8.

A systems theory approach to the feedback stabilization of infinitesimal and finite-amplitude disturbances in plane Poiseuille flow

By SANJAY S. JOSHI†, JASON L. SPEYER AND JOHN KIM

School of Engineering and Applied Science, University of California, Los Angeles
Los Angeles, CA 90024, USA

(Received 14 February 1995 and in revised form 15 July 1996)

A systems theory framework is presented for the linear stabilization of two-dimensional laminar plane Poiseuille flow. The governing linearized Navier–Stokes equations are converted to control-theoretic models using a numerical discretization scheme. Fluid system poles, which are closely related to Orr–Sommerfeld eigenvalues, and fluid system zeros are computed using the control-theoretic models. It is shown that the location of system zeros, in addition to the well-studied system eigenvalues, are important in linear stability control. The location of system zeros determines the effect of feedback control on both stable and unstable eigenvalues. In addition, system zeros can be used to determine sensor locations that lead to simple feedback control schemes. Feedback controllers are designed that make a new fluid–actuator–sensor–controller system linearly stable. Feedback control is shown to be robust to a wide range of Reynolds numbers. The systems theory concepts of modal controllability and observability are used to show that feedback control can lead to short periods of high-amplitude transients that are unseen at the output. These transients may invalidate the linear model, stimulate nonlinear effects, and/or form a path of ‘bypass’ transition in a controlled system. Numerical simulations are presented to validate the stabilization of both single-wavenumber and multiple-wavenumber instabilities. Finally, it is shown that a controller designed upon linear theory also has a strong stabilizing effect on two-dimensional finite-amplitude disturbances. As a result, secondary instabilities due to infinitesimal three-dimensional disturbances in the presence of a finite-amplitude two-dimensional disturbance cease to exist.

1. Introduction

A basic problem in fluid dynamics is the theoretical understanding of how instability in laminar shear flow leads to transition to turbulence. Since laminar flow is preferred in many applications, the suppression of fluid instabilities to maintain laminar flow would be very useful. Towards this goal, active boundary layer control of instability has been proposed. The nonlinear aspects of the transition process are still not clearly known. It has been shown (Orszag & Patera 1983) that some shear flows may sustain two-dimensional finite-amplitude instabilities that cause infinitesimal three-dimensional disturbances to be highly unstable. This two-dimensional primary instability/three-dimensional secondary instability process may be one nonlinear mechanism that leads to transition. Conversely, the behaviour of infinitesimal

† Present address: Jet Propulsion Laboratory, 4800 Oak Grove Drive, Pasadena, CA 91109, USA.

(linear) disturbances in laminar shear flow is well understood (Orr 1907; Sommerfeld 1908; Drazin & Reid 1981). Therefore, linear analysis provides a natural starting point to begin to develop active control schemes that may eventually lead to full transition control. It is the purpose of this paper to develop feedback controllers based on linear theory that stabilize two-dimensional plane Poiseuille flow to infinitesimal disturbances. In addition, it will be shown that a controller designed upon linear theory has a strong stabilizing effect on two-dimensional finite-amplitude instabilities. As a result, secondary three-dimensional instabilities as described in Orszag & Patera (1983) cease to exist in such a system.

Most prior work in the area of laminar flow linear instability suppression has concentrated on the wave superposition approach. A nice survey of past work is given in Joslin, Erlebacher & Hussaini (1994). The basic idea is that boundary layer instabilities appear as a combination of many sinusoidally growing waves of certain frequencies, phases, and amplitudes. If these wave parameters are known, or if they can be determined, a second wave may be stimulated in the flow that is exactly out of phase with the instability wave. In this way, the two waves may destructively interfere and flow may be stabilized. Disturbance of the flow field to cause a wave motion to appear has been experimentally demonstrated using several methods such as vibrating ribbons (Schubauer & Skramstad 1947), vibrating wires (Milling 1981), and heating elements (Nosenchuck 1982). In addition, several authors have numerically obtained wave superposition results based on Navier-Stokes simulations (Beringen 1984; Metcalfe *et al.* 1986). Most of the results, however, report incomplete destruction of instability waves. Joslin *et al.* (1994) explain that wave cancellation is very sensitive to the wave parameters and postulate that incomplete destruction reported in past studies was due to improper phase or amplitude properties of the cancelling wave.

In addition, Bower, Kegelman & Pal (1987) considered the Orr-Sommerfeld equation in designing an input to channel flow that may counteract the effects of a disturbance that excites instabilities. They showed that if an oscillating flat pulse function at the lower boundary of a channel excited inherent instabilities, a second oscillating flat pulse function could be constructed downstream that negated excitation of the instabilities. Much like the wave superposition approach, their aim was not to stabilize the underlying dynamics of the problem, but rather to 'cancel' the effects of a specific disturbance.

Unlike past work, our aim is to use systems theory to construct a combination fluid-actuator-sensor-controller *system* that is inherently stable. In essence, the approach changes the philosophy of the problem from thinking about how inputs can mitigate an inherently unstable system to thinking about how sensors and actuators can be added to form an entirely new *stable* system. Recently, mathematical control systems theory has begun to be applied to fluid systems (Burns & Ou 1994; Gunzburger, Hou & Suobodny 1992; Choi, Moin & Kim 1993). A control theory approach for laminar flow linear instability suppression will be shown to have several advantages over the traditional wave cancellation approach. It will eliminate the need to explicitly measure phase and frequency of instabilities. Also, it will provide a framework to select sensor locations in order to have the least complex controller. Further, feedback control will be shown to be extremely robust to changing Reynolds numbers given proper sensor location. In addition, linear feedback controllers will be shown to have a strong stabilizing effect on two-dimensional finite-amplitude disturbances.

This paper is organized as follows. In §2, we formulate the linear channel flow problem using the linearized Navier-Stokes equations. Boundary input in the form

of blowing/suction and boundary output in terms of shear are represented within the equations. In §3, we introduce the concepts of zeros and poles of a system, as well as control-theoretic models. The governing partial-differential equation for the system is converted into a set of first-order, ordinary differential equations via a Galerkin method. These first-order, ordinary differential equations are then converted into a control-theoretic model. Section 4 describes the infinite-dimensional nature of the channel flow system and how it affects the selection of actuation. Section 5 describes the numerical model and the verification of the calculated poles and zeros. Section 6 introduces feedback control design. It is shown that judicious sensor placement, based on zero locations, can lead to simple control schemes. Furthermore, the control system is extremely robust to change in Reynolds number. Section 7 explores unobservable modal reinforcement as a possible path of ‘bypass’ transition in a controlled system. It then shows how a particular control model, called the modal-canonical state space model, may be used to assess observability of modal reinforcement. Section 8 demonstrates multiple-wavenumber instability control. Section 9 demonstrates that a linear controller has a strong stabilizing effect on two-dimensional, finite-amplitude instabilities. As a result, secondary three-dimensional instabilities as described by Orszag & Patera (1983) cease to exist. Finally, §10 outlines conclusions.

2. Problem formulation

2.1. Dynamic equations

We consider two-dimensional plane Poiseuille flow between two parallel stationary plates. Let the channel be of finite length and finite height, with the centreline at zero. The flow in the channel is described by the unsteady nonlinear incompressible Navier–Stokes equations. In order to study the linear stability of the system, we follow the standard procedure. Consider small perturbations in the velocities of $\hat{u}(x, y, t)$ in the horizontal direction, $\hat{v}(x, y, t)$ in the vertical direction, and $\hat{p}(x, y, t)$ in the pressure field. Let the primary flow be represented by $U(y)$ with U_c being the centreline velocity. The linearized incompressible Navier–Stokes equations may be formed by substituting the primary flow and small perturbations into the nonlinear incompressible Navier–Stokes equations and disregarding the second-order terms involving the perturbations,

$$\frac{\partial \hat{u}(x, y, t)}{\partial t} + U(y) \frac{\partial \hat{u}(x, y, t)}{\partial x} + \frac{dU(y)}{dy} \hat{v}(x, y, t) = -\frac{\partial \hat{p}(x, y, t)}{\partial x} + \frac{1}{Re} \nabla^2 \hat{u}(x, y, t), \quad (2.1)$$

$$\frac{\partial \hat{v}(x, y, t)}{\partial t} + U(y) \frac{\partial \hat{v}(x, y, t)}{\partial x} = -\frac{\partial \hat{p}(x, y, t)}{\partial y} + \frac{1}{Re} \nabla^2 \hat{v}(x, y, t), \quad (2.2)$$

$$\frac{\partial \hat{u}(x, y, t)}{\partial x} + \frac{\partial \hat{v}(x, y, t)}{\partial y} = 0, \quad (2.3)$$

where the flow variables are non-dimensionalized by the channel half-height, H , and centreline velocity, U_c . Re is the Reynolds number defined as $(U_c H / v)$ where v is the kinematic viscosity. By introducing a ‘stream function’, $\psi(x, y, t)$,

$$\hat{u}(x, y, t) \triangleq \frac{\partial \psi(x, y, t)}{\partial y} \quad (2.4)$$

and

$$\hat{v}(x, y, t) \triangleq -\frac{\partial \psi(x, y, t)}{\partial x}, \quad (2.5)$$

(2.1)–(2.3) may be combined into a single equation,

$$\frac{\partial}{\partial t} \frac{\partial^2 \psi}{\partial x^2} + \frac{\partial}{\partial t} \frac{\partial^2 \psi}{\partial y^2} = -U(y) \frac{\partial^3 \psi}{\partial x^3} - U(y) \frac{\partial}{\partial x} \frac{\partial^2 \psi}{\partial y^2} + \frac{d^2 U(y)}{dy^2} \frac{\partial \psi}{\partial x} + \frac{1}{Re} \nabla^2 (\nabla^2 \psi). \quad (2.6)$$

Assume periodic boundary conditions in the streamwise (x) direction. For channel flow, with rigid plates at $y = -1$ and $y = 1$, the no-slip boundary conditions become

$$\psi(x, y = -1, t) = 0, \quad (2.7)$$

$$\frac{\partial \psi}{\partial y}(x, y = -1, t) = 0, \quad (2.8)$$

$$\psi(x, y = 1, t) = 0, \quad (2.9)$$

$$\frac{\partial \psi}{\partial y}(x, y = 1, t) = 0. \quad (2.10)$$

With an initial condition

$$\psi(x, y, t = 0) = g(x, y) \quad (2.11)$$

the boundary value problem is completely formed. Existence and uniqueness of solutions for the linearized Navier–Stokes equations have been studied in Ladyzhenskaya (1969), Kreiss & Lorenz (1989), and Temam (1984). Equations (2.6)–(2.11) represent the starting point for construction of a feedback control system. These equations neither include any control terms nor do they describe any sensing of flow field variables.

2.2. Boundary input

We consider the case of blowing/suction at the lower wall of the channel. The boundary conditions are now modified from before to include boundary input, represented as the *known* separable function $q(t)w(x)f(y)$,

$$\psi(x, y = -1, t) = q(t)w(x)f(y = -1), \quad (2.12)$$

$$\frac{\partial \psi}{\partial y}(x, y = -1, t) = q(t)w(x) \frac{\partial f(y = -1)}{\partial y} = 0, \quad (2.13)$$

$$\psi(x, y = 1, t) = 0, \quad (2.14)$$

$$\frac{\partial \psi}{\partial y}(x, y = 1, t) = q(t)w(x) \frac{\partial f(y = 1)}{\partial y} = 0. \quad (2.15)$$

Note that these conditions constrain the function $f(y)$ such that

$$f(y = -1) \neq 0, \quad (2.16)$$

$$\frac{\partial f(y = -1)}{\partial y} = 0, \quad (2.17)$$

$$f(y = 1) = 0, \quad (2.18)$$

$$\frac{\partial f(y = 1)}{\partial y} = 0. \quad (2.19)$$

Many functions may be equally appropriate. One such function is

$$f(y) = \frac{1}{2}y^4 + \frac{1}{4}y^3 - y^2 - \frac{3}{4}y + 1. \quad (2.20)$$

In order to relate boundary conditions on ψ to blowing/suction in the wall-normal direction, we use (2.5) to relate $\widehat{v}(x, y, t)$ and $\psi(x, y, t)$. Then (2.12) becomes

$$\widehat{v}(x, y = -1, t) = -q(t) \frac{\partial w(x)}{\partial x} f(y = -1). \quad (2.21)$$

Note that $\widehat{v}(x, y, t)$ is related to the *derivative* of $w(x)$. The homogeneous equation (2.6) and the inhomogeneous boundary condition (2.12) can be converted into an inhomogeneous equation with homogeneous boundary conditions by introducing

$$\phi(x, y, t) \triangleq \psi(x, y, t) - q(t)f(y)w(x). \quad (2.22)$$

Then by substituting into (2.6), we obtain

$$\begin{aligned} \frac{\partial}{\partial t} \frac{\partial^2 \phi}{\partial x^2} + \frac{\partial}{\partial t} \frac{\partial^2 \phi}{\partial y^2} &= -U(y) \frac{\partial^3 \phi}{\partial x^3} - U(y) \frac{\partial}{\partial x} \frac{\partial^2 \phi}{\partial y^2} + \frac{d^2 U(y)}{dy^2} \frac{\partial \phi}{\partial x} + \frac{1}{Re} \frac{\partial^4 \phi}{\partial x^4} + 2 \frac{1}{Re} \frac{\partial^2}{\partial x^2} \frac{\partial^2 \phi}{\partial y^2} \\ &+ \frac{1}{Re} \frac{\partial^4 \phi}{\partial y^4} - \frac{\partial q(t)}{\partial t} \frac{\partial^2 w(x)}{\partial x^2} f(y) - \frac{\partial q(t)}{\partial t} w(x) \frac{\partial^2 f(y)}{\partial y^2} - q(t) \frac{\partial^3 w(x)}{\partial x^3} U(y) f(y) \\ &- q(t) \frac{\partial w(x)}{\partial x} U(y) \frac{\partial^2 f(y)}{\partial y^2} + q(t) \frac{\partial w(x)}{\partial x} \frac{d^2 U(y)}{dy^2} f(y) + \frac{1}{Re} q(t) \frac{\partial^4 w(x)}{\partial x^4} f(y) \\ &+ 2 \frac{1}{Re} q(t) \frac{\partial^2 w(x)}{\partial x^2} \frac{\partial^2 f(y)}{\partial y^2} + \frac{1}{Re} q(t) w(x) \frac{\partial^4 f(y)}{\partial y^4}. \end{aligned} \quad (2.23)$$

The boundary conditions in terms of ϕ are now

$$\phi(y = -1) = 0, \quad (2.24)$$

$$\frac{\partial \phi(y = -1)}{\partial y} = 0, \quad (2.25)$$

$$\phi(y = 1) = 0, \quad (2.26)$$

$$\frac{\partial \phi(y = 1)}{\partial y} = 0. \quad (2.27)$$

2.3. Boundary output

We use the streamwise component of shear at a single boundary point, $z(x_i, y = -1, t)$, as our boundary output, which is given by

$$z(x_i, y = -1, t) = \frac{\partial \widehat{u}(x_i, y = -1, t)}{\partial y}. \quad (2.28)$$

By expressing $\widehat{u}(x_i, y = -1, t)$ in terms of the stream function (2.4),

$$z(x_i, y = -1, t) = \frac{\partial^2 \psi(x_i, y = -1, t)}{\partial y^2}, \quad (2.29)$$

and by observing (2.22)

$$z(x_i, y = -1, t) = \frac{\partial^2 \psi(x_i, y = -1, t)}{\partial y^2} = \frac{\partial^2 \phi(x_i, y = -1, t)}{\partial y^2} + q(t) \frac{\partial^2 f(y = -1)}{\partial y^2} w(x_i). \quad (2.30)$$

3. Zeros, eigenvalues, and control-theoretic models

Linear stability analysis of (2.6) (Drazin & Reid 1981) shows that the system is linearly unstable for a range of Reynolds numbers. The goal of this paper is to

stabilize the system using control theory. To do this, we first transform the governing equations into special control-theoretic models.

3.1. System transfer function

We have defined a single-input/single-output (SISO) system in the sense that only one scalar function, $q(t)$, defines the entire input and one scalar function, $z(t)$, defines the output. A common form of control model for a finite-dimensional SISO system is the transfer function model. The transfer function, $H(s)$, is defined as the Laplace transform of the output, $z(t)$, divided by the Laplace transform of the input, $q(t)$, where zero initial conditions are assumed. Then

$$H(s) \triangleq \frac{\mathcal{L}[z(t)]}{\mathcal{L}[q(t)]} = \frac{Z(s)}{Q(s)}. \quad (3.1)$$

For finite-dimensional systems, $Z(s)$ and $Q(s)$ take the form of polynomials in the complex variable s . These polynomials may be factored to yield an equivalent representation,

$$H(s) \triangleq \frac{Z(s)}{Q(s)} = \frac{\prod_{j=1}^J (s - \zeta_j)}{\prod_{i=1}^I (s - p_i)}. \quad (3.2)$$

In this form, $p_1 \dots p_I$ are the *poles* of the system. The poles of any system are dependent solely on the physics of the underlying system, independent of any particular input or output. Unstable modes of the system appear as poles whose real part is greater than zero. As will be seen in later sections, the poles are closely related to the eigenvalues of the Orr–Sommerfeld equation. The values $\zeta_1 \dots \zeta_J$ are the *zeros* of the system. They are heavily dependent on which particular inputs and outputs are used on the system. As will be seen later, the position of these zeros will dictate sensor locations and will reveal the effect of feedback control on the eigenvalues. A graphical representation of the transfer function can be produced by plotting the poles and zeros in the complex s -space.

3.2. State-variable model

Much of modern control theory is based on the state-variable representation of a dynamic system. This representation relies on the basic fact that the motion of any finite-dimensional dynamic system may be expressed as a set of first-order ordinary differential equations. As a simple example of a state variable model (Franklin, Powell & Emami-Naeini 1988), Newton's law for a constant single mass, M , moving in one dimension, x , under a force, $F(t)$, is

$$M \frac{d^2x(t)}{dt^2} = F(t). \quad (3.3)$$

If we define one state variable as the position $x_1 \triangleq x(t)$ and the other state variable as the velocity $x_2 \triangleq dx(t)/dt$, (3.3) can be written as

$$\frac{dx_1}{dt} = x_2, \quad (3.4)$$

$$\frac{dx_2}{dt} = \frac{F(t)}{M}. \quad (3.5)$$

Furthermore, the first-order linear ordinary differential equations can be expressed using matrix notation

$$\begin{bmatrix} \frac{dx_1}{dt} \\ \frac{dx_2}{dt} \end{bmatrix} = \begin{bmatrix} 0 & 1 \\ 0 & 0 \end{bmatrix} \begin{bmatrix} x_1 \\ x_2 \end{bmatrix} + \begin{bmatrix} 0 \\ 1 \end{bmatrix} \frac{F}{M} \quad (3.6)$$

or

$$\frac{dx}{dt} = Ax + Bq. \quad (3.7)$$

If we take output as position, x_1 ,

$$z = [1 \ 0] \begin{bmatrix} x_1 \\ x_2 \end{bmatrix} \quad (3.8)$$

or

$$z = C \cdot x \quad (3.9)$$

The matrix A , and the vectors B and C are called the state space matrices of the single-input, single-output (SISO) system. More specifically, the A matrix is referred to as the dynamic matrix of the system. It can be shown that the poles of the system are simply the eigenvalues of the A matrix. In the more general case of multiple-input, multiple-output (MIMO) systems, B and C are matrices. For generality, we may add another term, Dq , to the output equation to account for systems in which there is direct feedthrough from the input to the output. Then,

$$z = C \cdot x + Dq \quad (3.10)$$

In the case of no direct feedthrough, $D = 0$, the state space and transfer function models are related as

$$H(s) \triangleq \frac{Z(s)}{Q(s)} = C(sl - A)^{-1}B. \quad (3.11)$$

3.3. State-space formulation for channel system

We will convert our problem into a set of first-order ordinary differential equations and then form a state-space model from these equations. The state-space model can then be represented with transfer function poles and zeros. We will proceed in this way for two reasons. First, our system lends itself to decomposition into first-order ordinary-differential equations by use of a Galerkin method. More importantly, however, the state-space model lends itself to extremely elegant ways to control eigenvalues of a system in well prescribed ways. It should be noted that unlike the single-mass example given above, the channel system requires an infinite number of ordinary differential equations to describe its motion. This is known as an infinite-dimensional system. As a result, any finite number of ordinary-differential equations used in a state-space model will not completely describe the system. The difficulties associated with such a system are taken up after a discussion of the Galerkin method used to obtain the ordinary-differential equations.

3.3.1. First-order system

We use a standard Galerkin procedure to convert the governing partial differential equation (2.23) into a system of ordinary-differential equations. Assume an

approximate solution of (2.23) as

$$\phi_a(x, y, t) \triangleq \sum_{n=-N}^N \sum_{m=0}^M a_{nm}(t) P_n(x) \Gamma_m(y). \quad (3.12)$$

By using Fourier functions, e^{inx_0x} , for $P_n(x)$ and basis functions constructed from Chebyshev polynomials for $\Gamma_m(y)$ (Joshi 1996), we obtain a first-order system. Define inner products in the streamwise (x) and normal (y) directions respectively:

$$[e^{inx_0x}, e^{imx_0x}]_x \triangleq \frac{1}{L} \int_{-L/2}^{L/2} e^{inx_0x} e^{-imx_0x} dx = \delta_{mn}, \quad \alpha_0 \triangleq \frac{2\pi}{L}, \quad (3.13)$$

and

$$[\Gamma_m(y), \Gamma_n(y)]_y \triangleq \int_{-1}^1 \frac{\Gamma_n(y) \Gamma_m(y)}{(1-y^2)^{1/2}} dy, \quad (3.14)$$

where L is the non-dimensional length of the finite-length channel. Applying the orthogonality of the basis functions in x , we obtain a system of first-order ordinary differential equations:

$$\begin{aligned} & - \sum_{m=0}^M \frac{\partial a_{lm}(t)}{\partial t} l^2 \alpha_0^2 \beta_{mk}^0 + \sum_{m=0}^M \frac{\partial a_{lm}(t)}{\partial t} \beta_{mk}^2 = \sum_{m=0}^M a_{lm}(t) il^3 \alpha_0^3 \beta_{mk}^{0+} - \sum_{m=0}^M a_{lm}(t) il \alpha_0 \beta_{mk}^{2+} \\ & + \sum_{m=0}^M a_{lm}(t) il \alpha_0 \beta_{mk}^{0-} + \frac{1}{Re} \sum_{m=0}^M a_{lm}(t) l^4 \alpha_0^4 \beta_{mk}^0 - 2 \frac{1}{Re} \sum_{m=0}^M a_{lm}(t) l^2 \alpha_0^2 \beta_{mk}^2 \\ & + \frac{1}{Re} \sum_{m=0}^M a_{lm}(t) \beta_{mk}^4 + \frac{\partial q(t)}{\partial t} \{S_{lk}^1\} + q(t) \{S_{lk}^2\}, l = -N \dots N, k = 0 \dots M, \end{aligned} \quad (3.15)$$

where

$$S_{lk}^1 \triangleq - \left[\frac{\partial^2 w(x)}{\partial x^2}, P_l(x) \right]_x [v(y), \Gamma_k(y)]_y - [w(x), P_l(x)]_x \left[\frac{\partial^2 v(y)}{\partial y^2}, \Gamma_k(y) \right]_y \quad (3.16)$$

and

$$\begin{aligned} S_{lk}^2 \triangleq & - \left[\frac{\partial^3 w(x)}{\partial x^3}, P_l(x) \right]_x [U(y)v(y), \Gamma_k(y)]_y - \left[\frac{\partial w(x)}{\partial x}, P_l(x) \right]_x \left[U(y) \frac{\partial^2 v(y)}{\partial y^2}, \Gamma_k(y) \right]_y \\ & + \left[\frac{\partial w(x)}{\partial x}, P_l(x) \right]_x \left[\frac{d^2 U(y)}{dy^2} v(y), \Gamma_k(y) \right]_y + \frac{1}{Re} \left[\frac{\partial^4 w(x)}{\partial x^4}, P_l(x) \right]_x [v(y), \Gamma_k(y)]_y \\ & + 2 \frac{1}{Re} \left[\frac{\partial^2 w(x)}{\partial x^2}, P_l(x) \right]_x \left[\frac{\partial^2 v(y)}{\partial y^2}, \Gamma_k(y) \right]_y + \frac{1}{Re} [w(x), P_l(x)]_x \left[\frac{\partial^4 v(y)}{\partial y^4}, \Gamma_k(y) \right]_y. \end{aligned} \quad (3.17)$$

In this system, α_0 is the fundamental wavenumber in the x -direction, defined as $2\pi/L$, and the β coefficients are defined in terms of the following scalar products, where the $\Gamma(y)$ are the basis functions in y :

$$\beta_{mk}^j \triangleq \left[\frac{\partial^j \Gamma_m(y)}{\partial y^j}, \Gamma_k(y) \right]_y, \quad j = 0 \dots 4, \quad (3.18)$$

$$\beta_{mk}^{0+} \triangleq [U(y)\Gamma_m(y), \Gamma_k(y)]_y, \quad (3.19)$$

$$\beta_{mk}^{0-} \triangleq \left[\frac{d^2 U(y)}{dy^2} \Gamma_m(y), \Gamma_k(y) \right]_y, \quad (3.20)$$

$$\beta_{mk}^{2+} \triangleq \left[U(y) \frac{\partial^2 \Gamma_m(y)}{\partial y^2}, \Gamma_k(y) \right]_y. \quad (3.21)$$

3.3.2. Transformation to state-space form

We may visualize (3.15) in block matrix form as

$$\begin{aligned} & \begin{bmatrix} M_{-N} & 0 & \cdots & 0 \\ 0 & M_{-N+1} & 0 & 0 \\ 0 & 0 & \ddots & 0 \\ 0 & 0 & 0 & M_N \end{bmatrix} \begin{bmatrix} \frac{d\vec{a}_{l=-N}}{dt} \\ \frac{d\vec{a}_{l=-N+1}}{dt} \\ \vdots \\ \frac{d\vec{a}_{l=N}}{dt} \end{bmatrix} \\ &= \begin{bmatrix} K_{-N} & 0 & \cdots & 0 \\ 0 & K_{-N+1} & 0 & 0 \\ 0 & 0 & \ddots & 0 \\ 0 & 0 & 0 & K_N \end{bmatrix} \begin{bmatrix} \vec{a}_{l=-N} \\ \vec{a}_{l=-N+1} \\ \vdots \\ \vec{a}_{l=N} \end{bmatrix} + \begin{bmatrix} Y_1 & Y_2 \end{bmatrix} \begin{bmatrix} \frac{q(t)}{dq(t)} \end{bmatrix} \quad (3.22) \end{aligned}$$

where $\vec{a}_{l=p}$ denotes a column vector of all a_{lk} coefficients whose first index, l , is the value p . In compact notation,

$$\mathbf{M} \frac{d\mathbf{a}}{dt} = \mathbf{Ka} + \begin{bmatrix} Y_1 & Y_2 \end{bmatrix} \begin{bmatrix} \frac{q(t)}{dq(t)} \end{bmatrix}. \quad (3.23)$$

Assuming non-singularity of the \mathbf{M} matrix, we may invert to obtain

$$\frac{d\mathbf{a}}{dt} = \mathbf{M}^{-1} \mathbf{Ka} + \begin{bmatrix} \mathbf{M}^{-1} Y_1 & \mathbf{M}^{-1} Y_2 \end{bmatrix} \begin{bmatrix} \frac{q(t)}{dq(t)} \end{bmatrix} \quad (3.24)$$

where \mathbf{a} , \mathbf{K} , Y_1 and Y_2 are all complex. By expanding in terms of real and imaginary parts, we obtain

$$\begin{aligned} \frac{da_R}{dt} + i \frac{da_I}{dt} &= \mathbf{M}^{-1} \mathbf{K}_R a_R + i \mathbf{M}^{-1} \mathbf{K}_I a_R + i \mathbf{M}^{-1} \mathbf{K}_R a_I - \mathbf{M}^{-1} \mathbf{K}_I a_I \\ &+ \mathbf{M}^{-1} Y_{1R} q(t) + i \mathbf{M}^{-1} Y_{1I} q(t) + \mathbf{M}^{-1} Y_{2R} \frac{dq(t)}{dt} + i \mathbf{M}^{-1} Y_{2I} \frac{dq(t)}{dt}. \quad (3.25) \end{aligned}$$

where the subscript R or I indicates real or imaginary parts. Define

$$\tilde{\mathbf{p}} \triangleq \begin{bmatrix} \mathbf{a}_R \\ \mathbf{a}_I \\ q(t) \end{bmatrix}. \quad (3.26)$$

Then the state space system is

$$\frac{d\tilde{\mathbf{p}}}{dt} = \begin{bmatrix} \mathbf{M}^{-1} \mathbf{K}_R & -\mathbf{M}^{-1} \mathbf{K}_I & \mathbf{M}^{-1} Y_{1R} \\ \mathbf{M}^{-1} \mathbf{K}_I & \mathbf{M}^{-1} \mathbf{K}_R & \mathbf{M}^{-1} Y_{1I} \\ 0 & 0 & 0 \end{bmatrix} \tilde{\mathbf{p}} + \begin{bmatrix} \mathbf{M}^{-1} Y_{2R} \\ \mathbf{M}^{-1} Y_{2I} \\ 1 \end{bmatrix} \frac{dq(t)}{dt} \quad (3.27)$$

We write (3.27) as

$$\frac{d\tilde{\mathbf{p}}}{dt} = \mathbf{A}\tilde{\mathbf{p}} + \mathbf{B}\frac{dq(t)}{dt} \triangleq \mathbf{A}\tilde{\mathbf{p}} + \mathbf{B}u(t) \quad (3.28)$$

where the input to the system is $dq(t)/dt$. Note since $q(t)$ in (2.12) is related to physical blowing/suction, it is important to keep in mind that the input to this model is the *derivative* of $q(t)$. In physical terms, any input derived from this model will be in terms of $dq(t)/dt$ and therefore must be integrated before it can be applied as physical blowing/suction.

3.3.3. Measurement equations

By observing (2.30) and using the assumed solution form (3.12)

$$\begin{aligned} z(x_i, y = -1, t) &= \frac{\partial^2 \psi(x_i, y = -1, t)}{\partial y^2} = \frac{\partial^2 \phi}{\partial y^2} + q(t) \frac{\partial^2 f(y = -1)}{\partial y^2} w(x_i) \\ &= \sum_{n=-N}^N \sum_{m=0}^M a_{nm}(t) P_n(x_i) \frac{\partial^2 \Gamma_m(y = -1)}{\partial y^2} + q(t) \frac{\partial^2 f(y = -1)}{\partial y^2} w(x_i) + \rho(t, x_i, y = -1) \end{aligned} \quad (3.29)$$

where $\rho(t, x_i, y = -1)$, the residual component of streamwise shear due to the truncated expansion, is assumed to be negligible compared to the two other terms. The second term on the right-hand side of (3.29) is made up of the known input terms (2.12). Denote

$$D \triangleq \frac{\partial^2 f(y = -1)}{\partial y^2} w(x_i). \quad (3.30)$$

By pulling out the complex time coefficients and denoting them as the vector \mathbf{a} as above we may construct a complex observation matrix, \mathbf{O}

$$z(x_i, y = -1, t) = \mathbf{O} \mathbf{a} + D q(t). \quad (3.31)$$

Finally, by creating $\tilde{\mathbf{p}}$ by stacking the real and imaginary parts of \mathbf{a} , as well as $q(t)$, we may construct an observation equation in state-variable form

$$\begin{bmatrix} z_R(x_i, y = -1, t) \\ z_I(x_i, y = -1, t) \end{bmatrix} = \begin{bmatrix} \mathbf{O}_R & -\mathbf{O}_I & D \\ \mathbf{O}_I & \mathbf{O}_R & 0 \end{bmatrix} \tilde{\mathbf{p}}. \quad (3.32)$$

Since we may measure only real output (shear), we are left with only the top half of the observation matrix,

$$z_R(x_i, y = -1, t) = [\mathbf{O}_R \quad -\mathbf{O}_I \quad D] \tilde{\mathbf{p}}. \quad (3.33)$$

In order to describe the system in traditional control terms, define

$$\mathbf{C} \triangleq [\mathbf{O}_R \quad -\mathbf{O}_I \quad D]. \quad (3.34)$$

Then,

$$z_R(x_i, y = -1, t) = \mathbf{C} \tilde{\mathbf{p}} \quad (3.35)$$

3.3.4. Initial conditions

We have not accounted for the initial value (2.11) in our boundary value problem. We may account for the initial condition by assuming it can be written as a series expansion in terms of $P_n(x)$ and $\Gamma_m(y)$. Then

$$\begin{aligned} \phi(x, y, t = 0) &= \psi(x, y, t = 0) - s(t = 0)f(y)w(x) = g(x, y) - s(t = 0)f(y)w(x) \\ &= \sum_{n=-N}^N \sum_{m=0}^M b_{nm} P_n(x) \Gamma_m(y) \end{aligned} \quad (3.36)$$

where b_{nm} are assumed known. Then

$$\mathbf{a}(t = 0) = \mathbf{b}. \quad (3.37)$$

Since \mathbf{a} and \mathbf{b} are both complex, stack the real and imaginary components to arrive at an initial condition on $\tilde{\mathbf{p}}$:

$$\tilde{\mathbf{p}}(t = 0) = \begin{bmatrix} b_R \\ b_I \\ q(t = 0) \end{bmatrix}. \quad (3.38)$$

We have now defined the system completely in the state-variable form of (3.7), (3.9) where \mathbf{A} and \mathbf{B} are given in (3.28), \mathbf{C} is given in (3.35), and the initial condition is (3.38). Although we have shown the state-space formulation using a single input and a single output, we may formulate the multiple input/multiple output case similarly. In that case, the multiple input functions are represented as a *sum* of separable functions in (2.12) and multiple outputs are represented as a vector whose components are of the form (3.35). It should be noted that in the multiple input case, it is important for physical implementation that for any finite stretch in the x -direction, only one of the multiple input functions is non-zero.

4. Infinite-dimensional nature of the channel problem and effect on actuator design

In a system described by partial-differential equations, such as the channel flow problem, no finite-dimensional model will capture all the dynamics of the system. Such a system is called infinite-dimensional. By examining the Galerkin approximate solution (3.12), we see that the approximate solution can converge only as $N, M \rightarrow \infty$. This would result in an infinite number of ordinary differential equations. Each n value included in the approximate solution is referred to as adding an additional wavenumber in the dynamic model. Even for just one wavenumber, $n = N$ (say), we see the assumed Galerkin solution requires an infinite number of terms in the y -direction,

$$\phi_a(x, y, t) \triangleq \sum_{m=0}^{M \rightarrow \infty} a_{Nm}(t) P_N(x) \Gamma_m(y). \quad (4.1)$$

Interestingly, by examining the structure of the \mathbf{A} matrix in the resulting state-space model, we see that the dynamics associated with each individual wavenumber are decoupled from the others. This is characterized by a block diagonal form of the \mathbf{A} matrix, (4.2). As a result, we may separate the problem of determining system poles into a set of smaller problems that include only one wavenumber at a time:

$$\mathbf{A} = \begin{bmatrix} [\mathbf{A}_{(n=1)}] & 0 & \cdots & \infty \\ 0 & [\mathbf{A}_{(n=2)}] & 0 & 0 \\ 0 & 0 & \ddots & 0 \\ \infty & 0 & 0 & [\mathbf{A}_{(n=\infty)}] \end{bmatrix}. \quad (4.2)$$

Indeed, the eigenvalues (poles) of the entire \mathbf{A} matrix are simply the eigenvalues (poles) of each smaller \mathbf{A} matrix block. Offsetting this computational advantage, however, is the fact that the locations of the zeros are not decoupled by wavenumber. Therefore, even though the poles of the system can be calculated separately using only one wavenumber in a particular computation, the zeros of the system force all

the wavenumbers in the model to be considered together. This can easily be seen from an examination of the transfer functions associated with just two wavenumbers. Consider two transfer functions obtained by using two distinct wavenumbers and the same input, $u(t)$, and output, $z(t)$:

$$H_{(n=1)} = \frac{N_{(n=1)}(s)}{D_{(n=1)}(s)}, \quad H_{(n=2)} = \frac{N_{(n=2)}(s)}{D_{(n=2)}(s)}. \quad (4.3)$$

The roots of $N(s)$ are the zeros and the roots of $D(s)$ are the poles. In terms of input and output,

$$z = H_{(n=1)}u, \quad z = H_{(n=2)}u. \quad (4.4)$$

Considered together, however,

$$z = [H_{(n=1)} + H_{(n=2)}]u = \left[\frac{D_{(n=2)}(s)N_{(n=1)}(s) + D_{(n=1)}(s)N_{(n=2)}(s)}{D_{(n=1)}(s)D_{(n=2)}(s)} \right] u. \quad (4.5)$$

The poles of the new, combined transfer function are clearly those of each model separately. The zeros, however, are the roots of a completely new polynomial $D_{(n=2)}(s)N_{(n=1)}(s) + D_{(n=1)}(s)N_{(n=2)}(s)$, which, in general, has little to do with either of the original numerators.

We have seen that an infinite expansion is needed to fully model the channel system. Since in practice an infinite expansion cannot be used to create a state-space model, we will always have some part of the system dynamics that is unmodelled. Furthermore, we have seen that the \mathbf{A} (dynamic) matrix may be decoupled by wavenumber.

Consider a partition of the state-space model as

$$\frac{dx}{dt} = \begin{bmatrix} \frac{dx_m}{dt} \\ \frac{dx_u}{dt} \end{bmatrix} = \begin{bmatrix} \mathbf{A}_m & 0 \\ 0 & \mathbf{A}_u \end{bmatrix} \begin{bmatrix} x_m \\ x_u \end{bmatrix} + \begin{bmatrix} \mathbf{B}_m \\ \mathbf{B}_u \end{bmatrix} u(t), \quad (4.6)$$

$$z = [\mathbf{C}_m \quad \mathbf{C}_u] x, \quad (4.7)$$

where the subscripts m and u represent the modelled and unmodelled parts of the system. In the channel flow problem, the unmodelled part is meant to denote only the dynamics of wavenumbers left out of the finite-dimensional model. Note that both \mathbf{A}_u and \mathbf{A}_m are of infinite dimension; \mathbf{A}_u because of the infinite number of wavenumbers left out of the reduced-order model and \mathbf{A}_m because of the infinite number of expansion functions needed in y for each of the finite number of modelled wavenumbers. One way to avoid considering unmodelled wavenumber dynamics is to ensure that the control input, $u(t)$, has no effect whatsoever on the unmodelled wavenumber dynamics. In terms of the state-space model (4.6), this is equivalent to rendering $\mathbf{B}_u = 0$. This is known as making the unmodelled wavenumber dynamics uncontrollable. By examining (3.27), we see that the \mathbf{B} matrix is formed from terms of S_{lk}^1 in (3.16). If $w(x)$ in (3.16) is such that $S_{lk}^1 = 0$, then those components of the \mathbf{B} matrix are zero. Equivalently, we must ensure that the projection of $w(x)$ onto the *unmodelled* wavenumbers is zero. Owing to the orthogonality of Fourier components, we select $w(x)$ to be made up of modelled Fourier components only.

5. Single-wavenumber channel model

Consider the channel model shown in figure 1. The total non-dimensional length of the channel, L , is 4π . In this case, the fundamental wavenumber, $\alpha_0 = 0.5$. Only one

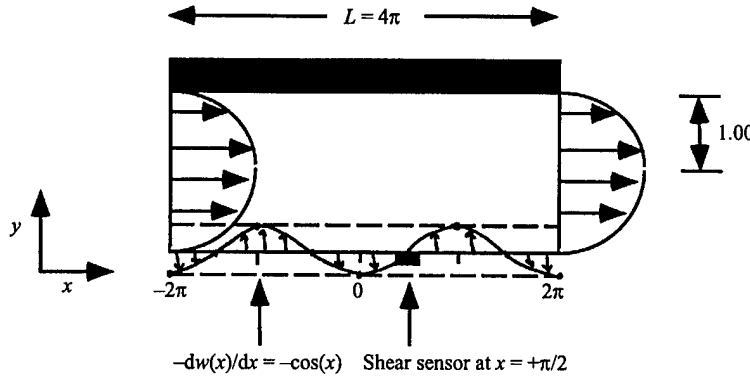


FIGURE 1. System model for Poiseuille flow. Input is applied along the bottom plate as $w(x) = \sin(x)$ and shear is measured at $x = \pi/2$ with $Re = 10000$ and $\alpha = 1.0$.

wavenumber is included in the model, corresponding to $\alpha = l\alpha_0 = 1.00$. The Reynolds number is chosen as $Re = 10000$. Input is distributed along the bottom plate with a sinusoidal weighting function in order to render the unmodelled wavenumber dynamics uncontrollable as described in §4. In terms of the input function, $w(x)$, see (2.12)

$$w(x) = \sin(x). \quad (5.1)$$

Note that the physical blowing/suction, $\hat{v}(x, y, t)$, takes the form

$$\hat{v}(x, y, t) = -q(t) \frac{\partial w(x)}{\partial x} f(y = -1) = -q(t) \cos(x) f(y = -1) \quad (5.2)$$

see (2.21). This type of input may be achieved in practice by a large number of independently controllable actuators that are distributed along the lower channel wall. The $f(y)$ function is chosen as in (2.20). The sensor location is $x = +\frac{1}{2}\pi$. In order to visualize the control-theoretic model, the system **A**, **B**, and **C** matrices are transformed to transfer function form, $H(s)$. Figure 2 shows the locations of the poles and zeros in the s -plane for the single-wavenumber model.

5.1. Relation of poles to eigenvalues of the Orr–Sommerfeld equation

Poles of the transfer function or, equivalently, eigenvalues of the **A** matrix are closely related to the eigenvalues of the Orr–Sommerfeld equation. Assume a solution of (2.6) of the form

$$\psi(x, y, t) \triangleq \beta(y) e^{i\alpha x} e^{-i\alpha c t}. \quad (5.3)$$

By substituting into (2.6), we obtain the familiar Orr–Sommerfeld equation in the normal-mode form,

$$[U(y) - c] \left(\frac{\partial^2 \beta(y)}{\partial y^2} - \alpha^2 \beta(y) \right) - \frac{\partial^2 U(y)}{\partial y^2} \beta(y) = \frac{1}{i\alpha Re} \left[\frac{\partial^4 \beta(y)}{\partial y^4} - 2\alpha^2 \frac{\partial^2 \beta(y)}{\partial y^2} + \alpha^4 \beta(y) \right]. \quad (5.4)$$

Here, the Reynolds number, Re , is known; the wavenumber, α , is assumed real and known; the complex wave speed, c , is the eigenvalue of the problem; and the function $\beta(y)$ is the eigenvector of the problem. Stability of a flow for a given value of Re and α is determined by the imaginary part of c . If the imaginary part is positive, the solution (5.3) becomes an unbounded exponential and flow is unstable. Poles of the

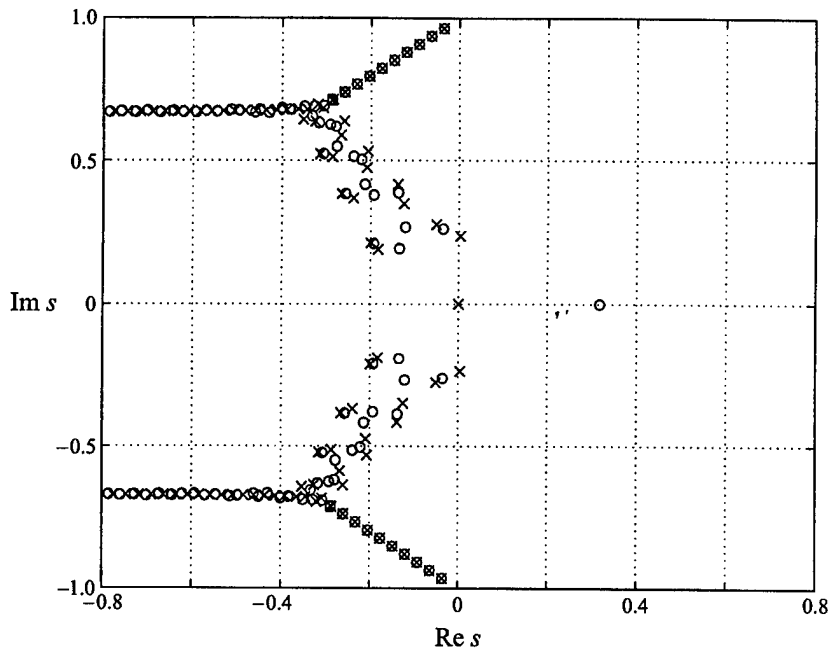


FIGURE 2. Pole (\times) and zero (\circ) configuration for the system model of figure 1. Note that all poles and zeros appear in complex-conjugate pairs. Each pair of complex-conjugate poles represents one mode of the system. One pair of poles is to the right of the imaginary axis. This indicates the system has one unstable mode. Note that the single pole at the origin represents a built-in integrator due to $u(t) = dq(t)/dt$. Channel model: $Re = 10000$, shear sensor at $\pi/2$, $w(x) = \sin(x)$, $L = 4\pi$, $\alpha = 1.0$.

transfer function in the Laplace domain at $s = p_i$ correspond to solutions in the time domain of $e^{p_i t}$. As a result, we observe that poles of the transfer function are related to eigenvalues of the Orr-Sommerfeld equation as

$$p_i \equiv -i\alpha c. \quad (5.5)$$

In order to validate our linear code, we compare our poles to eigenvalues produced in Orszag (1971). Orszag (1971) obtained Orr-Sommerfeld eigenvalues for the channel problem with $\alpha = 1.00$ and $Re = 10000$. He reported only one slightly unstable eigenvalue at $s = 0.00373967 + i0.23752649$ ($c = 0.23752649 - i0.00373967$). The eigenvalue is seen as unstable by its positive real part. We obtained identical results including the one unstable mode at

$$s = 0.00373967 \mp i0.23752649.$$

All other stable modes obtained in the present study are identical to those reported in Orszag (1971). The goal of our control system will be to move these unstable poles into the stable half of the s -plane or, equivalently, make sure the controlled-system poles all have real parts less than zero.

5.2. Verification of model zeros

Verification of the system zeros is more difficult due to the fact that no published results exist to our knowledge. We use the channel code simulation used in Kim, Moin & Moser (1987) to verify our zeros. This code is a spectral channel flow code which uses periodic boundary conditions. Consider the transfer function model (3.2)

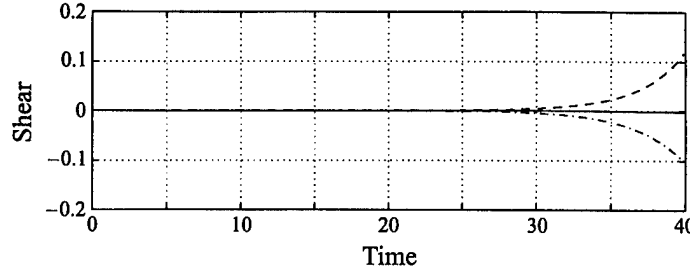


FIGURE 3. Output from the Navier–Stokes simulation with input applied as $u(t) = e^{+0.317557t}$. Although an unbounded input is applied, near zero output is observed at sensor location $\pi/2$ (solid curve). Sensor location 0 (dashed curve) and sensor location π (dash-dot curve) do not show zero output. Channel model: $Re = 10000$, shear sensor at $\pi/2$, $w(x) = \sin(x)$, $L = 4\pi$, $\alpha = 1.0$.

with $J = 1$ and $I = 1$:

$$H(s) = \frac{Z(s)}{U(s)} = \frac{(s - \zeta_1)}{(s - p_1)}. \quad (5.6)$$

In the Laplace domain,

$$sZ(s) - p_1Z(s) = sU(s) - \zeta_1U(s). \quad (5.7)$$

Assuming zero initial conditions and transforming into the time domain, (5.7) becomes

$$\frac{dz(t)}{dt} - p_1z(t) = \frac{du(t)}{dt} - \zeta_1u(t) \quad (5.8)$$

where $z(t)$ is the output function and $u(t)$ is the input function. If the input is taken as

$$u(t) = e^{\zeta_1 t} \quad (5.9)$$

then the right-hand side of (5.8) becomes zero and the system behaves as if zero input has been applied. As a result, $z(t)$ remains zero for all time. Therefore, we may verify zeros of the system by applying non-zero input in special ways and observing zero output. Note from figure 2 that for sensor location $x = +\frac{1}{2}\pi$, one zero exists in the right half plane at $s = +0.317557 + 0i$. This represents an ideal zero to check as this corresponds to an unbounded, unstable input. Figure 3 shows output from the Navier–Stokes simulation with input $u(t) = dq(t)/dt = e^{+0.317557t}$. Note that even though an unbounded, exponentially growing input is applied to the system, near zero output is observed at the sensor, thus verifying that ζ_1 is indeed a zero of the system. This is contrasted with measurements at different sensor locations that grow rapidly. With a sensor at a different location, the zeros of the system change position so zero output is no longer expected for this particular input. Absolute zero is not observed at sensor location $x = \frac{1}{2}\pi$ due to slight numerical inaccuracies in the model.

6. Feedback control and stabilization

At this point, with the construction of a valid state-variable model, any number of control schemes may be employed to stabilize the system. A general control system is shown in figure 4. The output of the system is fed into a controller. The output of the controller is then used to create an input to the system. The design of a controller that achieves certain system characteristics is the goal of control system design. Several

modern control techniques may be applied that require a state-variable model. In this paper, the primary goal will be system stability. For this purpose, a simple constant gain feedback with integral compensator will be shown to be sufficient.

6.1. Constant gain feedback with integral compensator

Figure 5 shows an integral compensator feedback control scheme. K is referred to as the gain of the feedback. The output of the system, in this case shear, is multiplied by a feedback gain, integrated in time, and then fed back as blowing and suction at the input. Note that the integrator is required because of the structure of the input given in (3.27), i.e. the input is taken as the derivative of suction/blowing. The signal, $r(t)$, is called the reference signal. It is used to define the desired output. In our case, we would like the shear output, $z(x_i, y = -1, t)$, to be zero. Therefore, we set $r(t)$ to zero. Then

$$u(t) \triangleq \frac{\partial q(t)}{\partial t} = -Kz(x_i, y = -1, t). \quad (6.1)$$

Therefore, assuming $q(0) = 0$,

$$q(t) = -K \int_0^t z(x_i, y = -1, \tau) d\tau \quad (6.2)$$

and by observing (2.21), we may describe physical blowing and suction at the boundary:

$$\hat{v}(x, y = -1, t) = -q(t) \frac{\partial w(x)}{\partial x} f(y = -1) = K \cos(x) \int_0^t z(x_i, y = -1, \tau) d\tau \quad (6.3)$$

As defined earlier,

$$H(s) \triangleq \frac{\mathcal{L}[z(t)]}{\mathcal{L}[u(t)]} = \frac{Z(s)}{U(s)}. \quad (6.4)$$

Therefore,

$$Z(s) = H(s)U(s). \quad (6.5)$$

In the absence of feedback, one mode is unstable. Also, one pole exists at the origin for the integrator. Consider a new transfer function from the reference input, $r(t)$, to the output, $z(t)$, in the presence of feedback:

$$u(t) = r(t) - Kz(t). \quad (6.6)$$

By taking the Laplace transform of (6.6),

$$U(s) = R(s) - KZ(s). \quad (6.7)$$

Then

$$Z(s) = H(s)[R(s) - KZ(s)]. \quad (6.8)$$

Finally,

$$\frac{Z(s)}{R(s)} = \frac{H(s)}{1 - KH(s)}. \quad (6.9)$$

The new poles of the feedback system are defined by

$$1 - KH(s) = 0. \quad (6.10)$$

As K gets larger and larger, it is clear that the poles of the new system tend toward the zeros of $H(s)$. In this way, modes of the system can sometimes be changed to

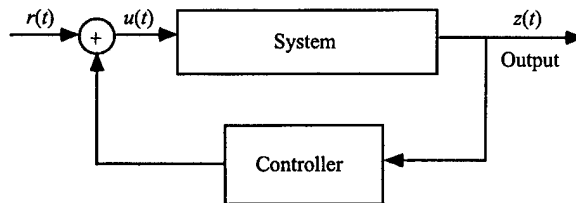


FIGURE 4. Feedback control. The output of the system is fed into a controller and then to the input.

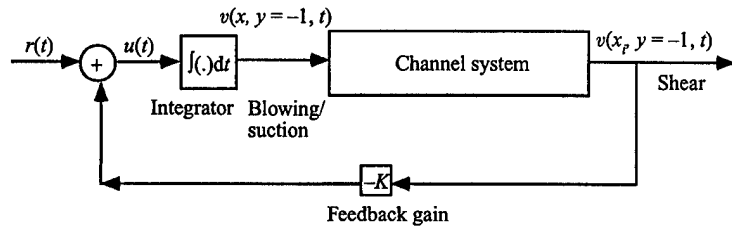


FIGURE 5. Feedback control for channel system. The output of the system is multiplied by a feedback gain, integrated in time, and then fed back at the input. The reference signal, $r(t)$, equals 0.

form a stable system (Franklin *et al.* 1988). Unstable modes that appear as poles on the right hand side of the complex s -plane and 'marginally stable' poles on the $\text{Im}(s)$ -axis are drawn to the left-hand side by applying feedback.

6.2. Sensor placement

We have seen that, by applying feedback, poles of the system will eventually be drawn to zeros of the system. In the channel flow system of figure 2, any feedback will cause either the pole at the origin (integrator pole) or the unstable mode poles to be drawn to the zero on the real axis in the right-hand plane, thus making the system unstable to a greater degree. Therefore, finding a transfer function that has all zeros in the left-hand plane becomes an important objective. The poles of the system are independent of sensing or actuation. However, the zeros of the system are dependent on both the type and location of sensing and the type and location of actuation. Figure 6 shows the pole/zero configuration for the channel model with the shear sensor at three different locations. Only the top half of the s -plane is shown since the bottom half is a mirror image projected across the real axis as shown in figure 2. The poles of all the models are in the same location as expected. However, the zeros are different in all three cases. In figures 6(a) and 6(b), we observe a lone zero in the right-hand s -plane. However, when the sensor is placed at $x = +\pi$, figure 6(c) shows all zeros in the left-hand plane. In fact, there is a region around $x = \pi$ that results in all zeros in the left-hand plane. By placing a shear sensor at $x = \pi$, simple feedback with integral compensation will allow stabilization with the proper value of gain, K . In the case of sensor locations that result in right-hand-plane, so called 'non-minimum phase', zeros stabilization is still possible. However, more complex controllers (Bryson & Ho 1975; Ogata 1990) must be designed that are beyond the scope of this paper.

6.3. Root locus analysis and numerical simulation

One way to visualize how system poles will change as the feedback gain, K , changes is to construct a root locus plot. This is a plot of all poles of a system as the feedback

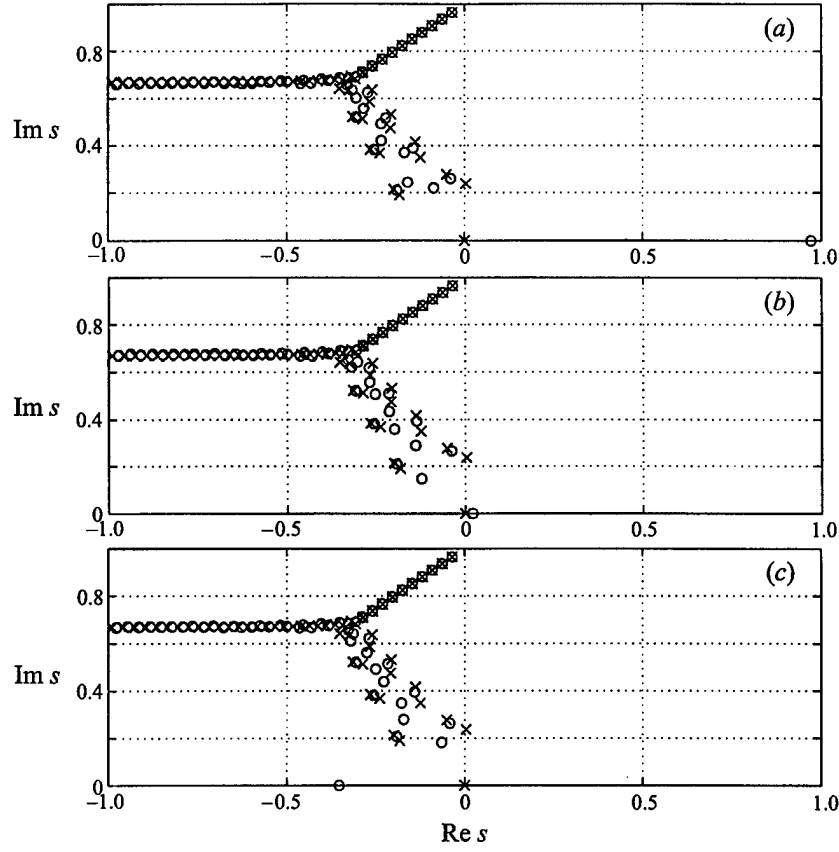


FIGURE 6. Pole (x)/zero (o) configuration. Channel model: $Re = 10000$, $w(x) = \sin(x)$, $L = 4\pi$, $\alpha = 1.0$. Only the top half of the s -plane is shown. Shear sensor at (a) $\pi/4$ (b) $3\pi/4$, (c) π .

gain varies from $K = 0$ to $K = \infty$. Figure 7 shows such a plot for the system shown in figure 6(c). When K reaches 0.1, all feedback system poles (closed-loop-poles) lie on the left-hand plane and no instabilities exist in the new feedback system. Numerical results obtained from the Navier-Stokes simulation for the new feedback controlled system are shown in figure 8. The computation is carried out without feedback until $t = 50$, after which the feedback is turned on. We see that the growing instability is quickly suppressed. At the instant the controller is turned on, the simulation shows a high transient response due to the non-continuous nature of the input at that time instant. In terms of the state space defined in (3.28), (3.35),

$$\frac{d\tilde{p}}{dt} = \mathbf{A}\tilde{p} + \mathbf{B}u(t), \quad (6.11)$$

$$z(x_i, y = -1, t) = \mathbf{C}\tilde{p}, \quad (6.12)$$

$$u(t) = -Kz(x_i, y = -1, t). \quad (6.13)$$

Then, in a closed loop,

$$\frac{d\tilde{p}}{dt} = \mathbf{A}\tilde{p} - \mathbf{B}(Kz(x_i, y = -1, t)) \quad (6.14)$$

$$= \mathbf{A}\tilde{p} - \mathbf{B}K\mathbf{C}\tilde{p} = (\mathbf{A} - \mathbf{B}K\mathbf{C})\tilde{p} \quad (6.15)$$

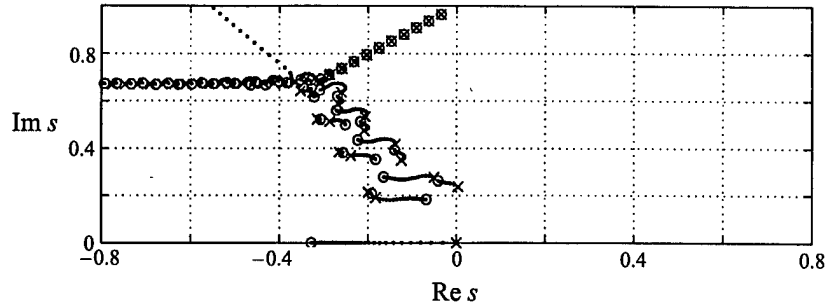


FIGURE 7. Root locus plot for channel system with input as in the channel model (figure 1) and shear output at $x = \pi$. The poles start at the open-loop poles shown with \times 's. As K increases, they start to move toward the location of the system zeros, shown as \circ 's. The pole at position $s = (0,0)$ moves directly to the left. The unstable pole moves quickly to a position just to the left of the imaginary axis. Near $0.7 < y < 1.0$, $-0.6 < x < -0.4$, we see a pole moving towards a zero that is out of the range of this figure. Channel model: $Re = 10000$, shear sensor at π , $w(x) = \sin(x)$, $L = 4\pi$, $\alpha = 1.0$. Only the top half of the s -plane is shown.

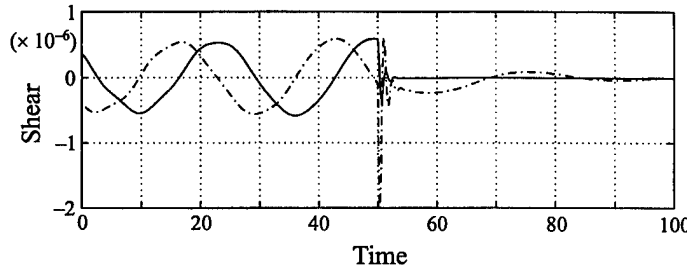


FIGURE 8. Navier-Stokes simulation of feedback control. Shear is multiplied by a feedback gain, integrated, and fed back into the input. Channel model: $Re = 10000$, feedback shear sensor at π , $w(x) = \sin(x)$, $L = 4\pi$, $\alpha = 1.0$. Curve 1 (solid) shows shear at location π ; curve 2 (dot-dash) shows shear at location $\pi/2$.

The solution to this equation is

$$\tilde{p}(t) = e^{At - BK\tilde{C}t} \tilde{p}(t=0). \quad (6.16)$$

This solution will approach zero as $t \rightarrow \infty$ since the eigenvalues of $A - BKC$ (closed-loop poles) are all stable.

6.4. Robustness in the presence of Reynolds number uncertainty

A major advantage of feedback control systems is their robustness to system uncertainty. From a practical point of view, Reynolds numbers may not be known exactly or may change frequently as in the flight of an airplane, for example. Figure 9 shows the open-loop pole/zero configurations for systems with varying Reynolds numbers. Note that these systems start with all zeros in the left-hand s -plane. A root locus analysis shows that a feedback system with $K = 0.1$ stabilizes both systems. Indeed, a feedback gain of $K = 0.1$ stabilizes systems for a wide range of Reynolds numbers from $Re = 1000$ to $Re = 40000$. Figure 10 shows the least-stable pole in both the controlled and uncontrolled systems for several Reynolds numbers. Recall that a pole with real part less than zero is stable. We see near $Re = 5772$, an unstable pole appears in the open-loop (uncontrolled) system. Unstable eigenvalues continue to exist in the open-loop system until

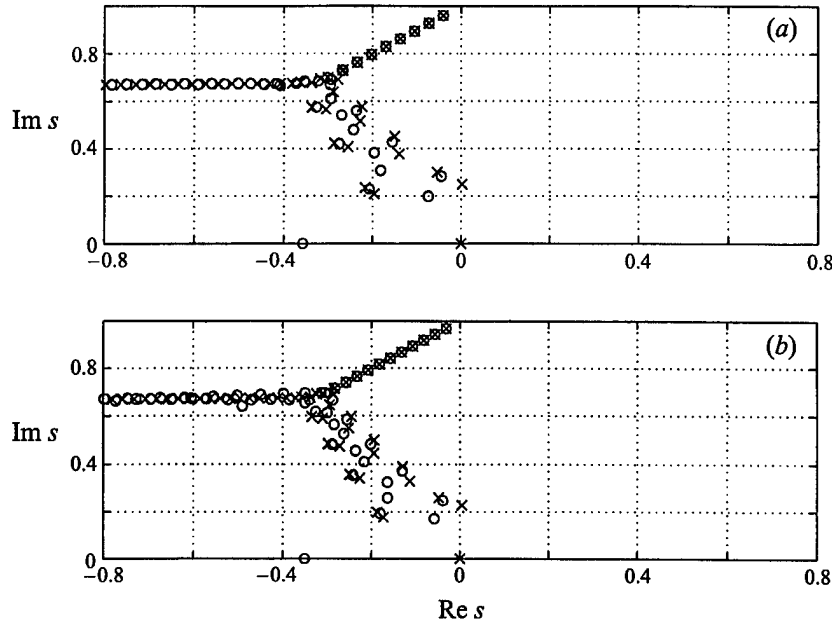


FIGURE 9. Pole (\times)/zero (\circ) configuration. Channel model: shear sensor at π , $w(x) = \sin(x)$, $L = 4\pi$, $\alpha = 1.0$. Only the top half of the s -plane is shown. (a) $Re = 7500$, (b) $Re = 12500$.

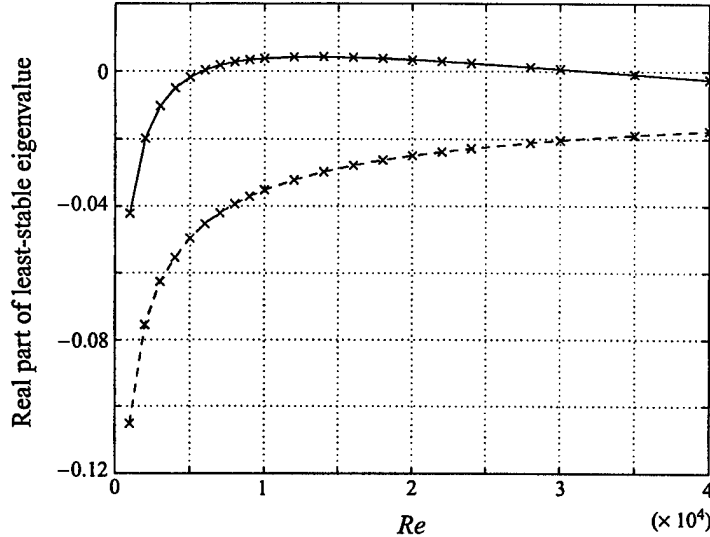


FIGURE 10. Real part of least-stable pole for open-loop (solid line) and closed-loop (dashed line) channel system with $1000 \leq Re \leq 40000$. Shear sensor at π , $w(x) = \sin(x)$, $L = 4\pi$, $\alpha = 1.0$. Data points are shown as \times 's.

$30000 \leq Re \leq 35000$. An identical feedback controller, with gain $K = 0.1$, however, stabilizes the system for Reynolds numbers in the range $1000 \leq Re \leq 40000$. Clearly, the feedback controller is extremely robust to changes in Reynolds number.

7. Unobservable transient response as a path of bypass transition

Recently, some authors (Trefethen *et al.* 1993; Butler & Farrell 1992; Farrell 1988; Henningson 1994) have suggested a possible path of bypass transition in Poiseuille flow that is caused by high transient response due to the non-self-adjointness of the evolution matrix. This high-transient behaviour is due to the non-orthogonality of the eigenmodes and not caused by any single mode, but rather a combination of many modes. In this section, we suggest a possible different form of bypass transition *in a controlled system* due to a single mode. In the presence of any type of control, it is possible that energy from an input is fed into a mode such that the mode is reinforced during the transient period before it eventually dies out. During the transient period, however, the mode may grow to an amplitude large enough to trigger nonlinear effects that induce transition to turbulence. This may be a possible path of bypass transition in a controlled system.

Single modes may be characterized in linear systems in terms of modal controllability and modal observability. Modal controllability implies that a particular mode may be affected by the actuators chosen (blowing/suction in our case). Modal observability implies that a particular mode may be measured by the sensors chosen (shear in our case). A particular mode may be non-observable, non-controllable, or both. This will be seen in §§7.1 and 7.2. If high-transient modes are controllable and observable, control theory may be used to suppress them. However, if high-transient modes are unobservable, the high transients will never be seen and feedback control cannot be used to suppress them.

7.1. Modal canonical form

The state-space formulation provides an excellent framework for assessing the reinforcement of each mode individually. Consider an n -dimensional state space with scalar input and output

$$\frac{dx}{dt} = Ax + Bu, \quad (7.1)$$

$$z = Cx. \quad (7.2)$$

We may perform a similarity transformation on the system to produce a new state-space representation with the same input–output relationship, but with a different interpretation of the state variables. Let

$$P \triangleq [v_1 \ v_2 \ \dots \ v_n] \quad (7.3)$$

where v_j is the j th eigenvector of the A matrix and n is the dimension of the A matrix. A new representation is constructed as (Grace *et al.* 1992; Kailath 1980)

$$\frac{d\tilde{x}}{dt} = P^{-1}AP\tilde{x} + P^{-1}Bu, \quad (7.4)$$

$$z = CP\tilde{x} \quad (7.5)$$

where $\tilde{x} \triangleq P^{-1}x$. The new representation is written as

$$\frac{d\tilde{x}}{dt} = \tilde{A}\tilde{x} + \tilde{B}u, \quad (7.6)$$

$$z = \tilde{C}\tilde{x} \quad (7.7)$$

where the real eigenvalues of the original A matrix appear on the diagonal of \tilde{A} and the complex eigenvalues appear in a 2×2 block on the diagonal of \tilde{A} . For an A

matrix with eigenvalues $(\alpha_1, \sigma \pm j\omega, \alpha_2)$, the $\tilde{\mathbf{A}}$ matrix is

$$\tilde{\mathbf{A}} = \begin{bmatrix} \alpha_1 & 0 & 0 & 0 \\ 0 & \sigma & \omega & 0 \\ 0 & -\omega & \sigma & 0 \\ 0 & 0 & 0 & \alpha_2 \end{bmatrix}. \quad (7.8)$$

In this form, each state-variable pair represents a mode of the system. Furthermore, the modes are block decoupled so that each mode is represented by the 2×2 system

$$\begin{bmatrix} \frac{d\tilde{x}_1}{dt} \\ \frac{d\tilde{x}_2}{dt} \end{bmatrix} = \begin{bmatrix} \sigma & \omega \\ -\omega & \sigma \end{bmatrix} \begin{bmatrix} \tilde{x}_1 \\ \tilde{x}_2 \end{bmatrix} + \begin{bmatrix} \tilde{b}_1 \\ \tilde{b}_2 \end{bmatrix} u, \quad (7.9)$$

$$z_1 = [\tilde{c}_1 \quad \tilde{c}_2] \begin{bmatrix} \tilde{x}_1 \\ \tilde{x}_2 \end{bmatrix}, \quad (7.10)$$

where ω , σ , \tilde{b}_1 , \tilde{b}_2 , \tilde{c}_1 , and \tilde{c}_2 are all scalars. This is known as the modal canonical state-space form. All modes can be monitored directly for high-transient reinforcement in this form.

7.2. Modal observability and controllability

It is easy to see that if \tilde{b}_1 and \tilde{b}_2 are zero, no input can affect the mode and the mode is uncontrollable. Similarly, if \tilde{c}_1 and \tilde{c}_2 are zero, then the motion of \tilde{x}_1 and \tilde{x}_2 cannot be measured at the output, z_1 , and the mode is unobservable. In terms of stabilization, an uncontrollable mode is not problematic as long as it is stable. However, if an unstable mode is uncontrollable, nothing can be done to stabilize it. Observability may be a problem even if modes are stable. If an unobservable mode is highly amplified by control energy, no attempt could be made to suppress it since it would not be observed at the output. In terms of poles and zeros, uncontrollable or unobservable modes both show up as pole/zero cancellations in the complex s -plane. As can be seen from figure 2, many poles and zeros for the channel system lie on top of each other, indicating that certain modes in the system are either uncontrollable, unobservable, or both. Although a mode may not be physically observable at the output, the modal canonical formulation allows us to numerically observe the state evolution of each mode directly. In this way, we may assess the risk of highly amplified modes triggering bypass transition. This is done for the controlled system simulated in figure 8. The uncontrolled linear system is simulated with an initial condition for 200 time steps at which time a feedback controller with gain $K = 0.1$ is turned on. Figure 11 shows the state evolution of the modes with poles at $s = -0.1474 \pm 0.8514i$ and $s = -0.3252 \pm 0.6361i$ as well as the state evolution of the one unstable mode.[†] In addition, figure 11(a) shows the shear measurement at the output. We see that the unstable mode dies out quickly as soon as the feedback is turned on. In addition, the mode at $s = -0.1474 \pm 0.8514i$ gains almost no energy after the feedback is activated. This indicates that the mode is not a bypass mode. The mode at $s = -0.3252 \pm 0.6361i$ is seen to gain a lot of energy after the controller is started. Indeed, the amplitude of the transient response is nearly twice that of the unstable mode. This represents a possible bypass mode since such an amplitude

[†] Note that amplitudes shown as a result of linear system simulations should only be used for comparison with each other since the linear model has been scaled to unity open-loop feedforward gain, i.e. $H(s) = \kappa Z(s)/U(s)$ where $\kappa = 1$.

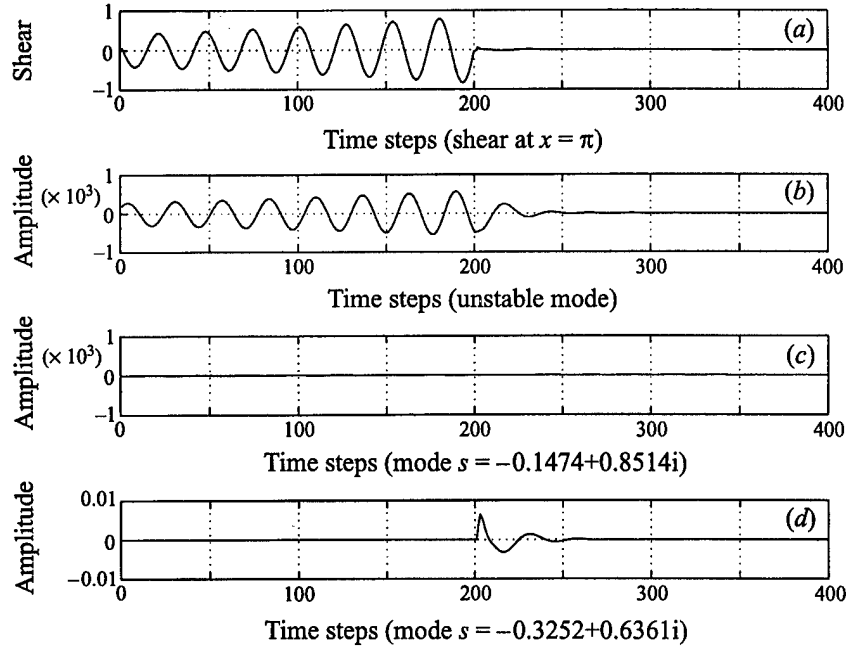


FIGURE 11. Linear model state evolution of system modes with control applied at $t = 200$: (a) measured shear, (b) the state evolution of the unstable mode, (c) the state evolution of the mode at $s = -0.1474 + 0.8514i$, (d) the state evolution of the mode at $s = -0.3252 + 0.6361i$. Channel model: $Re = 10000$, shear sensor at π , $w(x) = \sin(x)$, $L = 4\pi$, $\alpha = 1.0$.

may force the system into the nonlinear region where transition to turbulence may be triggered. Furthermore, the high energy nature of the mode cannot be observed at the shear sensor since this mode is unobservable. This can be seen from the plot of the shear sensor output. Modal un-observability is also suggested by noting the relatively low \tilde{c}_1 and \tilde{c}_2 values of 0.5155, -0.1131 compared to the \tilde{c}_1 and \tilde{c}_2 values of -162.85, 234.66 for the unstable mode which is clearly seen at the output. Fortunately, the high energy nature of the mode does not lead to a bypass transition in this case. This is verified by the Navier-Stokes simulation in figure 8, which shows no nonlinear effects. If the instability were allowed to grow to a higher amplitude before the controller was applied, however, the highly amplified mode in the transient response might have triggered nonlinear effects.

8. Multiple instability control

Although most work has focused on suppression of single instabilities, more realistic models should include multiple wavenumbers. Indeed, for a given Reynolds number, an infinite number of wavenumbers exist. Each wavenumber contributes its own poles and zeros to the control-theoretic model. Consider a model with non-dimensional channel length 20π , where input is applied as $w(x) = \sin(x) + \sin(0.9x)$. In this model, wavenumbers of 0.9 and 1.0 are included. Both wavenumbers lead to unstable modes. The pole/zero configuration of this new two-wavenumber model with shear sensor at π is shown in figure 12(a). Note that in comparison to the one-wavenumber model, more poles and zeros exist. The original one-wavenumber model contained one 'fork' structure of poles, while the two-wavenumber model contains two 'fork'

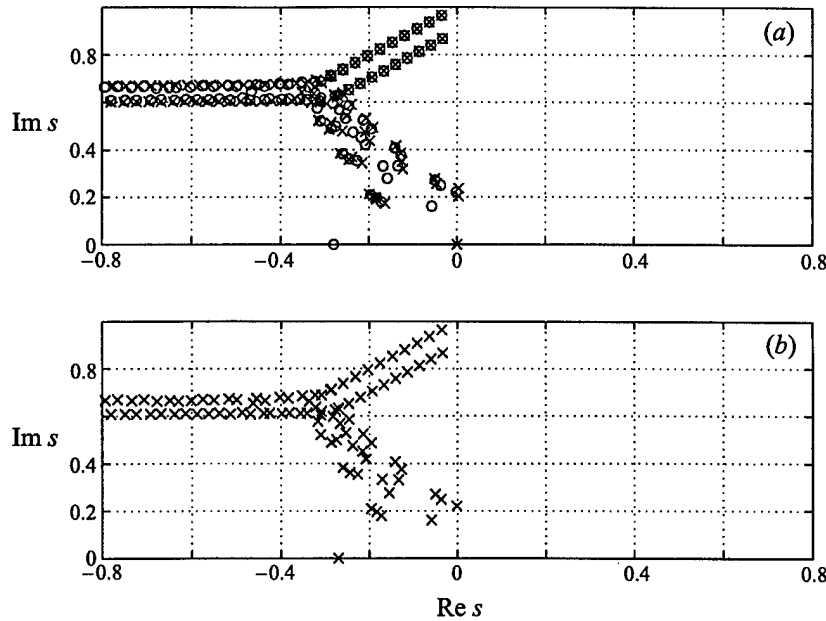


FIGURE 12. (a) Pole (\times) and zero (\circ) configuration of channel system of length 20π , including wavenumbers of 0.90 and 1.00. $Re = 10000$, shear sensor at π , $w(x) = \sin(x) + \sin(0.9x)$. Only the top half of the s -plane is shown. (b) Same as (a) but showing closed-loop poles after feedback with gain $K = 0.1$.

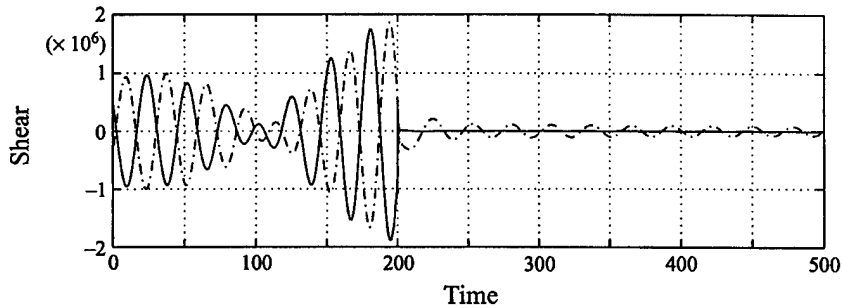


FIGURE 13. Navier-Stokes simulation of channel system of length 20π , including wavenumbers of 0.90 and 1.00. $Re = 10000$, feedback shear sensor at π , $w(x) = \sin(x) + \sin(0.9x)$, feedback gain $K = 0.1$. Curve 1 (solid) shows shear at location π ; curve 2 (dash-dot) shows shear at location 2π .

structures. It can be visualized that in a model with several wavenumbers, several 'forks' will stack on top of each other in the s -plane. Near $s = i0.2$ are two unstable poles in the right-hand plane that represent the two unstable modes in the system. As seen before, all zeros lie in the left hand s -plane. Figure 12(b) shows the closed-loop poles after feedback with gain $K = 0.1$. Results from the Navier-Stokes simulation are shown in figure 13. The computation is carried out without feedback until $t = 200$. A combination of two growing waves is seen at the shear sensor. At $t = 200$, feedback with integral compensation is applied and the system is stabilized.

9. Effect of linear controllers on two-dimensional finite-amplitude disturbances

The critical Reynolds number above which linear instabilities exist in plane Poiseuille flow is $Re \approx 5772$. Below this Reynolds number, Poiseuille flow is linearly stable. However, transition from laminar to turbulent flow occurs in experiments at much lower Reynolds numbers, typically around $Re = 1000$. Moreover, even for super-critical Reynolds number flows, linear instabilities predict extremely slow growth rates. In practice, transition occurs orders of magnitude more quickly. Therefore, linear stability alone does not dictate transition. Transition to turbulence is generally accepted to be a nonlinear three-dimensional phenomenon. In previous sections, we constructed two-dimensional linear controllers based on the two-dimensional linearized Navier–Stokes equations. By applying these controllers to plane Poiseuille flow with infinitesimal two-dimensional disturbances, we saw that we may linearly stabilize the system so that the flow could no longer support those disturbances. If we apply our linear controllers to flows that contain finite-amplitude disturbances, we can no longer use linear analysis to describe the flow dynamics as nonlinear terms become relevant. However, the application of a controller based on linear analysis does change the nonlinear system.

Many authors (Orszag & Patera 1983; Bayly, Orszag & Herbert 1988) have explored the effect of two-dimensional finite-amplitude disturbances on three-dimensional infinitesimal disturbances in plane Poiseuille flow. Above $Re \approx 2900$, for two dimensions, stable non-attenuating finite-amplitude equilibria exist in plane Poiseuille flow. Below $Re \approx 2900$, non-decaying, finite-amplitude equilibria do not exist. However, in flows with $1000 \leq Re \leq 2900$, the timescale for decay is so large that the flow may be considered in ‘quasi-equilibrium’. It has been shown that in the presence of such two-dimensional finite-amplitude disturbances, infinitesimal three-dimensional disturbances are highly unstable and may cause transition in shear flows. Figure 14 shows the energy of a single-wavenumber, two-dimensional finite-amplitude disturbance ($\alpha = 1.0$) and a single-wavenumber-pair, three-dimensional infinitesimal disturbance ($\alpha = 1.0, \beta = \mp 1.0$) obtained through direct numerical simulation at $Re = 3000$. The maximum amplitude of the two-dimensional finite-amplitude disturbance is $0.1U_c$. At this Reynolds number, wavenumber, and initial energy level, we see the two-dimensional finite-amplitude disturbance decaying slowly. The three-dimensional disturbance, on the other hand, is seen to rapidly gain energy. Orszag & Patera (1983) show that the two-dimensional instability acts as a mediator for transfer of energy from the mean flow to the three-dimensional disturbance, but does not directly provide energy. The growth rate of the three-dimensional disturbance is orders of magnitude larger than that of the Orr–Sommerfeld instabilities.

Orszag & Patera show, in the case where $Re \leq 1000$, that the attenuation of finite-amplitude two-dimensional disturbances is large enough that three-dimensional disturbances do not become unstable. The fact that high attenuation of the two-dimensional finite-amplitude disturbance prevented three-dimensional instability below $Re \approx 1000$ suggests that if controllers can be created that speed up the attenuation of the finite-amplitude two-dimensional disturbance for flows with Reynolds numbers greater than 1000, three-dimensional instability may be eliminated. We have seen in §6 that linear controllers did stabilize infinitesimal two-dimensional disturbances. Figure 15 shows the effects of the linear controller of §6 when applied to a system with the same finite-amplitude two-dimensional disturbance and infinitesimal three-dimensional disturbance shown in figure 14. The linear controller

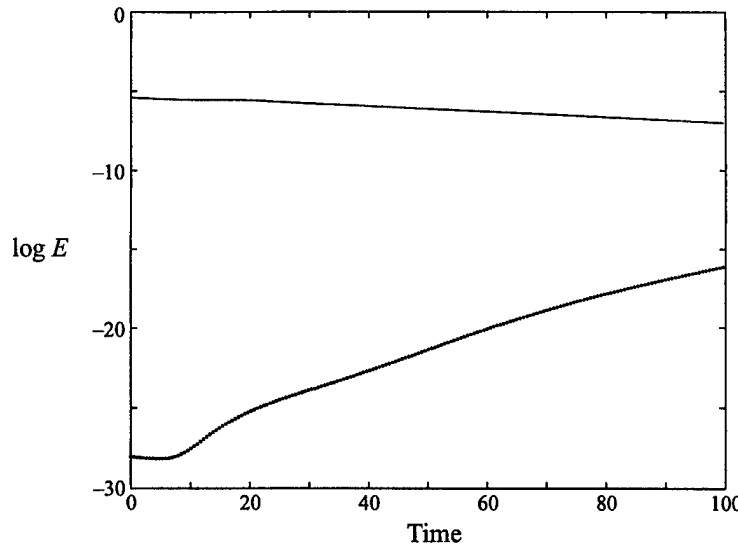


FIGURE 14. Energy of a two-dimensional finite-amplitude disturbance ($\alpha = 1.0$) and a three-dimensional infinitesimal disturbance ($\alpha = 1.0, \beta = \mp 1.0$) for $Re = 3000$. Solid line represents the total energy of the two-dimensional finite-amplitude disturbance and the dotted line represents that of the three-dimensional infinitesimal disturbance.

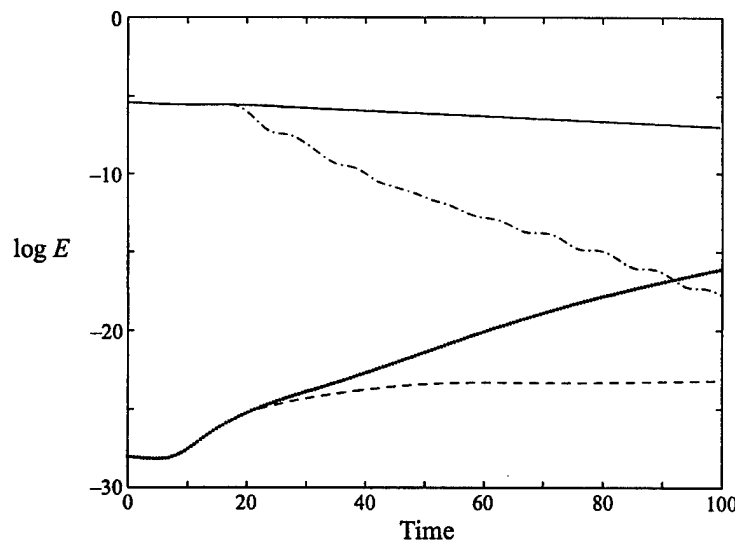


FIGURE 15. Effect of linear controller when applied at $t = 15$ for $Re = 3000$. The top two lines show the two-dimensional finite-amplitude disturbance without (solid) and with (dash-dot) linear control. We see at $t = 15$ that the controlled two-dimensional finite-amplitude disturbance is highly damped. The bottom two lines show the infinitesimal three-dimensional disturbance without (dot) and with (dashed) linear control. That without controller quickly fails to gain energy, while that with controller quickly fails to gain energy.

dramatically increased the attenuation of the finite-amplitude two-dimensional disturbance. As a result, the infinitesimal three-dimensional disturbance was rendered stable. Clearly, the linear controller not only stabilized the two-dimensional linear system, but also had a stabilizing effect on the three-dimensional nonlinear system. These results show the promise of linear controllers even in nonlinear systems.

10. Conclusions

In this paper, we have developed feedback controllers that linearly stabilize plane Poiseuille flow. We used a Galerkin spectral method to generate state-space models. Indeed, any (convergent) numerical method that reduces the governing partial differential equations into a set of ordinary-differential equations may be used. It is important to note, however, that the meaning of the state variables in the state-space model changes as different numerical methods are employed. Even though state variables may not have any specific physical meaning, some numerical methods may result in favourable divisions of system dynamics. In the plane Poiseuille flow case, the spectral Galerkin method with the use of Fourier components in the x -direction and combination-Chebyshev polynomials in the y -direction led to modelled dynamics that were de-coupled by wavenumber. This led to a block diagonal form of the A matrix. As a result, we were clearly able to describe modelled and unmodelled dynamics in terms of wavenumber dynamics included and not included in our finite-dimensional model. This also led us to the concept of using distributed control to render certain wavenumbers 'uncontrollable'. If other numerical methods had been used, this concept would not have been so transparent. Furthermore, plane Poiseuille flow can be linearly stabilized with simple feedback controllers if sensors are placed at judicious locations. Both the position and the type of sensing and actuation change the zeros of single-input/single-output models. In our case, we have seen that certain shear sensor locations lead to 'minimum-phase' systems and some locations lead to 'non-minimum phase' systems. Minimum-phase systems are in general easier to control than non-minimum phase systems. As a result, we were able to stabilize plane Poiseuille flow with a constant gain feedback, integral compensator controller. In addition, the controller was extremely robust to a wide range of Reynolds numbers. Also, we have shown that one danger of feedback control is that the linear transient response of a controlled system can lead to high amplitudes for a short period of time. If these amplitudes are high enough, it is possible that they may invalidate the linear model and enhance nonlinear effects. Furthermore, the high transients may not be observable at the output so that feedback control cannot be used to suppress them. Finally, we have shown that linear controllers have a strong stabilizing effect on two-dimensional finite-amplitude disturbances. As a result, three-dimensional secondary instabilities can be rendered stable.

This research was performed under grant number F49620-93-1-0332 from the United States Air Force. The authors would like to thank Professors J. S. Gibson and Robert Kelly of the UCLA Mechanical and Aerospace engineering department for many helpful discussions and suggestions. The authors are also grateful to Mr. Jaisig Choi who performed the computations presented in §9. Computer resources have been provided by the NAS program at NASA Ames Research Center.

REFERENCES

BAYLY, B. J., ORSZAG, S. A. & HERBERT, T. 1988 Instability mechanisms in shear-flow transition. *Ann. Rev. Fluid Mech.* **20**, 359–391.

BERINGEN, S. 1984 Active control of transition by periodic suction and blowing. *Phys. Fluids* **27**, 1345–1348.

BOWER, W. W., KEGELMAN, J. T. & PAL, A. 1987 A numerical study of two-dimensional instability-wave control based on the Orr-Sommerfeld equation. *Phys. Fluids* **30**, 998–1004.

BRYSON, A. E. JR. & HO, T.-C. 1975 *Applied Optimal Control*. Taylor and Francis.

BURNS, J. A. & OU Y.-R. 1994 Feedback control of the driven cavity problem using LQR designs. *Proc. 33rd Conf. on Decision and Control, December, 1994*, pp. 289–294.

BUTLER, K. M. & FARRELL, B. F. 1992 Three-dimensional optimal perturbations in viscous shear flows. *Phys. Fluids A* **4**, 1637–1650.

CHOI, H., MOIN, P. & KIM, J. 1994 Active turbulence control for drag reduction in wall bounded flows. *J. Fluid Mech.* **262**, 75–110.

DRAZIN, P. G. & REID, W. H. 1981 *Hydrodynamic Stability*. Cambridge University Press.

FARRELL, B. F. 1988 Optimal perturbations in viscous shear flows. *Phys. Fluids* **31**, 2093–2102.

FRANKLIN, G., POWELL, J. D. & EMAMI-NAEINI, A. 1988 *Feedback Control of Dynamic Systems*. Addison-Wesley.

GRACE, A., LAUB, A. J., LITTLE, J. N. & THOMPSON, C. M. 1992 *Control System Toolbox: For use with MATLAB*. The Math Works.

GUNZBURGER, M. D., HOU, L. & SVOBODNY, T. 1992 Boundary velocity control of incompressible flow with an application to viscous drag reduction. *SIAM J. Control Optimization* **30**, 167–181.

HENNINGSON, D. S. 1994 Bypass transition – Proceedings from a Mini-workshop. *Tech. Rep.* Royal Institute of Technology, Department of Mechanics, S-100,44, Stockholm, Sweden.

JOSHI, S. S. 1996 A systems theory approach to the control of plane Poiseuille flow. PhD thesis, UCLA, Department of Electrical Engineering.

JOSLIN, R. D., ERLEBACHER, G. & HUSSAINI, M. Y. 1994 Active control of instabilities in laminar boundary layer flow- Part I: An overview. *ICASE Rep. 94–97*. NASA Langley Research Center, Hampton, VA.

KAILATH, T. 1980 *Linear Systems*. Prentice-Hall.

KIM, J., MOIN, P. & MOSER, R. 1987 Turbulence statistics in fully developed channel flow at low Reynolds numbers. *J. Fluid Mech.* **177**, 133–166.

KREISS, H.-O. & LORENZ, J. 1989 *Initial Boundary Value Problems and the Navier-Stokes Equations*. Academic.

LADYZHENSKAYA, O. A. 1969 *The Mathematical Theory of Viscous Incompressible Flow*. Gordon and Breach.

NOSENCHUCK, D. M. 1982 Passive and active control of boundary layer transition. PhD thesis, California Institute of Technology.

OGATA, K. 1990 *Modern Control Engineering*. Prentice-Hall.

ORR, W. M'F. 1907 The stability or instability of the steady motions of a perfect liquid and of a viscous liquid. *Proc. R. Irish Acad. A* **27**, 9–68.

ORSZAG, S. A. 1971 Accurate solution of the Orr Sommerfeld stability equation. *J. Fluid Mech.* **50**, 689–703.

ORSZAG, S. A. & PATERA, A. T. 1983 Secondary instability of wall-bounded shear flows. *J. Fluid Mech.* **128**, 347–385.

REED, H. L. & NAYFEH, A. H. 1986 Numerical perturbation technique for stability of flat plate boundary layer with suction. *AIAA J.* **24**,

SCHUBAUER, G. B. & SKRAMSTAD, H. K. 1947 Laminar boundary layer oscillations and stability of laminar flow. *J. Aeronaut. Sci.* **14**, 68–78.

SOMMERFELD, A. 1908 Ein Beitrag zur hydrodynamicischen Erklaerung der turbulenten Flues-sigkeitsbewegungen. *Proc. 4th Intl Congress of Mathematics*, Vol. III, pp. 116–124.

TEMAM, R. 1984 *Navier-Stokes Equations*. North-Holland.

TREFETHEN, L. N., TREFETHEN, A. E., REDDY, S. C. & DRISCOLL, T. A. 1993 Hydrodynamic stability without eigenvalues. *Science* **261**, 578–584.

Application of neural networks to turbulence control for drag reduction

Changhoon Lee and John Kim^{a)}

Department of Mechanical and Aerospace Engineering, University of California at Los Angeles,
Los Angeles, California 90095-1597

David Babcock and Rodney Goodman

Department of Electrical Engineering, California Institute of Technology, Pasadena, California 91125

(Received 16 September 1996; accepted 24 February 1997)

A new adaptive controller based on a neural network was constructed and applied to turbulent channel flow for drag reduction. A simple control network, which employs blowing and suction at the wall based only on the wall-shear stresses in the spanwise direction, was shown to reduce the skin friction by as much as 20% in direct numerical simulations of a low-Reynolds number turbulent channel flow. Also, a stable pattern was observed in the distribution of weights associated with the neural network. This allowed us to derive a simple control scheme that produced the same amount of drag reduction. This simple control scheme generates optimum wall blowing and suction proportional to a local sum of the wall-shear stress in the spanwise direction. The distribution of corresponding weights is simple and localized, thus making real implementation relatively easy. Turbulence characteristics and relevant practical issues are also discussed. © 1997 American Institute of Physics. [S1070-6631(97)02706-2]

I. INTRODUCTION

The ability to control turbulent flows is of significant economic interest. Successful control of turbulent boundary layers by reducing drag, for example, can result in a substantial reduction in operational cost for commercial aircraft and marine vehicles. Recent studies^{1,2} show that near-wall streamwise vortices are responsible for high skin-friction drag in turbulent boundary layers. Some attempts have been made to reduce the skin-friction drag by controlling the interactions between these vortices and the wall. Choi *et al.*,² for example, used blowing and suction at the wall equal and opposite to the wall-normal component of velocity at $y^+ = 10$. They showed that this control effectively mitigated the streamwise vortices, giving approximately 25% drag reduction in a turbulent channel flow. Although the method employed in their work is impractical, since the information at $y^+ = 10$ is usually not available, it demonstrates a control scheme which reduces skin-friction drag by manipulation of the near-wall streamwise vortices. Another way to control the streamwise vortices is to impose spanwise oscillation by a moving wall or externally imposed body force.^{3,4} These methods, however, require a large amount of energy input.

A systematic approach using suboptimal control theory has also been tried in the past. This approach, which attempts to minimize a cost function, was successfully applied to the stochastic Burgers equation.⁵ Moin and Bewley⁶ applied a similar approach to a turbulent channel flow to achieve up to 50% drag reduction. The control, however, requires information from the entire velocity field inside the flow domain and excessive computational time, making it impractical to implement in real situations. For practical implementation, a control scheme should utilize only quantities that are easily

measurable at the wall, and should be fast enough to be applied in real time.

The objective of the present work is to seek wall actuations, in the form of blowing and suction at the wall, dependent on the wall-shear stress to achieve a substantial skin-friction reduction. This requires knowledge of how the wall-shear stresses respond to wall actuations, i.e., the correlation between the wall-shear stresses and the wall actuations. Because of the complexity of the solutions to the Navier-Stokes equations, however, it is not possible to find such a correlation in closed form or to approximate it in simple form. Instead, we use a neural network to approximate the correlation which then predicts the optimal wall actuations to achieve the minimum value of the skin-friction drag. Neural networks have been used to obtain complicated, nonlinear correlations without *a priori* knowledge of the system that is to be controlled. Jacobson and Reynolds,⁷ for instance, used a neural network to obtain about 7% drag reduction in their simulation of an artificial flow. In this paper, we describe how we constructed and trained a neural network off-line, and then implemented an on-line control scheme (blowing and suction at the wall) for drag reduction based on that neural network. Applying this control scheme to direct numerical simulations of turbulent channel flow at low Reynolds number, we observed about 20% drag reduction. We then describe how examination of the weight distribution from the on-line neural network led to a very simple control scheme that worked equally well while being computationally more efficient.

In Sec. II, a brief description of the architecture of the neural network used in the present work is given. In Sec. III, results obtained from control using an off-line trained network are presented, while results obtained from control using a network with continuous on-line training are given in Sec. IV. In Sec. V, a simple control law based on the weight distribution from the successful neural network control is presented. A few turbulence statistics are given in Sec. VI,

^{a)}Corresponding author. Telephone: (310)825-4393; Fax: (310)206-4830;
Electronic mail: jkim@turb.seas.ucla.edu

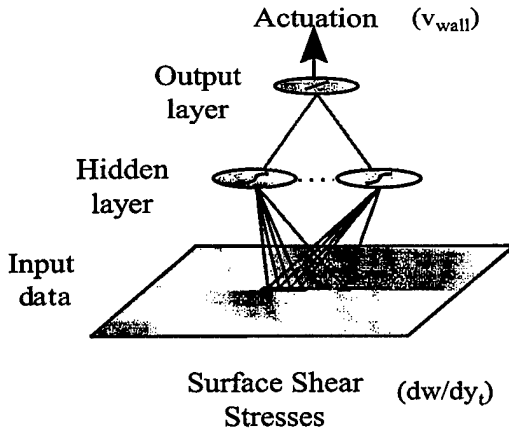


FIG. 1. Neural network architecture.

followed in Sec. VII by a discussion of practical implementation and the conclusions.

In this paper we use (x, y, z) for the streamwise, wall-normal, and spanwise coordinates, respectively, and (u, v, w) for the corresponding velocity components.

II. NEURAL NETWORK

In this section we describe the construction of a neural network to learn the correlation between wall-shear stresses and wall actuations from a given data set. Although a neural network generally requires no prior knowledge of the system (or “plant”), knowledge about the near-wall turbulence structures provides a guideline for the design of the network architecture. Initially $\partial u / \partial y$ and $\partial w / \partial y$ at the wall at several instances of time were used as input data fields and the actuation at the wall was used for the output data of the network. Experimentally we found that only $\partial w / \partial y$ at the wall from the current instance of time was necessary for sufficient network performance. Because we wanted the output to be based only on a local input area, we designed our network using shared weights. The network had a single set of weights (a template) that is convolved over the entire input space to generate output values; that is, we used the same set of weights for each data point and the training involves iterating over all data points. The template extracts spatially invariant correlations between input and output data. The size of the template was initially chosen to include information about a single streak and streamwise vortex, and then was varied to find an optimal size.

We used a standard two-layer feedforward network with hyperbolic tangent hidden units and a linear output unit (see Fig. 1). The functional form of our final neural network is

$$v_{jk} = W_a \tanh \left(\sum_{i=-(N-1)/2}^{(N-1)/2} W_i \frac{\partial w}{\partial y} \Big|_{j,k+i} - W_b \right) - W_c, \quad (1)$$

$$1 \leq j \leq N_x, \quad 1 \leq k \leq N_z,$$

where the W 's denote weights, N is the total number of input weights, and the subscripts j and k denote the numerical grid point at the wall in the streamwise and spanwise directions respectively. N_x and N_z are the number of computational

domain grid points in each direction. The summation is done over the spanwise direction. Seven neighboring points ($N=7$), including the point of interest, in the spanwise direction (corresponding to approximately 90 wall units with our numerical resolution) were found to provide enough information to adequately train and control the near-wall structures responsible for the high-skin friction. Note that the blowing and suction are applied at each grid location according to (1) as a numerical approximation of distributed blowing and suction on the surface. A scaled conjugate gradient learning algorithm⁸ was used to produce rapid training. For given pairs of $(v_{jk}^{\text{des}}, \partial w / \partial y|_{jk})$, network was trained to minimize the sum of a weighted-squared error given by

$$\text{error} = \frac{1}{2} \sum_j \sum_k e^{\lambda |v_{jk}^{\text{des}}|} (v_{jk}^{\text{des}} - v_{jk}^{\text{net}})^2, \quad (2)$$

where v^{des} is the desired output value and v^{net} is the network output value given by Eq. (1). The weights were initialized with a set of random numbers. Note that the error defined in (2) exponentially emphasizes (proportional to λ) large actuations. This error scaling was chosen based on Choi *et al.*'s² observation that large actuations are more important for drag reduction. Usually within 100 training epochs, the error reached its asymptotic limit.

III. OFF-LINE TRAINING AND CONTROL

As an initial experiment we investigated whether we could train a neural network to predict the velocity at $y^+ = 10$ from only the wall-shear stresses. The rationale behind this experiment was to duplicate an existing control law using only measurements available at the wall such that the output from the network could be used as input to the actuator. The network should yield a similar amount of drag reduction to that obtained by Choi *et al.*² through prediction of the velocity at $y^+ = 10$. The training data consisted of 100 time steps of output obtained from a numerical simulation of channel flow under the control employed by Choi *et al.*,² i.e., using the wall-normal velocity at $y^+ = 10$. The flow regime is turbulent channel flow with $Re_\tau = 100$, where Re_τ is the Reynolds number based on the wall-shear velocity, u_τ , and the channel half-width, δ . All numerical simulations presented in this paper were obtained using a modified version of Kim *et al.*'s⁹ spectral code with the computational domain $(4\pi, 2, 4\pi/3)\delta$, and a grid resolution of $(32, 65, 32)$ in the (x, y, z) directions, respectively. Each time step contained a 32×32 array of input values $(\partial w / \partial y|_w)$ and corresponding actuations, $-v$ at $y^+ = 10$.

We trained several networks with one hidden unit and different sized input templates: 7×1 , 7×3 , 7×5 , 9×1 , 9×3 , 11×1 , and 11×3 (the number of input points in the spanwise direction by the number of input points in the streamwise direction). After training was completed, the distribution of input weights was examined to see whether there was a discernible pattern in the input template. The weight distributions in the spanwise direction at the same streamwise location for different input templates are shown in Fig. 2. The same pattern for all 7 input template sizes was observed, and is similar to a finite difference approximation of

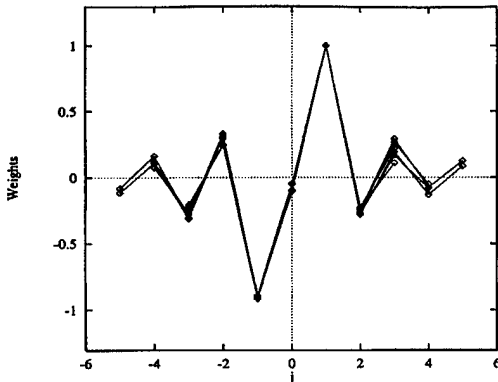


FIG. 2. Weight distribution from off-line trainings for various sizes of the input template: $7 \times 1, 7 \times 3, 7 \times 5, 9 \times 1, 9 \times 3, 11 \times 1, 11 \times 3$. Weights are normalized by W_1 .

spanwise differentiation. Increasing the number of hidden units only marginally improved performance, whereas increasing the template size significantly reduced the final training error.

We then applied a control scheme to a regular channel flow by fixing the final input weights obtained from the off-line training. This was perhaps a somewhat naive approach since the weights were obtained from fully controlled flow data and the shear stresses used for the training were already altered by the actuations. Nevertheless, two cases were tested: a control scheme based on 7 weights in the spanwise direction, and another based on the same 7 weights plus 3 more in the immediate downstream location. These 10 weights were chosen because among all weights obtained from the off-line training they had non-negligible values. In Fig. 3, the mean shear stress variations at the wall (i.e., drag) obtained with these two controls are plotted along with the no-control case. Nearly 18% drag reduction was achieved, with slightly better performance from the 10-weight network.

These results demonstrate that a correlation exists between the shear stresses at the wall and the desired actua-

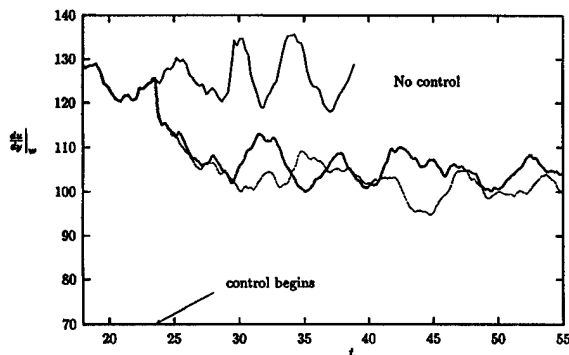


FIG. 3. Mean wall-shear stress histories for various control laws compared to the no-control case: —, no control; —, control with 7 fixed weights obtained from off-line control; ···, control with 10 fixed weights from the same off-line control. All runs with control shown in this paper were integrated over at least 20 time units that is much longer than the typical turn-over time of the streamwise vortices, 1 time unit.

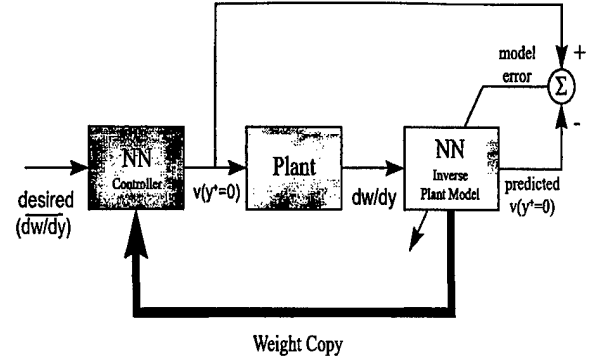


FIG. 4. Schematic representation of adaptive inverse model control.

tions, and that control based on this correlation produces a significant amount of drag reduction. This fixed-weight control scheme, however, was deduced from fully controlled flow data; thus it does not guarantee the same performance for other flow situations.

IV. ON-LINE CONTROL

In the previous section we showed how successful control based on off-line training can be obtained. However, since the system we are trying to control is time-varying and nonlinear, this approach is not likely to generalize well. Continuous on-line training allows a controller to adapt to the evolution of the system. In this section, we describe an adaptive controller for on-line training and control.

There are various schemes for on-line neural network control. The most direct scheme is adaptive-inverse model control.¹⁰ A schematic representation of this approach is shown in Fig. 4. Here the plant denotes the numerical solver of the Navier-Stokes equations. This configuration employs a neural network to model the (possibly time-varying) inverse plant mapping from wall-shear stress $\partial w / \partial y|_w$ to the wall-normal actuations, and then uses a copy of the model as the controller with the desired shear stresses as input. One restriction of this technique is that it usually requires an initial model training phase using random plant inputs and corresponding plant outputs. This, however, caused no serious problems since usually one time step was enough for model training because of the shared-weight architecture in our application (each time step is 1024 data points and our networks only have a few weights). Once the model represents a reasonably close approximation to the actual plant inverse, a copy is then implemented as a feedforward controller.

The desired inputs to the controller are a fractional reduction in the shear stress from the previous step, i.e.,

$$\left(\frac{\partial w}{\partial y} \right)_{t+\Delta t}^{\text{des}} = \eta \left(\frac{\partial w}{\partial y} \right)_t, \quad (3)$$

where $0 < \eta < 1$. Based on the networks and techniques we investigated, this indirect suppression of $\partial w / \partial y|_w$, instead of $\partial u / \partial y|_w$, turns out to be more efficient in achieving drag reduction. The output of the controller, which is the input to the plant, is the predicted actuation necessary to produce this shear-stress reduction. The quantity η should be chosen such

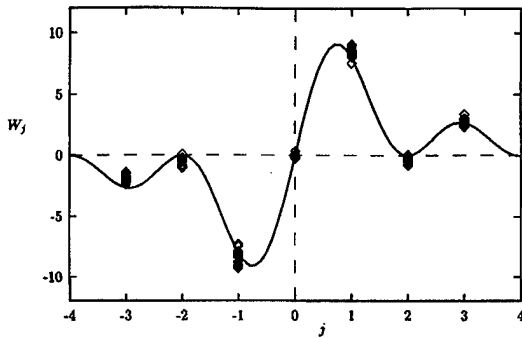


FIG. 5. Distribution of the weights: \diamond , from on-line training; $-$, $A(1 - \cos(\pi j))/j$. $\Delta z^+ = 13$.

that sets of the desired large amplitude outputs are among the sets that are well represented by the training sets. Good performance was achieved for the range of $\eta = 0.8 - 0.85$.

A turbulent channel flow at Reynolds number $Re_\tau = 100$ was used to test the neural network. We allowed all the weights in the network to adapt and examined the input template pattern after each time step. As the control began, the weight distribution immediately assumed a fixed pattern similar to the off-line pattern. There was no appreciable change in the relative magnitudes of the template weights over time, indicating that the pattern is preserved. The absolute magnitudes, however, did vary indicating the need for gain and bias adaptation for each layer. The number of hidden layers, the number of the hidden units, the size of the input template, and the error scale of the training error [λ of Eq. (2)] were 1, 1, 7×1 , and 5, respectively. We varied the values of the error scale and found 5 to be optimum, with larger values causing an instability in training. We also varied the number of the hidden units, but the network with a single hidden unit produced the best result. The converged weight distributions for 20 consecutive time steps after an asymptotic state was reached are shown in Fig. 5. The pattern is only slightly different from the one obtained from the off-line training (see Fig. 2). It should be noted that this pattern emerged immediately after the on-line control began.

Time histories of the wall-shear stress for 3 different input template sizes are shown in Fig. 6. All other network parameters are kept the same. The abscissa represents non-dimensional time normalized by u_τ and δ . One time unit roughly corresponds to the time for a fluid particle traveling with the centerline velocity to move about 20 channel half widths. The computations were carried out long enough to ensure that a statistically steady state was reached. As the control began, the drag quickly drops to about 80% of that observed without control, for the two cases with template sizes of 7×1 and 9×1 . The template size of 5×1 , however, did not produce as much reduction, indicating that at least 7 spanwise points (which extended about 90 wall units, with our grid resolution) should be used for good performance. At the initial stage of our study, we tested a control using both $\partial w / \partial y|_w$ and $\partial u / \partial y|_w$ as input, with a 7×5 input template. It produced about the same amount of reduction, but with excessive training time due to a significantly larger number

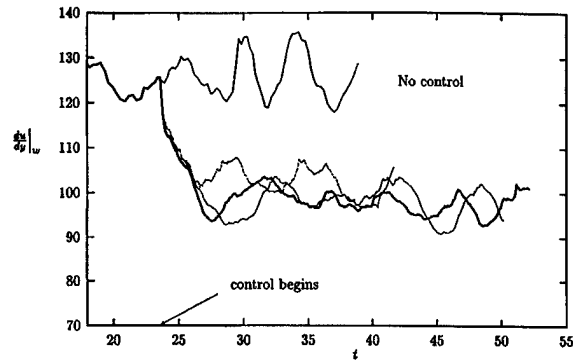


FIG. 6. Mean wall-shear stress histories for on-line control with different input template sizes: $-$, no control; \cdots , control with 5×1 ; $--$, control with 7×1 ; $-$, control with 9×1 .

of weights. Furthermore, it did not produce coherent patterns in the weight distributions.

Since the 7 weights showed a fixed pattern, we fixed the input template weights to this pattern and used a single hidden unit network, giving only 4 adaptable parameters (a bias and gain for each layer). This simplified network had the following functional form:

$$v_{jk} = W_a \tanh(W_b g - W_c) - W_d \quad (4)$$

with

$$g = \sum_{i=-3}^3 W_i \frac{\partial w}{\partial y} \Big|_{j,k+i}, \quad (5)$$

where W_i 's are the fixed-weight pattern obtained from the previous on-line control. On-line control using this network produced a similar amount of drag reduction. The weight variations with time were also monitored. The bias weights (W_c and W_d) were negligibly small. Those controlling the gain (W_a and W_b), which had finite values, changed in time significantly, although the product of the two gain-weights remained almost constant. This suggests that effective control can be achieved by simply using g with an adjustable amplitude. This will be discussed in the following section.

V. A SIMPLE CONTROL SCHEME

Since the control based on the network given by Eq. (4) produced a substantial reduction in drag, this section develops a control scheme based only on the weighted sum of the wall-shear stress. The distribution of the weights can be approximated by (see Fig. 5):

$$W_j = A \frac{1 - \cos(\pi j)}{j}, \quad (6)$$

where $j=0$ corresponds to the point where the control is applied. Since only the relative values are important, the constant A has no special meaning. A computation with a twice higher resolution was run to confirm that Eq. (6) gives the proper form of the weight distribution (see Fig. 7). It turns out that Eq. (6) is the inverse Fourier transform of $ik_z / |k_z|$, where k_z is the wave number in the spanwise direction, for the finite maximum wave number, i.e.,

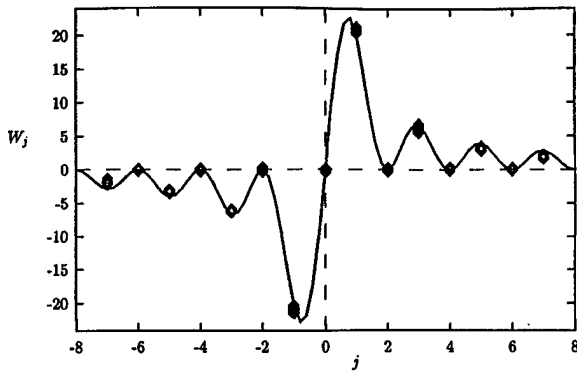


FIG. 7. Distribution of the weights: \diamond , from on-line training; —, $A(1-\cos(\pi j))/j$. $\Delta z^+=6$.

$$\int_{-k_m}^{k_m} \frac{ik_z}{|k_z|} \exp(-ik_z z) dk_z = 2 \frac{1 - \cos(k_m z)}{z}, \quad (7)$$

where $k_m = \pi/\Delta z$ is the maximum wave number and Δz is the numerical grid spacing. Replacing z with $j\Delta z$ in the right-hand-side of Eq. (7) leads to Eq. (6). From this result and the convolution theorem, one can suggest the following simple control law for wall transpiration:

$$\hat{v}_w = C \frac{ik_z}{|k_z|} \left. \frac{\partial \hat{w}}{\partial y} \right|_w = C \frac{1}{|k_z|} \frac{\partial}{\partial z} \left(\frac{\partial \hat{w}}{\partial y} \right), \quad (8)$$

where the “hat” denotes a Fourier transformed quantity and C is a positive scale factor determining the amplitude of the actuation. Equation (8), which should produce similar drag reduction as the result with 7 fixed weights [Eq. (4)], implies that the optimum blowing and suction at the wall is proportional to $\partial(\partial w/\partial y)/\partial z$ with the high wave number component suppressed by $1/|k_z|$. Note that the wall-normal actuation proportional to $\partial(\partial w/\partial y)/\partial z$ counteracts the up-and-down motion induced by a streamwise vortex (see Fig. 8), consistent with that used by Choi *et al.*² Smith *et al.*¹¹ discussed the stability of the near-wall turbulence structure to a local adverse pressure gradient imposed near the surface.

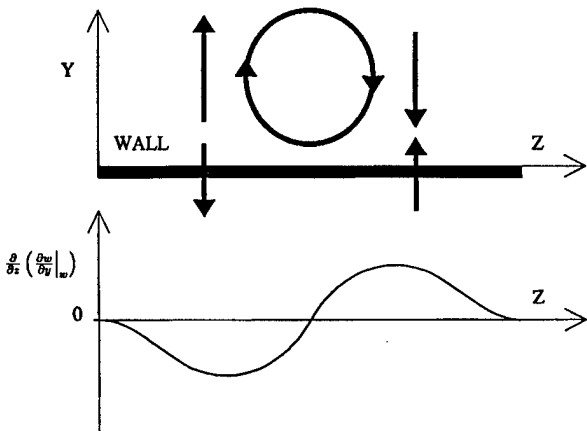


FIG. 8. A schematic of a flow field induced by a streamwise vortex and corresponding $\partial(\partial w/\partial y)|_w/\partial z$.

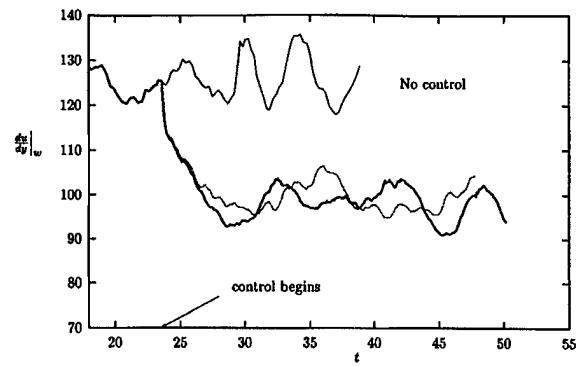


FIG. 9. Mean wall-shear stress histories for various control schemes compared to the no-control case: —, no control; —, on-line control with neural network with 7×1 template; ···, control with 7 fixed weights.

The suction at the left side of the vortex in Fig. 8 can relieve such adverse pressure gradient, thus preventing the surface-layer eruption. Choi *et al.*² reported that actuation based only on the local value of $\partial(\partial w/\partial y)/\partial z$, which is also a dominant term of the Taylor expansion of v at some distance away from the wall, did not produce such a substantial drag reduction. This indicates that suppression of high wave number components by $1/|k_z|$, or equivalently using locally weighted value of $\partial w/\partial y$, plays a key role in reducing drag. Note that the weights at even numbered grid points away from the center point vanish. This is beneficial for physical implementation, since sensors and actuators cannot be placed at the same location.¹² Because the Fourier integral is computed for a finite value of k_m , the values of the weight at noninteger j in Eq. (6) have no meaning. Equation (8) is equivalent to

$$v_{jk} = C \sum_{i=-(N-1)/2}^{(N-1)/2} W_i \left. \frac{\partial w}{\partial y} \right|_{j,k+i}, \quad (9)$$

where W_i is given by Eq. (6). The magnitude of the weights decays with increasing distance from the center, which allows for good approximation using only a small number of weights, i.e., successful control requires only local values of the shear stress. A natural concern is how different grid spacings affect the control. Since the above control law [Eq. (9)] is simply another expression of Eq. (8), which is a good approximation as long as k_m is large enough, the control should be relatively independent of resolution. This was confirmed by a computation with a higher resolution.

Control based on Eq. (9) with 7 points produced the same amount of drag reduction (20%) as the neural network control (see Fig. 9). The constant C is chosen so that the root-mean-squared (rms) value of the actuation is kept at $0.15u_\tau$. Blowing and suction of this magnitude at the wall suppress the near-wall streamwise vortices by counteracting the up-and-down motions associated with these vortices (see Fig. 8).

The fact that a control scheme that is essentially linear [Eq. (9)] produced the same amount of drag reduction as on-line control with a nonlinear network led to the following question: Can the same weight pattern be captured when on-line control with a “linear” network is used? To answer

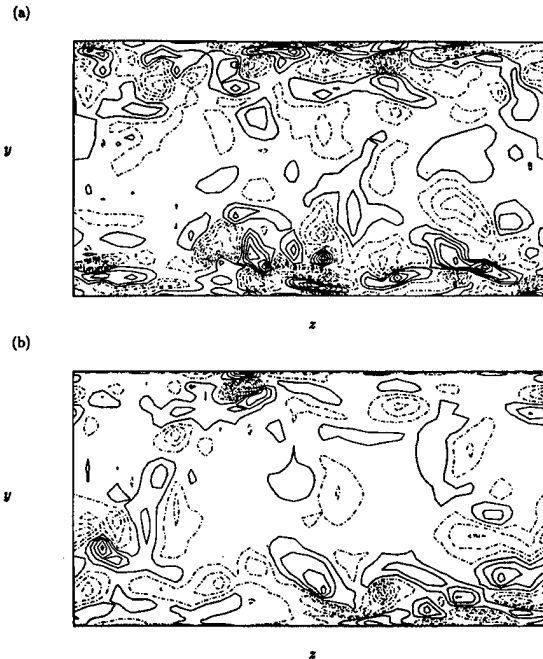


FIG. 10. Contours of streamwise vorticity in a cross-flow plane: (a) no control; (b) control using 7 fixed weights. The contour level increment is the same for both figures. Negative contours are chain-dotted.

this question, we tested an on-line controller utilizing a linear network. The hyperbolic tangent function in Eq. (1) was replaced with a linear function and the hidden layer was removed. All other parameters were kept the same as the nonlinear network case. The linear network seemed to produce almost the same pattern in weights as the one produced by our nonlinear network. Also, drag was reduced by the same amount. The pattern that was obtained by averaging over time, however, was not well preserved in time. The weight W_3 of Eq. (1), for example, frequently showed order of magnitude excursions resulting in a large standard deviation, 1.5, compared to the value of the weight, 0.3 (weights were normalized by the maximum amplitude W_1). The nonlinear network, however, produced more constant weights; the standard deviation of W_3 was only 0.15. This result indicates that the nonlinearity should add robustness by bounding the weights. This can simplify hardware implementation by limiting the signals and subsequently the necessary dynamic range of the processing circuitry.

VI. TURBULENCE STATISTICS

The computed flow fields for a no-control case and a successful control case, based on the 7-point weighted sum of $\partial w / \partial y|_w$ [Eq. (9)], were examined to investigate the mechanism by which the drag reduction is achieved. The most salient feature of the controlled case was that the strength of the near-wall streamwise vortices was drastically reduced. In Fig. 10, contours of streamwise vorticity in a cross plane are shown. This result further substantiates the notion that a successful suppression of the near-wall stream-

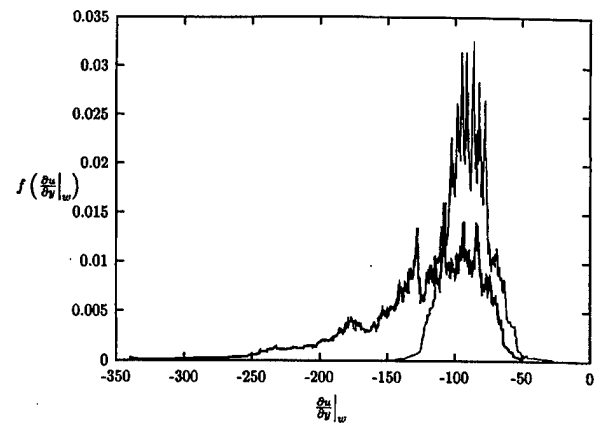


FIG. 11. Probability-density function of the wall-shear stress: —, no control; —, control with 7 fixed weights. The area under each curve is normalized to one.

wise vortices leads to a significant reduction in drag. Note that for the controlled case the wall actuations were applied at both walls.

The probability-density function of the wall-shear stress in the streamwise direction is shown in Fig. 11. It is evident that the control is very effective in suppressing large fluctuations, thus reducing the mean-skin friction. Furthermore, the root-mean-square (rms) values of turbulent fluctuations in the wall region are also reduced as shown in Fig. 12(a). The same trend was observed by Choi *et al.*² The rms vorticity fluctuations are also significantly reduced, except for ω_x very

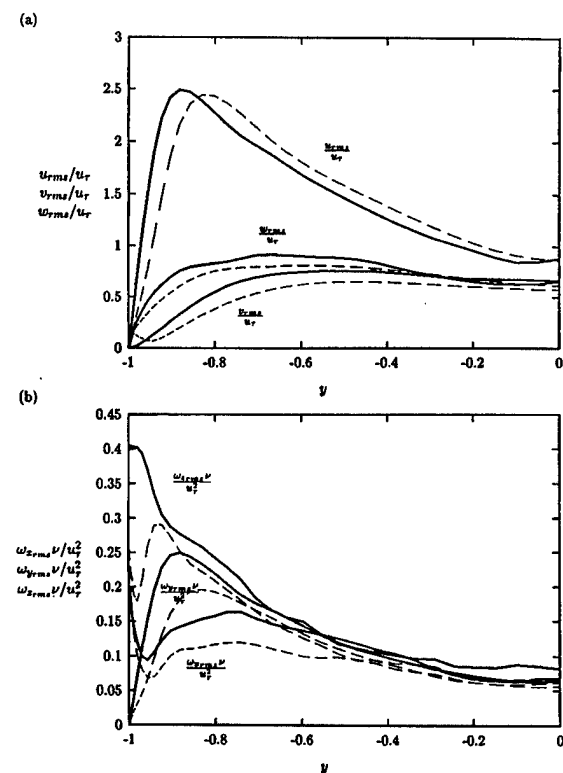


FIG. 12. Root-mean-square fluctuations normalized by the wall variables: —, no control; —, control with 7 fixed weights. (a) Velocity fluctuations; (b) vorticity fluctuations.

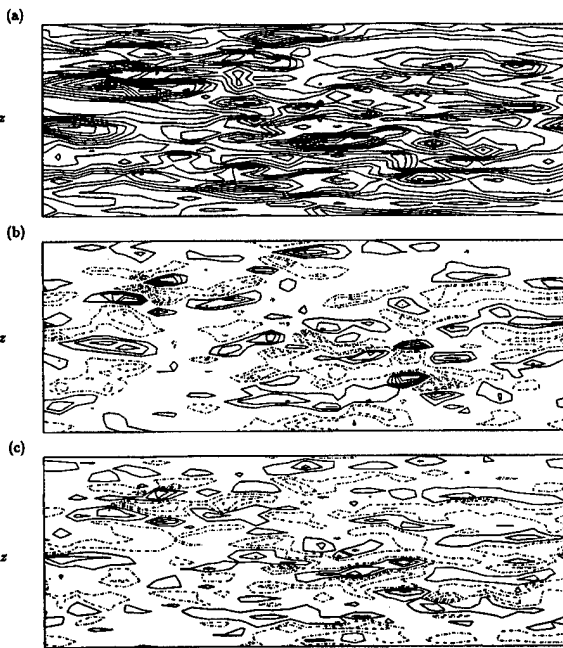


FIG. 13. Contours of the wall actuation: (a) control using $\partial w / \partial y|_w$ with 7 fixed weights; (b) control using information at $y^+ = 10$. Negative contours are chain-dotted.

close to the wall. The increase for the latter is caused by additional $\partial v / \partial z$ due to the wall actuation. The rms fluctuations of ω_z at the wall, which is mainly due to $\partial u / \partial y$ at the wall, is also decreased. This indicates that the control scheme led to a reduction in the mean shear and its variance at the wall by suppressing large fluctuations as shown in Fig. 11. The reduction in the rms fluctuations in ω_x and ω_y indicates that the control scheme indeed reduced the strength of the near-wall streamwise vortices and the wall-layer streaks.

Figure 13 compares the distribution of wall actuation used in our control with that from Choi *et al.*'s² v -control using the information at $y^+ = 10$ for the same wall-shear stress distribution. The corresponding wall-shear stress distribution is also shown in Fig. 13. The wall actuations indicate a strikingly similar distribution to each other, even though the wall actuation of our control is based only on the wall-shear stress $\partial w / \partial y|_w$. Basically our control scheme detects edges of locally high-shear stress regions by measuring the spanwise variation of $\partial w / \partial y$, and applies appropriate wall actuation as shown in Figs. 13(a) and 13(b). Since high-shear stress regions are usually elongated in the streamwise direction, only spanwise variation is necessary for detecting the edges. Since $\partial w / \partial y$ is a direct measurement of streamwise vortices (see Fig. 8), it provides more appropriate information than $\partial u / \partial y$. This is consistent with our finding that $\partial w / \partial y$ at several points in spanwise direction are enough for good performance of control.

VII. DISCUSSION AND CONCLUSION

We have presented a successful application of a neural network to turbulence control for drag reduction. First we

were able to construct and train a neural network off-line to find a correlation between the wall-shear stress and the desired wall actuations coming from the information at $y^+ = 10$. Based on the optimal network structure from the off-line training, we successfully implemented an on-line inverse model controller in numerical experiments of a turbulent channel flow, resulting in about 20% drag reduction. Finally, we were able to deduce a simple control scheme [Eq. (9)] for drag reduction based on observation of the weight distribution from a successful control case. This control scheme uses a minimal amount of wall-shear stress information and requires only simple operations, thus rendering a scheme whose actual hardware implementation would be relatively easy.

Beginning with a nonlinear network, we found a simple linear control scheme from the pattern of the weights, suggesting the use of a linear network. Although a linear network produced a similar pattern, the pattern was not well preserved in time. The weights can vary significantly increasing the difficulty in circuit implementation due to the larger required dynamic range. The nonlinear network, however, produced bounded weights simplifying hardware implementation. This suggests that a certain amount of nonlinearity is beneficial to capture a stable coherent pattern for our system.

Although the present control scheme is a significant improvement over earlier approaches that require velocity information within the flow, there is a technical issue before the present control scheme can be implemented in real practice. Precise control of blowing and suction distributed over a surface is difficult to implement. Other approaches, such as surface movements by deformable surface, may prove to be more practical.

There are also several fundamental issues that must be addressed. First, our numerical experiments were performed in a very low Reynolds number flow. It remains to be seen whether the same control scheme extends to higher Reynolds numbers. If the main cause of high-skin friction in turbulent boundary layers at higher Reynolds numbers is also due to the near-wall streamwise vortices, the same scheme should work equally well. Detection of these vortices through the wall-shear stress would become more difficult, however, because the scales associated with these vortices decrease as the Reynolds number increases.

Another important issue is the influence of the spatial resolution of sensors and actuators on performance. We showed that a simple control scheme with 4 neighboring points in the spanwise direction (3 among 7 weights are zeros), which span 90 wall units, performed very well. This suggests that the distance between sensors should be about 20 wall units. As the Reynolds number increases, the physical separation between sensors must decrease. We note in passing that recent advances in micromachined sensors and actuators make these scales feasible,¹³ and the present work is part of a joint research project aimed at integrating micron-sized sensors and actuators with analog VLSI control circuitry.

A third issue is determining an appropriate scale factor C in Eq. (9). We tested a range of C and empirically found

that values yielding an actuation rms value between $0.1u_r$ and $0.15u_r$ gave the best performance. Smaller values resulted in less reduction, while larger ones caused rapid fluctuations of the wall-shear stress over time. The experiments were only performed for $Re_r=100$ and 180, from which the optimum value was deduced, but we expect that the same amplitude level should produce similar reductions for higher Reynolds number flows. We further note that for this amplitude the required power input per unit area to produce the actuation, $p_w v_w + 0.5 \rho v_w^3 (\sim 0.1 \rho u_r^3)$ was significantly less compared to the power saved due to the reduced drag, $\Delta C_f / C_f \cdot \tau_w U_c (\sim 3.5 \rho u_r^3)$ for 20% reduction in C_f . Here p_w , ρ , C_f , τ_w and U_c are the wall pressure, density, friction coefficient, averaged wall-shear stress in the streamwise direction, and centerline velocity, respectively. Note that we did not account for device loss to deliver blowing and suction nor the power consumed by sensors in this estimate.

One final practical issue worth mentioning is the time delay between sensing and actuation. None was included in any of our numerical experiments. In a real situation, however, there will be a finite time delay between sensing and actuation. The process time for the simple control scheme should be negligible since a weighted summation is an involved process, thus not imposing any restriction on the time delay. Ideally, sensors should register the response of the near-wall structures to be controlled due to wall actuations, which will take a certain amount of time. Blowing and suction at the wall, however, can produce an immediate spurious response at nearby sensors due to local conservation. One possible remedy to this problem is an under-relaxation of the actuation signal with past signals, accounting for the response of a longer time scale. For example, an underrelaxation scheme using the following formula

$$v_{jk}^{t+\Delta t} = \xi C \sum_i W_i \left. \frac{\partial w}{\partial y} \right|_{j,k+i}^t + (1 - \xi) v_{jk}^t \quad (10)$$

could take into account all past signals with a single parameter ξ ($0 < \xi < 1$). We used this approach successfully in our numerical experiment for $Re_r=180$ and found that there is an optimum ξ depending on temporal resolution.

The most significant finding of the present study is that a single spanwise strip of $\partial w / \partial y|_w$ is enough to achieve significant drag reduction. Additional information about $\partial w / \partial y|_w$ in the streamwise direction or $\partial u / \partial y|_w$ in either direction reduced the efficiency of our neural-network based control. We also tested different-sized input templates and found that as the template size increased in the streamwise direction, the training time became excessive and the fixed pattern in the weight disappeared, indicating that too many unnecessary weights caused training problems.

ACKNOWLEDGMENTS

We are grateful to Dr. Gary Coleman for comments on a draft of this paper and Tim Berger for preparation of Figs. 10 and 13. We also are grateful to a referee for suggestion about the linear network. This work is supported by AFOSR Grants Nos. F49620-93-1-0332 and F49620-95-1-0263 (Dr. James M. McMichael, Program Manager). It is also supported in part by the Center for Neuromorphic Systems Engineering as a part of the National Science Foundation Engineering Research Center Program under Grant No. EEC-9402726. Computer time has been supplied by the San Diego Supercomputer Center, NASA Ames Research Center and by the NAS program at NASA Ames Research Center.

- ¹J. Kim, "Study of turbulence structure through numerical simulations: The perspective of drag reduction," AGARD Report No. R-786, AGARD FDP/VKI Special Course on "Skin Friction Drag Reduction," 2-6 March 1992, VKI, Brussels (1992).
- ²H. Choi, P. Moin, and J. Kim, "Active turbulence control for drag reduction in wall-bounded flows," *J. Fluid Mech.* **262**, 75 (1994).
- ³R. Akhavan, W. J. Jung, and N. Mangiavacchi, "Turbulence control in wall-bounded flows by spanwise oscillations," *Appl. Sci. Res.* **51**, 299 (1993).
- ⁴J. Kim, C. Lee, T. Berger, J. Lim, and H. Choi, "Effects of electromagnetic force on near-wall turbulence," *Bull. Am. Phys. Soc.* **40**, 1989 (1995).
- ⁵H. Choi, R. Temam, P. Moin, and J. Kim, "Feedback control for unsteady flow and its application to the stochastic Burgers equation," *J. Fluid Mech.* **253**, 509 (1993).
- ⁶P. Moin and T. Bewley, "Application of control theory to turbulence," in the 12th Australasian Fluid Mechanics Conference, Sydney 10-15 December 1995 (unpublished), p. 109.
- ⁷S. L. Jacobson and W. C. Reynolds, "Active control of boundary layer wall shear stress using self-learning neural networks," AIAA Shear Flow Conference, Orlando, 1993 (unpublished), p. 1.
- ⁸M. Moller, "Efficient training of feed-forward neural networks," Ph.D. thesis, Aarhus University, Denmark, 1993.
- ⁹J. Kim, P. Moin, and R. Moser, "Turbulence statistics in fully-developed channel flow at low Reynolds number," *J. Fluid Mech.* **177**, 133 (1987).
- ¹⁰B. Widrow, "Adaptive inverse control," In the Second IFAC Workshop on Adaptive Systems in Control and Signal Processing, Lund, Sweden, 1987 (unpublished), pp. 1-5.
- ¹¹C. R. Smith, J. D. A. Walker, A. H. Haidari, and U. Sobrun, "On the dynamics of near-wall turbulence," *Philos. Trans. R. Soc. London Ser. A* **336**, 131 (1991).
- ¹²This staggered distribution of sensors and actuators would result in actuators at only half the grid points and this might reduce the effectiveness of the control. This problem can be solved simply by increasing resolution twice so that actuators locate at every grid point of the old grid system (these correspond to half the grid points in the new grid system) still with sensors located in staggered positions. This is possible since the weight distribution does not depend on the grid distance, but depends on the grid index as shown in Figs. 5 and 7.
- ¹³C. Liu, Y. C. Tai, J. B. Huang, and C. M. Ho, "Surface micromachined thermal shear stress sensor," in ASME Application of Microfabrication to Fluid Mechanics, Chicago, 1994 (unpublished), pp. 9-15.

Suboptimal control of turbulent channel flow for drag reduction

By CHANGHOON LEE¹†, JOHN KIM¹
AND HAECHON CHOI²

¹Department of Mechanical and Aerospace Engineering,
University of California, Los Angeles, CA 90095-1597, USA

²Department of Mechanical Engineering, Seoul National University, Seoul, Korea

(Received 13 May 1997 and in revised form 27 October 1997)

Two simple feedback control laws for drag reduction are derived by applying a suboptimal control theory to a turbulent channel flow. These new feedback control laws require pressure or shear-stress information only at the wall, and when applied to a turbulent channel flow at $Re_\tau = 110$, they result in 16–22% reduction in the skin-friction drag. More practical control laws requiring only the local distribution of the wall pressure or one component of the wall shear stress are also derived and are shown to work equally well.

1. Introduction

Recent studies have shown that near-wall streamwise vortices are responsible for high skin-friction drag in turbulent boundary layers. Many attempts aiming at controlling these vortices have been made in order to achieve a skin-friction drag reduction in turbulent boundary layers. Most of such attempts, however, have been *ad hoc*, largely based on physical intuition. The active control by Choi, Moin & Kim (1994), for example, used blowing and suction at the wall that is equal and opposite to the wall-normal component of the velocity at $y^+ = 10$, resulting in as much as 25% reduction in their numerical simulation. This approach, however, is impractical since the required velocity information at $y^+ = 10$ is not normally available. For any practical implementation a control scheme should be based solely on quantities measurable at the wall.

A more systematic approach based on an optimal control theory was proposed by Abergel & Temam (1990). Choi *et al.* (1993) proposed a ‘suboptimal’ control procedure, in which the iterations required for a global optimal control were avoided by seeking an optimal condition over a short time period. The suboptimal control procedure was successfully applied to control of the Burgers equation. Bewley & Moin (1994) were the first to apply the suboptimal control procedure to a turbulent flow and reported about 17% drag reduction. The procedure developed by Bewley & Moin (1994) still requires velocity information inside the flow in order to solve the adjoint problem, from which a feedback control input was derived. In spite of this obvious drawback, however, the fact that a control theory applied to a turbulent flow resulted in a substantial drag reduction is encouraging, since their control procedure was derived rigorously from a control theory, in which a pre-determined

† Present address: Department of Mechanical Engineering, University of Seoul, Seoul, Korea.

cost functional was minimized. Hill (1993, 1994) derived a control input as a function of the streamwise wall shear only by modeling the near-wall flow with a spanwise velocity growing linearly, and normal velocity growing quadratically, with normal distance from the wall. About 15% drag reduction was obtained from this study. We, however, derive a simple control scheme by minimizing cost functionals that are related to the streamwise vortices, which have been found to be responsible for large local drag in turbulent boundary layers. We also tried to minimize drag directly by having drag itself in the cost functional, but it was not successful (see § 3). The objective of this paper is to demonstrate that a wise choice of the cost functional coupled with a variation of the formulation can lead to a more practical control law.

We present how to choose a cost functional and how to minimize it to yield simple feedback control laws that require quantities measurable only at the wall. One of the laws requires spatial information on the wall pressure over the entire wall and the other requires information, also over the entire wall, on one component of the wall shear stress. We then derive more practical control schemes that only require local wall pressure or local surface shear stress information, and show that they work equally well.

2. Suboptimal procedure

We follow a similar procedure used by Choi *et al.* (1993) and Bewley & Moin (1994). The problem under consideration is a turbulent channel flow, for which the governing equations are the Navier–Stokes and continuity equations with the no-slip boundary condition:

$$\frac{\partial u_i}{\partial t} + u_j \frac{\partial u_i}{\partial x_j} = -\frac{\partial p}{\partial x_i} + \frac{1}{Re} \frac{\partial^2 u_i}{\partial x_j \partial x_j}, \quad (2.1)$$

$$\frac{\partial u_j}{\partial x_j} = 0, \quad (2.2)$$

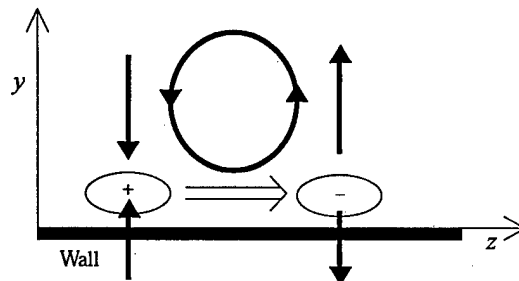
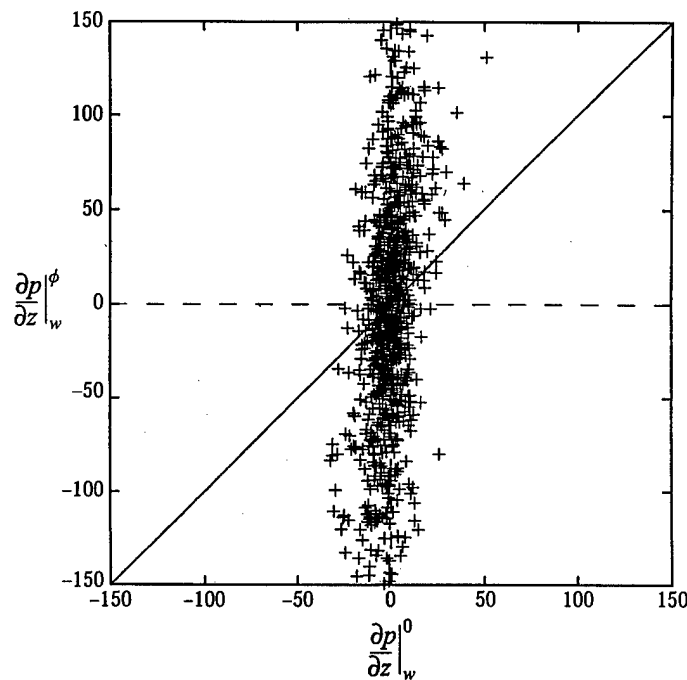
with

$$u_i|_w = \phi(x, z, t) \delta_{i2}, \quad (2.3)$$

where t is the time, x_1, x_2, x_3 are the streamwise, wall-normal, and spanwise directions respectively, u_i are the corresponding velocity components, p is the pressure, and Re is the Reynolds number, and the control input is the wall-normal velocity at the wall, ϕ .

All variables are non-dimensionalized by the wall shear velocity, u_τ , and the channel half-width, δ . We also use interchangeably x, y, z for x_i and u, v, w for u_i . Periodic boundary conditions are imposed in the streamwise and spanwise directions. The flow rate in the streamwise direction is kept constant, and the drag is measured by the mean pressure gradient necessary to maintain the constant flow rate.

We found that the choice of the cost functional to be minimized is critical in the performance of the control. Since the streamwise vortices have been known to be responsible for large drag in turbulent boundary layers, we tried to choose the cost functional that is directly related to them. This is based on our conjecture that a suitable manipulation of the streamwise vortices would lead to drag reduction. We carefully selected two cost functionals based on our observation of a successful control of Choi *et al.* (1994). As shown in figure 1, Choi *et al.*'s (1994) blowing and suction, which are equal and opposite to the wall-normal velocity component at $y^+ = 10$, effectively suppress a streamwise vortex by counteracting up-and-down

FIGURE 1. Schematic of a pressure field induced by a control based on $y^+ = 10$.FIGURE 2. Correlation between a pressure field of a no-control case and a pressure field modified by a control based on information at $y^+ = 10$. A line indicating no change of the pressure field is drawn for guidance.

motion induced by the vortex. This blowing and suction creates locally high pressure in the near-wall region marked with '+', and low pressure in the region marked with '-' in figure 1. A crucial aspect of the present analysis is the observation that this blowing and suction *increases* the pressure gradient in the spanwise direction under the streamwise vortex near the wall. To demonstrate this behaviour, we examine computed flow fields. Figure 2 shows a scatter plot between two pressure gradient fields: $\partial p / \partial z | w^0$ is the pressure gradient before the control is applied and $\partial p / \partial z | w^\phi$ is the pressure gradient at the same location after the control of Choi *et al.* (1994) is applied for one time step. It is apparent that the control increased the pressure gradient significantly. For the uncontrolled case, Re_τ based on the wall-shear velocity and the channel half-width is about 110. The spectral code of Kim, Moin & Moser (1987) is used for all the computations presented here. Simulations are carried out

using $32 \times 65 \times 32$ spectral modes (with dealiasing in the streamwise and spanwise directions) with the computational domain of $4\pi\delta \times 2\delta \times 4\pi\delta/3$, respectively.

The above argument suggests that we should seek blowing and suction that increases the pressure gradient in the spanwise direction near the wall for a short time period (i.e. in the suboptimal sense) in order to achieve a similar drag reduction to that achieved by Choi *et al.*'s (1994) control. The cost functional $\mathcal{J}(\phi)$ to be minimized is then

$$\mathcal{J}(\phi) = \frac{\ell}{2A\Delta t} \int_S \int_t^{t+\Delta t} \phi^2 dt dS - \frac{1}{2A\Delta t} \int_S \int_t^{t+\Delta t} \left(\frac{\partial p}{\partial z} \right)_w^2 dt dS, \quad (2.4)$$

where the integrations are over the wall (S) in space and over a short duration in time Δt , which typically corresponds to the time step used in the numerical computation, and ℓ is the relative price of the control since the first term on the right-hand side represents the cost of the actuation ϕ . Note that there is a minus sign in front of the second term since we want to maximize the pressure gradient. It should be noted that the spanwise pressure gradient at the wall will be eventually reduced when the strength of the near-wall streamwise vortices is reduced through successful control. Here, blowing and suction that increase the spanwise pressure gradient for the next step are sought as a suboptimal control.

To minimize the cost functional, we first define the differential states of the velocity and pressure, (θ_i, ρ) , using a Fréchet differential (Finlayson 1972),

$$\theta_i = \frac{\mathcal{D}u_i(\phi)}{\mathcal{D}\phi} \tilde{\phi}, \quad (2.5)$$

$$\rho = \frac{\mathcal{D}p}{\mathcal{D}\phi} \tilde{\phi}, \quad (2.6)$$

where

$$\frac{\mathcal{D}f(\phi)}{\mathcal{D}\phi} \tilde{\phi} = \lim_{\epsilon \rightarrow 0} \frac{f(\phi + \epsilon \tilde{\phi}) - f(\phi)}{\epsilon}, \quad (2.7)$$

$\tilde{\phi}$ being an arbitrary perturbation field to ϕ .

Next, we choose the Crank–Nicolson scheme for the linear terms and a Runge–Kutta scheme for the nonlinear terms to yield a discretized form of (2.1) and (2.2):

$$u_i^{n+1} - \frac{\Delta t}{2Re} \frac{\partial^2 u_i^{n+1}}{\partial x_j \partial x_j} + \frac{\Delta t}{2} \frac{\partial p^{n+1}}{\partial x_i} + R^n = 0, \quad (2.8)$$

$$\frac{\partial u_j^{n+1}}{\partial x_j} = 0, \quad (2.9)$$

with

$$u_i^{n+1}|_w = \phi \delta_{i2}, \quad (2.10)$$

where the superscripts $n+1$ and n denote the time step, and R^n includes the nonlinear terms and the explicit parts of the pressure gradient and viscous terms. The Fréchet differential of (2.8)–(2.10) yields the governing equations for the differential states (θ_i, ρ) ,

$$\theta_i^{n+1} - \frac{\Delta t}{2Re} \frac{\partial^2 \theta_i^{n+1}}{\partial x_j \partial x_j} + \frac{\Delta t}{2} \frac{\partial \rho^{n+1}}{\partial x_i} = 0, \quad (2.11)$$

$$\frac{\partial \theta_j^{n+1}}{\partial x_j} = 0, \quad (2.12)$$

with

$$\theta_i^{n+1}|_w = \tilde{\phi} \delta_{i2}. \quad (2.13)$$

Note that $(\mathcal{D}R^n/\mathcal{D}\phi) \tilde{\phi} = 0$. Hereinafter, we drop the superscript $n+1$ and all variables are understood to be at the $(n+1)$ th time step. Note that there is no contribution from the nonlinear terms, thus making the equations linear. Generally, the suboptimal formulation depends on the time advancement scheme used, as shown here (see also Choi *et al.* 1993). Dropping the nonlinear terms may miss important flow dynamics. However, we found from our numerical tests with the full nonlinear terms included that the contribution from the nonlinear terms is negligible in our boundary control with short optimization interval Δt ; it turns out that the conservation of mass due to the wall actuation dominates the near-wall dynamics.

Under the approximation that $2Re/\Delta t \gg k^2$, where $k = (k_x^2 + k_z^2)^{1/2}$, and k_x and k_z denote the streamwise and spanwise wavenumbers in the x - and z -directions respectively†, the above equations have the following solutions in the semi-infinite domain with periodic conditions in the x - and z -directions (see the Appendix):

$$\hat{\theta}_1(y) = \frac{ik_x}{k} \hat{\phi} (\exp[-(2Re/\Delta t)^{1/2}y] - e^{-ky}), \quad (2.14)$$

$$\hat{\theta}_3(y) = \frac{ik_z}{k} \hat{\phi} (\exp[-(2Re/\Delta t)^{1/2}y] - e^{-ky}), \quad (2.15)$$

$$\hat{\theta}_2(y) = \hat{\phi} e^{-ky}, \quad (2.16)$$

$$\hat{\rho}(y) = \frac{2}{k \Delta t} \hat{\phi} e^{-ky}, \quad (2.17)$$

where $\hat{\theta}_j$, $\hat{\rho}$, and $\hat{\phi}$ are the Fourier coefficients of θ_j , ρ , and $\tilde{\phi}$ respectively. For the channel geometry, we originally considered both walls and found that the interaction between two walls is negligible as long as the typical wavelength ($\sim 2\pi/k$) associated with near-wall structures is much smaller than the channel width.

The Fréchet differential of the cost functional (2.4) becomes

$$\frac{\mathcal{D}\mathcal{J}}{\mathcal{D}\phi} \tilde{\phi} = \frac{\ell}{A\Delta t} \int_S \int_t^{t+\Delta t} \phi \tilde{\phi} dt dS - \frac{1}{A\Delta t} \int_S \int_t^{t+\Delta t} \left. \frac{\partial p}{\partial z} \right|_w \left. \frac{\partial \rho}{\partial z} \right|_w dt dS. \quad (2.18)$$

The Fourier representation of the above equation is

$$\frac{\widehat{\mathcal{D}\mathcal{J}}}{\mathcal{D}\phi} \hat{\phi}^* = \ell \hat{\phi} \hat{\phi}^* - \left. \frac{\widehat{\partial p}}{\partial z} \right|_w \left. \frac{\widehat{\partial \rho}}{\partial z} \right|_w, \quad (2.19)$$

where the hat denotes the Fourier coefficient, and the superscript * denotes the complex conjugate. From (2.17), $\widehat{\partial \rho / \partial z}|_w$ can be expressed in terms of $\hat{\phi}^*$,

$$\left. \frac{\widehat{\partial \rho}}{\partial z} \right|_w = -\frac{2ik_z}{k \Delta t} \hat{\phi}^*. \quad (2.20)$$

Equation (2.19) then reduces to

$$\frac{\widehat{\mathcal{D}\mathcal{J}}}{\mathcal{D}\phi} \hat{\phi}^* = \ell \hat{\phi} \hat{\phi}^* - \frac{2k_z^2}{k \Delta t} \hat{p}_w \hat{\phi}^*. \quad (2.21)$$

† It can be shown that $2Re/\Delta t k_{max}^2 \sim Re^{1/4} \gg 1$. Here we used $u\Delta t/\Delta x \sim O(1)$ and $k_{max} \sim k_\eta \sim Re^{3/4}$, where k_η is the wavenumber corresponding to the Kolmogorov length scale.

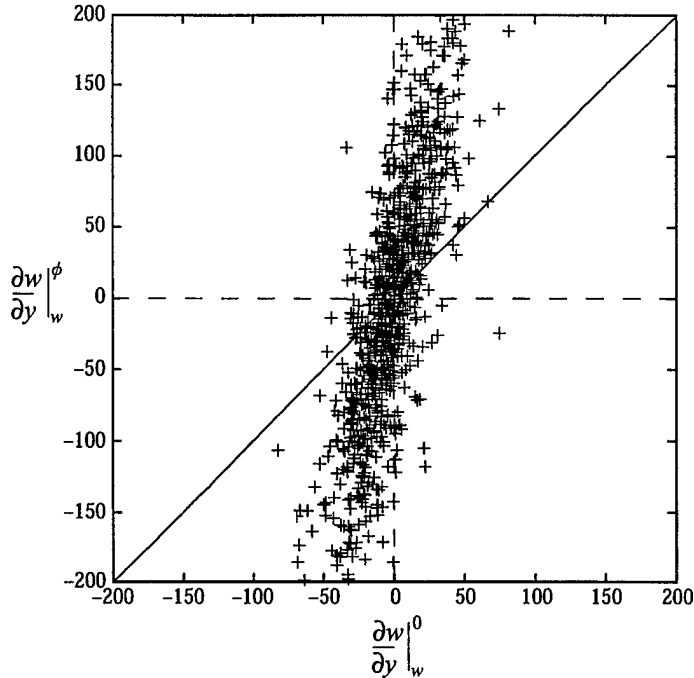


FIGURE 3. Correlation between a spanwise wall-shear stress of a no-control case and a spanwise wall-shear stress modified by a control based on $y^+ = 10$. A line indicating no change of the spanwise wall-shear stress field is drawn for guidance.

For an arbitrary $\hat{\phi}$, equation (2.21) should be satisfied, yielding

$$\widehat{\frac{\mathcal{D}\mathcal{J}}{\mathcal{D}\phi}} = \ell\hat{\phi} - \frac{2k_z^2}{k\Delta t}\hat{p}_w. \quad (2.22)$$

From the requirement that the Fréchet differential of the cost functional be minimized, i.e. $\mathcal{D}\mathcal{J}/\mathcal{D}\phi = 0$, the optimum $\hat{\phi}$ then becomes

$$\hat{\phi} = C \frac{k_z^2}{k} \hat{p}_w, \quad (2.23)$$

where C is a positive scale factor that determines the cost of the actuation. Equation (2.23) indicates that the optimum wall actuation is negatively proportional to the second spanwise derivative of the wall pressure, with the high-wavenumber components reduced by $1/k$.

Another wall quantity that indicates similar changes of the near-wall dynamics due to the altered pressure field is the spanwise shear at the wall, $\partial w/\partial y$. Owing to the added pressure gradient in the spanwise direction below the streamwise vortex, the spanwise flow near the wall is also induced, thus increasing the spanwise shear stress at the wall (see figure 1). The scatter plot between the spanwise shear stress at the wall from two different fields, one of which is from an unperturbed channel and the other with the control based on $y^+ = 10$, is shown in figure 3. Thus another choice for the cost functional to be minimized is

$$\mathcal{J}(\phi) = \frac{\ell}{2A\Delta t} \int_S \int_t^{t+\Delta t} \phi^2 dt dS - \frac{1}{2A\Delta t} \int_S \int_t^{t+\Delta t} \left(\frac{\partial w}{\partial y} \right)_w^2 dt dS. \quad (2.24)$$

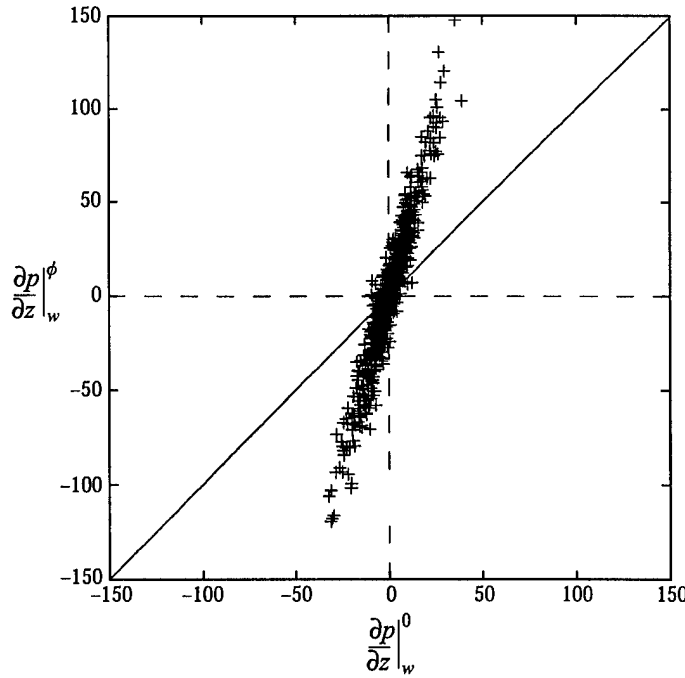


FIGURE 4. Correlation between a pressure field of a no-control case and a pressure field modified by a control based on equation (2.23).

Following the procedure that led to equation (2.23) yields the optimum actuation:

$$\hat{\phi} = C \frac{ik_z}{k} \left. \widehat{\frac{\partial w}{\partial y}} \right|_w . \quad (2.25)$$

Equation (2.25) indicates that the optimum wall actuation should be proportional to the spanwise derivative of the spanwise shear at the wall, with the high-wavenumber components reduced by $1/k$. Note that the scale factor C in equations (2.23) and (2.25) is arbitrary. As mentioned before, the suboptimal formulation depends on the time-advancement scheme used. However, if we used a different implicit scheme, only the resulting constant C would be different. This does not cause a problem since C is chosen such that the r.m.s. value of the wall actuation is maintained at a given value.

In the following simulations, we set the r.m.s. value of ϕ to be equal to that of the wall-normal velocity at $y^+ = 10$, which gives the same r.m.s. value of wall actuations as that of Choi *et al.* (1994).

3. Results

The above control laws (2.23) and (2.25) are tested in a turbulent channel flow. The pressure gradient at the wall is monitored to see if the equation (2.23) control increases the pressure gradient when the control law is applied. It behaves as expected, as shown in figure 4. The spanwise shear stress at the wall also increases when the equation (2.25) control is applied (see figure 5). These results also confirm that a suboptimal procedure without the nonlinear terms does not cause an error for our

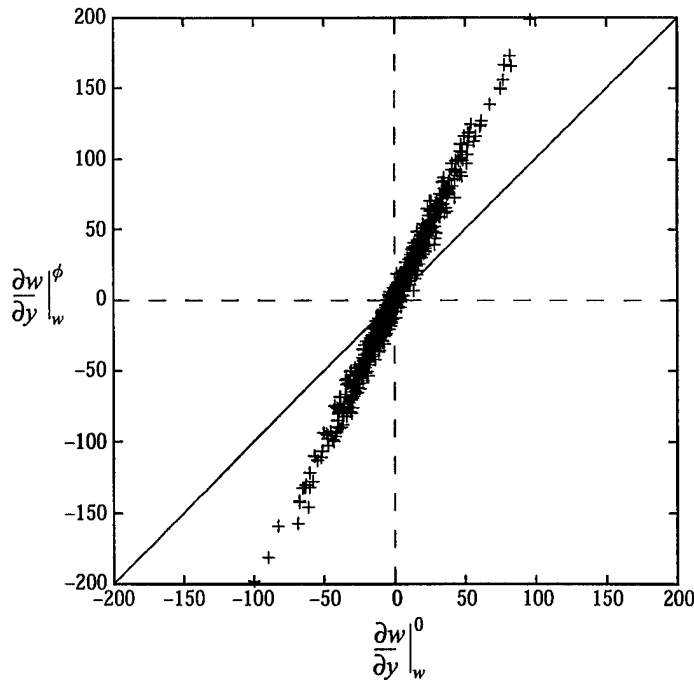


FIGURE 5. Correlation between a spanwise wall-shear stress of a no-control case and a spanwise wall-shear stress modified by a control based on equation (2.25).

boundary controls. Since these control laws specifically increase the wall pressure gradient or spanwise wall-shear stress, correlations between these variables before and after control are much higher than those corresponding to the control based on $y^+ = 10$ information. This suggests that the controls based on equations (2.23) and (2.25) modify the flow in a different manner from the control based on information at $y^+ = 10$.

Time histories of the mean streamwise wall-shear stress for different control laws are shown in figures 6 and 7. As control begins, an immediate drop in the shear stress is observed for all cases. At the same expense (i.e. the same r.m.s. value of ϕ), the control based on (2.25), which reduces drag by as much as 22%, is apparently more effective than that based on (2.23) which reduces drag by 16%. This indicates that the spanwise wall-shear stress is a better quantity for control input.

The control laws presented above, however, are still impractical to implement, since they are expressed in terms of the Fourier coefficients (i.e. in wavenumber space), which require information over the entire spatial domain. Therefore, the inverse transforms of k_z^2/k and ik_z/k are sought numerically so that the convolution integral can be used to express the control laws in physical space. The discrete representation of each control law then becomes†:

$$\phi(x_j, z_k) = C \sum_{j'} \sum_{k'} W_{jk}^p p_w(x_{j+j'}, z_{k+k'}) \quad (3.1)$$

† Since k_z^2/k and ik_z/k are not periodic in the wavenumber space, a high resolution was used to obtain W_{jk}^p and W_{jk}^w to minimize aliasing error.

		k (= z/Δz)						
		0	1	2	3	4	5	6
j (= x/Δx)	0	1.0000	0.4427	0.0031	0.0440	0.0044	0.0138	0.0032
	1	0.0413	0.0007	0.0040	0.0037	0.0029	0.0021	-0.0016
	2	0.0110	0.0057	0.0019	0.0011	0.0002	0.0000	-0.0003

TABLE 1. The weight distribution of equation (3.1), W_{jk}^p . The weights are symmetric between j and $-j$ and k and $-k$. The weights are normalized by W_{00}^p . Bold faced weights are used in the calculation of figure 6. Here, $Δx^+ = 40$ and $Δz^+ = 13$ ($Δx = 3Δz$).

		k (= z/Δz)						
		0	1	2	3	4	5	6
j (= x/Δx)	0	0.0000	1.0000	0.1039	0.2679	0.0852	0.1419	-0.0671
	1	0.0086	0.0537	0.0503	0.0310	0.0340	0.0148	0.0237
	2	0.0001	-0.0104	0.0059	0.0051	0.0100	0.0074	0.0092

TABLE 2. The weight distribution of equation (3.2), W_{jk}^w . The weights are symmetric between j and $-j$ and antisymmetric between k and $-k$. The weights are normalized by W_{01}^w . Bold faced weights are used in the calculation of figure 7. Here, $Δx^+ = 40$ and $Δz^+ = 13$ ($Δx = 3Δz$).

and

$$\phi(x_j, z_k) = C \sum_{j'} \sum_{k'} W_{j'k'}^w \left. \frac{\partial w}{\partial y} \right|_w (x_{j+j'}, z_{k+k'}), \quad (3.2)$$

respectively. The subscripts, j and k , denote the discretizing indices in the x - and z -directions respectively. The weights, W_{jk}^p and W_{jk}^w , are given in tables 1 and 2. Note that the weights decay rapidly with distance from the point of interest, suggesting that the optimum actuation can be obtained by a local weighted average of the pressure or spanwise shear stress. The results obtained using a 37-point average for the pressure and an 11-point average for the spanwise shear stress yield about the same drag reduction as that obtained from full integration using equations (2.23) and (2.25) (see figures 6 and 7). The weights used in these calculations are bold-faced in tables 1 and 2. It is remarkable that localized information can produce such a significant drag reduction, especially for the control with the spanwise shear stress.

The weight distribution W_{jk}^w for $j = 0$ is very similar to the one found in the application of neural networks to the same turbulent flow (Lee *et al.* 1997), in which only a single strip of the spanwise shear information was used in the network. The control law of Lee *et al.*,

$$\hat{\phi} = C \frac{ik_z}{|k_z|} \left. \frac{\partial w}{\partial y} \right|_w, \quad (3.3)$$

produces almost the same distribution of blowing and suction as the present results. Note that blowing and suction from equation (2.25) are nearly the same as those from equation (3.3) because the near-wall structures have relatively slow variation in the streamwise direction (the $k_x = 0$ component is dominant). This blowing and suction distribution is also very similar to the one based on $y^+ = 10$ data (see Lee *et al.* 1997).

In figure 8, contours of the streamwise vorticity in a cross-flow plane for the control with equation (2.25) are compared with a no-control case. Significant reduction in

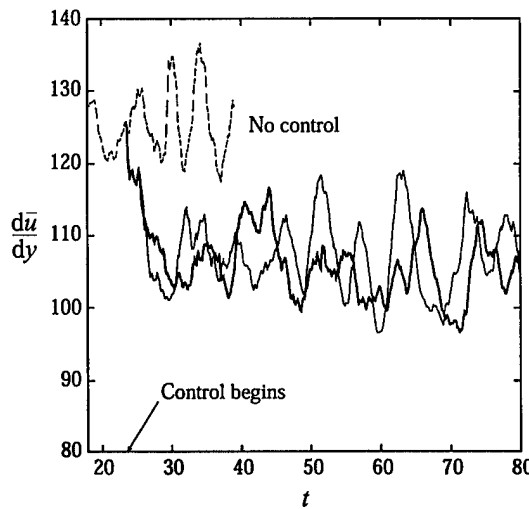


FIGURE 6. Mean streamwise wall-shear stress for various control laws based on the wall pressure, compared to the no-control case: thick solid line, the control law expressed in Fourier space, equation (2.23); thin solid line, the control law expressed in physical space, equation (3.1) with the integration radius of $6\Delta z$. $\Delta t^+ \simeq 0.2$.

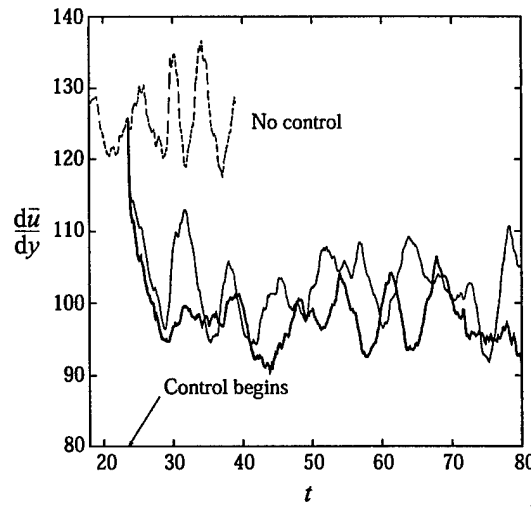


FIGURE 7. Mean streamwise wall-shear stress for various control laws based on the spanwise wall-shear stress compared to the no-control case: thick solid line, the control law expressed in Fourier space, equation (2.25); thin solid line, the control law expressed in physical space, equation (3.2) with 11 points in the spanwise direction only. $\Delta t^+ \simeq 0.2$.

the strength of the streamwise vortices is evident. This again confirms the notion that a successful manipulation of the near-wall streamwise vortices can lead to drag reduction. The mean streamwise velocity and root-mean-square velocity near the wall are shown in figures 9 and 10, respectively, and compared with the no-control case. The trends are very similar to Choi *et al.* (1994) and Lee *et al.* (1997).

Finally, we mention that we tried to find a feedback control scheme minimizing the

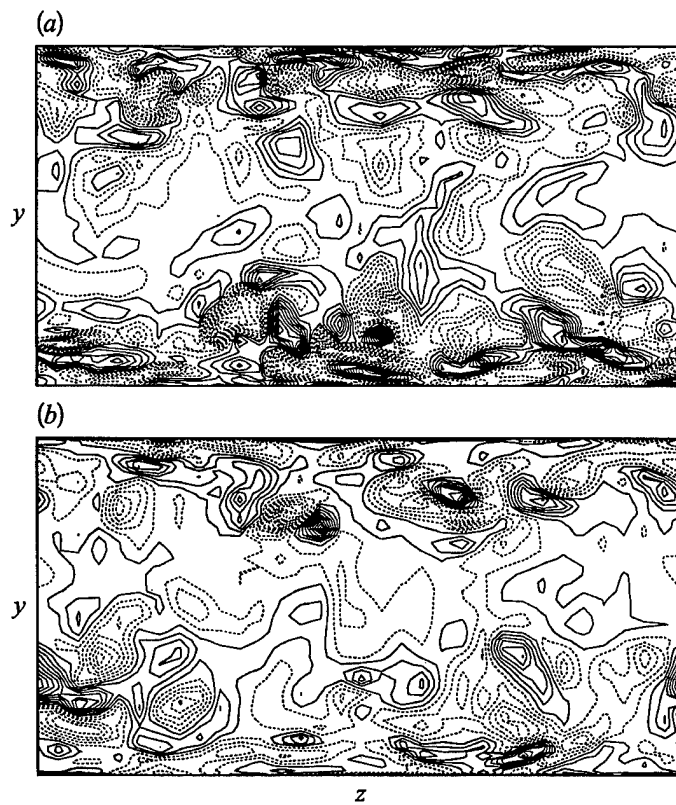


FIGURE 8. Contours of the streamwise vorticity in a cross-flow plane: (a) no control; (b) control based on wall-shear stress (equation (2.25)). The contour level increment is the same for both figures. Negative contours are dashed.

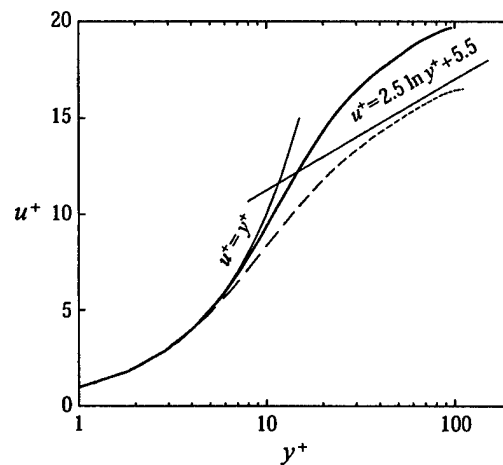


FIGURE 9. The mean streamwise velocity normalized by u_τ : Thick solid line, control law (2.25); dashed line, no control. For the controlled case, the velocity is normalized by the controlled u_τ .

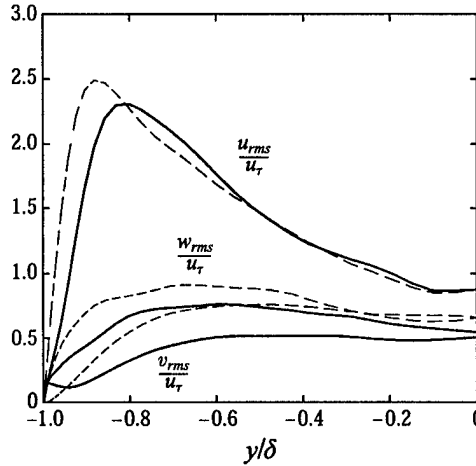


FIGURE 10. The root-mean-square velocity normalized by u_r of the uncontrolled flow: thick solid line, control law (2.25); dashed line, no control.

following cost functional:

$$\mathcal{J}(\phi) = \frac{\ell}{2A\Delta t} \int_S \int_t^{t+\Delta t} \phi^2 dt dS + \frac{1}{2A\Delta t} \int_S \int_t^{t+\Delta t} \left(\frac{\partial u}{\partial y} \right)_w^m dt dS, \quad (3.4)$$

with $m = 1$ or 2 . This cost functional is the most natural choice since it contains the quantity directly related to drag. We followed the same procedure to derive the following control schemes:

$$\hat{\phi} = 0, \quad (3.5)$$

for $m = 1$, and

$$\hat{\phi} = -C \frac{ik_x}{k} \left. \frac{\partial \hat{u}}{\partial y} \right|_w, \quad (3.6)$$

for $m = 2$. Equation (3.5) obviously does not reduce drag and equation (3.6) increased drag in our numerical simulations. This failure appears to be due to the neglect of the nonlinear terms in our formulation, since the numerical solution of the optimum wall actuations with the full nonlinear terms gave different results (Bewley & Moin 1994). This suggests that even in a short time interval the nonlinear terms should be included in the suboptimal formulation when drag itself is chosen as the cost functional. Manipulation of the streamwise vortices by wall actuation, however, can be accomplished through a linear process as shown in the previous section. It appears that having a term that is directly related to near-wall streamwise vortices in the cost functional indirectly includes the nonlinear effect. This is probably related to the fact that near-wall streamwise vortices are self-sustained by a nonlinear process (Hamilton, Kim & Waleffe 1995). If the nonlinear terms are included, of course, it is impossible to derive the feedback control law in closed form without approximation. Hill (1993), on the other hand, considered the nonlinear term by modelling the near-wall flow using the Taylor series expansion and presented a feedback control law in closed form, which resulted in about 15% drag reduction.

4. Summary

We have obtained two simple feedback control laws for drag reduction by applying a suboptimal control procedure to a turbulent flow. This was possible since we selected two cost functionals guided by the successful control based on quantities monitored at $y^+ = 10$. The present control laws perform very well, resulting in substantial drag reductions when applied to a turbulent channel flow. More convenient control schemes requiring only local information were also derived, and were shown to work equally well. They require quantities measurable only at the surface and thus should be easier to implement in practice. The present results further substantiate the notion that a successful manipulation of the near-wall streamwise vortices is the key to boundary-layer control for drag reduction.

We are grateful to Dr Gary Coleman and Mr Hong Zhang for useful discussions. This work was supported by AFOSR grant F49620-95-10263 (Program Managers, Drs James M. McMichael and Marc N. Glauser). Computer time was provided by the NAS Program of NASA Ames Research Center, the San Diego Supercomputer Center, and the DoD High Performance Computing Center. H.C. acknowledges the support by KOSEF through Turbo and Power Machinery Research Center.

Appendix. Derivation of the solution (2.14)–(2.17)

Equations for the differential states (θ_i, ρ) , (2.11), (2.12) can be rewritten in terms of the Fourier coefficients,

$$\hat{\theta}_1 - \frac{\Delta t}{2Re} \left(\frac{d^2}{dy^2} - k^2 \right) \hat{\theta}_1 + \frac{ik_x \Delta t}{2} \hat{\rho} = 0, \quad (A 1)$$

$$\hat{\theta}_2 - \frac{\Delta t}{2Re} \left(\frac{d^2}{dy^2} - k^2 \right) \hat{\theta}_2 + \frac{\Delta t}{2} \frac{d\hat{\rho}}{dy} = 0, \quad (A 2)$$

$$\hat{\theta}_3 - \frac{\Delta t}{2Re} \left(\frac{d^2}{dy^2} - k^2 \right) \hat{\theta}_3 + \frac{ik_z \Delta t}{2} \hat{\rho} = 0, \quad (A 3)$$

$$ik_x \hat{\theta}_1 + ik_z \hat{\theta}_3 + \frac{d\hat{\theta}_2}{dy} = 0, \quad (A 4)$$

with

$$\hat{\theta}_i(0) = \hat{\phi} \delta_{i2}, \quad \hat{\theta}_i(\infty) = 0, \quad (A 5)$$

where $\hat{\theta}_i$ and $\hat{\rho}$ are defined as follows:

$$\theta_i = \sum_{k_x} \sum_{k_z} \hat{\theta}_i(y) e^{ik_x x} e^{ik_z z}, \quad (A 6)$$

$$\rho = \sum_{k_x} \sum_{k_z} \hat{\rho}(y) e^{ik_x x} e^{ik_z z}. \quad (A 7)$$

The operation $ik_x \cdot (A 1) + d/dy (A 2) + ik_z \cdot (A 3)$ together with equation (A 4) yields

$$\frac{d^2 \hat{\rho}}{dy^2} - k^2 \hat{\rho} = 0, \quad (A 8)$$

which has a non-growing solution,

$$\hat{\rho} = \hat{\rho}_w e^{-ky}, \quad (A 9)$$

with a wall value, $\hat{\rho}_w$, which will be determined later. Using (A 9), we can find solutions to equations (A 1), (A 2), (A 3),

$$\hat{\theta}_1(y) = \frac{\Delta t}{2} i k_x \hat{\rho}_w (\exp[-(k^2 + 2Re/\Delta t)^{1/2}y] - e^{-ky}), \quad (A 10)$$

$$\hat{\theta}_3(y) = \frac{\Delta t}{2} i k_z \hat{\rho}_w (\exp[-(k^2 + 2Re/\Delta t)^{1/2}y] - e^{-ky}), \quad (A 11)$$

$$\hat{\theta}_2(y) = \left(\hat{\phi} - \frac{\Delta t}{2} k \hat{\rho}_w \right) \exp[-(k^2 + 2Re/\Delta t)^{1/2}y] + \frac{\Delta t}{2} k \hat{\rho}_w e^{-ky}. \quad (A 12)$$

With these, equation (A 4) reduces to

$$\left(- \left(k^2 + \frac{2Re}{\Delta t} \right)^{1/2} \left(\hat{\phi} - \frac{\Delta t}{2} k \hat{\rho}_w \right) - \frac{\Delta t}{2} k^2 \hat{\rho}_w \right) \exp[-(k^2 + 2Re/\Delta t)^{1/2}y] = 0. \quad (A 13)$$

Since $2Re/\Delta t \gg k^2$, equation (A 13) yields

$$\hat{\rho}_w = \frac{2}{\Delta t k} \hat{\phi}. \quad (A 14)$$

With this, equations (A 10), (A 11), (A 12), (A 9) become equations (2.14), (2.15), (2.16), (2.17), respectively.

REFERENCES

ABERGEL, F. & TEMAM, R. 1990 On some control problems in fluid mechanics. *Theor. Comput. Fluid Dyn.* **1**, 303.

BEWLEY, T. & MOIN, P. 1994 Optimal control of turbulent channel flows. In *Active Control of Vibration and Noise* (ed. K. W. Wang, A. H. Von Flotow, R. Shoureshi, E. W. Hendricks & T. W. Farabee). ASME DE-Vol. 75.

CHOI, H., MOIN, P. & KIM, J. 1994 Active turbulence control for drag reduction in wall-bounded flows. *J. Fluid Mech.* **262**, 75.

CHOI, H., TEMAM, R., MOIN, P. & KIM, J. 1993 Feedback control for unsteady flow and its application to the stochastic Burgers equation. *J. Fluid Mech.* **245**, 509.

FINLAYSON, B. A. 1972 *The Method of Weighted Residuals and Variational Principles*. Academic.

HAMILTON, J. M., KIM, J. & WALEFFE, F. 1995 Regeneration mechanisms of near-wall turbulence structures. *J. Fluid Mech.* **287**, 317.

HILL, D. C. 1993 Drag reduction at a plane wall. *Annual Research Briefs*. Center for Turbulence Research, Stanford University.

HILL, D. C. 1994 Drag reduction strategies. *Annual Research Briefs*. Center for Turbulence Research, Stanford University.

KIM, J., MOIN, P. & MOSER, R. 1987 Turbulence statistics in fully developed channel flow at low Reynolds number. *J. Fluid Mech.* **177**, 133.

LEE, C., KIM, J., BABCOCK, D. & GOODMAN, R. 1997 Application of neural networks to turbulence control for drag reduction. *Phys. Fluids* **9**, 1740.

IN-PLANE MICROACTUATOR FOR FLUID CONTROL APPLICATION

Faiz Sherman, Steve Tung, Chang-Jin "CJ" Kim*, Chih-Ming Ho, and Jason Woo**

Mechanical and Aerospace Engineering Department

** Electrical Engineering Department

University of California, Los Angeles,

Los Angeles, CA 90095-1597, U.S.A. (* E-mail: cjkim@seas.ucla.edu)

ABSTRACT

We introduce a new approach that alters the local flow condition using electrostatically driven microactuator moving in the in-plane direction such that form drag of the actuator can be eliminated. This is in contrast to the electromagnetically driven microflap moving normal to the substrate. A 60 μm X 200 μm plate moving parallel to the substrate surface induces a "spanwise velocity" into the flow field. This spanwise velocity, when applied to the near-wall streaks, increases the transport of high-speed fluid away from the wall, therefore causing reduction in viscous drag. The microplate is attached at the end of a microcantilever capable of, even in non-resonance, large tip deflection ($> 100 \mu\text{m}$), tested at the operation frequencies of 500-1200 Hz. The cantilever is of a high-aspect-ratio structure (2 μm wide, 6-17 μm thick silicon) to ensure parallel motion over a long distance and provide robustness against out-of-plane deflection under external disturbances from the flow. We report the design and one-mask fabrication of the in-plane microactuator array made from Silicon-On-Insulator (SOI) wafers and experimental verification of the induced Stoke's flow and a local fluid flow.

INTRODUCTION

Most of the work done in active control of fluid flow has been performed in macroscale [1]; it involved changing the skin friction by wall motion, heating and cooling the wall, and injecting mass. The key issues that arise are the spatial resolution, operational frequency of the actuator, and the power consumption of such devices. For these reasons, MEMS actuators have become a very attractive option for active control of fluid flow [2]. They provide excellent spatial resolution and high operational frequency with low power consumption.

Active control of "streaks" (high speed fluid approaching the wall region) in microscale has been shown feasible only recently [2-5]. The work involved magnetically actuated microflaps moving in the out-of-plane direction. This actuator produced an upward

velocity against streaks, thereby reducing the viscous drag caused by the high speed fluid. Since this actuator was of millimeter scale in overall size and magnetically driven, the operational frequency was limited and the power consumption was relatively high (mW).

The goal of this paper is to realize an in-plane microactuator that can be used to generate a local fluid field, which will eventually serve to reduce viscous drag in fluid flow. The device is made flush to the substrate and operates in the in-plane direction to be free from "form drag" (drag induced due to a physical presence of an object obstructing a flow), in contrast to the microflaps [4]. The reported in-plane microactuator is electrostatically driven and is much smaller in size, therefore allowing for lower power consumption ($< 1 \mu\text{W}$) and higher operating frequency. The in-plane microactuator is approximately 100 times smaller than the magnetic microflap actuator.

THEORY AND MODELING

Flow Theory

The formation of regions that contribute to viscous drag is due to high speed fluid streaks moving along the wall. This creates a region of high viscous drag. This phenomenon occurs generally due to a presence of a vortex pair. As shown in Fig. 1, high speed fluid approaches the wall region due to a counter rotating vortex pair. It is expected that the fluid flow generated to counter the downward motion will reduce the viscous wall drag.

The physical sizes of the streaks are a function of Reynolds number. For the case where Reynolds number is 10,000 (a parameter similar to test condition of the magnetic microflap [3]), the streaks have an average width of 900 μm and an average length of 30 mm. With these streak dimensions, three criteria for the in-plane microactuator are required. The first is that the actuator end plates be as long as possible in order to interact with as much of the streak (from their length point of view).

Secondly, the actuators should produce large enough plate displacement in order to affect the streaks (from their width point of view); otherwise, they would not have an effect on the streaks. Thirdly, the induced flow velocity also must be large enough to interfere with the down flow of the incoming high speed fluid. This dictates that the actuators need to operate at high frequency.

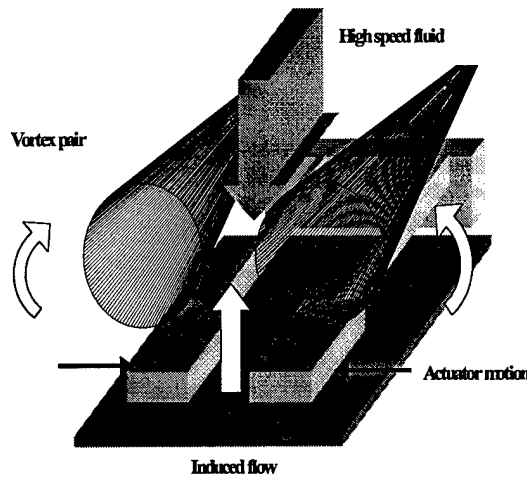


Fig. 1 Schematic of streak formation

Previous modeling effort [6] and data from the magnetic microflap actuator [3] suggest an induced velocity on the order of 1-10 cm/s to be sufficient to cause substantial reduction in viscous drag ($> 20\%$). To satisfy these three criteria, our actuators are made to move long end plates (200 μm long) a distance over 100 μm with high operating frequency (0.5–1.2 kHz).

Design and Dynamic Modeling of the Actuator

Our actuators are electrostatically driven using angled electrodes [7]. Embedded in these electrodes are isolation bumpers that are 40 μm X 40 μm in size. The bumpers serve to prevent shorting between the cantilever beam and the pulling electrode. Their size allows for a timed release of the actuators while still insuring the isolation bumpers remain anchored to the substrate. The actuator consists of a large end plate (60 μm wide, 200 μm long) attached at the end of a long cantilever beam (500-800 μm). The end plates have release holes that are 6 μm X 6 μm . This size allows for short timed HF release step. The supporting cantilever is 2-4 μm wide and 6-17 μm thick. This gives a high-aspect-ratio device that is rigid in the out-of-plane direction and flexible in the in-plane direction. The actuators are configured in an array format in pair formation as shown in Fig. 2. This formation allows for maximum induction of fluid flow. They are also designed to be recessed so that the

top surface of the plates and the electrodes are on the same plane as the substrate to prevent any interference on the oncoming fluid.

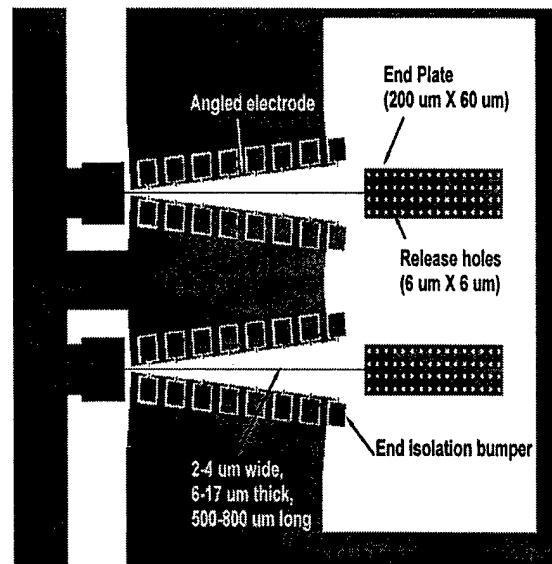


Fig. 2 Design layout of in-plane microactuators (top view)

With the intention of operating these devices at large deflection under high frequency conditions, we need to characterize their performance that encompasses the resonance modes and frequencies. An understanding of the effect of the large end plate on the dynamic response of the actuators is necessary for the successful operation of the actuators.

Finite element model using a commercial package (ANSYS) is done to determine the response of the cantilever-plate system. Both a modal analysis and a harmonic response analysis are performed for the case of a 4 μm wide, 20 μm thick, and 500 μm long actuator with an end plate that is 60 μm wide and 200 μm long. Fig. 3 shows the first resonance mode of the actuator, occurring at 2.5 kHz. Up to the actuator's fundamental frequency, the end plate follows the beam without any relative rotation to the cantilever tip and does not attenuate the amplitude.

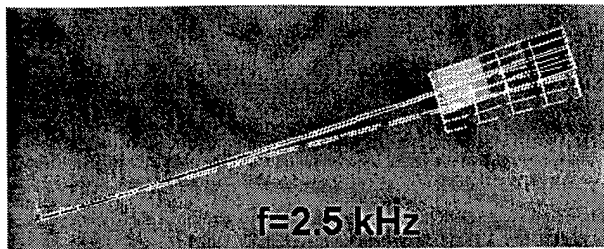


Fig. 3 Fundamental mode of in-plane microactuator

The second mode of the device is in the out-of-plane direction, Fig. 4, at 6.2 kHz. The third mode occurs at 34.7 kHz. At this mode, the rotational effect of the end plate keeps the overall in-plane motion of the end plate almost stationary, Fig. 5.

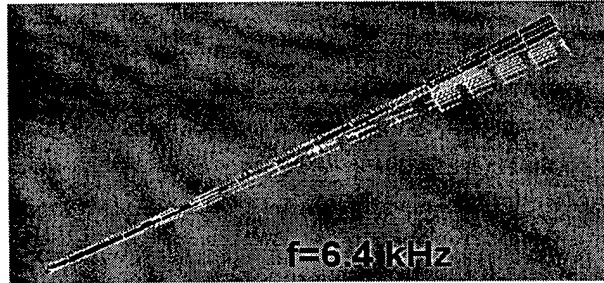


Fig. 4 Second resonance mode of in-plane microactuator (side view)

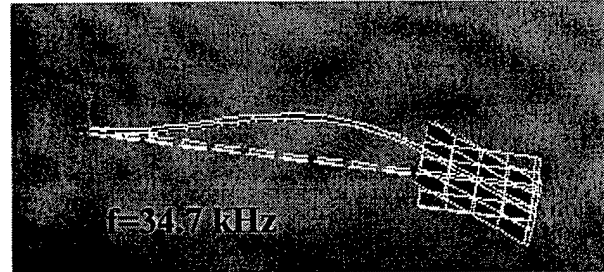


Fig. 5 Third resonance mode of in-plane microactuator

FABRICATION

Fabrication of the in-plane microactuators is done on Silicon-On-Insulator (SOI) wafers with a single mask and three processing steps. The SOI wafers are custom-ordered from a commercial service to our specifications in order to meet several requirements. The first requirement is that the wafers be heavily doped on both the handle wafer (i.e., the main substrate) and the device wafer (i.e., top layer). This is needed because no metalization process will be performed. Therefore, in

order to have a driving signal carried, the silicon must be both a structural material and a conductive base. The second requirement is that the sacrificial oxide on the SOI wafer be thick (~3 μm) to help releasing the large end plates and maintain enough gap from the substrate over the long travel during operation. Electrical breakdown through the oxide layer under high actuation voltage is yet another consideration. Finally, the thickness of the top silicon (device layer) is required to vary from 6 μm to 18 μm in order to fabricate high-aspect-ratio structures with narrow beam width (as small as 2 μm).

The fabrication begins by using a Bond and Etch Back Silicon-On-Insulator (BESOI) wafer, Fig. 6 (a). The SOI wafer is made from two highly doped (100) 4 inch wafers (0.005 $\Omega\text{-cm}$). Wet oxide of 1.5 μm is grown on each wafer. The wafers are then bonded, oxide to oxide, at room temperature. They are then placed in an 800 $^{\circ}\text{C}$ furnace to strengthen the bond. On completion of the annealing, one side of the bonded wafer undergoes grinding to the target device thickness. Once the target thickness is reached, the wafers are polished to give a finished surface.

After photoresist is patterned to define the device, the wafers are sent to MCNC [8] for a deep reactive-ion etch (DRIE) which is performed through the device layer. Oxide is an effective etch stop layer for the DRIE, but end point detection was also used to accommodate for the varying thickness of our device layers, Fig. 6(b). The photoresist is then removed in-house and the wafers are diced to 1 cm X 1 cm chips which are used for actual flow experiments. Finally, the test chips undergo a release process, Fig 6(c). The release process is a timed etch of the sacrificial oxide. The Oxide underneath the actuators is removed in 8 minutes of 49% HF. All the other structures have significantly larger anchor areas, therefore allowing them to remain anchored after the end plates have been released.

Releasing/drying was a challenge, despite the thickness of the beam (over 10 μm), due to the length (up to 1000 μm overall) and the existence of large plates at the end. The standard CO_2 supercritical drying [9] and surface passivation by self-assembled monolayer (SAM) coating [10], both proven effective for simple beams [11], produced a dismal result (< 10% yield) for the in-plane microactuators. For the CO_2 drying, it is speculated that the difficulty stemmed from replacing the methanol under the large plates with the CO_2 liquid through the narrow and deep trenches made by DRIE. Similar problems also make the SAM coating method ineffective.

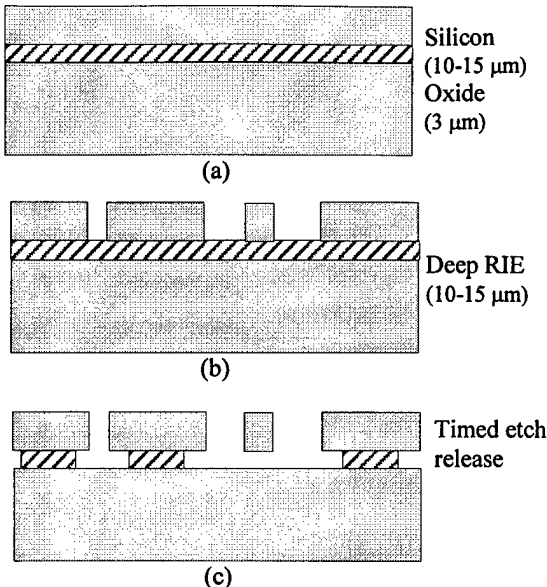


Fig. 6 Flow Process (a) SOI wafer, (b) DRIE on device layer, (c) releasing structure by timed etch

A dramatic improvement has been found when the chip was loaded “upside down” on completion of the methanol soak, apparently helping the methanol drip by gravity in lighter CO_2 liquid. Rinsing times are also increased to provide longer time for diffusion. The release process consists of 8 min in 49% HF followed by 30 minutes DI rinse in three successive baths (10 minutes each). The chips are then transferred to methanol and kept for yet another 30 minutes before CO_2 drying. Twenty rinses are done with a dwelling time of 3 minutes in between each rinse. This release method yielded a success close to 100 %.

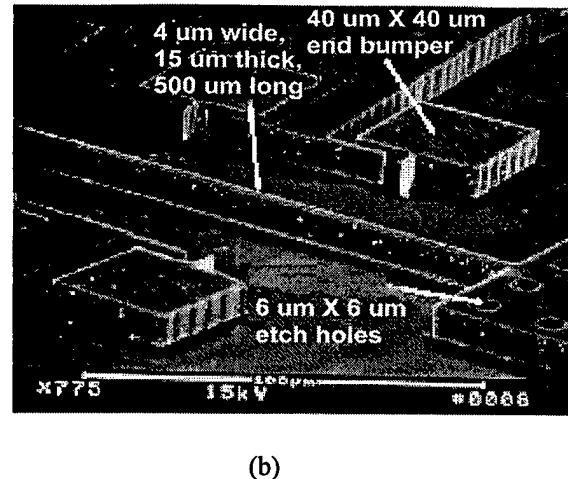
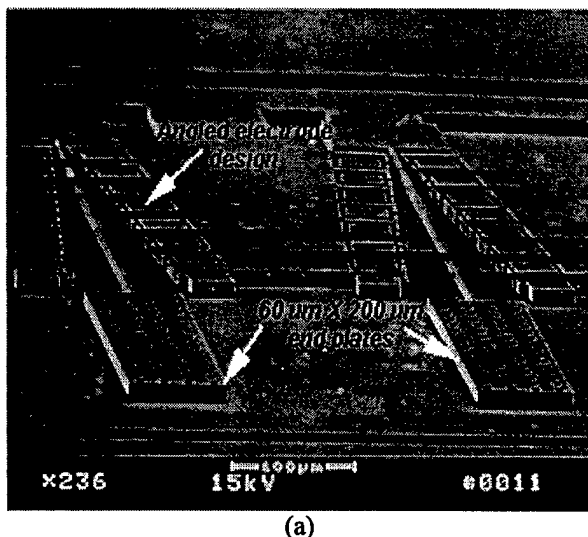


Fig. 7 SEM pictures of the fabricated in-plane microactuators (a) a pair of microactuators (b) close-up view near the cantilever end and the plate

Fig. 7 (a) shows a pair of the released actuator with the angled electrode configuration used to drive it. As shown, the actuators are designed to be recessed to prevent an unwanted effect on the on-coming fluid flow. In addition, this design serves as a shield for the actuators against any perturbation in the flow that might cause the devices to break off. Fig 7 (b) is the close-up showing the high-aspect-ratio beam, the end plate, release holes on it, angled drive electrodes, and electrostatic isolation bumpers.

TESTING

Two flow experiments are performed. The first is to verify that the actuator is capable of generating a local flow. The generated flow being sought for is Stoke's flow. The second is to verify that the actuators do indeed generate a net upward flow that can be used to counter the flow being brought in by a vortex pair. In the second experiment, flow visualization technique is used.

To verify Stoke's flow, a hot-wire anemometer is placed above the microactuator. The position of the hot-wire above the end plate is approximately 400 μm, Fig. 8. The hot-wire is turned on and a signal is recorded before activating the actuator. The actuator is then turned on. The actuator is made to displace the end plate 100 μm peak-to-peak at a frequency of 500 Hz. The signal from the hot-wire is recorded, Fig 9. The signal picked up by the hot-wire shows the induced Stoke's flow following the frequency of the actuators.

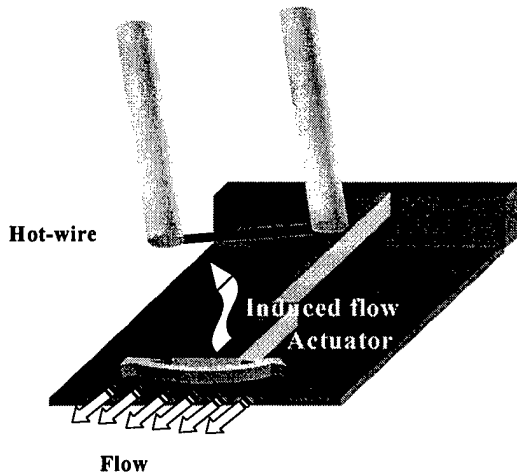


Fig. 8 Experimental set-up to verify induction of Stoke's flow

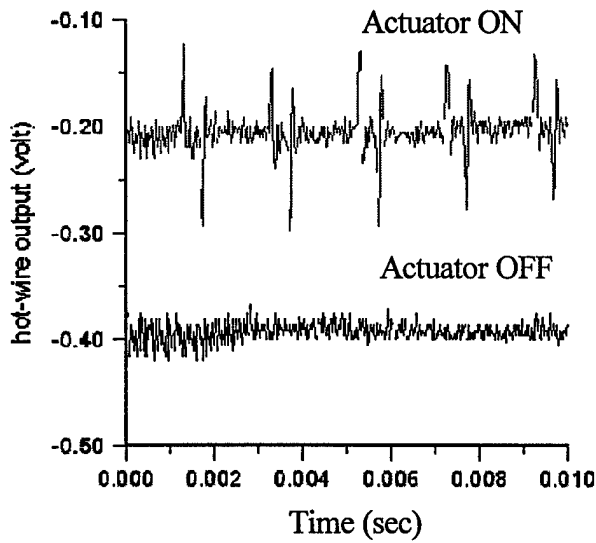


Fig. 9 Stoke's flow detection due to actuator motion picked up by hot-wire

In the second experiment, smoke is introduced into an array of actuators. A laser sheet is placed on top of the actuators, Fig. 10. The entire experiment is enclosed in a controlled environment that allows for stagnant fluid. Once the smoke is introduced onto the actuators, it can be seen as a white feature, Fig. 11(a). When the actuators are turned on, the smoke is seen to displace upwards and diffuse away. This observation was clear during direct viewing. The flow visualization technique allowed for the visual verification of the possible induced flow.

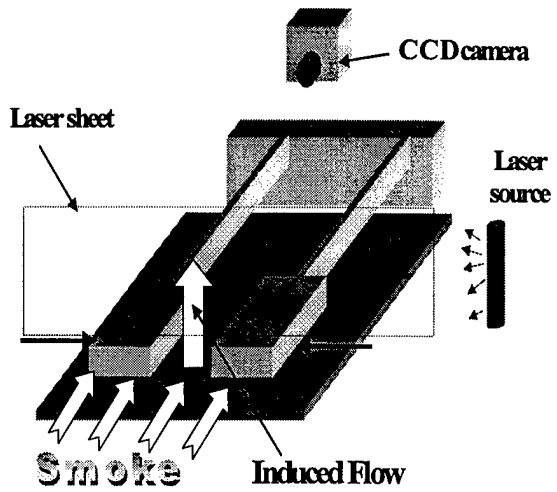


Fig. 10 Experimental set-up used to visualize induced flow by actuator array

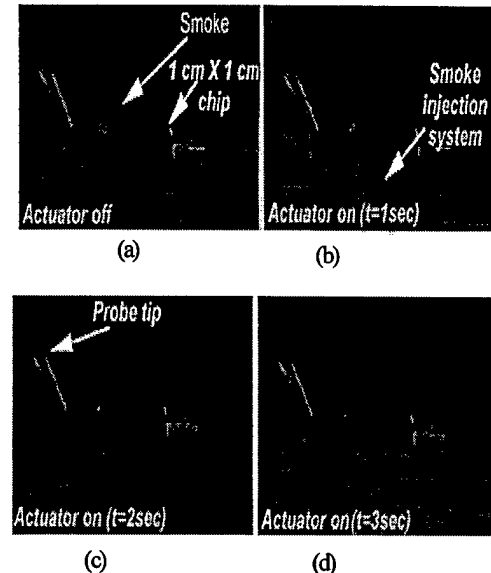


Fig. 11 Flow visualization of induced flow by actuator array

SUMMARY

High-aspect-ratio, in-plane microactuators have been designed, fabricated, and tested for fluid control. The goal is to let the microactuator induce a fluid flow so that the induced flow ultimately counters the high speed fluid generated by a vortex pair moving towards a wall region; thus reducing viscous drag. The reported in-plane microactuators are tested to perform as designed and to generate a local fluid flow. The induced upward flow was verified by the use of a hot-wire and a flow visualization by laser.

ACKNOWLEDGEMENTS

We would like to thank Prof. John Kim for the helpful discussions and James Liu for his help in conducting the flow visualization experiments. This work is partially supported by AFOSR-URI project.

REFERENCES

[1] Hefner, J. N. and Bushell, D. M., "Viscous Drag Reduction in Boundary Layers", *Progress in Astronautics and Aeronautics*, Vol. 123, pp. 203-324, 1990.

[2] Ho, C-M., Tung, S., Lee, G-B., Tai, Y-C., Jiang, F., and Tsao, T., "MEMS - A Technology for Advancements in Aerospace Engineering", *35th Aerospace Science Meeting & Exhibit*, Reno, pp. 1-10, Jan 6-10, 1997.

[3] Tsao, T., Liu, C., Tai, Y-C., and Ho, C-M., "Micromachined Magnetic Actuator for Active Fluid Control", *ASME Int. Mech. Eng. Congress and Expo.*, Chicago, pp.31-8, 1994.

[4] Ho, C-M., and Tai, Y-C., "REVIEW: MEMS and its Application for Flow Control", *Journal of Fluids Engineering*, Vol. 118, pp. 437-447, Sept., 1996.

[5] Ho, C-M., and Tai, Y-C., "Micro-Electro-Mechanical Systems (MEMS) and Fluid Flows", *Annual Review of Fluid Mechanics*, Vol. 30 pp. 579-612, 1998.

[6] Lee, C. and Kim, J., "Application of Neural Networks to Turbulence Control for Drag", Paper submitted to *Journal of Fluid Mechanics*.

[7] Legtenberg, R., Berenschot, E., Elwenspock, M., and Fluitman, J., "Electrostatic Curved Electrode Actuators", *Proc. IEEE Micro Electro Mechanical System Workshop*, Amsterdam, pp. 37-42, Feb., 1995.

[8] MCNC Center for Microelectronics Systems Technologies, Research Triangle Park, NC, USA.

[9] Mulher, G., Soane, D., and Howe, R., "Supercritical Carbon Dioxide Drying of Microstructures", *Proc 7th Int. Conf. Solid-State Sensors and Actuators (Transducer '93)*, Yokohama, Japan, pp. 296-299, June, 1993.

[10] Srinivasan, U., Houston, M., Howe, R., and Moboudian, R., "Self-assembled Fluorocarbon Films for Enhanced Stiction Reduction", *Proc 9th Int. Conf. Solid-State Sensors and Actuators (Transducer '97)*, Chicago, pp. 1399-1402, June, 1997.

[11] Kim, J., and Kim, C-J., "Comparative Study of Various Release Methods For Polysilicon Surface Micromachining", *IEEE Proc. 10th Int. Workshop on MEMS*, Japan , pp.442-447, 1997.

Flow Control by Using High-Aspect-Ratio, In-plane Microactuators

Faiz Sherman, Steve Tung**, Chang-Jin "CJ" Kim, Chih-Ming Ho, and Jason Woo*

Mechanical and Aerospace Engineering Department

*Electrical Engineering Department

University of California, Los Angeles,

Los Angeles, CA 90095-1597, U.S.A. (E-mail: cjkim@seas.ucla.edu)

**Presently with Litton Guidance and Control Systems
5500 Canoga, Woodland Hills, CA 91367

ABSTRACT

The successful design, modeling, fabrication, and testing of high-aspect-ratio large deflection in-plane microactuators are presented. The large displacement, in-plane actuator has a unique application in the area of fluid flow control. Unlike previously used electromagnetically actuated microflap in which motion was normal to the substrate, we introduce a novel design that alters the local fluid flow by moving the actuators parallel to the substrate. This new approach of "in-plane motion" allows for a condition free of "form drag." Furthermore, electrostatic drive allows for lower power consumption (μW). The actuator includes microplates that are $60 \mu\text{m} \times 200 \mu\text{m}$. These microplates, when moved parallel to the substrate surface, induces a "spanwise velocity" into the flow field above them. This induced velocity field, when applied to the near-wall streaks, would increase the transport of high-speed fluid away from the wall, therefore causing reduction in viscous drag. The actuators are made from silicon-on-insulator (SOI) wafers using a one mask deep reactive-ion-etching (DRIE) process. The microplates are suspended by a high-aspect-ratio cantilever structure (2 μm wide, 6-18 μm thick silicon) to ensure robustness against any disturbances in the out-of-plane direction. We present experimental verification of both the induced Stoke's flow and a local fluid flow created by our in-plane microactuators.

Key words: *Silicon-on-insulator, high aspect ratio, deep reactive ion etching, viscous drag reduction, in-plane actuator, large deflection*

INTRODUCTION

Conventional techniques for active control of fluid flow consist of changing the skin friction by wall motion, heating and cooling the wall, and injecting mass. These techniques are all being implemented in macroscale [1]. However, they suffer from severe limitation in the areas of spatial resolution, operational frequency of the actuator, and the power consumption. It therefore becomes apparent that MEMS actuators offer a very attractive solution for active control of fluid flow [2]. The inherent nature of MEMS devices offers excellent spatial resolution and high operational frequency with low power consumption.

Recently published work on magnetically actuated microflaps moving in the out-of-plane direction has shown the feasibility of active control of “streaks” (high speed fluid approaching the wall region) in microscale [2-5]. The control was done by displacing a microflap in the out-of-plane direction so as to produce an upward velocity against the streaks. This induced velocity field counteracts a streak, thereby reducing the viscous drag caused by the high speed fluid. The size of the microflaps used was of millimeter scale and magnetically driven. The operational frequency is thus limited, and the power consumption was relatively high (mW).

The goal of this paper is to realize the induction of a local fluid flow caused by in-plane actuation of an array of electrostatically driven microdevices. This induced local fluid flow could eventually serve to reduce viscous drag. The devices are made flush to the substrate and operate in the in-plane direction to be free from “form drag” (drag induced due to a physical presence of an object obstructing a flow). This is in contrast to the microflaps [4]. The reported in-plane microactuators are electrostatically driven and are approximately 10 times smaller than the magnetic microflap actuator, allowing for low power consumption ($< 1 \mu\text{W}$) and high operating frequency (500-1000 Hz).

THEORY AND MODELING

Flow Theory

Generally, the presence of a counter-rotating vortex pair gives rise to a region of high viscous drag, Fig. 1. These occurrences are known as “streaks”. Streaks bring in high speed fluid downward to the wall region increasing drag. It is expected that the viscous wall drag will be reduced if an upward flow is induced to counteract this downward motion of the high speed flow.

The physical sizes of the streaks are a function of Reynolds number. For this paper we choose a Reynolds number that is 10,000 (a parameter similar to test condition of the magnetic microflap [3]). With a Reynolds number of 10,000 the streaks have an average width of 900 μm and an average length of 30 mm. These physical feature sizes of the streaks dictate the design criteria of the microdevice. With such values of streak width and length, three criteria for the in-plane microactuator are required. The first is that the actuator end plates be as long as possible in order to interact with as much of the streak (from their length point of view). Secondly, the actuators should produce large enough plate displacement in order to affect the streaks (from their width point of view); otherwise, they would not have an effect on the streaks. Thirdly, the induced flow velocity must be large enough to interfere with the down flow of the incoming high speed fluid. The last condition dictates the actuators operate at relatively high frequency (~ 1 kHz).

An important parameter obtained from previous modeling effort [6] and data from the magnetic microflap actuator [3] suggest an induced velocity on the order of 1-10 cm/s to be sufficient to cause substantial reduction in viscous drag ($> 20\%$). To satisfy the criteria imposed by the flow conditions, our actuators are made to move long microplates (200 μm long) a distance over 100 μm with high operating frequency (0.5–1.2 kHz).

Design of the Actuator

The actuators consist of large microplates (60 μm wide, 200 μm long) attached at the end of a long cantilever beams (500-800 μm), see Fig. 2. The cantilever beams are electrostatically driven using angled electrodes [7,8]. Isolation bumpers (40 μm X 40 μm) are embedded within these electrodes to prevent shorting between the cantilever beams and driving electrodes. The size of the bumpers are designed to be large enough to allow for a timed release of the actuators while still ensuring good anchor to the substrate. The length of the supporting cantilever beams range from 500 to 800 μm and width and thickness range from 2-4 μm and 6-18 μm , respectively. These dimensions constitutes a high-aspect ratio device that is rigid in the out-of-plane direction and yet flexible in the in-plane direction. The microplates have within them 6 μm X 6 μm etch holes to control the HF etching time for release process. The actuators are configured in an array format in pair formation as shown in Fig. 2. This pair formation allows for maximum induction of fluid flow. They are also designed to be in a recessed area so that the top surface of the plates and the electrodes are on the same plane as the substrate surface (wall) to prevent any interference on the oncoming fluid.

Modeling of the Actuator

Electrostatic performance, resonance modes, and frequencies require rigorous analysis due to the fact that our actuators are operated under large deflection and high frequency conditions. An understanding of the effect of the large end plate on the dynamic response of the actuators is also necessary for the successful operation of the actuators.

Electrostatic modeling was performed via the coupling of a commercial finite element software (ANSYS) and a Fortran program. The material properties used for the modeling are: Young's modulus of 180 GPa, density of 2330 kg/m^3 , and Poisson's ratio of 0.27. Our modeling effort was compared with both previous experimental data [7] and data that was obtained by our in-plane actuators. Fig. 3 shows merit of predictability of our model with respect to the data.

Finite element model using ANSYS is done to determine the dynamic response of the cantilever-plate system. Both a modal analysis and a harmonic response analysis are performed for the case of a 4 μm wide, 18 μm thick, and 500 μm long actuator with an end plate that is 60 μm wide and 200 μm long. Fig. 4(a) shows the first resonance mode of the actuator, occurring at 2.5 kHz. Up to the actuator's fundamental frequency, the end plate follows the beam without any relative rotation to the cantilever tip and does not attenuate the amplitude. The second mode of the device is in the out-of-plane direction, Fig. 4(b), at 6.2 kHz. The third mode occurs at 34.7 kHz. At this mode, the rotational effect of the end plate keeps the overall in-plane motion of the end plate almost stationary, Fig. 4(c).

FABRICATION

Fabrication of the in-plane microactuators is done on commercially available, custom-ordered, Silicon-On-Insulator (SOI) wafers. The wafers had to meet three constraints imposed on them; a certain level of conductivity, thickness of sacrificial oxide, and the thickness of the top silicon. First, the high conductivity is required in order to have both a driving signal on the top silicon and a ground potential on the bottom silicon carried without metalization. Therefore the wafers needed to be heavily doped on both the handle wafer (i.e., the main substrate) and the device wafer (i.e., top layer). Second, the thickness of sacrificial oxide on the SOI wafer needs to be thick such that the cantilever and end plates are released, safety bumpers anchored, and the gap large enough to ensure long travel over the substrate during operation. Electrical breakdown through the oxide layer under high actuation voltage is yet another consideration. We used 3 μm thick oxide. Third, we varied the thickness of the top silicon (device layer) from 6 μm to 18 μm in order to fabricate high-aspect-ratio structures with narrow beam width (as small as 2 μm).

The fabrication consists of a single mask and three processing steps. We begin by using a Bond and Etch Back Silicon-On-Insulator (BESOI) wafer, Fig. 5 (a). The SOI wafer is made from two highly doped (100) 4 inch wafers (0.005 Ωcm). Wet oxide of 1.5 μm is grown on each wafer, and the wafers are then bonded, oxide to oxide, at room temperature. They are then placed in an 800 $^{\circ}\text{C}$ furnace to strengthen the bond. On completion of the annealing, one

side of the bonded wafer undergoes grinding to the target device thickness. Once the target thickness is reached, the wafers are polished to give a finished surface.

After photoresist is patterned to define the device, the wafers are sent to MCNC [9] for a deep reactive-ion etch (DRIE) which is performed through the device layer to the sacrificial oxide, Fig. 5(b). To account for non-uniformity across the wafer, a 15% over etch was used in combination with an end-point detection system. The photoresist is then stripped in-house and the wafers are diced to 1 cm X 1 cm dies which are used for actual flow experiments. Finally, the test chips undergo a release process, Fig 5(c). The release process is a timed etch of the sacrificial oxide. The oxide underneath the actuators is removed in 8 minutes of 49% HF. All the other structures have significantly larger anchor areas, therefore allowing them to remain anchored after the cantilevers and end plates have been released.

Releasing/drying was a challenge, despite the thickness of the beam (over 10 μm), due to the length (up to 1000 μm overall) and the existence of large plates at the end. The standard CO_2 supercritical drying [10] and surface passivation by self-assembled monolayer (SAM) coating [11,12], both proven effective for simple beams [13], produced a dismal result (< 10% yield) for the in-plane microactuators. For the CO_2 drying, it is speculated that the difficulty stemmed from replacing the methanol under the large plates with the CO_2 liquid through the narrow and deep trenches made by DRIE. Similar problems also make the SAM coating method ineffective.

A dramatic improvement has been found for the CO_2 drying when the chip was loaded “upside down” on completion of the methanol soak, apparently helping the methanol drip by gravity in lighter CO_2 liquid. Rinsing times are also increased to provide longer time for diffusion. The release process consists of 8 min in 49% HF followed by 30 minutes deionized (DI) water rinse in three successive baths (10 minutes each). The chips are then transferred to methanol and kept for yet another 30 minutes before CO_2 drying. Twenty CO_2 rinses are done with a dwelling time of 3 minutes in between each rinse. This release method provided a success close to 100% yield.

Fig. 6 (a) shows a pair of the recessed released actuator with the angled electrode configuration used to drive it. The recess serves a function of preventing any unwanted effects on the on-coming fluid flow. In addition, this design type shields the actuators against any perturbation in the flow that might cause the devices to break off. Fig. 6 (b) is the close-up showing the high-aspect-ratio beam, the end plate, release holes on it, angled drive electrodes, and electrostatic isolation bumpers.

TESTING

The two goals of this work were to verify Stoke's flow and net induced local flow in the direction opposite to the flow being brought in by a vortex pair. Verification of Stoke's flow was done by standard micro hot-wire, while that of the induced flow was done by a flow visualization technique.

To verify Stoke's flow, a hot-wire anemometer is placed 400 μm above the microactuator's end plate, Fig. 7. The hot-wire is turned on and a signal is recorded before activating the actuator. Then the actuator is turned on and made to displace the end plate 100 μm peak-to-peak at a frequency of 500 Hz. While the signal from the hot-wire is being recorded, the actuator is turned off again, Fig. 8. Fig. 8 clearly indicates that the signal obtained from the hot-wire is that of the induced Stoke's flow following the frequency of the actuator.

In the second experiment, a smoke generator introduces smoke onto a pair of actuators. A laser sheet shining through the smoke is placed on top of the actuators, Fig. 9. The entire experiment is enclosed in a controlled environment that allows for stagnant fluid. Once the smoke is introduced onto the actuators, it can be seen as a white feature, Fig. 10 (a). Fig. 10 (b) shows a zoomed up view of the smoke on top of the end plates. A reflection on the silicon is also seen. When the actuators are turned on, it was clearly seen that the smoke is displaced upward, therefore verifying net induced flow, Fig. 10(c). The upward flow is indicated by the clear separation that exist between the smoke and the die.

SUMMARY

Successful modeling, fabrication, and flow experiments have been presented in this paper. Our electrostatic and modal models accurately predict the performance of our microactuators. Using SOI wafers, we also demonstrated the one mask process required to fabricate the microdevices. In addition, the realization of both Stoke's flow and a net induced flow has been presented. These induced flows were verified by the use of a hot-wire and a flow visualization technique, respectively. It is through the successful design and fabrication of high-aspect-ratio, in-plane microactuators that made flow experiments possible. The unique MEMS design enabled a large enough induced flow to be detected via conventional fluid mechanics tools (hot-wire and flow visualization). The next step is to let the microactuator induce a fluid flow so that the induced flow ultimately act to counter the high speed fluid generated by an artificial vortex pair moving along a wall region; thus verifying reduction in viscous drag.

ACKNOWLEDGEMENTS

We would like to thank Prof. John Kim for the helpful discussions and James Liu for his help in conducting the flow visualization experiments. This work is partially supported by AFOSR-URI project.

REFERENCES

- [1] J. N. Hefner and D. M. Bushell, "Viscous Drag Reduction in Boundary Layers", *Progress in Astronautics and Aeronautics*, Vol. 123, pp. 203-324, 1990.
- [2] C.-M. Ho, S. Tung, G.-B Lee, Y.-C Tai, F. Jiang, and T. Tsao, "MEMS – A Technology for Advancements in Aerospace Engineering", *35th Aerospace Science Meeting & Exhibit*, Reno, NV, pp. 1-10, Jan 6-10, 1997.
- [3] T. Tsao, C. Liu, Y.-C. Tai, and C-M. Ho, "Micromachined Magnetic Actuator for Active Fluid Control", *ASME Int. Mech. Eng. Congress and Expo.*, Chicago, Il, pp.31-38, 1994.

[4] C.-M. Ho, and Y.-C. Tai, "REVIEW: MEMS and its Application for Flow Control", *J. Fluids Engineering*, Vol. 118, pp. 437-447, Sept., 1996.

[5] C.-M. Ho, and Y.-C. Tai, "Micro-Electro-Mechanical Systems (MEMS) and Fluid Flows", *Annual Review of Fluid Mechanics*, Vol. 30 pp. 579-612, 1998.

[6] C. Lee and J. Kim, "Application of Neural Networks to Turbulence Control for Drag", Paper submitted to *Journal of Fluid Mechanics*.

[7] R. Legtenberg, E. Berenschot, M. Elwenspock, and J. Fluitman, "Electrostatic Curved Electrode Actuators", *Proc. IEEE Micro Electro Mechanical System Workshop*, Amsterdam, Netherlands, pp. 37-42, Feb., 1995.

[8] S. Saffer, J. Simon, C.-J. Kim, "Mercury-Contact Switch with Gap-Closing Microcantilever," *SPIE Micromachined Devices & Components II*, Austin, TX, pp. 204-209, Oct. 1996.

[9] MCNC Center for Microelectronics Systems Technologies, Research Triangle Park, NC, U.S.A.

[10] G. Mulher, D. Soane, and R. Howe, "Supercritical Carbon Dioxide Drying of Microstructures", *Proc. 7th Int. Conf. Solid-State Sensors and Actuators (Transducer '93)*, Yokohama, Japan, pp. 296-299, June, 1993.

[11] U. Srinivasan, M. Houston, R. Howe, and R. Moboudian, "Self-assembled Fluorocarbon Films for Enhanced Stiction Reduction", *Proc 9th Int. Conf. Solid-State Sensors and Actuators (Transducer '97)*, Chicago, pp. 1399-1402, June, 1997.

[12] B. Sridharan, "A Study of Packaging and Surface Passivation for MEMS Devices" *Masters Thesis*, UCLA, June, 1998.

[13] J. Kim and C-J. Kim, "Comparative Study of Various Release Methods For Polysilicon Surface Micromachining", *Proc. IEEE Micro Electro Mechanical System Workshop*, Nagoya, Japan , pp. 442-447, Jan., 1997.

Biography:

Faiz Sherman received the B.S. and M.S. degree in mechanical engineering from the University of California, Los Angeles, in 1993 and 1995 respectively. In 1993 he was the departmental scholar, allowing him to pursue graduate studies and research as an undergraduate. In 1996 he was an Institute of Plasma and Fusion Research (IPFR) scholar. Coming from a background in experimental and theoretical heat transfer, he is now pursuing a Ph.D. candidate in MEMS. His research interests included in-plane microactuators for fluid flow control and Radio Frequency MEMS switches.

Steve Tung is an engineer specialist at Litton Guidance and Control Systems. His research interests include micromachining technology, fluid dynamics, and inertial guidance systems. He is currently working on the development of a bulk micromachined vibratory gyroscope. Dr. Tung received his B.S. degree in 1984 from the National Taiwan University and his Ph.D. degree in 1992 from the University of Houston, both in mechanical engineering. From 1992 to 1993, he was a lecturer in fluid mechanics at the mechanical engineering department of the University of Houston. In September 1993, he joined the fluid mechanics laboratory at the University of California, Los Angeles as a postdoctoral researcher. His research at UCLA focused on the development of an integrated system of micromachined sensors and actuators for active flow control.

Chang-Jin (CJ) Kim received the Ph.D. degree in mechanical engineering from the University of California at Berkeley in 1991 with a study on MEMS (Topic: Polysilicon Microgrippers). He received the B.S. degree from Seoul National University and M.S. from Iowa State University with the Graduate Research Excellence Award. He joined the faculty at UCLA in Mechanical and Aerospace Engineering Department in 1993 after post-doctoral work at UC Berkeley and the University of Tokyo. His research is in MEMS, especially the issues related to mechanical engineering, including design and fabrication of microstructures, microactuators and systems, use of surface tension in microscale, and micromanufacturing. He has developed three graduate courses in MEMS at UCLA and is also active in various MEMS professional courses. He is the recipient of the 1995 TRW Outstanding Young Teacher Award and the 1997 NSF CAREER Award.

He served as Chairman of the Micromechanical Systems Panel of the ASME Dynamic Systems and Control Division in 1996 and co-organized the Symposium on Micromechanical Systems since 1994 for the ASME International Mechanical Engineering Congress & Exposition, for which he edited the Proceedings of MEMS in 1996 and 1997. Prof. Kim also organized the 1996 ASME Satellite Broadcast Program, RMEMS: Case Studies of Commercial Products and served as General Co-chairman of the 6th IEEE International Conference on Emerging Technologies and Factory Automation (ETFA'97). He is currently serving in the Technical Program Committees of the IEEE Micro Electro Mechanical Systems Workshop and the SPIE Symposium on Micromachining and Microfabrication.

Professor Ho, Chih-Ming received his Ph.D. in Mechanics from The Johns Hopkins University and his BS in Mechanical Engineering from National Taiwan University. He is the Ben Rich - Lockheed Martin Professor and the Director of the Center for Micro Systems at UCLA. Professor Ho was elected a member of National Academy of Engineering. He is a Fellow of the American Physical Society and a Fellow of the American Institute of Aeronautics and Astronautics. He was an Associate Editor of the ASME Journal of Fluids Engineering from 1990 to 1993 and was an Associate Editor of the AIAA Journal from 1985 to 1987.

Jason C. S. Woo received the B. A. Sc. (Hons) degree in engineering science from the University of Toronto, Canada, in 1981, and the M. S. and Ph. D. degrees in electrical engineering from Stanford University in 1982 and 1987, respectively. He joined the department of electrical engineering of UCLA in 1987 and is currently a professor. He served on the IEEE IEDM program committee from 1989-1990, 1994-1996, and was the publicity vice chairman in 1992 and the publicity chairman in 1993. He is also the workshop chairman and a technical committee member of the VLSI Technology Symposium since 1992. He received a faculty development from IBM from 1987-1989.

His research interests are in the physics and technology of novel device and device modeling. He has done work on low temperature device for VLSI and space applications, SOI BiCMOS and GeSi BiCMOS. Significant achievements

include the analysis and fabrication of cryogenic Bipolar transistors, the identification of hot-carrier reliability failure modes at reduced temperatures, the first demonstration of GeSi quantum-well MOSFET's, and the investigation of device physics/technology for deep submicron SOI CMOS. He has also worked on technology such as drain engineering and alternative gate dielectrics to improve cryogenic CMOS performance and reliability. He has authored or co-authored over 90 papers in technical journals and refereed conference proceedings in these areas.

FIGURE CAPTIONS

Fig. 1 Formation and counteraction of streaks

Fig. 2 Design layout of in-plane microactuators

Fig. 3 Pull-in voltage prediction

Fig. 4 Modes of in-plane microactuator

(a) Fundamental mode (top view), (b) Second resonance mode, (c) Third resonance mode (top view)

Fig. 5 Flow Process (a) SOI wafer, (b) DRIE on device layer, (c) releasing structure by timed etch

Fig. 6 SEM pictures of the fabricated in-plane microactuators

(a) a pair of microactuators, (b) close-up view near the cantilever end and the plate

Fig. 7 Experimental set-up to verify induction of Stoke's flow

Fig. 8 Detection of Stoke's flow (500 Hz)

Fig. 9 Experimental set-up to detect induced flow

Fig. 10 Flow visualization of induced flow by actuator pair

(a) Smoke on full die, (b) Zoomed view of smoke on top of actuator pair (actuator is *off*), (c) Upward displacement of smoke when actuator is turned *on*

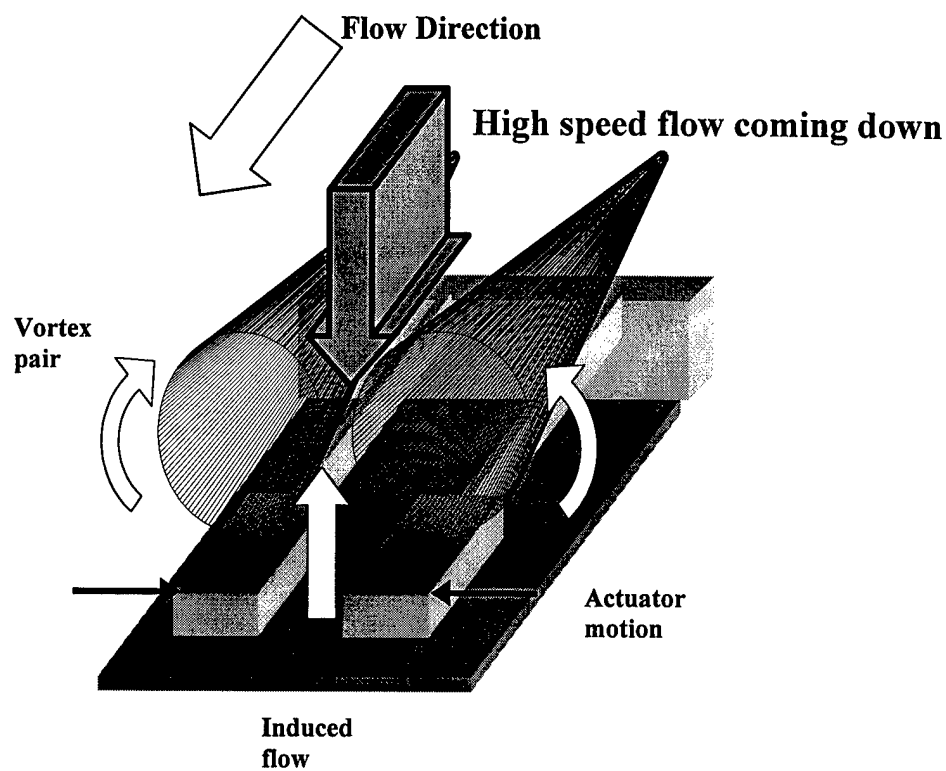


Fig. 1.

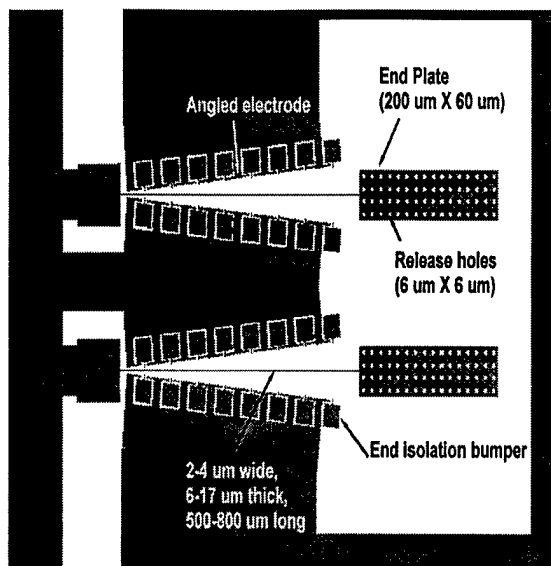


Fig. 2.

Electrostatic Model (500 um long, 12 um thick) Current experimental value

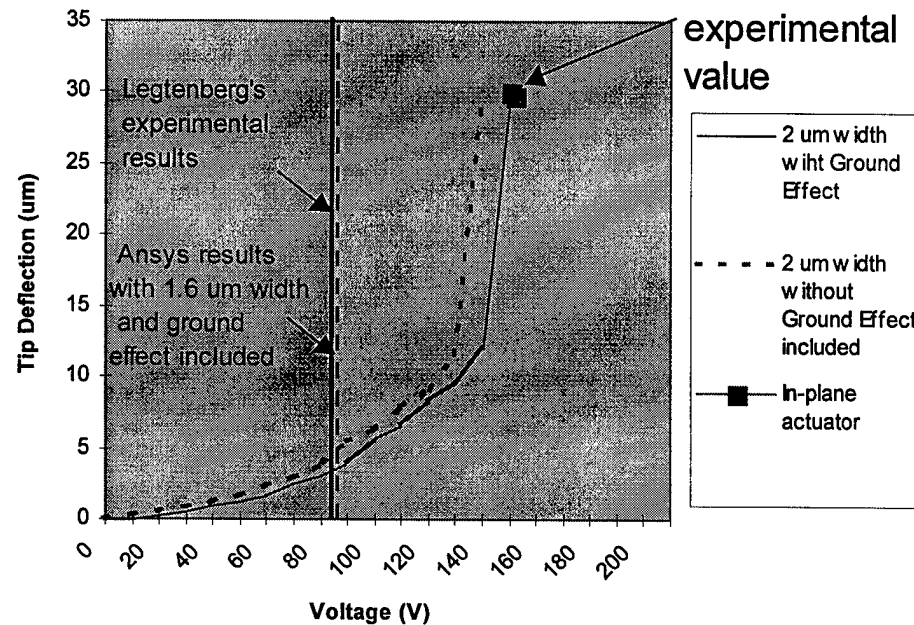
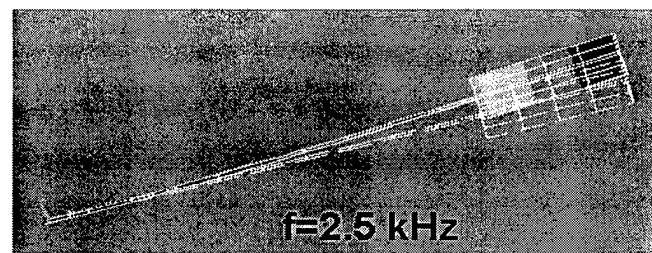
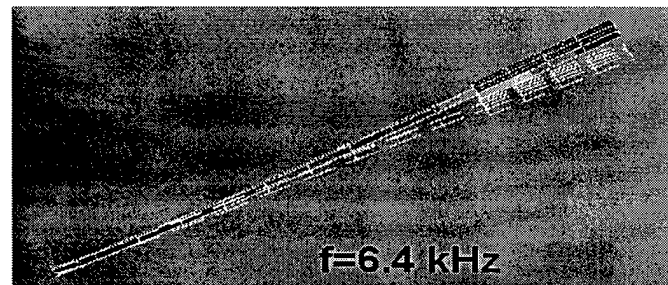


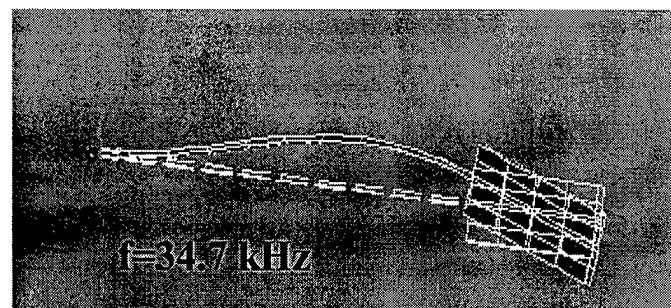
Fig. 3.



(a)



(b)



(c)

Fig. 4.

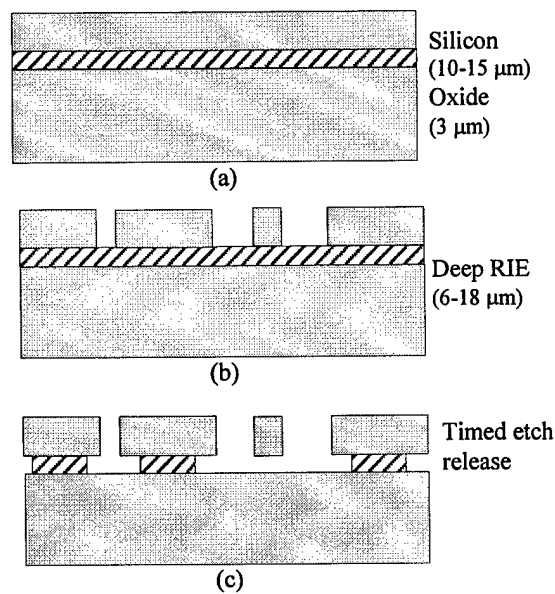
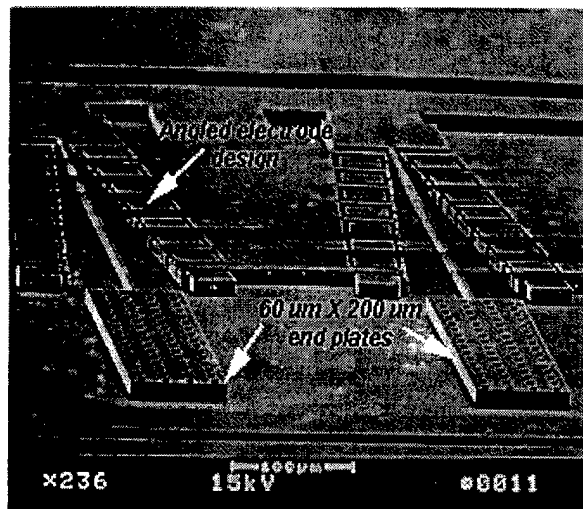
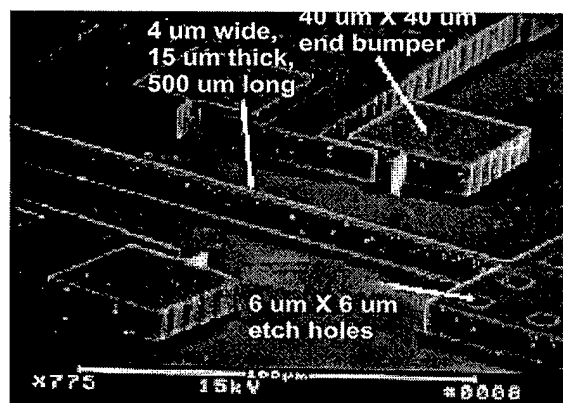


Fig. 5.



(a)



(b)

Fig. 6.

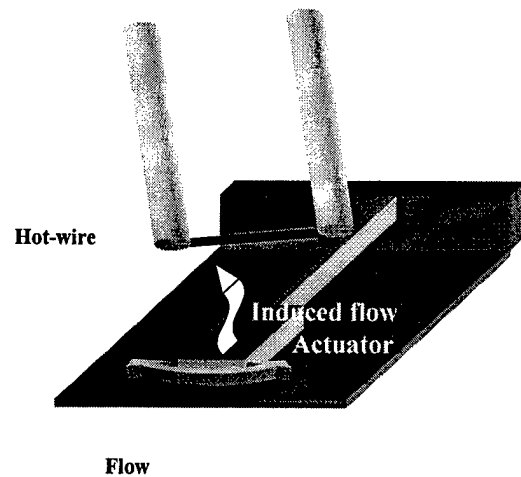


Fig. 7.

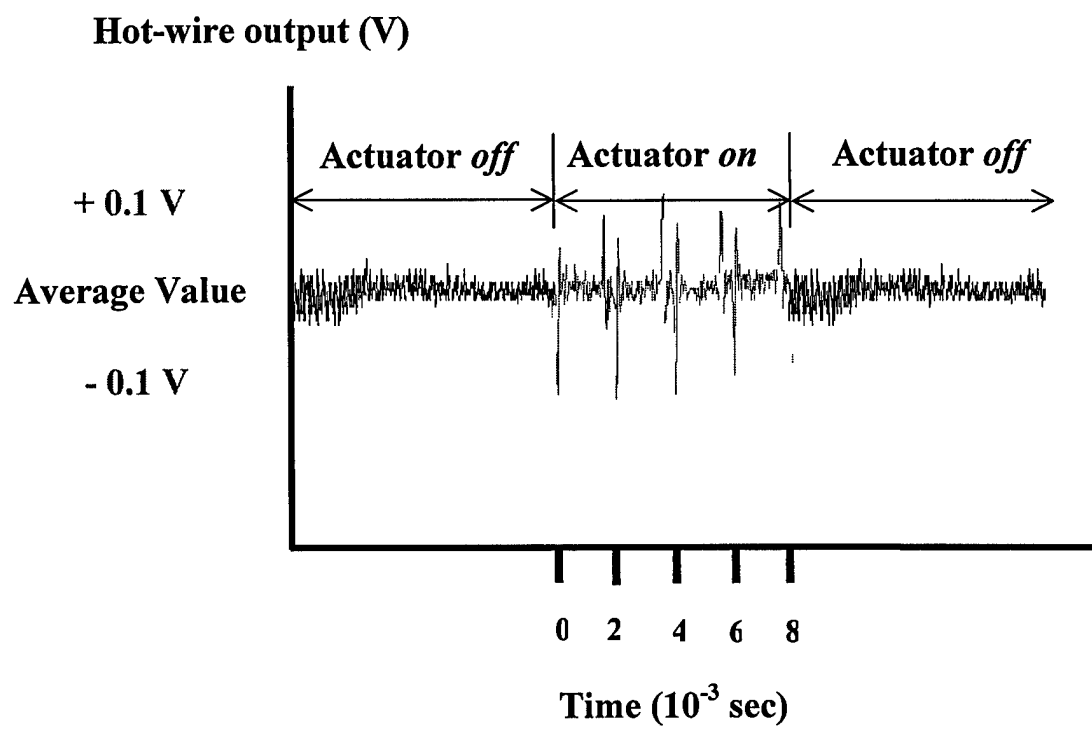


Fig. 8.

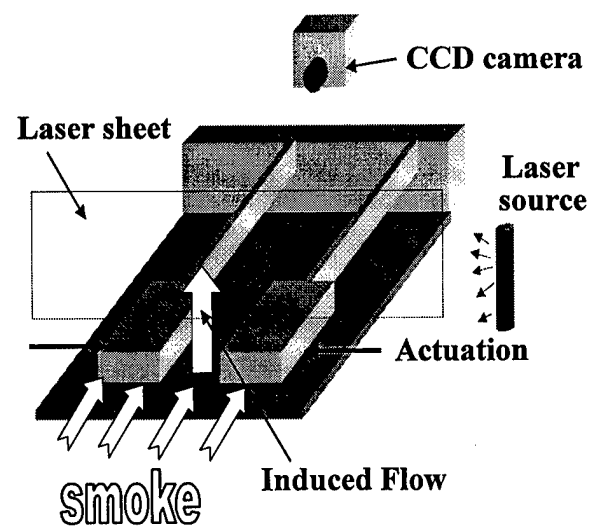


Fig. 9.

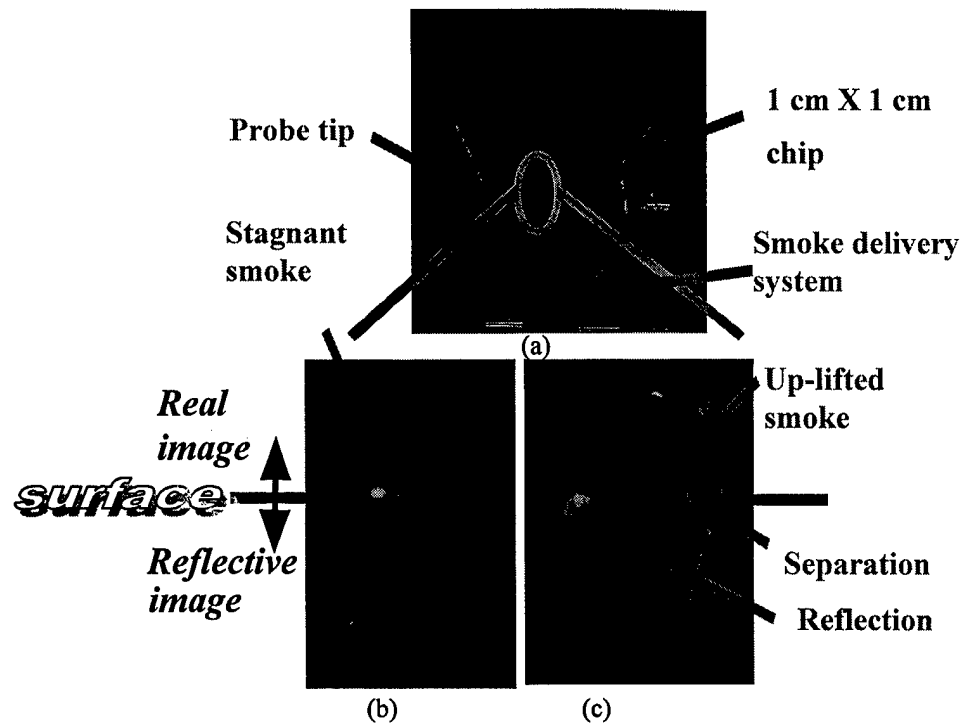


Fig. 10.